

ROBSON ROSA DA SILVA

New photonic structures:

I – Self assembly of 1D Te structures; II – Multifunctional biopolymers and reused plastics.

Novas estruturas fotônicas:

I – Auto-organização de estruturas 1D de Te; II – Biopolímeros e plásticos reutilizados multifuncionais.

A thesis submitted to the Institute of Chemistry,
São Paulo State University, in partial fulfillment
of the requirements for the degree of Doctor in
Chemistry.

Supervisor: Dr. Sidney J. L. Ribeiro
Co-supervisor: Dr. Pedro H. C. Camargo

Araraquara
2016

CATALOGUING DATA

S586n	<p>Silva, Robson Rosa da</p> <p>New photonic structures: I - Self assembly of 1D Te structures; II - Multifunctional biopolymers and reused plastics = Novas estruturas fotônicas: I - Auto-organização de estruturas 1D de Te; II – Biopolímeros e plásticos reutilizados multifuncionais / Robson Rosa da Silva. – Araraquara: [s.n.], 2016 259 p.: il.</p> <p>Tese (doutorado) – Universidade Estadual Paulista, Instituto de Química Orientador: Sidney José Lima Ribeiro Coorientador: Pedro Henrique Cury Camargo</p> <p>1. Telúrio. 2. Nanoestruturas. 3. Biopolímeros. 4. Plásticos. 5. Materiais óticos. I. Título.</p>
-------	--

CURRICULUM VITAE

IDENTIFICATION

Full name: Robson Rosa da Silva

Name in scientific citations: Silva, R. R.; Silva, Robson Rosa da; Silva, Robson Rosa; Da Silva, Robson R.; Da Silva, Róbson Rosa; Silva, Robson R.

Birth information: December 31st, 1988.

Nationality: Brazilian

Birth city: Itauçu-GO

Marital Status: Married

Filiation: Doracilda Rodrigues da Silva, Baltazar Rosa da Silva

Occupation: Chemist

PROFESSIONAL ADDRESS

1234 Paulino Rodella Av, APT 302 BL 04, Jardim das Flores, Araraquara-SP, ZIP 14801-788

FORMAL EDUCATION

2012: Master's degree in Chemistry.

São Paulo State University, UNESP, São Paulo-Brazil

Supervisor: Prof. Dr. Sidney José Lima Ribeiro

2009: Bachelor's degree in Chemistry

Universidade Federal de Goiás, UFG, Goiânia-Brazil

PUBLICATIONS IN SCIENTIFIC JOURNALS

Published papers

Silva, R.R.; Salvi, D. T. B.; Santos, M. V.; Barud, H. S.; Marques, L. F.; Santagneli, S. H. Tercjak, A.; Ribeiro, S. J. L. Multifunctional organic-inorganic hybrids based on cellulose acetate and 3-glycidoxypropyltrimethoxysilane. **Journal of Sol-Gel Science and Technology**. 2016, *in press*. doi: 10.1007/s10971-016-4089-x

Silva, R. R.; Mejia, A. H. G.; Ribeiro, S.J.L.; Shrestha, L. K.; Ariga, K.; Oliveira Jr., O. N.; Camargo, V. R.; Maia, L. J. Q.; Araujo, C. B. Facile synthesis of tellurium nanowires and study of their third-order nonlinear optical properties. **Journal of Brazilian Chemistry Society**, 2016, *in press*. doi: 10.5935/0103-5053.20160145.

Pinto, E. R. P.; Barud, H. S.; Silva, R. R.; Polito, W. L.; Calil, Vanessa L.; Cremona, M.; Ribeiro, S. J. L.; Messaddeq, Y. Transparent composites prepared by bacterial cellulose and castor oil based polyurethane as substrate for flexible OLEDs. **Journal Materials Chemistry C**, v. 3, p.11581-11588, 2015 (cover).

M. Luo, H. Huang, S.-I. Choi, C. Zhang, R. R. da Silva, H.-C. Peng, Z.-Y. Li, J. Liu, Z. He and Y. Xia. Facile synthesis of Ag nanowires with no plasmon resonance peak in the visible region by using Pd decahedra of 16 nm in size as seeds. **ACS Nano**, v. 9, p. 10523-10532, 2015.

Tireli, A. A.; Guimarães, I. R.; Terra, J. C. S.; Silva, R. R. ; Guerreiro, M. C. Fenton-like processes and adsorption using iron oxide-pillared clay with magnetic properties for organic compound mitigation. **Environmental Science and Pollution Research**. v. 22, p. 870-881, 2015.

Nigoghossian, K.; Santos, M. V. ; Barud, H. S.; Silva, R. R. ; Rocha, L. A.; Caiut, J. M. A. ; Assunção, R. M.N. ; Spanhel, L.; Poulain, M.; Messaddeq, Y. ; Ribeiro, S. J. L. Orange pectin mediated growth and stability of aqueous gold and silver nanocolloids. **Applied Surface Science**, v. 341, p. 28-36, 2015.

Moraes, M. L.; Lima, L. R.; Silva, R. R.; Cavicchioli, M.; Ribeiro, S. J. L. Immunosensor based on immobilization of antigenic peptide NS5A-1 from HCV and silk fibroin in nanostructured films. **Langmuir**, v. 29, p. 130221130155006-3834, 2013.

Silva, R. R.; Dominguez, C. T.; Santos, M. V.; Barbosa-Silva, R.; Cavicchioli, M.; Christovan, L. M. ; De Melo, L. S. A. ; Gomes, A. S. L.; Araújo, C. B.; Ribeiro, S. J. L. Silk

fibroin biopolymer films as efficient hosts for DFB laser operation. **Journal Materials Chemistry C**, v. 1, p. 7181, 2013.

Marques, L. F.; Corrêa, C. C.; Silva, R. R.; Santos, M. V.; Ribeiro, S. J. L.; Machado, F. C. Structure, characterization and near-infrared emission of a novel 6-connected uninodal 3D network of Nd(III) containing 2,5-thiophenedicarboxylate anion. **Inorganic Chemistry Communication**, v. 37, p. 66-70, 2013.

Marques, L. F.; Cantarut Jr., A. A. B. I; Correa, C. C.; Lahoud, M. G.; Silva, R. R.; Ribeiro, S. J. L.; Machado, F. C. First crystal structures of lanthanide-hydrocinnamate complexes: hydrothermal synthesis and photophysical studies. **Journal Photochemistry Photobiology A.**, v. 252, p. 69-76, 2012.

Silva, R. R., Alves, O. L.; Gomes, D. C. C. Síntese e estudo da condutividade em hexaazomacrocíclicos de cobalto (II) com ligantes aromáticos. **Enciclopédia biosfera**, v.6, 2010.

Accepted articles for publication.

Barud, H. G. O.; Barud, H. S.; Silva, R. R.; Tercjak, A.; Lustrri, W. R.; Oliveira Junior, O. B.; Ribeiro, S. J. L. A multipurpose natural and renewable polymer: bacterial cellulose in medical applications. **Carbohydrate Polymers**. 2016 (accepted).

Patents

Qin, D.; Xia, Y.; Yang, Y.; Li, J.; Sun, X.; Silva, R. R.; Yang, M. Silver nanowires, methods of making silver nanowires, core-shell nanostructures, methods of making core-shell nanostructures, core-frame nanostructures, methods of making core-frame nanostructures. US20160082418

Silva, R. R.; Maturi, F. E.; Barud, H. S. Ribeiro, S. J. L. Process for obtaining transparent and flexible composites based on expanded polystyrene disposal and bacterial cellulose. Disclosure ID: 15CI045 (accepted)

Amaral, T. S.; Barud, H. S.; Silva, R. R.; Ribeiro, S. J. L. Production of ZnO nanowires from bacterial cellulose. Disclosure ID: 15CI074 (accepted)

Book chapters

Ribeiro, S. J.L.; Santos, M. V.; Silva, R. R.; Pecoraro, E.; Gonçalves, R. R.; Caiut, J. M. A. The sol-Gel handbook: synthesis, characterization and applications. Wiley-VCH Verlag GmbH & Co. KGaA, v. 3, chap. 30, 2015.

Publication of extended abstract at international events

Silva, R. R.; Dominguez, C. T.; Santos, M. V.; Cavicchioli, M.; Barbosa-Silva, R.; Christovam, L. M.; Melo, L. S. A.; Ribeiro, S. J. L.; Araujo, C. B.; Gomes, A. S. L. Efficient distributed feedback dye laser in silk fibroin films. Conference on Lasers and Electro-Optics, San Jose-United States, 2012.

Publication & poster presentation of extended abstract in national events

Silva, R. R.; Maia, L. J. Q.; Ribeiro, S. J. L. Preparation and study of 1D multifunctional composites. In: 34th Annual Meeting of the Brazilian Chemical Society - International Year of Chemistry - 2011: Chemistry for a better world, Florianópolis-Brazil, in 2011.

Silva, R. R.; Ribeiro, S. J. L. Preparation of magneto-luminescent nanomaterials based on 1D nanostructures of tellurium. In: XIX XIX Journey of Young Scientists of the Association of Grupo Montevideo Universities - Science in the bicentennial of Latin American peoples, Ciudad del Este-Paraguay, 2011.

Silva, R. R.; Alves, L. O.; Cangussú, D. Synthesis and conductivity study of cobalt (III) hexaazomacrocycles with aromatic ligands. In: Scientific Initiation Seminar VII and IV Jornada Research and Graduate Studies, State University of Goiás - Scientific Initiation Seminar VII and IV Journey of Research and Graduate UEG, Anapolis-Brazil, 2009.

Silva, R. R.; Foggia, M. P. S. A.; Sartoratto, P. P. C. Coating of maghemite nanoparticles with amphiphilic polymer. In: VI Congress of Research, Education and Extension (CONPEEX) -

VI Congress of Research, Teaching and Extension, Federal University of Goiás, Goiânia-Brazil, 2009. p.8528-8533.

Sartoratto, P. P. C.; Silva, R. R.; Foggia, M. P. S. A. Functionalisation of nanoparticles maghemite bilayers with long-chain carboxylic acids. In: VI Congress of Research, Teaching and Extension (CONPEEX) - VI Congress of Research, Teaching and Extension-Research, Goiania-Brazil, 2009. p.8452-8456.

Silva, R. R.; Alves, L. O.; Gomes, D. C. C. Synthesis and conductivity study of cobalt (III) hexaazomacrocycles with aromatic ligands. In: 49th Brazilian Congress of Chemistry (CBQ) - XLIX Brazilian Congress of Chemistry: Chemistry and Sustainability, Proceedings, Porto Alegre-Brazil, 2009.

Silva, R. R.; Bermudez, V. C. Z. Thermal and spectroscopic study of linear polyethyleneimine /calcium triflate system. In: 49th Brazilian Congress of Chemistry (CBQ) - XLIX Brazilian Congress of Chemistry: Chemistry and Sustainability, Proceedings, Porto Alegre-Brazil, 2009.

Silva, R. R.; Sartoratto, P. P. C.; Caiado, K. L. Preparation of maghemite-silica nanocomposites. In: 15th Workshop on the Scientific Initiation - Proceedings / Abstracts of the 60th Annual Meeting of the Brazilian Society for the Advancement of Science, Campinas-Brazil, in 2008.

Silva, R. R.; Sartoratto, P. P. C. Preparation and study of magneto-optical properties of nanocomposites based on silica-maghemite. In: 4th Congress of Research, Teaching and Extension - Science, Education and Social Commitment, Goiânia- Brazil, 2007. p.1175-1178.

Abstract publications & poster presentation at international events

Silva, R. R.; Dominguez, C. T.; Santos, M. V.; Cavicchioli, M.; Barbosa-Silva, R.; Christovam, L. M.; Melo, L. S. A.; Ribeiro, S. J. L.; Gomes, A. S. L.; Araujo, C. B. Silk fibroin biopolymer films as efficient hosts for DFB Laser and Random Laser operation. 3rd International Conference on Multifunctional, Hybrid and Nanomaterials, Sorrento-Italy, 2013.

Silva, R. R.; Duarte, A.P.; Gressier, M.; Menu, M. J.; Dexpert-Ghys, J. Caiut, J. M., Franco Júnior, A. Ribeiro, S. J. L. Magneto-luminescent particles. [Eu(tta)₃(Bpy-Si)] modified Fe₂O₃@SiO₂ particles. 3rd International Conference on Multifunctional, Hybrid and Nanomaterials, Sorrento-Italy, 2013.

Barud, H. S.; Santos, M. V.; Santos, D. B.; Lima, L. R.; Silva, R. R.; Júnior, A. M. A.; Leite, R.; Saska, S.; Cavicchioli, M.; Messaddeq, Y.; Ribeiro, S. J. L. Multifunctional nanomaterials based on bacterial cellulose. 7th International Symposium on Advanced Materials and Nanostructures. Sorocaba-Brazil, 2012

Silva, R. R.; Ribeiro, S. J. L. Preparation of magneto-luminescent nanomaterials based on 1D nanostructures of tellurium. In: XIX XIX Journey of Young Scientists of the Association of Grupo Montevideo Universities - Science in the bicentennial of Latin American peoples, Ciudad del Este-Paraguay, 2011.

Ribeiro, S. J. L.; Silva, R. R.; Vorpapel, A. J.; Santos, M. V.; Santos, D. B.; Cavicchioli, M.; Christovam, L. M. Multifunctional organic-inorganic hybrids based on biocellulose, fibroin membranes and vegetable oils. In: XIV International Sol-Gel Conference - XIV International Sol-Gel Conference, Hangzhou-China, 2011.

Abstract publications & poster presentations in national events

Silva, R. R.; Barud, H. S., Maia, L. J. Q.; Ribeiro, S. J. L. Growth of one-dimensional tellurium nanostructures in bacterial cellulose. In: 34th Annual Meeting of the Brazilian Chemical Society - International Year of Chemistry - 2011: Chemistry for a better world, Florianópolis-Brazil, 2011.

Silva, R. R.; Foggia, M. P. S. A.; Sartoratto, P. P. C. Preparation and characterization of colloidal suspensions of maghemite/ Pluronic. In: 33th Annual Meeting of the Brazilian Chemical Society, Águas de Lindóia-Brazil, 2010.

Silva, R. R.; Sartoratto, P. P. C. Preparation of silica maghemite monoliths. In: 31st Annual Meeting of the Brazilian Chemical Society, Águas de Lindóia-Brazil, 2008.

Projects in e-learning chemistry education

2011-2/ 2012-1: Use of information technology and communication in the graduate discipline of Oleochemistry. Coordinator: Prof. Dr. Sidney José Lima Ribeiro; Financial Aid: Pro-rector of Graduate Studies (PROPG)-UNESP

2013-1/2014-1: Use of information and communication tools (ICT) in the 'special topics' discipline: Advanced Materials for Photonic Applications and stimulus actions to internationalization of the Post-Graduate Program in Chemistry (www.sampaproject.com). Coordinator: Prof. Dr. Sidney José Lima Ribeiro; Financial Aid: PROPG-UNESP. Function: e-tutor and web designer.

International experience

1) Georgia Institute of Technology

Atlanta, Georgia, United States

Supervision: Dr. Younan Xia

Project: a) Synthesis of ultrathin silver nanowires for photonic application, b) Synthesis of photonic crystals based on Au@Ag core-shell nanospheres, c) Preparation of magnetic-plasmonic nanoparticles based on the incorporation of magnetic nanoparticles into Au nanocages for biological application

Duration: 03/2014 – 03/2015

2) National Institute of Materials Science

Tsukuba, Ibaraki, Japan

Supervision: Dr. Lok Kumar Shrestha, Dr. Katsuhiko Ariga

Project: Preparation of multifunctional nanowires and nanotubes containing lanthanide ions based on 1D Te nanostructures as sacrificial template.

Duration: 09/2013 – 10/2013

3) Tras-Os-Montes e Alto Douro University,

Vila Real, Portugal

Supervision: Dra. Verónica Zea Bermudez

Fellowship Program *Luso-Brazilian Santander Universities*

Project: Thermal and spectroscopic Properties of solid-state batteries.

Duration: 09/2008 – 02/2009

International event production

Ribeiro, S. J. L., Pecoraro, E., Caiut, J. M. A., Nalin, M., Santagnelli, S. H., Manzani, D., Silva, R. R., Oliveira, T. J., Silva, M. M. 1st Advanced School on Materials for Photonic Applications: Glasses, Optical Fibers and Sol-Gel Materials, Institute of Chemistry, São Paulo State University, Araraquara-SP-Brazil. 2012

SUPERVISION

Student: Vanessa Rodrigues Camargo.

Curso: Licenciatura em Química.

Projeto: Estruturas unidimensionais de Te como suporte para preparação de materiais multifuncionais contendo íons lantanídeos.

Student: Natália Mendes Sanches.

Curso: Licenciatura em Química.

Projeto: Preparação de filmes híbridos orgânico-inorgânicos baseados em fibroína e íons lantanídeos para aplicações em sensoriamento de pH por monitoramento de luminescência.

Student: Fernando Eduardo Maturi.

Curse: Licenciatura em Química;

Project: Preparação de materiais fotônicos baseados em poliestireno expandido reciclado

Student: Thais Rodrigues Arroio.

Curse: Licenciatura em Química.

Project: Microesferas de fibroína incorporadas com nanopartículas ferromagnéticas.

ROBSON ROSA DA SILVA

Tese apresentada ao Instituto de Química,
Universidade Estadual Paulista, como parte
dos requisitos para obtenção do título de
Doutor em Química.

Araraquara, 23 de maio de 2016.

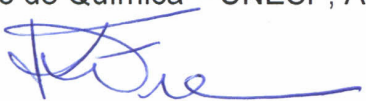
BANCA EXAMINADORA



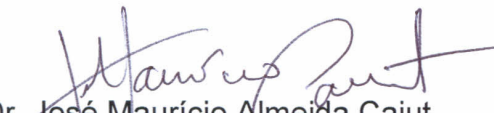
Prof. Dr. Sidney José Lima Ribeiro (Orientador)
Instituto de Química – UNESP, Araraquara -SP



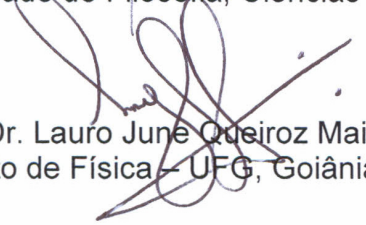
Prof. Dr. Marcelo Nalin
Instituto de Química – UNESP, Araraquara - SP



Prof^a. Dr^a. Regina Célia Galvão Frem
Instituto de Química – UNESP, Araraquara - SP



Prof. Dr. José Maurício Almeida Caiut
Faculdade de Filosofia, Ciências e Letras – USP, Ribeirão Preto - SP



Prof. Dr. Lauro Juné Queiroz Maia
Instituto de Física – UFG, Goiânia - GO

DEDICATION

This work is dedicated to the people that I care most: words are just not expressive enough. To my lovely wife Ranyella whose love is the greatest gift of my life and whose commitment, support and patience are true model for all.

ACKNOWLEDGMENTS

I ought to thank those that had a direct impact on my scholastic studies. First, the most gratitude to God for the gift of life and by always putting very special people along this track. I owe my advisor Sidney Ribeiro for his constant guidance. I am greatly indebted to him for the freedom extended to me and to engage my creativity as the same time. I am grateful that him long valuable resources and pushed me to work with high quality partner researchers whenever my dedication was lagging. I am very fortunate to have him as advisor, mentor and friend. His open-mindedness has greatly influenced my perception about scientific research.

I would like to thank Prof. Pedro Camargo for their insightful comments on my PhD studies who leverage me to work in an area that interest me. It has been a pleasure and honor to work with highly talented mentors outside. I have had the fortune of working with Prof. Katsuhiko Ariga and his team under mentoring of Dr. Lok Shresthra at National Institute of Materials. I'd like to thank each and every one of the members of Ariga group. Though it is impossible for me to thank everyone individually, I sincerely appreciate them all. I've learned much both technically and personally. I would like to express my sincere appreciation to Prof. Younan Xia for giving me the opportunity to join his team at Georgia Institute of Technology. I greatly appreciate your patience and guidance during this time. His dedication, untiring approach towards research, boundless energy and ability to cut complex concepts to simpler ones are inspirational. Thank you to make me a better scientist. I would also thank Prof. Dong Qin for your kindness and encouraging words. I would like to express my deepest thanks to all past and present members of Prof. Younan Xia for their endless support. I am glad to have built essential friendship in Atlanta with dear Denna Cummings, Dr. Ping Lu, Dr. Sang-Il Choi,(and whole Korean soccer team that I used to play with), Dr. Xiaohu Xia and Dr. Hsi-Chieh Peng. I am extremely grateful to have the chance to meet Ming Luo, Xuan Yang, Jessica Shang and Xiyu Li. I don't have words to thank you for your supportive Friday's pool car to 'buy foods' (the most useful pretext to have a break and share the funniest time together). I could not forget to mention Legna Figueroa for her endless encouraging support together with Madeline Vara and Aleksey Ruditskiy. Thank you so much to give me joy and funny company for almost half year, office-mates.

Sincere thanks go to all of my lab-mates, past and current, of the Laboratory of Photonics at Araraquara. I specially acknowledge my coworkers Vanessa Camargo, Fernando Maturi,

Natalia Mendes, Daniela Vassalo, Livia Christovam, Luana Alves, Mariana Garcia, Lais Lima, Dr. Denise Bonemer, Dr. Maurício Cavicchioli, Dr. Silvia Santagneli, Dr. Adriana Duarte (UFMS) and Dr. Lippy Marques (UERJ) for helping me with the synthesis and characterization of materials throughout the years. I would like to express my sincere gratefulness to Leandro Carneiro, Rafael Miguel and Molíria dos Santos for willingness to help, their friendship and for making each day enjoyable. I would like to single out and thank Dr. Hernane Barud, for setting the example of scientist and friendship.

My deepest appreciations go to my wife Ranyella Siqueira for her loving friendship, understanding, never ending support and for embracing my struggles as their own. Words will never ever express my gratitude for your help.

I gratefully mention the encouragement and unlimited support from my family throughout my graduate career. Undoubtedly, I have the biggest fans in the whole universe standing me up and holding me strong.

I would like thanks the financial support of the Brazilian agencies: Coordenação de Aperfeiçoamento de Pessoal de Nível Superior (CAPES), and Fundação de Amparo à Ciência e Tecnologia do Estado de São Paulo (FAPESP) for the Grant No. 2013/12367-6. I also thank the following publishers for their kind permission to reproduce previously published text and figures: The Royal Chemistry Society and Springer Publishing.

ABSTRACT

One-dimensional Te nanostructures (Te1D) in the shape of whiskers, wires and helices were prepared by a facile one-pot synthesis in the presence of aqueous Pluronic® F68 solution at low temperatures (< 100 °C) and ambient pressure. The shape of Te1D nanostructures could be maneuvered according with the reaction kinetics. We evaluate some techniques to assemble Te1D nanostructures on the pursuit for complex nanoarchitectures. Bundles of Te nanowhiskers and nanowires were achieved by self-assembly in liquid-liquid interface or by drop-cast technique in Si/SiO₂ substrates. 1D hybrid structures have been conceived by using Te1D nanostructures as sacrificial template to attach metallic nanoparticles or even produce metallic 1D nanostructures. For example, 1D hybrid nanostructures were easily prepared by decorating Te nanowires with Ag nanoparticles in aqueous solution of poly(vinylpyrrolidone). Au 1D nanostructures with nodular-like shape were prepared by galvanic displacement of Au³⁺ ions in a mixture of Te nanohelices, ascorbic acid and an aqueous solution of poly(vinylpyrrolidone). Furthermore, Te1D nanohelices were functionalized with a layer of resorcinol-formaldehyde resin at mild synthesis conditions. The RF resin allowed us to fashion an intermediate pathway to explore the deposition of optically active compounds like Tb³⁺ hydroxylcarbonate or Au nanoparticles. Seeking practical applications, these nanostructures should be hosted over rigid or flexible films possessing excellent optical properties. Pure natural polymers and epoxy sol-gel hybrids films were evaluated as potential host for luminophors. The fabrication of epoxy hybrids is based on the incorporation of 3-glycidoxypropyltrimethoxysiloxane on the homogenous solution of natural polymer with subsequent casting over flat surface. Particularly, flexible silk fibroin and cellulose acetate films and their derivative hybrids displayed excellent optical properties to host optically active compounds. For instance, red emitting Eu³⁺ compounds and fluorescent dyes were hosted on pure natural polymer and hybrid films and the optical features of the luminescent films were investigated thoroughly. Distributed feedback dye-lasers were fabricated by doping silk fibroin diffraction gratings with Rhodamine 6G. Owing its ability to mimic patterned surfaces at nanoscale resolution, dye-doped SF gratings were fabricated using replica-casting patterning against a commercial blank digital versatile disc as template. A modified DFB Laser based on SF films with Ag or SiO₂ light scattering particles randomly distributed on the grating unveiled an enhancement of laser intensity with narrowing of emission peak linewidth. Flexible and highly transparent SF- and CA-epoxy

hybrids (> 85%) containing red fluorescent Eu^{3+} β -diketonate complex and $\text{YVO}_4:\text{Eu}^{3+}$ nanoparticles at low relative content (< 5 wt%) were tailored. In general, the outcome is homogeneous films with epoxy and/or unhydrolyzed alkoxy silane functions available for further chemical modification.

Owing the limited feedstock of natural polymers for high demanding production of optical devices, it is equally important develop materials based on the reuse of synthetic polymers. Thin films of polystyrene were conceived by dissolving waste-recovered expanded-polystyrene (EPS) in D-limonene, a green solvent from citrus oil. Transparent EPS films doped with Eu^{3+} β -diketonate complex displayed excellent transparency and light waveguiding, These assertions provide a framework that motivates the research on a) engineering of 1D hybrids nanostructures with tunable optical properties and b) flexible natural polymer/epoxy hybrid with enhanced functionality or plastic recycled as potential optical hosts sought in photonic applications.

Keywords: Tellurium. Phenol-formaldehyde resin. Hybrids. Lanthanide. Silk Fibroin, Cellulose Acetate, 3-glycidoxypropyltrimethoxysilane. Expanded polystyrene. D-limonene.

RESUMO

Nanoestruturas unidimensionais de telúrio (Te1D) na forma de whiskers, fios e hélices foram preparados com facilidade por uma síntese em etapa única na presença de solução aquosa de Pluronic® F68 à baixas temperaturas ($< 100\text{ }^{\circ}\text{C}$) e pressão ambiente. A forma das nanoestruturas puderam ser controladas de acordo com a cinética da reação. Estruturas empacotadas de nanowhiskers e nanofios de Te foram obtidas via auto-organização em interface líquido-líquido e pela técnica de drop-cast em substrato de Si/SiO₂. Estruturas híbridas 1D foram obtidas utilizando nanoestruturas Te1D como molde de sacrifício para anexar nanopartículas metálicas ou mesmo produzir nanoestruturas 1D metálicas. Por exemplo, nanoestruturas híbridas 1D foram preparadas decorando nanofios de Te com nanopartículas de Ag em solução aquosa de poli(vinilpirrolidona). Nanoestruturas 1D de Au com forma de nódulos foram preparados por deslocamento galvânico de íons Au³⁺ em uma mistura de nanohélices de Te, ácido ascórbico e solução aquosa de poli(vinilpirrolidona). Além disso, nanohélices de Te foram funcionalizadas com uma camada resina resorcinol-formaldeído em condições brandas de síntese. A resina de resorcinol-formaldeído é uma via intermédia para explorar a deposição de compostos opticamente ativos tais como nanopartículas de hidroxicarbonato de Tb³⁺ ou nanopartículas de Au. Para aplicações práticas é essencial que estas nanoestruturas possam ser suportadas em filmes rígidos ou flexíveis de alta qualidade óptica. Filmes de polímeros naturais puros e filmes híbridos de sol-gel epóxi foram avaliados como potenciais matrizes hospedeiras para luminóforos. A fabricação de híbridos é baseada na incorporação de 3-glicidoxipropiltrimetoxissilano na solução homogênea de polímero natural com posterior secagem sobre uma superfície plana. Particularmente, filmes flexíveis de fibroína da seda e acetato de celulose e os seus híbridos derivados exibiram excelentes propriedades ópticas para hospedar compostos opticamente ativos. Por exemplo, compostos de Eu³⁺ emissores na região do vermelho e corantes fluorescentes foram incorporados em matriz pura de polímero e híbridos epóxi e suas propriedades ópticas foram investigadas. Laser de corantes por feedback distribuído (DFB) foram fabricados dopando grades de difração de fibroína de seda com Rodamina 6G. Devido a sua capacidade de replicar superfícies padronizadas com resolução nanométrica, grades de fibroína da seda dopadas com corante foram depositadas contra a grade de difração de uma mídia de disco compacto comercial. Lasers modificados de DFB baseados em filmes de fibroína contendo nanopartículas espalhadoras de luz de SiO₂ e Ag

aleatoriamente distribuídas na grade de fibroína demonstraram aumento da intensidade do laser, além de estreitamento da largura do pico de emissão. Filmes híbridos flexíveis e transparentes (> 85%) de fibroína da seda e acetato de celulose modificados com função epóxi e contendo compostos fluorescentes na região do vermelho como complexos β -dicetonato de Eu^{3+} e nanopartículas de $\text{YVO}_4:\text{Eu}^{3+}$ em baixa proporção relativa mássica (<5%) foram preparados. De maneira geral, o resultado são filmes homogêneos com funções epoxi e/ou alcoxissilano não hidrolisados disponíveis para outras modificações químicas. Devido a matéria-prima limitada de polímeros naturais para uma alta demanda de fabricação de dispositivos ópticos, é igualmente importante desenvolver materiais com base na reutilização de polímeros sintéticos. Filmes finos de poliestireno foram concebidos por dissolução de poliestireno expandido (EPS) recuperado de resíduos em D-limoneno, um solvente verde proveniente de óleos cítricos. Filmes transparentes dopados com complexos β -dicetonato de Eu^{3+} demonstraram excelente transparência e aptos para uso em guias de luz. Estes resultados são motivadores para a) a engenharia de nanoestruturas 1D com propriedades ópticas sintonizáveis bem como, b) desenvolvimento de híbridos flexíveis e transparentes baseados em híbridos de polímeros naturais com alta funcionalidade química ou polímeros sintéticos reciclados como potenciais matrizes hospedeiras ópticas almejadas em aplicações fotônicas.

Palavras-Chave: Telúrio. Resina resorcinol-formaldeído. Híbridos. Lantanídeos. Fibroína da seda. Acetato de celulose. 3-glicidoxipropiltrimetoxissilano. Poliestireno expandido. D-limoneno.

SYMBOL TABLE

$A_{0 \rightarrow J}$	Spontaneous emission coefficients of ${}^5D_0 \rightarrow {}^7F_J$
$S_{0 \rightarrow J}$	Emission curve areas of ${}^5D_0 \rightarrow {}^7F_J$ transitions
$\tilde{\nu}$	Average transition energy in cm^{-1}
$\sigma_{0 \rightarrow J}$	energy baricenters
AA	Ascorbic acid
AFM	Atomic force microscopy
A_{nrad}	Non-radiative decay rate
A_{rad}	Radiative decay rate
ATR-FTIR	Attenuated total reflection - Fast Fourier Transform Infrared
Au1D	One-dimensional nanostructures of gold
BSE	Back-scattered electrons
CA	Cellulose acetate
CA-GPTMS	Cellulose acetate/3-glycidyloxypropyltrimethoxysilane hybrids
CP-MAS	Cross Polarization Magic Angle Spinning
CT	Charge-transfer
CTAB	Cetyltrimethylammonium bromide
CTAC	Cetyltrimethylammonium chloride
CW	continuous wave
$C\beta$	β -carbon
D_{ED}	electric and magnetic dipole strength
D_{ED}	Magnetic dipole strength
DFB	Distributed feedback
DSC	Differential Scanning Calorimetry
DTA	Differential thermal analysis
DVD	Digital versatile disc
EDS	Energy-dispersive spectroscopy
EDX	Energy-dispersive X-ray
E_g	Band gap energy
EPS	Expanded polystyrene

FCC	Face centered cubic
FEG-SEM	Field Emission Gun - Scanning Electron Microscopy
FFT	Fast-Fourier Transform
GPTMS	Glycidoxypropyltrimethoxysilane
	Planck's Constant is divided by 2π
HRTEM	High-Resolution Transmission Electron Microscopy
l_s	thickness scattering mean free path
LSP	Localized surface plasmons
LSPR	Localized surface plasmon resonance
MTT	Tetrazolium 3-(4,5-dimethylthiazol-2-yl)-2,5-diphenyl tetrazolium bromide).
n	Refractive index
NPs	Nanoparticles
n_w	Number of water molecules
OD	Optical density
PBS	Phosphate buffer
PS	polystyrene
PVP	Poly(vinylpyrrolidone)
RC	Replica-casting
RF	Resorcinol-formaldehyde resin
Rh6G	Rhodamine 6G.
RL	Random laser
SAED	Selected area electron diffraction
SAXS	Small angle X-ray diffraction
SF	Silk fibroin
SF	Silk fibroin
SF _{Ag}	Silk fibroin grating samples containing Ag nanoparticles
SFGPTMS	Silk fibroin/3-glycidyloxypropyl trimethoxysilane hybrids
SFRod	Silk fibroin doped with Rhodamine 6G
SFSi	Silk fibroin grating containing silica nanoparticles
Te@Ag	One-dimensional hybrid nanostructures of tellurium and silver
Te@Au	One-dimensional hybrid nanostructures of tellurium and gold

Te@C	One-dimensional tellurium nanostructures coated carbon shell
Te@RF	One-dimensional Te nanostructures covered with resorcinol-formaldehyde resin.
Te@RF/Au	One-dimensional Te nanostructures covered with resorcinol-formaldehyde resin with attached Au nanoparticles
TeA	Tellurium derivative nanostructures described in 3.1.1
TeB	Tellurium derivative nanostructures described in 3.1.2
TEM	Transmission Electron Microscopy
TG	Thermogravimetry
TGA	Thermogravimetric analysis
TMS	Tetramethylsilane
T ⁿ	Silicon linked with n siloxane units
T _{onset}	Degradation onset temperature
TPPM	Two Pulse Phase Modulation
<i>tta</i>	Thenoyltrifluoroacetate
UV-vis	Ultraviolet – visible
<i>w</i>	Thickness
XRD	X-ray diffraction
η	Quantum efficiency
λ_{em}	Emission wavelength
λ_{exc}	Excitation wavelength
σ_s	Scattering cross section
τ	Experimental emission lifetime
τ_{rad}	Radiative lifetime
χ	Lorentz local field correction term
Ω	Judd-Ofelt intensity parameters radiative
<i>c</i>	Velocity of light
<i>e</i>	Electronic charge
ω	Angular frequency of the transition

TABLE OF CONTENTS

1.	STATE OF THE ART	25
1.1.	Tellurium	26
1.1.1.	<i>One-dimensional Te nanostructures</i>	28
1.1.2.	<i>One-dimensional Te hybrids</i>	30
1.1.3.	<i>Te@C hybrid nanostructures</i>	31
1.1.4.	<i>Assembly of 1D Te derivative nanostructures</i>	34
1.2.	Biopolymers as flexible transparent substrates	35
1.2.1.	<i>Natural polymers for photonics</i>	36
1.2.2.	<i>Silk Fibroin</i>	41
1.3.	Organic-inorganic hybrid	44
2.	OBJECTIVES AND THESIS ORGANIZATION	48
3.	STUDY OF THE SYNTHESIS TE NANOWHISKERS, NANOWIRES AND NANOHELICES AND FABRICATION OF TE@X 1D HYBRIDS (X = AG, AU OR RESORCINOL-FORMALDEHYDE RESIN)	52
3.2.	Experimental Section	54
3.1.1.	<i>Standard synthesis of Te1D nanostructures in Pluronic® F68</i>	54
3.1.2.	<i>Scaling up the synthesis of Te1D nanostructures by twenty times</i>	54
3.1.3.	<i>Synthesis of 1D Te@Ag hybrid nanostructures</i>	55
3.1.5.	<i>Synthesis of 1D Te@resorcinol-formaldehyde (RF) nanocables</i>	56
3.1.6.	<i>Synthesis of Te@RF/X nanocomposites, with X= YVO₄:Eu³⁺, Au nanospheres or Ag nanocubes</i>	56
3.1.6.1.	<i>Synthesis of YVO₄:Eu³⁺ nanoparticles</i>	56
3.1.6.2.	<i>Synthesis of Au nanospheres</i>	57
3.1.6.3.	<i>Synthesis of Ag nanocubes</i>	57
3.1.7.	<i>Preparation of 1D Te@RF/(LaCeTb)CO₃OH nanostructures</i>	58
3.1.8.	<i>Preparation of 1D Te@RF/Au nanostructures</i>	58
3.2.	Results and discussion	58
3.2.1.	<i>Tellurium nanowhiskers and nanowires</i>	58
3.2.2.	<i>Liquid-liquid-air interface (polar/apolar solvent)</i>	63
3.2.3.	<i>Self-assembly by drop casting method</i>	64

3.2.5.	<i>Tellurium nanohelices</i>	70
3.2.6.	<i>Te@Au hybrids nanostructures from Te nanohelices</i>	72
3.2.7.	<i>Te@resorcinol-formaldehyde (RF) core-shell nanocables from Te nanohelices</i>	74
3.2.8.	<i>Synthesis of Te@RF hybrid materials</i>	78
3.3.	Conclusions	87
4.	SILK FIBROIN BIOPOLYMER FILMS AS EFFICIENT FLEXIBLE HOST FOR DISTRIBUTED FEEDBACK LASER	93
4.1.	Experimental Section	95
4.1.1.	<i>Extraction of silk fibroin</i>	95
4.1.2.	<i>Preparation of silver nanoparticles</i>	96
4.1.3.	<i>Synthesis of silica nanoparticles</i>	96
4.1.4.	<i>Fabrication of DFB silk fibroin gratings</i>	96
4.1.5.	<i>Characterization</i>	97
4.1.6.	<i>Experimental setup for the lasing measurements</i>	97
4.2.	Results and discussion	98
4.3.	Conclusions	110
5.	FUNCTIONAL AND TRANSPARENT HYBRIDS BASED ON SILK FIBROIN AND 3-GLYCIDOXYPROPYLTRIMETHOXYSILANE	115
5.1.	Experimental section	117
5.1.1.	<i>Materials</i>	117
5.1.2.	<i>Preparation of aqueous SF solution</i>	117
5.1.3.	<i>Preparation of free-standing silk fibroin/3-glycidoxypropyltrimethoxysilane hybrid films</i>	117
5.1.4.	<i>Preparation of YVO₄:Eu³⁺ nanoparticles</i>	117
5.1.5.	<i>Preparation of luminescent silk fibroin/3-glycidoxypropyl trimethoxysilane hybrid films</i>	118
5.1.6.	<i>Cytotoxicity assay</i>	118
5.1.7.	<i>Instrumentation</i>	119
5.2.	Results and discussion	120
5.3.	Conclusion	139

6.	MULTIFUNCTIONAL ORGANIC-INORGANIC HYBRIDS BASED ON CELLULOSE ACETATE AND 3-GLYCIDOXYPROPYLTRIMETHOXYSILANE	146
6.1.	Experimental section.....	148
6.1.1.	<i>Materials</i>	<i>148</i>
6.1.2.	<i>Synthesis of luminescent tris(2-thenoyltrifluoroacetato)europium(III) dihydrate complex.....</i>	<i>148</i>
6.1.3.	<i>Preparation of cellulose acetate/3-glycidoxypropyltrimethoxysilane hybrid films.....</i>	<i>148</i>
6.1.4.	<i>Preparation of luminescent cellulose acetate/3-glycidoxypropyltrimethoxysilane hybrid film.....</i>	<i>148</i>
6.1.5.	<i>Instrumentation</i>	<i>149</i>
6.2.	Results and discussion	150
6.3.	Conclusion.....	165
7.	THIN FILMS BASED ON POLYSTYRENE WASTES RECOVERY FOR OPTICAL APPLICATIONS	170
7.1.	Experimental procedure.....	171
7.1.1.	<i>Materials</i>	<i>171</i>
7.1.2.	<i>Synthesis of luminescent [Eu(tta)₃(H₂O)₂] complex</i>	<i>172</i>
7.1.3.	<i>Fabrication of PS-Eu thin films by spin-coating</i>	<i>172</i>
7.1.4.	<i>Instrumentation</i>	<i>172</i>
7.2.	Results and discussion	173
7.3.	Conclusions	181
8.	DISCUSSION	184
9.	CONCLUSION.....	190

1. STATE OF THE ART

The size and shape in one-dimensional nanomaterials have attracted a great deal of interest due to the dependent quantum confinement effects of the atoms in low dimensionality and the employing of their structural arrangement in new potential applications like building blocks (CHATTOPADHYAY; CHEN; CHEN, 2011; FANG et al., 2010). Currently, the most successful examples of one-dimensional nanostructures on both scientific and technological perspectives are carbon nanotubes (VOLDER et al, 2013), Si (DASGUPTA et al, 2014) and Ag nanowires (DINH et al, 2013). Further, 1D nanostructures are considered ideal model system for investigating the size and morphology dependence in optical, electrical, magnetic and mechanical properties. One-dimensional semiconductor nanostructures are efficient transporters of electrons and excitons and substantial efforts have been paid attention to the emergence of anisotropic electro/optical effects for applications like ultrafast all-optical switching devices (TATSUURA et al., 2003; ZHU et al., 2006) frequency converters (HAN et al., 2012), optical limiting or light-emitting diodes (KIM et al., 2012) and lasers (HUANG et al., 2001). The assembly of 1D materials is responsible by emergence of new anisotropic properties which the manipulation into complex and ordered architectures have attracted great interest for the development of sensors and photonics applications (LIM; LIM, 2013). Likewise, the addition of optical materials into nanostructured 1D array may be interesting for optical gain studies such as stimulated emission processes in the development of field emitter devices. 1D binary compounds based in organic dyes have been explored to study the wave guiding and lasing properties to enhance the performance of optical and optoelectronic devices (ZHANG et al., 2013). Intrinsic luminescent 1D nanostructures such as binary semiconductors (i.e ZnSe, CdS, CdSe, PbTe, CdTe etc.) or oxides (ZnO) have been extensively studied as a stand-alone optical cavity and gain medium for nanolasers applications. In particular, intense research has focused in lanthanide ions. The great interest in the study of nanoparticle systems combining compounds based on lanthanide ions is due to the variety of possible applications concerning their outstanding spectroscopic properties. In fact the sharp spiked emission spectra regarding from UV to the IR spectral range, relative long lifetimes of excited states (μs , ms), large Stokes shifts ($> 150 \text{ nm}$), and high quantum yield (~ 1) make the lanthanide ions interesting compounds in photonic applications as luminescent markers in biology and medicine, lasers and optical amplifiers (BINNEMANS, 2009; BÜNZLI; ELISEEVA, 2010; BÜNZLI; PIGUET,

2005; CARLOS et al., 2009) and thermometry (BRITES et al., 2010; CHAMBERS; CLARKE, 2009). In crystals containing lanthanide ions in uniaxial morphology, interesting spectroscopic properties are investigated. Song et al., 2004 investigated the luminescence of nanowires and nanoparticles of $\text{LaPO}_4:\text{Eu}^{3+}$ and observed an enhancement of quantum efficiency in nanowires. The authors found that Eu^{3+} occupies additional crystallographic sites in anisotropic compound.

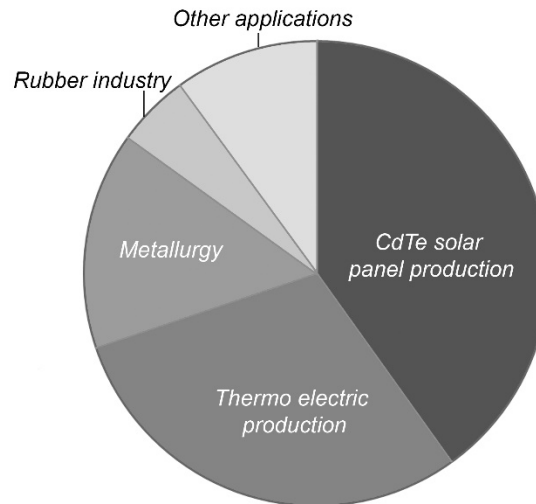
Luminescent $\text{Gd}_2\text{O}_3:\text{Eu}$ and $\text{Gd}_2\text{O}_3:\text{Yb-Er}$ nanorods and nanotubes have been investigated in optical imaging and fluorescent labeling applications (DEBASU et al., 2011). The authors concluded that the emission lifetime was dependent to the size of 1D nanostructures.

The possibility of organizing nanostructures, including nanowires and nanotubes based on lanthanide compounds energy converters of $\text{NaYF}_4:\text{Yb, Er}$ was explored in the assembly of macrostructures (super networks) (YE et al., 2010). The synthesis of nanophosphors opens very promising perspectives for applications in biology and energy. Among naturally occurring anisotropic materials, tellurium holds great promise as template for the preparation of one-dimensional luminescent nanostructures.

Next section will give a state of the art of tellurium nanostructures since the first studies and current efforts from both scientific and technological perspectives.

1.1. Tellurium

Tellurium is mostly obtained (90 %) from electrolytic refining of smelted copper (extracted from anode slimes). Japan is the largest producer of refined element. According with 2016 United States Geological Survey report, the world production of tellurium is estimated at 400 tons (GOLDFARB, 2015). The concentration of tellurium found in the most of rocks is below 3 ppb. To date, the abundance of tellurium is inferior to rare earth elements and eight times less abundant than gold. About 40% of high-purity tellurium is consumed for the production of CdTe solar panels as highlighted in Figure 1. In metallurgy, Te is usually used as an additive in steel, copper and lead alloys to improve machinability and resistance to vibration and fatigue. Tellurium can replace selenium or sulfur as vulcanizing agent, accelerator agent in the rubber industry, as well as a component of catalysts for synthetic fiber production. Other uses included those in photoreceptor devices and as a pigment to produce various colors in glass and ceramics. Figure 1. Global consumption estimates for the end use of tellurium are as follows: solar, 40%; thermoelectric power generation, 30%; metallurgy, 15%; rubber applications, 5%; and 10%, other.

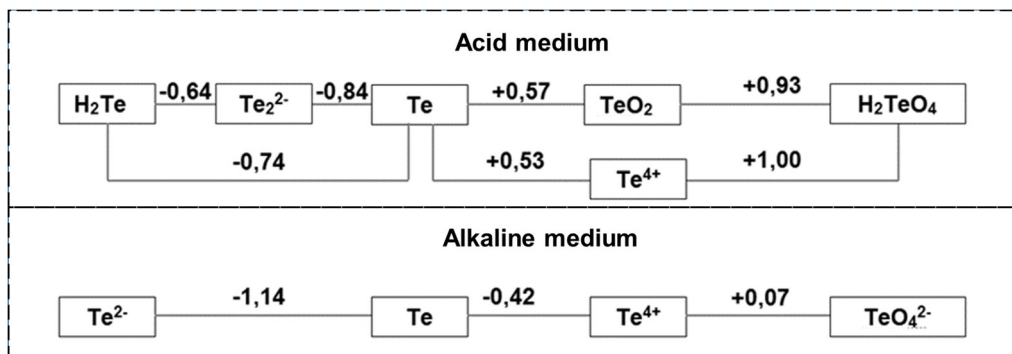


Reference: Goldfarb, R. (2015)

Tellurium, a metalloid belonging to group 16 of the periodic table, is a chemically stable and water insoluble element. Tellurium can exist in various redox states: telluride (-2), elemental tellurium (0), tellurite (+4), and tellurate (+6). In

Figure 2, there is illustrated the standard reduction potential of tellurium. Tellurium was first recognized a distinct element by Martin Heinrich Klaproth, a German chemist, in 1798 and was carefully investigated by Berzelius in 1826 (WEEKS, 1932). In 1914-1916, the Italian P. Fenaroli published a series of articles showing that tellurium acts as a coloring agent in glass. Only under reducing conditions, Te provides blue, red, pale pink or brown glasses whose colors are approximately the same as Te would have in aqueous colloidal suspension (BANCROFT, 1918, SILVERMAN, 1932).

Figure 2 - Standard reduction potential of Te in acid and alkaline media



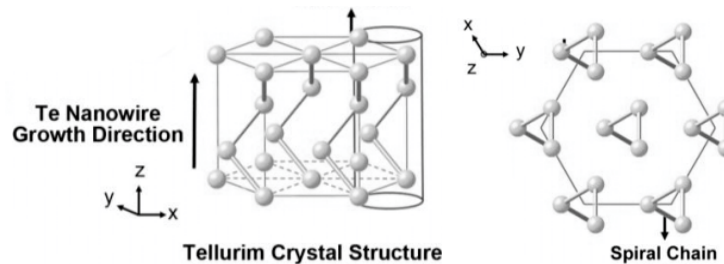
Reference: Vanysek, P. (1991).

The typical synthesis of tellurium glass coloring agent involved a mixture of sodium tellurate and sodium protalbinat (Albumin from egg white) with aqueous hydroxylamine hydrochloride (reducing agent). The glass color shifts from brown, red, or blue according with the increase of tellurium concentration. At this time, they estimated that the color changes were associated with the increase of size of the Te colloidal particles (BANCROFT, 1921).

1.1.1. One-dimensional Te nanostructures

Te in bulk form is a p - type narrow bandgap (0.33 eV) semiconductor at room temperature. Upon downscaling, Te crystallizes into helical-chains as a result of the discrete nature of its trigonal phase. The representation of Te structures is shown in Figure 3.

Figure 3 - Representation of Te trigonal structure. Te grows into NWs based on the spiral chains along the [001] direction.



Reference: Adapted from Tsai et al., (2015).

The first article describing richer insights about the optical properties and morphology of Te colloidal particles was reported in 1953 by Johnson, R.A (JOHNSON, 1953) with the help of electron microscopy. The aqueous colloidal suspensions of Te particles with color varying from amber to blue were prepared by reduction of Te^{4+} acid solutions by hypophosphorous acid/sodium hyposphosphite buffer solution in the presence of gum arabic as a stabilizer. Johnson, R. A (JOHNSON, 1953) first unveiled the one-dimensional shape of Te structures and confirmed that the color shift, previously described to occur in tellurium glasses (BANCROFT, 1921), was associated with the aspect ratio of Te structures.

Almost 20 years later, the Japanese Nishida & Kimoto carried out a detailed structural analysis of Te one-dimensional particles prepared by evaporation in argon at low pressure by using 1000 KV electron microscope (KIMOTO; NISHIDA, 1967). The anisotropic behavior of the trigonal lattice of Te “building blocks” enables the growth of one-dimensional Te (Te1D) particles. The burst of publications describing the preparation and applications of Te1D particles started in 2001 by Xia group in a communication, which also featured a cover of

Advanced Materials (MAYERS; XIA, 2002a). Previous efforts had been undertaken to tightly control the synthesis of Se nanowires by the same group (which has a nearly similar crystal structure Te) (GATES; YIN; XIA, 2000; GATES et al., 2002). The authors also reported the synthesis of Te1D particles in the shape of triangular, filamentary and needle-like structures (MAYERS; XIA, 2002b). Single-crystal Te nanotubes were achieved by using polyol method by cold-injection of telluric acid on ethyleneglycol, which in turn acts as both solvent and reducing agent. In the literature, the bottom-up synthesis of Te1D particles was further explored with a myriad of reducing agents, stabilizers, and Te sources.

Te1D nanostructures (LIN; YANG; CHANG, 2008a; LIU et al., 2003; SONG et al., 2008) have been synthesized by various approaches such as electrochemical deposition method, (SHE et al., 2009) photolysis (WEBBER; BRUTCHEY, 2009; ZHANG et al., 2007), vapor deposition (SEN et al., 2007), microwave (LIU et al., 2010a), laser-assisted synthesis (VASILEIADIS et al., 2013), and template-directed synthesis (WEI et al., 2003a; XI et al., 2006).

The methodology based on hydrothermal synthetic route is one of the most studied for the preparation of Te1D nanostructures. In general, tellurium precursor is water-soluble tellurates (Na_2TeO_3 , Na_2TeO_4 or $\text{H}_2\text{TeO}_4 \cdot 2\text{H}_2\text{O}$) in hydrothermal synthesis. Strong reducing agents such as hydrazine (N_2H_4) and sodium borohydride (NaBH_4) are usually introduced to produce the initial Te seeds. Other reducing agents are also explored in the literature such as ethylenediamine (XI et al., 2007), formamide (HCONH_2) (XI et al., 2005), sodium sulfite (Na_2SO_3) (LIU et al., 2004a), sodium thiosulfate ($\text{Na}_2\text{S}_2\text{O}_3$) (LIANG; QIAN, 2009), sodium tungstate (ZHANG; WANG; WEN, 2009) or biomolecules like alginic acid (LU; GAO; KOMARNENI, 2004), ascorbic acid (LI; ZHANG; QIAN, 2008), glucose (CAO et al., 2009), gluconate (GAO; LU; KOMARNENI, 2006), amino-acids (HE; YU; ZHU, 2005a) and starch (LU; GAO; KOMARNENI, 2005).

In many studies involving the hydrothermal method, low-soluble sources of tellurium precursors like TeO_2 or bulk Te^0 are mixed together with dissolution agents such as triethalonamine/fluoboric acid (HBF) (MA et al., 2011a), KOH/DMF(WEI et al., 2003a), NaBH_4 (GAUTAM; RAO, 2004), N_2H_4 (WANG et al., 2010b) and synthetic polymers such as polyethylene glycol (PEG), polyvinyl alcohol and polyvinylpyrrolidone (PVP) (WANG; WANG; WANG, 2008). The outcome is unstable Te^{2-} intermediates that are further oxidized to grow Te1D nanostructures under a dissolution-recrystallization method.

Lin and coworkers prepared Te nanorods with 250-880 nm in length and 8-20 nm in diameter by reducing TeO_2 in an aqueous solution of N_2H_4 at room temperature for different reaction times (10-120 min) (LIN; YANG; CHANG, 2008b). In this approach, no stabilizing agent was utilized during the nucleation and growth of Te nanorods. Noteworthy, in order to stop the growth of Te nanorods, the reaction batch diluted with a suspension of an aqueous solution of sodium dodecyl sulfate. Several non-hydrothermal/solvothermal routes in solution-phase approach have been developed along the last decade for the controlled synthesis of Te1D nanostructures. Usually, the main differences among the current protocols rely on the changes of Te precursors, reducing and stabilizing agents. Besides H_6TeO_6 , NaTeO_3 , Te, and TeO_2 precursors, $(\text{NH}_4)_2\text{TeS}_4$ (LIU et al., 2004b) and diethyldithiocarbamate tellurium (WANG et al., 2013, 2010a) have been also explored to produce Te1D nanostructures. It has to be pointing out that several studies address to the influence of stabilizing agent such as thiols (SREEPRASAD; SAMAL; PRADEEP, 2009), ionic liquids (MA et al., 2011b; THIRUMURUGAN, 2007; ZHU et al., 2004), zeolites (WEI et al., 2003b), ionic (LI; ZHANG; QIAN, 2008; PARK et al., 2015; XI et al., 2006), and nonionic (ZHU et al., 2011) surfactants.

There exist fascinating pursuits for the use of Te1D nanostructures on practical applications. Pristine Te1D nanostructures have shown remarkable performance in distinct applications: photoconductivity (LI et al., 2012; LIU et al., 2012), gas sensing (SEN et al., 2009; TSAI; LIN; CHANG, 2012; WANG et al., 2010b), antibacterial agent (CHOU et al., 2016), thermoelectrical applications (GAO et al., 2015; HEYMAN et al., 2014; PARK et al., 2015), supercapacitor electrode (TSAI et al., 2015) and battery cathode (DING et al., 2015). In addition, due to its high reactivity toward a wealth of chemicals, Te can be used as sacrificial template for the synthesis of telluride and metallic 1D nanostructures. Alternatively, Te1D nanostructures can be coated with an intermediate and functional carbonaceous layer for the deposition of a wide range of compounds such as oxide and metallic nanoparticles. These Te derivative 1D nanostructures and ongoing efforts are summerized in the next section.

1.1.2. One-dimensional Te hybrids

In 2005, the group of Prof. Shu-Hong Yu from University of Science and Technology of China published their first contribution of many to come on the synthesis of Te1D nanostructures and Te derivative 1D nanostructures (HE; YU; ZHU, 2005b). Shuttle-like scrolled Te nanotubes with flexible sharp ends and dendritic Te crystals were prepared under

hydrothermal conditions with the assistance of alginic acid, lysine, serine and histidine. In the same year, the group reported the large-scale synthesis of Te nanoribbons under mild reaction conditions by reducing NaTeO_3 with tetraethylene pentamine at $80\text{ }^\circ\text{C}$ and ambient pressure (HE; YU, 2005). One year later, the same group contributed with important articles on the synthesis of Te1D nanostructures: i) large-scale synthesis of ultrathin (4-9 nm in diameter), blue-violet luminescent Te nanowires and nanoribbons (QIAN et al., 2006a); ii) protocol for coating of Te nanowires with functional carbonaceous layer (; nanocables) (QIAN et al., 2006c). In this process, glucose molecules used as a carbon source were absorbed onto the dispersed ultrathin Te nanowires template in water. Under hydrothermal conditions, the adsorbed glucose molecules are polymerized, carbonized, on the surface of Te nanowires, which in turn induce the heterogeneous nucleation and growth of carbonaceous species. Therefore, Te@C nanocables are prepared instead of carbon spheres colloids, a common outcome obtained from homogeneous nucleation in the absence of any template.

From the synthesis of pristine Te nanowires and Te@C nanocables, they have successfully explored the conventional chemical templating route to achieve a myriad of 1D nanostructures (LIANG et al., 2013a). In the chemical templating (or sacrificial templating) the final material shape around the surface of the sacrificial template while the template is progressively consumed. The template once consumed can be recycled and repeatedly used as template (WANG et al., 2015).

1.1.3. Te@C hybrid nanostructures

Yu and coworkers extensively explored the preparation of Te@C nanocables for multiplex synthesis (LIANG et al., 2013a). Te nanowires are readily susceptible towards oxidation (LAN et al., 2007) and the direct deposition of oxide layer is hardly achieved without an intermediate and functional coating. Te@C nanocables displaying hydroxyl or carboxyl functional groups have been used to graft metal oxides or metal nanoparticles (LIANG et al., 2013a). After removal of Te cores from Te@C nanocables by chemical etching, pure carbonaceous nanofibers with chemically active surface can be obtained (QIAN et al., 2006c). Nevertheless, distinct strategies have been explored to produce a carbonaceous layer on the surface of Te1D nanostructures (LIANG et al., 2013a): i) Te@C nanocables have been prepared by reduction of Te salt precursor in the presence of carbohydrates and ionic surfactants under hydrothermal conditions (SONG et al., 2009; WANG et al., 2009a, 2009b). So far, glucose is widely employed as both reducing and carbonizing agent.

However, others polysaccharides like dextran (WANG et al., 2009b) have shown to deliver uniform coating of carbon. The major drawback of this method relies on the poor control over the size of both Te core and the carbon layer as well as aggregation issues; b) Te@C nanocables have also been prepared by carbonization of glucose under hydrothermal conditions in the presence of pristine Te1D nanostructures (LIANG et al., 2013b; QIAN, et al., 2006c); Once Te@C nanocables are submitted to oxidation for tellurium withdrawing, carbonaceous nanotubes of controlled dimensions are achieved which serve as template for the synthesis of 1D oxides (e.g. Fe₃O₄, TiO₂) or active surface to attachment of metallic nanoparticle (e.g. Au, Ag, Pt, Pd) as shown in Figure 4.

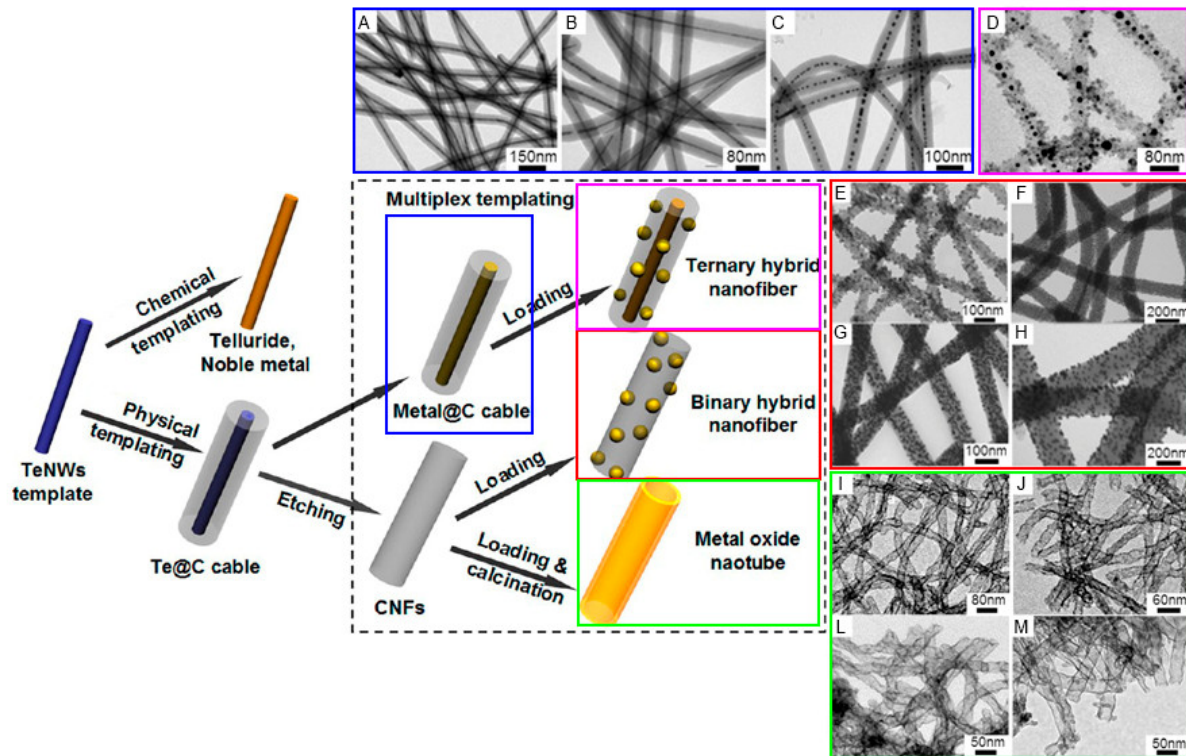
For example, carbonaceous fibers were used as sacrificial template to prepare uniform carbon@silica nanocables and silica nanotubes via sol-gel method followed by heat treatment (QIAN et al., 2006b). c) Two step synthesis involving the preparation of Te1D nanostructures coated with a carbon precursor (i.e. resin) under hydrothermal conditions and subsequent carbonization of the resulting nanostructures. The carbonaceous precursor usually regards a resin derived from polycondensation between phenolic compounds and formaldehyde.

To date, Qian and coworkers (QIAN, 2010) prepared Te@phenol-formaldehyde resin core-shell nanowires through one-pot synthesis under hydrothermal conditions. However, the authors did not explore subsequent carbonization step to achieve Te@C nanocables or even carbonaceous nanotubes.

Besides carbonaceous hybrids, previous efforts had led to the fabrication of single-crystalline telluride and metallic one-dimensional nanostructures by using Te1D nanostructures as sacrificial template. For example, Te1D nanostructures combine with other elements to produce materials of high technological relevance such as CdTe, PbTe, and Bi₂Te₃ (MOON et al., 2010a, 2010b; SAMAL; PRADEEP, 2010; YANG et al., 2014) by simple mixture of the salt of desired metal/semi-metal against Te nanowires or nanorods in solution-phase. Ultrathin Te nanowires were successfully used for the fabrication of high aspect ratio PbTe (LIANG et al., 2009b), CdTe (LIANG et al., 2009b), Ag₂Te (LIU et al., 2012) and PdPtTe nanowires (LI et al., 2013).

Tellurium nanowires have also been used to fabricate 1D metal and alloyed/multimetal chalcogenide nanowires (YANG et al., 2015; LIANG et al., 2013). Ultrathin Pt and Pd nanowires/nanotubes were easily achieved by simple galvanic displacement (LIANG et al., 2009a) with ultrathin Te nanowires.

Figure 4 - The panels outlined with blue rectangle display core/shell 1D nanostructures fabricated by using Te@C nanocables as templates: (A) Pt@CNFs, (B) Pd@CNFs, and (C) Au@CNFs. The panels outlined with pink rectangle highlight ternary 1D hybrid structures: (D) core/shell Au@C nanocables obtained by using Te@C nanocables as template and further decorated with Fe₃O₄ nanoparticles. The panels highlighted with red outline show the 1D binary hybrid nanofibers: Carbon nanofibers decorated with (E) Fe₃O₄, (F) TiO₂ oxide nanoparticles, or metallic nanoparticles: (G) Ag, and (H) Au. The panels outlined with green rectangles highlight the metal oxide nanotubes fabricated by templating against Carbon nanofibers: (I) TiO₂, (J) SnO₂, (L) ZrO₂, and (M) BaTiO₃.



Reference: Adapted from Liang et al. (2013a) with permission. Copyright 2013 American Chemical Society

Pristine ultrathin Te nanowires were also utilized as template to drive the growth of metal-organic framework (MOF) nanofibers (ZHANG et al., 2014). The active surface of Te1D nanostructures was used to induce the nucleation and growth of Zn(MeIM)₂ (ZIF-8; MeIM = 2-methylimidazole) nanocrystals (zeolite-type MOF), resulting in nanofibers with high-aspect-ratio and controllable diameters. Subsequently, the authors showed that Te@ZIF-8 core-shell nanofibers are exceptional precursor for the synthesis of doped carbon nanofibers through feasible calcination. These doped carbon nanofibers displayed excellent electrocatalytic performance for oxygen reduction reaction.

1.1.4. Assembly of 1D Te derivative nanostructures

In addition to the challenge on the control of morphology parameters, many efforts have been attempted to improve the assembly of these anisotropic crystals into well-aligned arrays. In this way, a limited number of reports describe the new properties as consequence of assembly of 1D tellurium nanostructures in applications such as optoelectronic and sensor devices. For example, Sen and coworkers describe the preparation of vertically aligned Te1D nanowires synthesized by physical vapor deposition approach (SEN et al., 2008). The Te1D array showed pronounced sensibility to N₂ and H₂S vapors and better selectivity for detection of chlorine gas. Similar approach has been used to study vertical Te nanowires and nanorods array as potential field emitters (CHAVAN et al., 2009; SAFDAR et al., 2013). Te1D papillae-like nanostructures prepared by self-catalyzed vapor transport and hierarchically organized in nano- and micrometer scale showed superhydrophilic surface (VELÁZQUEZ et al., 2012). This unusual property has been attributed to the rough surface resulting from parallel alignment between the Te1D nanostructures.

Liu and coworkers studied the photoconductivity of macro-scale assembled Te nanowires of large aspect ratio by Langmuir Blodgett technique (LIU et al., 2010b). The photoconductivity behavior was reversibly and intensity-dependent of the number of repeating one-dimensional nanostructures arrays assembled in parallel and crossed directions and patterned into periodic mesostructures.

Recently, an easy protocol for the alignment of Te nanowires in water/butanol interface has been demonstrated (MOON et al., 2011; NARAYANAN et al., 2015). The array of Te nanowires was transferred to silicon substrate and investigated to fragment analytes upon the application of low voltages (~1 V) for ion mass spectroscopy. The effect of aligned Te nanowires was strongly anisotropic on molecular ion intensity for many analytes including organic molecules and amino acids (NARAYANAN et al., 2015).

Additionally, since the synthesized 1D luminescent nanostructures are placed on cambered or flat substrates, their orientation is hardly controlled under drying of suspension in ordinary conditions. The alignment of 1D luminescent nanostructures into side-by-side either head-to-head assemblies is essential for the development of great and practical devices. The manipulation of 1D luminescent nanostructures in ordered arrays could be interesting for the study of optical gain medium in stimulated emission processes (lasing), field emission and wave

guiding devices, and component of optical sensors (EBAID et al., 2015; GUO; YING; TONG, 2014; HUANG, 2001a; PAN et al., 2005; SIRBULY et al., 2005; YANG et al., 2002).

In previous studies, we investigated the preparation of stable aqueous suspensions of Te1D nanostructures in the shape of long/flexible wires, spine-like and rods by using assisted synthesis in the presence protecting colloids (PCs) molecules derived from natural polymer sources (pectin and cellulose derived) as well as ionic and non-ionic surfactants (SILVA, 2012). Herein, Te1D nanostructures will be used as template to design arrays of 1D luminescent nanostructures and hybrids nanostructures containing metallic nanoparticles. This topic will be explored in Chapter 4.

Beyond that, a key requirement in constructing practical solid devices is to transfer uniformly aligned 1D luminescent nanostructures at large scale into a substrate. Usually, the alignment of 1D luminescent nanostructures on flat substrates have been achieved by using direct deposition either by vapor-liquid-solid and vapor-solid-solid processes at high temperature ($> 500\text{ }^{\circ}\text{C}$) (FUKUI et al., 2010; WANG et al., 2005) or seed-assisted chemical growth at comparatively lower temperatures (ZHANG et al., 2006). However, there is a growing need to fabricate 1D luminescent arrays over flexible rather than rigid photonics devices, eliminating mechanical and geometrical design constraints imposed by rigid and brittle films.

In general, flexible substrates are limited in terms of thermal stability so alternative techniques compatible with solution-phase methods have been evaluated for such purposes. Therefore, techniques for controlling the assembly and alignment of 1D nanostructures synthesized by solution-phase methods on flexible substrates include, for example, those that utilize electrical (SMITH et al., 2000) and magnetic fields (HANGARTER; MYUNG, 2005), contact printing (FAN et al., 2008), physical stretching (WU; SU; JIANG, 2012), liquid-liquid interfaces (MOON et al., 2011), Langmuir-Blodgett (TAO; HUANG; YANG, 2008), blown bubble (YU; CAO; LIEBER, 2007), and microfluid flow methods (HUANG, 2001b).

1.2. Biopolymers as flexible transparent substrates

Biopolymers, both natural polymers and polymers produced from natural feedstock by synthetic routes, show great potential as flexible substrates for electronics and photonics applications. The polymer source in a renewable approach from biomass is increasingly in focus for commercial trends and government policy. The advantages include wide structural and functional diversity, lower toxicities and biodegradability. Currently, there are two fields that biopolymers have been explored: a) biotronics: an emerging field in which biopolymers are

used in devices for photonics and electronics applications. b) biophotonics: photonics devices are used in biological systems whose fabrication can comprise biopolymers. It is important to note that a limited number of biopolymers fulfills the optical properties required for photonic applications. Beyond that, other implications for practical application rely on mechanical strength, thermal stability and chemical resistance. Specifically, natural polymers garnered a great deal of attention in the last 10 years as optical material.

1.2.1. Natural polymers for photonics

Nature itself has made exceptional use of structural natural polymers. Most natural materials are actually composites of a fibrous or crystalline polymer and an amorphous polymer binder, whose final material performs striking functions on protection, support, and structure. Examples include wood, seashells, invertebrates' exoskeleton, spider web fibers, and cocoons. Natural polymers can be simply defined as macromolecules that occur in nature. Silk, cellulose, hemicelluloses, lignin, and starch, deoxyribonucleic acid (DNA), chitin, chitosan are examples of natural polymers. Raw polymers found in nature are usually insoluble in water and in organic solvents. Additionally, raw natural polymers are opaque and inappropriate for the fabrication of optical materials. Potential limitations on natural polymers processing have been resolved by implementing a number of creative techniques. There are different physical and chemical routes to dissolve and give them desirable properties such as film forming, transparency, and chemical stability. Therefore, optically transparent natural polymers can be processed into relevant flexible host matrix to optically active components (e.g. luminescent compounds). Materials that can be isolated from the native environment and repurposed into freestanding film may serve as useful device technologies.

Important achievements have been made with regards the development of freestanding biopolymer films with exceptional optical, thermal and mechanical properties for photonic applications. Few examples will be highlighted indicating the wide range of applications of natural polymers in photonics.

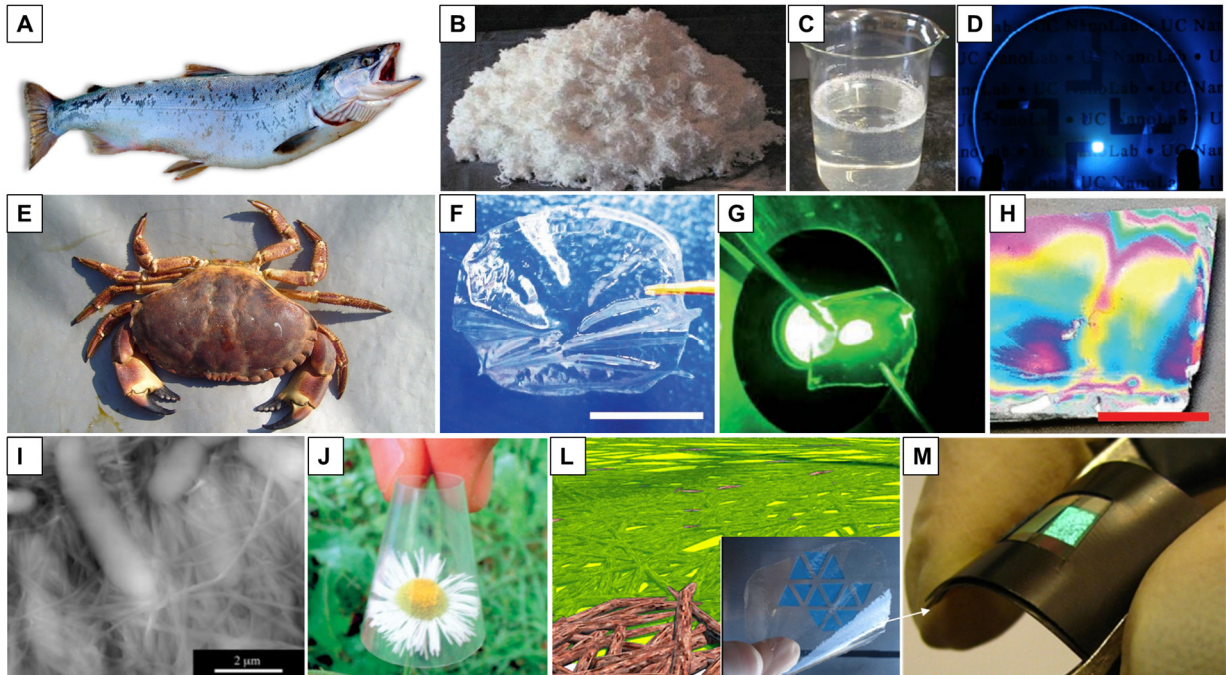
DNA-based biopolymer extracted through an enzyme isolation process from fish has been explored as photonic material. Prof. Y. Okahata from Tokyo Institute of Technology firstly demonstrated the feasibility to tailor transparent and water-insoluble DNA-based films derived from fish products (mostly sodium salt of DNA from salmon testes, see Figure 5B) around 20 years ago (TANAKA; OKAHATA, 1996). Natural DNA, which is an anionic polyelectrolyte,

is soluble in water but can be precipitated with cationic surfactants in water (PONTIUS; BERG, 1991). Okahata and coworkers found that DNA- Na^+ becomes soluble in polar organic solvents by replacing Na^+ ions with long single- and double chain alkyl quaternary ammonium ions (Figure 7C) (TANAKA; OKAHATA, 1996). Transparent films of DNA-alkyl quaternary ammonium were feasible upon drying of solution on a flat surface. Prof. Naoya Ogata from Chitose Institute of Science and Technology pioneered the use DNA for photonics and biotronics applications (KAWABE et al., 2000). With a collaboration between the Air Force Research Laboratory and Chitose Institute of Science and Technology, the team identified a material with potential for optoelectronic applications by extending prior strategy investigated by Okahata and coworkers to obtain transparent films through modification of native DNA with sodium hexadecyltrimethyl ammonium chloride (CTMA), a cationic surfactant (WANG et al., 2001b). The outcome is transparent films with enhanced solubility and thermal stability. DNA-CTMA films have been

described for substrate of organic light emitting diodes (OLEDs), light amplification host (LEE et al., 2008), gate dielectric in organic field-effect transistors (OFET) (STADLER et al., 2007), for conductive cladding layers in waveguides (GROTE et al., 2004), host for solid-state dye lasing devices (KAWABE et al., 2000) and dyes featuring nonlinear optical properties (GROTE et al., 2004; WANG et al., 2001b). Noteworthy, the optical losses of DNA-CTMA at the communications wavelengths have been previously measured to be 0.2 dB/cm at 1300 nm and 0.7 dB/cm at 1550 nm, which are relatively low values (STECKL, 2007). A more detailed review on the optical applications and outlooks of DNA-based polymers can be found in the work of Su and coworkers (SU; BONNARD; BURLEY, 2011), Steckl and coworkers (STECKL et al., 2011), and Kwon and coworkers (KWON; HOON CHOI; JIN, 2012).

Chitin is the second most abundant polysaccharide composed by linear 2-acetamido-2-deoxy-D-glucopyranose (N-acetyl-D-glucosamine) units linked by β -(1,4-) linkage. Native chitin is a semicrystalline biopolymer with a microfibrillar morphology usually found many fungal cell walls, nematodes, insect exoskeletons, and crustacean shells. Chitin is insoluble in the most of the solvents. In 2012, Yano and coworkers (SHAMS et al., 2012) prepared low thermal expansion and transparent crab shells. They investigated the fabrication of fibrous chitin and resin composites to make optically transparent films appropriated for contact lenses, sensors, and optical screens for flexible or flat panel displays, e-paper devices and solar cells.

Figure 5 - (A) Photography of an ordinary salmon (B) DNA solid powder extracted from salmon (C) Aqueous solution of DNA-cetyltrimethylammonium (DNA-CTAM), (D) DNA-CTAM thin films incorporated into blue-emitting OLEDs. (E) Picture of an ordinary crab; (F) and (G) Transparent film fabricated by airbrushing a suspension of chitin nanofibers (3 nm in diameter) in in hexafluoro 2-propanol. (H) Chitin reflective optical grating replica molded from a grating with 1200 grooves/mm. Scale Bar: (F) 1 cm; (H) 0.5 cm. (I) Atomic force microscopy image of bacterial cellulose pellicle; (J) Transparent freestanding bacterial cellulose sheet coated with acrylic resin. The final composite affords 60 wt% of bacterial cellulose content. (L) Transparent freestanding bacterial cellulose sheet coated with a polyurethane resin derived from castor-oil. (M) Transparent composite described in (L) being used as flexible substrate for the fabrication of OLED device.



Reference: (A-D) Adapted from Steckl et al., (2011). Copyright 2011 Optical Society of America. (E-H) Adapted from Zhong et al., (2011). Copyright 2011 John Wiley & Sons, Inc. (I, J) Adapted from Yano et al., (2005). Copyright 2005 John Wiley & Sons, Inc. (L, M) Adapted from Pinto et al., (2015). Copyright 2015 Royal Chemical Society.

Prof. Marco Rolandi group from Washington University has been contributing with important advances in the use of chitin nanofibers on optical applications (ZHONG et al., 2011). Although chitin is insoluble in water or common organic solvents, it is feasible to dissolve it in hexafluoro-2-propanol. The result is a suspension of ultrathin (3 nm) chitin nanofibers that can be self-assembled from micro- to nanofabrication of (patterned) transparent films by using airbrushing and soft lithography (replica molding and microcontact printing) techniques (see Figure 5, F-H).

The main derivative obtained from chitin is chitosan, which in turn is produced by the deacetylation of chitin. Chitosan is soluble in diluted acids. Although chitosan has film forming features, it hardly delivers the optical clarity desirable for photonic applications.

Natural cellulose fibers with a diameter of 20–50 μm are composed by thousands of micro- and nanofibril that can assembly into smooth films with reduced light-scattering effect. Despite the fact that cellulose is available in any plant, pure cellulose polymer can be synthesized by microorganisms. By feeding bacteria such as the specie *Gluconacetobacter xylinus* with glucose, they are able to extrude crystalline pure cellulose fibers with diameters bellow 100 nm into a 3D network (see Figure 5J). Since cellulose is the most abundant polymer in earth, several works have been dedicated on the pursuit for rational design of transparent cellulose films commercially comparable to the current engineered plastics. Unlike sheet of plant cellulose fibers, sheets of bacterial cellulose (BC) nanofibers display less pronounced light scattering comparing with plant cellulose fibers and exceptional mechanical and thermal properties, whose features are very attractive for the fabrication of flexible substrate for photonics. For example, Legnani and coworkers successfully prepared flexible Organic Light Emitting Diodes (OLEDs) on the pristine surface of BC nanofibers sheet (LEGNANI et al., 2008). An interesting random-lasing action have been shown in BC nanofibers doped with laser-dye molecules and light scattering particles by Santos and coworkers (SANTOS et al., 2014). By taking advantage of the 3D networks of BC nanofibers as host and gain medium, random-lasing action of dye-laser Rhodamine 6G molecules was achieved under diffuse regime in the presence of light scattering Ag or SiO_2 nanoparticles.

Previous efforts identifying the shortcomings to make very transparent films based on cellulose or BC fibers stimulated the development of distinct strategies. Therefore, three main approaches emerged:

a) Cellulose fibers can be dissolved in solution-phase methods through chemical derivatization (e. g. viscose process, carbamate process or with solvents like DMF/ N_2O_4 , DMSO/ N_2O_4 , CF_3COOH , $\text{HCOOH}/\text{H}_2\text{SO}_4$, Cl_2CHCOOH and TEMPO (2,2,6,6-tetramethylpiperidine-1-oxyl radical) or direct dissolution without derivatization with the help of high hydrogen bonding capacity solvents (e.g. DMAc/LiCl and ionic liquids). The solution of cellulose is further regenerated into transparent film in the presence of an appropriated solvent. It is important to highlight the works conducted by Prof. Lina Zhang from Wuand University and Prof. Isogai Akira from University of Tokyo. Both research groups have

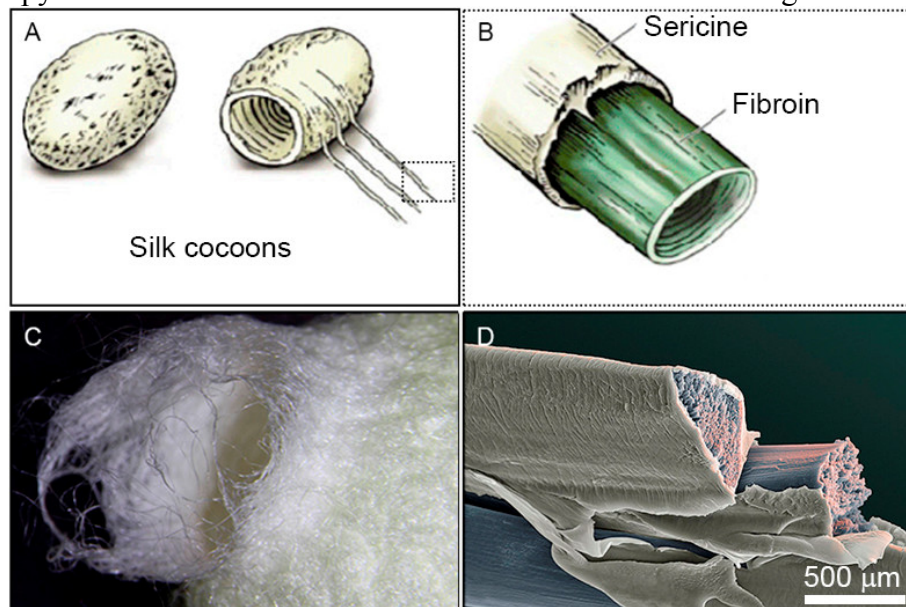
unveiled important pioneering dissolution approaches suitable to achieve transparent cellulose films (QI; CHANG; ZHANG, 2009; YAGYU et al., 2015). b) another approach to prepare transparent films based on cellulose involves the fabrication of cellulose composites. The additional components usually have similar refractive index than cellulose and fill the gap occupied by air among the fibers mat. The group of Prof. Hiroyuki Yano from Kyoto University has been contributing with several publications in the field of cellulose nanofibers by using this approach. In 2005, Yano and coworkers made a breakthrough in transparent paper technology by utilizing nanofibrillated cellulose impregnated with epoxy, acrylic (**Figure 5L**) and phenol-formaldehyde resins (YANO et al., 2005). The composites display high fiber content (60 wt%) with outstanding mechanical strength and low thermal expansion coefficient (NOGI et al., 2009). In addition to resins derived from synthetic monomers, an increasing number of approaches have been compelled to the fabrication of transparent composites based on BC and renewable biopolymers. Some of these composites include BC/chitosan (FERNANDES et al., 2009), BC/polyhydroxybutirate (BARUD et al., 2011), BC/polyvinyl alcohol (TANG; LIU, 2008), BC/boehmite-epoxi-siloxane (BARUD et al., 2012), BC/poly(L-lactic acid) (KIM et al., 2009), BC/ ϵ -caprolactone (BARUD et al., 2013), BC/epoxidized soy bean oil (RETEGI et al., 2012) among others. Recently, Pinto and coworkers prepared transparent composites with high content of BC nanofibers (>70 wt%) and polyurethane resin derived from castor-oil (PINTO et al., 2015). The low surface roughness, excellent mechanical and thermal stability of the BC/PU films grasped key roles for the construction of flexible OLED devices (Figure 7, M and N). c) The chemical modification of cellulose backbone with organic groups (e.g. nitro, esters, amine, etc.) allows to tune the processing conditions of transparent films in solution-phase with the use of common solvent (e.g aqueous and organic solvents). The chemical modification of cellulose is routinely conducted on hydroxyl groups in anhydroglucose units. The properties of cellulose derivatives depend on the type of functional groups in the side chains. Therefore, a new cellulose-based polymer can be fashioned by choice of an additional moiety to be combined with hydroxyl groups. It is possible to increase the solubility of cellulose derivatives depending of the extension of chemical modification and the molecular weight. For example, carboxymethylcellulose, hydroxypropylcellulose and cellulose acetate are cellulose derivatives that easily dissolve in common solvent such as water, ethanol, and acetone or chloroform, respectively to form transparent films.

1.2.2. Silk Fibroin

So far, silk fibroin is the most promising natural polymer for photonic applications. The silk fibers are basically composed of proteins. The silk proteins - fibroin and sericin silk - are stored in the glands of silkworm silk and spider as an aqueous solution. During the spinning process, the concentration of these proteins is gradually increased. Finally, the stretching stress is applied to produce a partially crystalline insoluble fibrous thread in which most of the polymer chains in the crystalline regions are oriented parallel to the fiber axis. Specifically, the cocoons of *Bombyx mori* are "structural bags" made from a single strand of silk with continuous length of 1000-1500 m.

Silk fibers have a distinct hydrophobicity and notorious crystallinity. Each raw silk yarn has a longitudinal groove, with two separate fibroin filaments irregularly intertwined and stuck together by sericin. Sericin is a smaller protein that surrounds silk fibroin fibers. Figure 6 illustrates the composition of silkworm silk cocoon. The percentage of fibroin and sericin is 75% and 25% of the total weight of the pod, respectively. Sericin is a protein resistant to oxidation and ultraviolet radiation, is antibacterial, it absorbs and releases moisture easily.

Figure 6 - Representation of (A) silk cocoon and (B) silk filaments. (C) Close-up photography of silk filament in an ordinary cocoon. (D) False-color scanning electron microscopy of fibroin/sericin core-shell of silk filaments with a triangular cross section.



Reference: (A-C) the author, (D) Adapted from Oliver Meckes, Eye of Science website (<http://www.eyeofscience.de/en/>)

Pure silk films have a combination of peculiarities including optical transparency in the visible range, ease of patterning, and the capacity to embed dopants and maintain their biochemical activity. The novelty on the use of silk fibroin in optics came with the collaborative work between biomedical researcher Prof. David Kaplan and the physicist Prof. Fiorenzo Omenetto from Tufts University, a specialist in nonlinear optics and nanostructured materials (such as photonic crystals and photonic crystal fibers). He has pioneered together with Prof. David Kaplan the use of silk as a material platform for optoelectronics and photonic applications.

The first publication in 2008 described the fabrication of a functional optofluidic device based on silk fibroin diffractive gratings infused with hemoglobin whose optical properties respond to oxy- and deoxygenation in the environment (LAWRENCE et al., 2008a). The functionalization of silk films was feasible due to the simple processing involving the drying of an aqueous solution of silk fibroin over a patterned surface with grooves spaces down to 125 nm followed by lift off. It should be pointed that this was not the first time that silk fibroin was applied as diffractive element.

In 2007, researches from Air Force Research Laboratory, Ohio, reported the use of films cast from silk ionic liquid solutions to produce patterned scaffolds with grooves spaces of 10 μm for cell growth of keratinocytes rather than specific use in photonic applications (GUPTA et al., 2007).

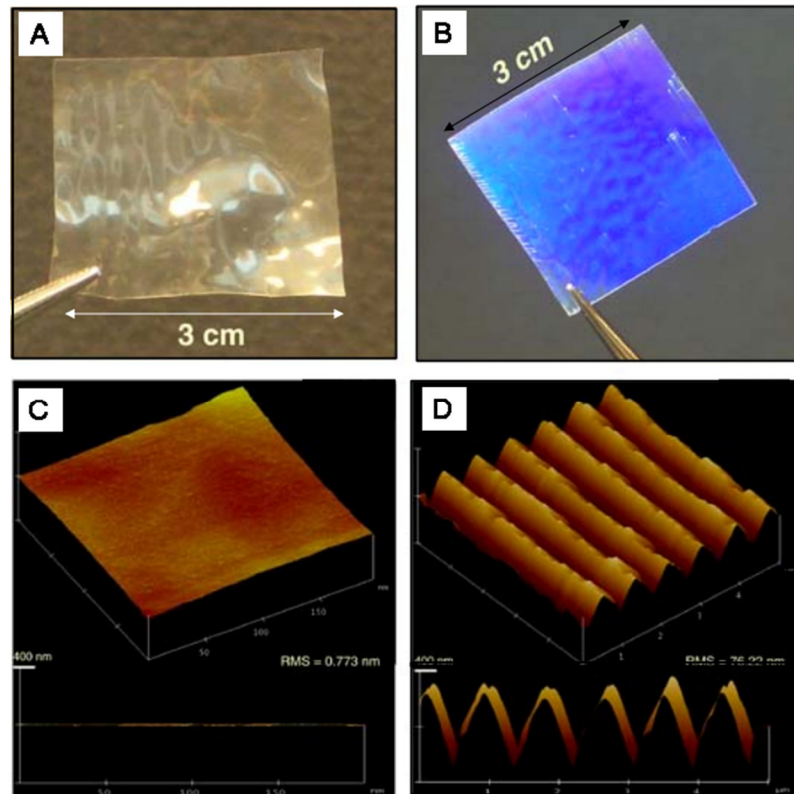
Thereafter, Omenetto and Kaplan published other notorious articles in 2008, reporting the use of silk fibroin films of controllable crystallinity as diffractive element by simple casting technique against 2D and 3D nanopatterns with sub-40 nm resolution (PERRY et al., 2008, LAWRENCE et al., 2008b). Figure 9 depicts flat and patterned free-standing silk films.

The application of silk in optics materials has been prompted by tremendous progress on the fabrication of flexible, stretchable and transparent silk substrates. Other techniques were later investigated to generate periodic nanopatterned silk fibroin films such as beam lithography and nanocontact imprinting (AMSDEN et al., 2010). The fabrication of periodic lattices in silk fibroin films goes far beyond aesthetic appeal. They have been conceived for colorimetric glucose (AMSDEN et al., 2009) and optofluidic oxygen sensors (DOMACHUK et al., 2009). Patterned silk films consisting of two-dimensional square lattice of air holes and doped with different fluorescent dyes displayed directional and wavelength-specific fluorescent enhancement. By evaluating the scattered light from the nanopatterned silk surface, an optical

sensor responsive to fluctuations of the refractive index between the air and patterned interface was demonstrated (MONDIA et al., 2010).

The authors also showed that silk fibroin could be processed to fabricate optical waveguides by direct ink writing in a communication article that was also cover of the *Advanced Materials* journal (PARKER et al., 2009).

Figure 7 - (A) Flat and (B) patterned surface. (C) and (D) show the Atomic Force Microscopy (AFM) images of topography of both surface and respective cross-sectional view of (A) and (B).



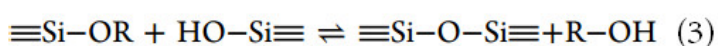
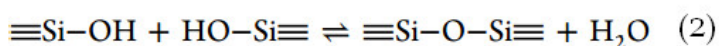
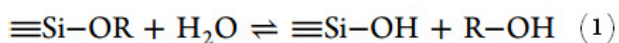
Reference: Adapted from Lawrence et al. (2008b). Copyright 2008 Springer International Publishing.

Tailoring transparent natural polymers for photonics often requires structural reinforcement. For these reasons, several recent studies have been reported seeking effectively to improve the physical and mechanical of natural polymers by the fabrication of inorganic-organic hybrid materials. The incorporation of organic-inorganic components has synergetic effects leading to hybrid materials with improved mechanical resistance, higher thermal and chemical stability and biocompatibility, and, in some cases, with functional properties (JUDEINSTEIN; SANCHEZ, 1996; SANCHEZ et al., 2005).

To this end, the sol-gel is the most studied approach to prepare transparent inorganic-organic hybrid materials with ameliorated thermal and mechanical properties. Beyond, the sol-gel methodology offers the ability to tune their chemical resistance. For example, the water solubility of films from some natural polymers is disadvantageous for long-lasting photonic applications while there exists a demand for disposable and environment-friendly optical devices with controllable degradability. Sol-gel methodology offers a set of tools and precursors to tightly manipulate the properties of the organic-inorganic hybrids based on natural polymers in solution-phase.

1.3. Organic-inorganic hybrid

Sol-gel chemistry is a valuable alternative approach to produce solid-state materials rather than traditional solid-state methods since the solution-phase precursors ensures a completely homogeneous mixture of components towards mild conditions. Noteworthy, the temperature required for material processing can be remarkably lowered leading to (nano) particles, and unconventional inorganic polymers such as glass or ceramics. Basically, the chemistry of the sol-gel process concerns in the hydroxylation and condensation of molecular precursors. Early studies of the fabrication of sol-gel silica material were conducted with silicon salts. In 1846, Ebelmen first reported the fabrication of a transparent glass achieved by exposing SiCl_4 to atmosphere (EBELMEN, 1846). Only eighteen year later the conception of ‘sol-gel’ was then clarified by Graham with his work on silica sols/gels with silicic acid as precursor (GRAHAM, 1864). The later years witnessed steady growth over the fabrication of advanced silica materials derived from sol-gel chemistry. It is important to note that the development of sol-gel silica chemistry has been followed by the accelerated progress on the synthesis of silicon precursors. Regardless, in 1928 Case & Reid (DEARING; REID, 1928) paved way for the high-yield synthesis ($> 70\%$) of alkyl orthosilicates and since they are the most common silica alkoxide precursor used for sol-gel silica materials. The hydrolysis (1) and condensation (2, 3) reactions that drive the aqueous sol-gel process of alkyl orthosilicates are displayed bellow.



The silica sol-gel method deals to the polymerization of alkyl orthosilicate precursors to an extended pure silicon oxide network under exclusion of water and alcohol. The experimental

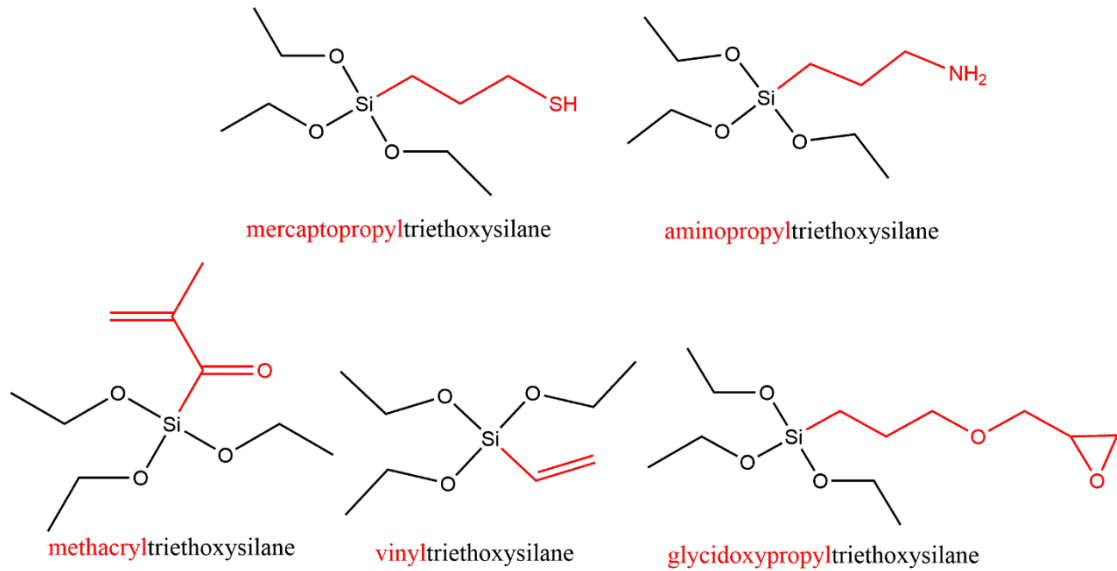
conditions have since been extensively evaluated and can be carefully tuned, for example through acid or alkaline catalysis, which in turn affect the structure of the gel and the final material. There are several experimental advantages of sol-gel process that triggered the progress on the fabrication of silica materials: i) atomic level mixing of reagents; ii) greater control over particle morphology and size whose features allow tailoring dense or porous silica materials upon lower energy consumption; iii) enable the incorporation of low thermally stable molecules like dyes and biomolecules at room temperature in entrapping silica matrix.

Earlier commercial applications of silica materials derived from sol-gel chemistry took place in Germany by Schott AG, in 1985, with the fabrication of antireflective Amiran glasses (COOK; MADER; SCHNABEL, 1985). In the same year, Schmidt disclosed basic findings emerging from a benchmark applied research in the synthesis of organically modified silicates (ORMOSILs) (SCHMIDT, 1985). ORMOSILs are hybrid molecular precursors where at least one of the $\equiv\text{Si-O-}$ linkages is replaced by a non-hydrolytic $\equiv\text{Si-C}\equiv$ group. Materials containing both organic and inorganic components (i.e. silicates) are particularly advantageous, once new features can be achieved by the combination of organic and inorganic building blocks. Significantly, the organic groups introduce new properties to the silica network like flexibility, hydrophobicity, mechanical strength, and bio affinity. Organic groups can play a dual role on the silica network according with Schmidt (SCHMIDT, 1985): i) Act as network former. In this case, the organic groups are essentially polymerizable monomers that may gather a further polymeric network through polyaddition or polycondensation reactions. Examples of polymerizable groups include vinyl, methacryl, or epoxy; ii) Act as network modifier. Organic groups can also endow non-polymerizable groups since they decrease the crosslink degree of silica network by obstructing bonds at the silicon atom. In this case, alkyl groups and even functional groups like mercapto and amino functions act as network modifiers. Some examples of ORMOSILS are displayed in Figure 8.

ORMOSILS are currently considered reinforcing components of transparent natural polymers films for photonic application. This interest relies upon the unique opportunity of combining the most remarkable properties of ORMOSILS and organic polymers through sol-gel approach in a controlled fashion. Flexibility, thermal stability and optical clarity are key dependent properties of the degree of component mixing at molecular level. In this case, segregation should be avoided because it leads to optical losses and lower material strength. The most

important guideline for intimate mixing of organic and inorganic counterparts concerns a common solvent since it provides enhanced diffusion.

Figure 8 - Some examples of organically modified siloxanes



Reference: the author

From the basic concepts, there are many possibilities to incorporate ORMOSILS into natural polymers. For example, it is possible to combine organic natural polymers and ORMOSILS components through van der Waals interactions or bind covalently in the polymer backbone. Since the functional groupings linked to the silane are manifold, a large variety of materials can be prepared using sol-gel approach at low temperature. For example, luminescent films were prepared by combining silk fibroin and aminopropyltriethoxysilane grafted with fluorescent oligothiophene (SAGNELLA et al., 2015). Fuentes and coworkers report the preparation of flexible and transparent films of chitosan with 3-amino-2-propyl- triethoxysilane (FUENTES et al., 1997) and also mercatopropysiloxane (FUENTES et al., 2010) films. Smitha and coworkers investigated the fabrication of transparent and hydrophobic inorganic-organic hybrid coatings of chitosan with methyltrimethoxysilane and vinyltrimethoxysilane (SMITHA et al., 2008). BC nanofibers and cellulose derivatives also have been modified with ORMOSILS to deliver transparent freestanding films appropriated to photonic applications. Barud and coworkers prepared transparent organic-inorganic hybrids from BC nanofibers coated with nanoparticulate boehmite and epoxy modified siloxane (BARUD et al., 2012). Organic-inorganic hybrid films based on cellulose derivatives have been investigated by the crosslink

of cellulose acetate with grafting precursor mixture of pentaerythritol triacrylate and aminopropyltriethoxysilane (SILVA et al., 2011). Achoudong and coworkers also studied the fabrication of transparent cellulose acetate films modified with vinyltrimethoxysilane that also exhibited high performance on acid gas removal (ACHOUNDONG et al., 2013).

Among the myriad of ORMOSILS available in the market, epoxy coupling silanes are very interesting modifiers to achieve transparent hybrids based on natural polymers films with enhanced functionality. Epoxy is a class of versatile polymer materials characterized by the presence of one or more oxirane ring or epoxy groups with their molecular structure. The epoxy function can be maintained to modify the hybrid network or polymerized in the presence of curing agents or UV light. Beyond that, epoxy ring-opening reactions with alcohols, amines, hydroxyl, and thiols offer a pathway to graft optically active compounds (i.e. luminescent nanostructures, quantum dot semiconductors or carbon dots, rare-earth complex) in the hybrid network.

Additionally, owing the limited feedstock of natural polymers for high demand optical devices, it is equally important develop materials based on the reuse synthetic polymers. The current level of synthetic polymers usage is roughly nonsustainable. Recycling provides opportunities to leverage the development of sophisticated materials based on recovered synthetic polymers and reduce the impact of their disposal in the environment. Beyond the aesthetic appeal, green recycling strategies are particularly interesting and demanding nowadays. Herein, we explored the fabrication of transparent spin-casting films of polystyrene recovered from disposal of reagents' packs made of expanded-polystyrene (EPS) for photonic applications.

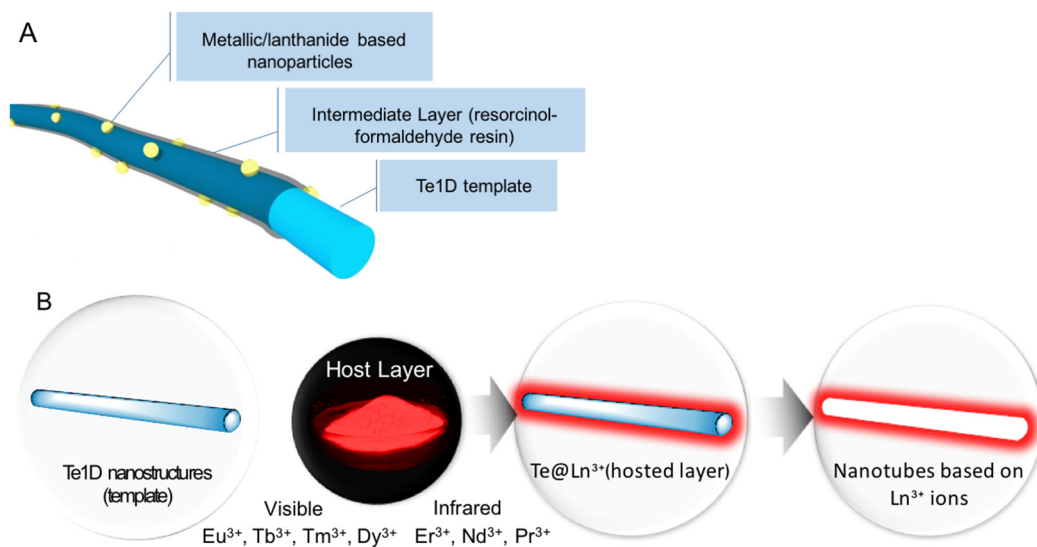
1. OBJECTIVES AND THESIS ORGANIZATION

The thesis is organized into the following Chapters

Chapter 3 describes the preparation of Te nanostructures and derivative hybrids in solution-phase. The goals of this chapter comprises:

- Study of the synthesis of one dimensional tellurium nanostructures through solution-phase approach by surfactant assisted method at different temperatures;
- Study the preparation of aligned arrays of one-dimensional tellurium nanostructures;
- Investigate the synthesis of one-dimensional Te@metallic nanoparticles or metallic derivative nanostructures by using Te as (sacrificial) template;
- Evaluate the functionalization of one-dimensional tellurium nanostructures with a carbonaceous precursor layer of *m*-dihydroxyphenol (resorcinol)-formaldehyde (RF) resin at low temperature in order to produce Te@RF nanocables;
- Study the attachment of metallic or lanthanide based nanoparticles on the surface of Te@RF nanocables as illustrated in Figure 9, A and B.

Figure 9 - (A) Metallic or lanthanide based nanoparticles attached on Te@resorcinol-formaldehyde resin nanocables (B) Te1D nanostructures as template for the synthesis of lanthanide based nanotubes.



Reference: the author.

On the pursue for practical photonic applications, the assembly of these hybrids in optically transparent host is highly desired. We will briefly lay out the current challenges and explore successes and ongoing efforts of the design of transparent host based on natural or recycled synthetic polymers for photonic applications. This work reports the preparation of optically transparent host from a) biopolymers and their epoxy sol-gel derivative hybrids; Particularly, silk fibroin and cellulose acetate biopolymers were investigated; b) recycled synthetic polymer. This study will explore recycled expanded-polystyrene to generate photonic materials. Remarkably, those polymers dissolve in solvents of distinct polarity. The design of optical materials from biopolymers and recycled synthetic polymers deals different synthetic protocols. For instance, well-known optically active compounds such as organic dyes and luminescent Eu^{3+} compounds will be incorporated in the host matrices in order to comparatively evaluate their optical properties. Chapter 4 and 5 give detailed information about the preparation of two optical materials based on silk fibroin host: distributed feedback laser and luminescent hybrid films rich in epoxy groups, respectively. Chapter 4 covers the preparation of lasing materials by doping silk fibroin patterned free-standing films with a dye laser and light scattering nanoparticles. The goals of Chapter 4 rely on:

- Study on the synthesis of SiO_2 and Ag light scattering nanoparticles;
- Prepare patterned free-standing silk film by casting an aqueous solution of silk fibroin doped with different concentration of Rhodamine 6G (dye laser) on polycarbonate grating from commercial digital versatile discs (DVD);
- Investigate the fabrication of distributed feedback lasers based on dye doped silk grating;
- Study the effect of the addition of SiO_2 nanoparticles and Ag nanoparticles in the lasing properties (threshold power pump and linewidth of laser emission) of dye doped silk films.

Chapter 5 describes the study of preparation of flexible and transparent silk fibroin containing different concentration of glycidoxypyltrimetoxysilane (GPTMS), a commercial epoxy coupling ORMOSILS. In this chapter, a detailed investigation on the optical and structural properties of the free-standing according with the GPTMS content is given. Besides pure silk film, hybrids of silk films and GPTMS are evaluated as host for luminescent lanthanide based nanoparticles seeking to achieve appropriated and functional substrates for photonic applications. Therefore, the goals of Chapter 5 endow:

- Prepare free-standing silk fibroin film rich in epoxy groups and still highly transparent in the visible region;
- Study the surface morphology, optical and structural features according with the GPTMS concentration in the hybrid; Evaluate the changes of silk conformation upon the introduction of GPTMS;
- Synthesize aqueous dispersible red emitting $\text{YVO}_4:\text{Eu}^{3+}$ nanoparticles and assess their optical properties when hosted in the hybrid films; As a general trend, this study is focused in to evaluate if the hybrid film is a potential substrate to host optically active compounds for optics.

Chapter 6 deals with the fabrication of hybrids films composed of cellulose acetate ($M_w = 29000 \text{ g}\cdot\text{mol}^{-1}$) and GPTMS. It is discussed the optical and spectroscopy features of hybrids films according with GPTMS content. Detailed investigation on the luminescence properties of hybrid host incorporated with red emitting Eu^{3+} β -diketonate complex has been shown together with theoretical spectroscopic studies for Eu^{3+} complex. The goals of Chapter 6 afford to:

- Study the preparation of functional, transparent and free-standing cellulose acetate films rich in epoxy and siloxane groups through the incorporation of GPTMS;
- Evaluate the optical and structural properties of cellulose acetate according with the content of GPTMS. Demonstrate that the hybrid films can be further modified by undertaking reactions with epoxy groups and non-hydrolyzed methoxy groups after the addition of GPTMS;
- Synthesize red emitting (thenoyltrifluoroacetate) europium (III) complex and incorporate in the cellulose acetate/GPTMS hybrids in order to produce red emitting luminescent films.
- Study the optical properties of luminescent hybrid films in comparison with the pure Eu^{3+} complex and estimate if the hybrid film is a potential substrate to host optically active compounds for photonic applications.

Alternatively, preliminary data concerning the use of recycled plastic as substrate for photonic application is described in Chapter 7. This chapter will present the processing of expanded-polystyrene into transparent thin films supported in glass substrates. D-limonene, a terpene derivative from citrus oil, dissolves expanded polystyrene and the resulting solution is used to

fabricate thin spin-casted films. In this case, it is also discussed the incorporation of red emitting Eu^{3+} β -diketonate complex. The goals of Chapter 7 include to:

- Study of the best conditions to process spin-coating of expanded polystyrene solution dissolved in D-limonene like concentration of the solution, time, spin speed, ramp rate, etc.
- Investigate the incorporation of Eu^{3+} β -diketonate complex and the effect of host matrix on their optical properties.
- Evaluate if the thin films are potential planar waveguide materials.

Finally, general Discussion and Concluding Remarks are set in the final portion of thesis.

2. STUDY OF THE SYNTHESIS Te NANOWHISKERS, NANOWIRES AND NANOHELICES AND FABRICATION OF Te@X 1D HYBRIDS (X = Ag, Au OR RESORCINOL-FORMALDEHYDE RESIN)

One-dimensional (1D) semiconductor nanostructures are emerging as one of the most powerful and diverse promising building blocks for the assembly and fabrication of a wide range of nanoelectronic and nanophotonic devices. Their physico-chemical properties are strongly dependent on the size confinement and can be tuned by modifying the size and morphology.

Tellurium is a p-type direct-gap metalloid with narrow band-gap (0.35 eV) at room temperature. For years, bulk Te has been extensively used as an alloying additive in metallurgy and thermoelectric modules. Currently, the major demand of Te embraces the fabrication of CdTe thin-film photovoltaic solar cells. Additionally, bulk crystalline tellurium shows interesting optical properties and has potential applications as holographic recording material, infrared photoconductive detector and for nonlinear infrared optics, such as second harmonic generation. Upon downscaling, Te crystallizes into parallel and long polymeric helical-chains packed by weak van der Waals interactions into a hexagonal lattice. As a result of the discrete nature of its trigonal phase, highly anisotropic nanostructures such as single-crystal nanowires, nanobelts, nanorods, nanowhiskers and nanotubes are easily tailored by fine-tuning of growth parameters on both vapor or solution-phase approaches.

The past years has witnessed steady growth in the number of reports describing a broad range of applications of Te nanostructures. Pristine Te nanowires exhibit broad absorption bands in the visible region and display strong fluorescence in the blue-violet region. Noteworthy, thin films composed by arrays of Te nanowires show reversibly switched photoelectric properties.¹ The low band-gap of Te allows the photostimulation of electron transfer using visible and infrared light rather than the shorter-wavelength light sources required for Si (band-gap energy, $E_g = 1.1$ eV) or ZnO ($E_g = 3.37$ eV), for example.² Recent efforts have been dedicated to the study of one-dimensional tellurium nanostructures for thermoelectric applications.³⁻⁵ Te is particularly attractive thermoelectric material because of their high Seebeck coefficient.⁶ Array of Te nanowires and nanotubes also exhibited excellent sensitivity to ammonia,⁷ carbon and nitrous oxide at room temperature.⁸ Monolayers of aligned ultrathin Te nanowires have been fashioned to fabricate high-power density piezoelectric devices displaying long-term stability and bending frequency stability.⁹

High quality one-dimensional noble metal and tellurides can be successfully synthesized or even core-shell nanostructures by using Te nanowires as chemical transforming (sacrificial) and physical template, respectively. A wide range of metal telluride nanowires ($MxTe$, $M=Ag, Bi, Pb, Cd, Zn, Cu, Co, Fe, PdPt$ etc.) and noble metal nanowires $Pt, Pd, AuPtPd$ nanowires can be synthesized with feasibility by using tellurium nanowires as chemical transforming template.¹⁰ Additionally, Te nanowires can be used as a physical template to fabricate carbon, crosslinked poly(vinylalcohol),¹¹ metal-organic framework,¹² amorphous calcium carbonate¹³ core-shell nanostructures. Qian et al. took advantage of template-free approach to produce biocompatible $Te@phenol-formaldehyde\ resin\ (PFR)$ core-shell nanowires with strong luminescence in the blue and green regions for cell labeling.¹⁴ These assertions provide a framework that motivates the design of well-controlled one-dimensional Te nanostructures

Xia's group pioneered the controlled synthesis of Te nanostructures in 2001.¹⁵ Nanowires with triangular cross section and in the shape of filamentary or needle-like nanostructures were prepared through the reduction of tellurium precursors (orthotelluric acid or tellurium oxide) in different solvent systems (ethylene glycol, water) via refluxing process. Te nanotubes were feasible to synthesize by using polyol method under self-seeding solution process.

Ultrathin nanowires (i.e. nanowires with diameter below 10 nm and a very high aspect ratio (AR, ratio between length to width) were achieved by precise control of the reduction kinetics of the anisotropic growth of Te in the presence of poly(vinylpyrrolidone) (PVP) under hydrothermal condition.¹⁶ Other routes endow surfactant-assisted synthesis in the presence of cationic surfactants such as cetyltrimethylammonium bromide (CTAB) or sodium dodecyl benzenesulfonate (SDBS)^{17,18} at ambient pressure.¹⁹ Several strategies have been developed to rationally design 1D Te nanostructures with unique morphologies. Flower-like superstructure of Te was prepared through a biphasic solvothermal method route using diethyldithiocarbamate tellurium (IV) as Te precursor and 2, 20-dithio-dibenzoic acid as reducing agent.²⁰ Feather- and flower-like superstructures of Te were specially achieved by self-assembly of Te nanowhiskers under hydrothermal conditions. Porous tridimensional network-structure composed of Te plates were recently fabricated by conversion of Sb_2Te_3 hexagonal nanoplates using tartaric acid. Tree-like Te nanostructures were synthesized using tellurium tetrachloride ($TeCl_4$) as a Te precursor and thioglycolic acid as reducing and capping agent.²¹ Strong binding chiral ligands (i.e. glutathione, cysteine, penicillamine) were recently applied to produce Te nanostructures with enantioselective lattice and shape chirality.²² Single crystal belt-twisted and belt-rolled Te nanotubes were achieved by the hydrothermal disproportionation of Na_2TeO_3 in aqueous ammonia solution without the presence of any specific capping agent or template.²³ Nevertheless,

further investigation is currently being undertaken to explore one-dimensional Te nanostructures with diverse morphology. In this work, Te nanowiskers, round-tip nanowires and nanohelices were fabricated by poloxamer-assisted one-pot synthesis in different temperatures at ambient pressure. Specially, this is the first report describing the synthesis of Te nanohelices whose structure is challenging to achieve by a direct synthesis method. One dimensional Te@Ag and Au1D nodular-like hybrids were synthesized by using Te nanowires and nanohelices as sacrificial template, respectively. This work also place emphasis on the preparation of optically active one-dimensional nanostructures based on Te nanostructures. Owing to their exclusive shape, Te nanohelices were chosen as model for the synthesis of optically active 1D hybrids. A functional coating of phenol-formaldehyde resin effectively preserved the shape of Te nanohelices and also played a pivotal role on the deposition of lanthanide hydroxycarbonates and metallic nanoparticles. The current findings stem from the potential utility of these nanocrystals in diverse optical applications.

3.2. Experimental Section

3.1.1. Standard synthesis of Te1D nanostructures in Pluronic® F68

An aqueous solution of TeO₂ (99.9+%) dissolved in HCl 4.8 mol L⁻¹. (50 μL, 0.02 g L⁻¹) and an aqueous solution of Pluronic® F68 (20 mL, 0.33745 wt%) in terms of monomer) were mixed under vigorous stirring in a glass vial (25 mL) at room temperature during 10 min. Afterwards, an aqueous solution of H₃PO₂ (200 μL, 0.3128 mol L⁻¹), was added into the mixture upon a Te:H₃PO₂ molar ratio of 1:10. The mixture was vigorously stirred for additional 10 min and divided into 4 test tubes with screw caps of 10 mL. The test tubes were kept in different temperatures set at 0-5 °C (refrigerator) and room temperature (~21 °C), 50 °C (dry-bath incubator) and 90 °C (dry-bath incubator) without stirring for 24h. The resulting suspension of Te1D nanostructures will be represented as **TeA X°C**, where **X** describes the temperature that the synthesis was undertaken.

3.1.2. Scaling up the synthesis of Te1D nanostructures by twenty times.

The scale-up synthesis of Te1D nanostructures was performed according to the following procedure in different temperatures: An aqueous solution of TeO₂ dissolved in HCl 4.8 mol L⁻¹ (2.5 mL, 0.02 g L⁻¹) and an aqueous solution of Pluronic® F68 (50 mL, 0.33475 wt%) were mixed at room temperature during 5 min. Afterwards, an aqueous solution of H₃PO₂ (413.5 μL, 50 wt%) was added into the mixture upon a Te:H₃PO₂ molar ratio of 20:100. The mixture was vigorously stirred for additional 10 min. The reaction mixture was divided into 5 test tubes with screw caps of 10 mL and transferred to an air convection drying oven set at 40 °C or 90 °C and kept for 24 h.

Comparing with the standard synthesis of Te1D nanostructures, the concentration of Te was increased 20x whereas the concentration of H_3PO_2 was increased 10x. The synthesis was also studied at an intermediate temperature of 60 °C. In this case, the batch volume was increase by 2x (i.e. 100 mL). The samples prepared in this protocol will be described by the following representation: **TeB X °C**, **X** describes the temperature that the synthesis was undertaken.

3.1.3. Synthesis of 1D Te@Ag hybrid nanostructures

Te@Ag hybrid one-dimensional nanostructures were prepared by the addition of different amount of AgNO_3 to pristine Te1D nanostructures synthesized using the protocol described in the item 1.2.2. Briefly, an aqueous stock suspension of **TeB 90 °C** (2 mL) was firstly collected by centrifugation at 4000 rpm during 10 min. Afterwards, the solid was washed once with MiliQ water (2 mL) at 4000 rpm. Thereafter, the solid was redispersed into MiliQ water (4 mL). We studied the deposition of Ag nanoparticles onto the surface of Te nanowires by adding different volumes of a fresh aqueous solution of AgNO_3 (5 mM). The fabrication of Te@Ag hybrids was investigated in the following Te:Ag molar ratios: 1:0.005, 1:0.01 and 1:0.025.

Additionally, we evaluated the introduction of poly(vinylpyrrolidone), PVP, aqueous solution in different concentrations as stabilizing agent in order to control the growth of Ag nanoparticles. Briefly, an aqueous stock suspension of **TeB 90°C** (500 μL) was firstly collected by centrifugation at 4000 rpm during 10 min. Afterwards, the solid was washed once with H_2O MiliQ (2 mL). The solid was redispersed in H_2O MiliQ (3.5 mL) and PVP ($M_w = 55000 \text{ g mol}^{-1}$) (4 mL, 0.058 wt% - 0.58 wt%) was introduced with subsequent addition of AgNO_3 (15.6 μL , 5 mM). The sample was kept overnight at 60°C and washed once with H_2O MiliQ.

Regardless, the reaction mixture was kept in test tube with a screw cap tightly sealed at 60 °C overnight.

3.1.4. Synthesis of 1D Te@Au hybrid structure

In 20 mL glass vial, a stock suspension of **TeB 60°C** stock suspension (794 μL , previously dialyzed in H_2O MiliQ) was added to a mixture of ascorbic acid (AA) 45 mM solution and PVP ($M_w = 55000 \text{ g mol}^{-1}$) 1 wt% (2.5 mL). The vial was placed in a shaker at room temperature. The stirring speed was set to 560 rpm. Afterwards, 100 μL of HAuCl_4 25 mM was injected. The reaction was allowed to proceed for additional 10 min. The resulting suspension was purified with subsequent washings with H_2O MiliQ. The washed solid was finally redispersed in PVP ($M_w = 55000 \text{ g mol}^{-1}$) 0.5 wt%.

3.1.5. Synthesis of 1D Te@resorcinol-formaldehyde (RF) nanocables

Briefly, in a 20 mL glass vial, 5.962 mL of Pluronic® F68 0.3375 wt% and 3.75 mg of resorcinol (1,3 dihydroxybenzene) were added to 1.537 mL of **TeB 60 °C** stock suspension previously dialyzed in H₂O MiliQ. Afterwards, 10 µL of NH₄OH 28 wt% was introduced under vigorous stirring. The reaction was kept under vigorous stirring for additional 40 min at room temperature. The resorcinol-formaldehyde (RF) resin coating was achieved by introducing 22.5 µL of formaldehyde. The reaction mixture was stirred for another 1 hour and further moved to an oil bath set at 50 °C. After 12 h, the resulting suspension was washed several times with H₂O MiliQ.

Tellurium core could be withdraw by adding H₂O:HCl:H₂O₂ etching solution prepared with a mixture of 2 mL of HCl 36.5 wt%, 5 mL of H₂O₂ 30 wt%, and 20 mL of H₂O MiliQ.

3.1.6. Synthesis of Te@RF/X nanocomposites, with X= YVO₄:Eu³⁺, Au nanospheres or Ag nanocubes

3.1.6.1. Synthesis of YVO₄:Eu³⁺ nanoparticles

Luminescent YVO₄:Eu³⁺ nanoparticles were prepared according with previous report.²⁴ Sodium orthovanadate (Na₃VO₄) was used as vanadate (VO₄³⁻) source. Na₃VO₄ was synthesized by the reaction of sodium oxide (Na₂O) with sodium metavanadate (NaVO₃) at 700 °C under a heating rate of 14 °C min⁻¹ and nitrogen atmosphere.²⁵ The mixture was kept in this temperature for additional 4 hours and then cooled to 200 °C. After 10 h, the mixture was cooled down to room temperature. The resulting white powder was further dissolved in MiliQ water to prepare Na₃VO₄ 0.2 mol L⁻¹.

Aqueous solutions of Y(NO₃)₃ 1 mol L⁻¹ (9 mL) and Eu(NO₃)₃ 1 mol L⁻¹ (1 mL) were mixed with 5 mL of sodium citrate solution 2 mol L⁻¹ under vigorous stirring at room temperature. A white milky suspension was immediately formed. Afterwards, 50 mL of an aqueous solution of Na₃VO₄ 0.2 mol L⁻¹ was added and the resulting mixture became transparent. The mixture was stirred for 45 min at 60 °C. Subsequently the suspension was dialyzed against Milli-Q water for 72 h.²⁶

3.1.6.1.1. Preparation of 1D Te@RF/YVO₄:Eu³⁺ nanoparticles

One of the strategies to design 1D luminescent nanostructures concerns the introduction of previously synthesized luminescent YVO₄:Eu³⁺ nanoparticles during the polymerization of RF resin on the surface of **TeB 60 °C** nanostructures. Therefore, 13.875 mL of an aqueous suspension of Pluronic® F68 0.3375 wt% was mixed to 3.8425 mL of dialyzed Te nanohelices aqueous stock suspension and 0.935 mL of an aqueous solution of resorcinol 1 wt% under vigorous magnetic

stirring (600 rpm) and at room temperature. 25 μL of NH_4OH 28 wt% was introduced and the reaction mixture was stirred for additional 40 min. Afterwards, 14 μL of formaldehyde was rapidly added. After 4 hours, 6 mL of the reaction mixture was divided into two glass vials. For each 3 mL of reaction mixture, different volumes of $\text{YVO}_4:\text{Eu}^{3+}$ nanoparticle suspension was added: A) 1000 μL and B) 1500 μL . The glass vials were placed in an oil bath set at 50 $^\circ\text{C}$ for 12 h under continuous magnetic stirring (600 rpm). The solid was collected by centrifugation at 8000 rpm and washed twice with MiliQ H_2O .

3.1.6.2. *Synthesis of Au nanospheres*

The initial Au seeds were prepared by adding 0.6 mL of an ice-cold aqueous solution of NaBH_4 10 mM into 10 mL of an aqueous solution of HAuCl_4 0.25 mM and CTAB 100 mM. Then, the mixture was left undisturbed at 27 $^\circ\text{C}$ for 3 h to ensure the complete decomposition of any NaBH_4 . In a 20 mL glass vial, 2 mL of an aqueous solution of HAuCl_4 0.5 mM was mixed with a solution of 2 mL of an aqueous solution of cetyltrimethylammonium chloride (CTAC) 200 mM, and 1.5 mL of an aqueous solution of ascorbic acid (AA) 100 mM. Afterwards, 100 μL of Au seeds were mixed subsequently. The reaction was allowed to proceed undisturbed in a thermostatic water bath set at 27 $^\circ\text{C}$ for 10 min. The product was collected by centrifugation at 14500 rpm for 30 min and washed once with water. The solid was redispersed in 2 mL of MiliQ water.

3.1.6.2.1. *Preparation of 1D Te@RF/Au nanospheres*

In a 20 mL glass vial, 0.05 g of Pluronic® F68, 3.8425 mL of dialyzed of **TeB 60 $^\circ\text{C}$** aqueous suspension, 0.935 mL of an aqueous solution of resorcinol 1 wt% and 25 μL of NH_4OH 28 wt% were consecutively mixed in 13.875 mL of H_2O under vigorous magnetic stirring (600 rpm) at room temperature for 40 min. Afterwards, 1 mL of the reaction mixture was withdraw and 50 μL of Au nanospheres was introduced in the reaction mixture. The reaction mixture was placed on an orbital shaker set at 560 rpm for 16 h at room temperature. The solid was collected by centrifugation at 12000 rpm and washed twice with MiliQ water. Therefore, the solid was redispersed in 500 μL of MiliQ water.

3.1.6.3. *Synthesis of Ag nanocubes*

In a 250 mL round bottom three neck 50 ml of ethylene glycol was added in an oil bath set at 152 $^\circ\text{C}$ for 45 minutes with magnetic stirring. During this time, the following solutions were prepared in ethyleneglycol: NaHS 3 mM (solution 1); HCl 3 mM (solution 2); polyvinylpyrrolidone (M.W. 55,000 g mol⁻¹) 2 wt% (solution 3), and CF_3COOAg 282 mM

(solution 4). After 45 minutes, 0.6 mL of solution 1 was added. After 4 minutes, 5 ml of solution 2 was added. After subsequent 2 minutes, 12.5 ml of solution 3 was added; After additional 2 minutes, 4 ml of solution 4 was quickly added. The reaction was monitored the LSPR peak of Ag nanocubes. Purification was carried out by crushing the Ag nanocubes in acetone followed by consecutive washing with MiliQ water. The final solid was redispersed in 9 mL of MiliQ water.

3.1.6.3.1. Preparation of 1D Te@RF/Ag nanocubes

The protocol is the same as described in the item 1.2.6.2.1 with the exception that the suspension of Au nanospheres was replaced by 10 μL of Ag nanocubes stock suspensions.

3.1.7. Preparation of 1D Te@RF/(LaCeTb)CO₃OH nanostructures

In a 20 mL glass vial, 200 μL of aqueous suspension of Te@RF nanocables were diluted to 3 mL with H₂O MiliQ at room temperature. The vial was placed on oil bath and the temperature was increased to 90 °C under a heat speed of 5 °C min⁻¹. 100 μL of a solution of La³⁺:Ce³⁺:Tb³⁺ (45:45:10 molar ratio) 0.1 mol L⁻¹. After 10 min, 100 μL of urea 3.33 mol L⁻¹ was dropwise. The reaction mixture was kept under vigorous stirring at 600 rpm for additional 30 min. The reaction was terminated by immersing the vial in ice. The solid was collected by centrifugation at 10000 rpm and washed twice. The solid was redispersed in 500 μL of MiliQ water.

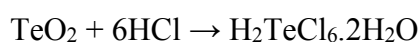
3.1.8. Preparation of 1D Te@RF/Au nanostructures

In a 20 mL glass vial, 200 μL of an aqueous suspension of Te@RF nanocables was diluted to 3 mL with H₂O MiliQ at room temperature. Afterwards, 300 μL of fresh solution of NaBH₄ 10 mmol L⁻¹ was rapidly added. After 2 min, 50 μL of H₂AuCl₄ 25 mmol L⁻¹ was injected. The reaction mixture was kept under vigorous stirring at 750 rpm for 15 min. The solid was collected by centrifugation at 6000 rpm and washed three times with H₂O MiliQ.

3.2. Results and discussion

3.2.1. Tellurium nanowhiskers and nanowires

The synthesis of 1D-Te nanostructures underlies the prior dissolution of tellurium precursor (*e.g.* TeO₂) with a concentrated HCl solution as described by the following equation:²⁷



The reduction of soluble chlorotellurate (IV) species by H_3PO_2 can be described according to the redox reaction:²⁸



During the synthesis of **TeA X °C** or **TeB X °C** nanostructures, the suspensions displayed several color changes as a function of the time: a clear pale yellow followed by a brownish color were observed within 60 min after the introduction of H_3PO_2 . Afterwards, the suspension developed a purple color, which progressively became blue within 24 h. The color shift from brownish to blue is associated with the increase of aspect ratio of the 1D-Te nanostructures.^{29,30}

SEM images of the resulting 1D-Te nanostructures are shown in the Figure 10. At low temperature, sphere-like shape nanostructures with 100 nm in diameter together with spike-like Te nanostructures were observed. The spheroids seems to exhibit roughness morphology leading to the formation of branches onto spheroid surface as showed at Figure 10, A and B.

The spheroidal particles may result from aggregation of elemental Te seeds, thereby decreasing their surface free energy. The aggregation of Te seeds is driven by an Ostwald Ripening mechanism¹⁵ so the assembly into spheroidal shape (smaller ratio surface area/volume shape) is more favorable comparing with other shapes. The branches emerge due to the anisotropic nature of elemental tellurium building blocks. On the course of the reaction, spheroidal nanoparticles were consumed (dissolution) as a function of newly one-dimensional Te nanostructures (recrystallization). It is suggested that the presence of surfactant molecules play a key role to prevent the aggregation among the nanoparticles via electrostatic and steric hindrance. Additionally, it should be pointing out that the presence of charged species such as halide ions could play an important role on the nucleation and growth steps since these species are naturally smaller than surfactant molecules. During the reduction of TeO_2 , the excess of chloride was used

to dissolve the tellurium precursor, thereby it could attach onto the surface of the in initial seeds and help to prevent eventual aggregation through electrostatic repulsion.

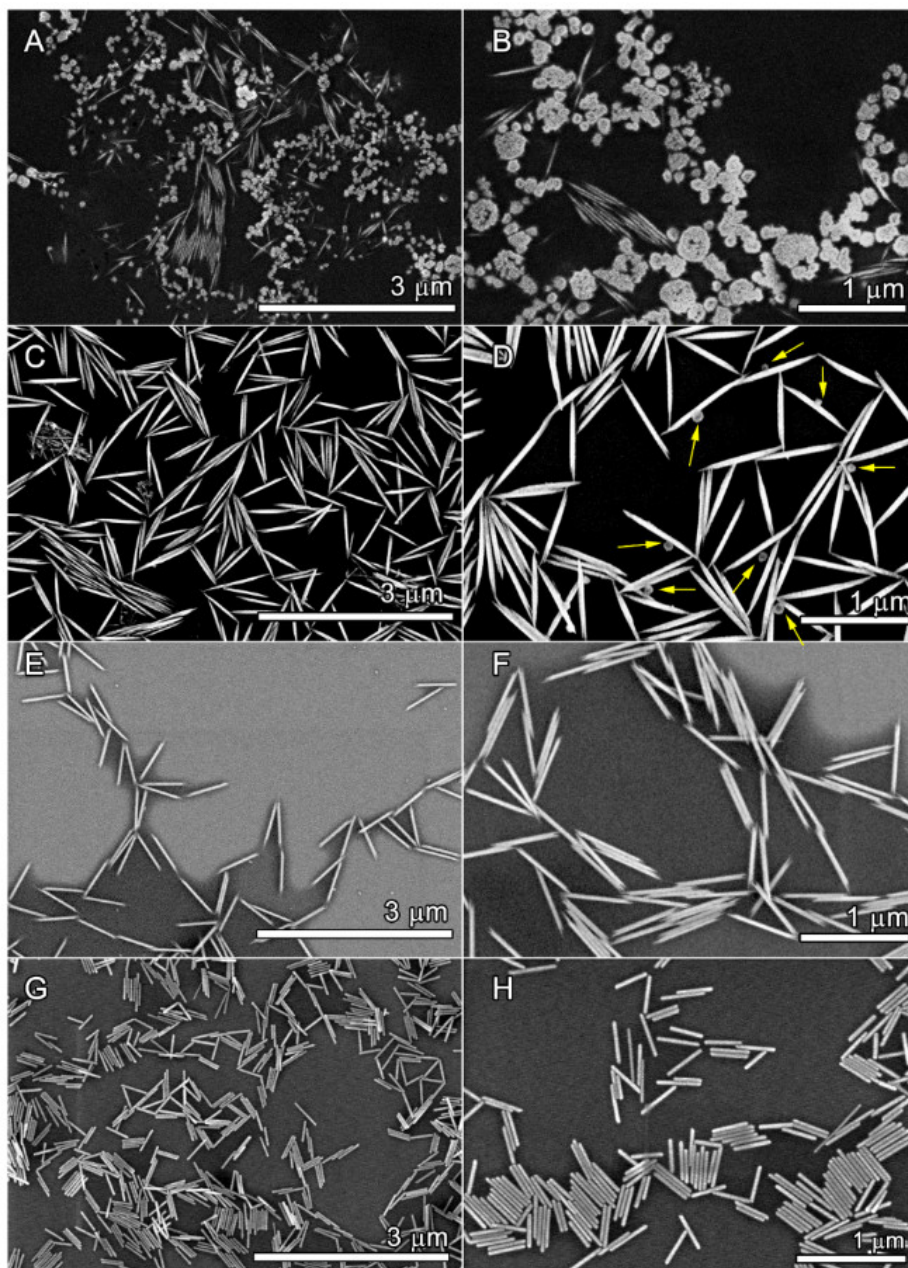


Figure 10. SEM images of products resultant from a synthesis of 1D Te nanostructures in the presence of Pluronic® F68 conducted in different temperatures. (A, B) **TeA 5 °C**; (C, D) **TeB 21 °C**; (E, F) **TeA 50 °C**; and (G, H) **TeA 90 °C**.

Therefore, when the reaction was carried at higher temperature, the seeds have been consumed to produce Te1D nanostructures as displayed in Figure 10, C-H. Particularly, the suspensions of

Te1D nanostructures prepared at 50 °C and 90 °C displayed excellent stability and any change of shape or occurrence of aggregation was observed within a period of 6 months.

The TEM images shown in Figure 11, A and B, reveal a wave-like structure in the ends of **TeB 40 °C** nanostructures (or Te nanowhiskers) prepared from a scale-up synthesis. The wave-like shape in the end of nanowhisker seems to be fashioned with a single 1D Te nanostructure. As highlighted in Figure 11B, the diameter of the tip is continually reduced in direction to the end of the Te nanowhisker. A detailed inspection of the tip was conducted through HRTEM analysis picture in Figure 11, C and D.

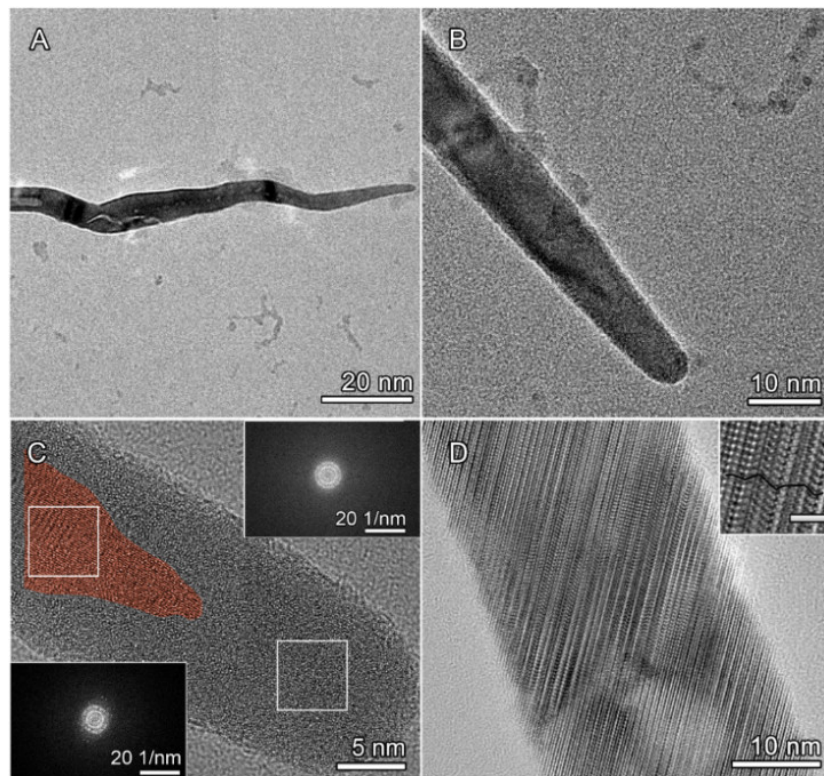


Figure 11. (A, B) TEM images from the end of a single Te nanowhisker (**TeB 40 °C**) prepared from a scale-up synthesis. (C) HRTEM image from the tip of a Te nanowhisker showing the fast-fourier transform (FFT) of two regions with distinct crystallinity. (D) HRTEM image of the middle portion of a single Te nanowhisker displaying considerable stacking disorder. The inset shows the magnified region of the HRTEM showed in panel (D) The black lines highlight the mismatch of crystalline planes order due to the stacking faults defects. The scale bar of the inset in (D) is 2 nm.

The Fast-Fourier Transform (FFT) of two distinct regions demonstrates that the end of the tips was formed by amorphous and crystalline phases. The region defined with reddish color corresponds to the Te crystalline phase whose FFT images displays a regular periodicity. On the other hand, the FFT of the very tip end do not show any periodicity, a typical feature of an

amorphous phase. The Figure 11D clearly shows that the middle portion of Te nanowhiskers have defects emphasized by the presence dislocation and stacking faults.

Figure 12, A and B, reveals that the **TeB 90 °C** nanostructures (or Te nanowires) were homogeneous in lateral size with an average diameter of 27 nm. Furthermore, the nanowires display round tips. Beyond that, the HRTEM images of Figure 12, C and D, confirms that the Te nanowires were single-crystal free of dislocations and stacking faults. The HRTEM images of Te nanowires also display a clear direction growth towards the [001].

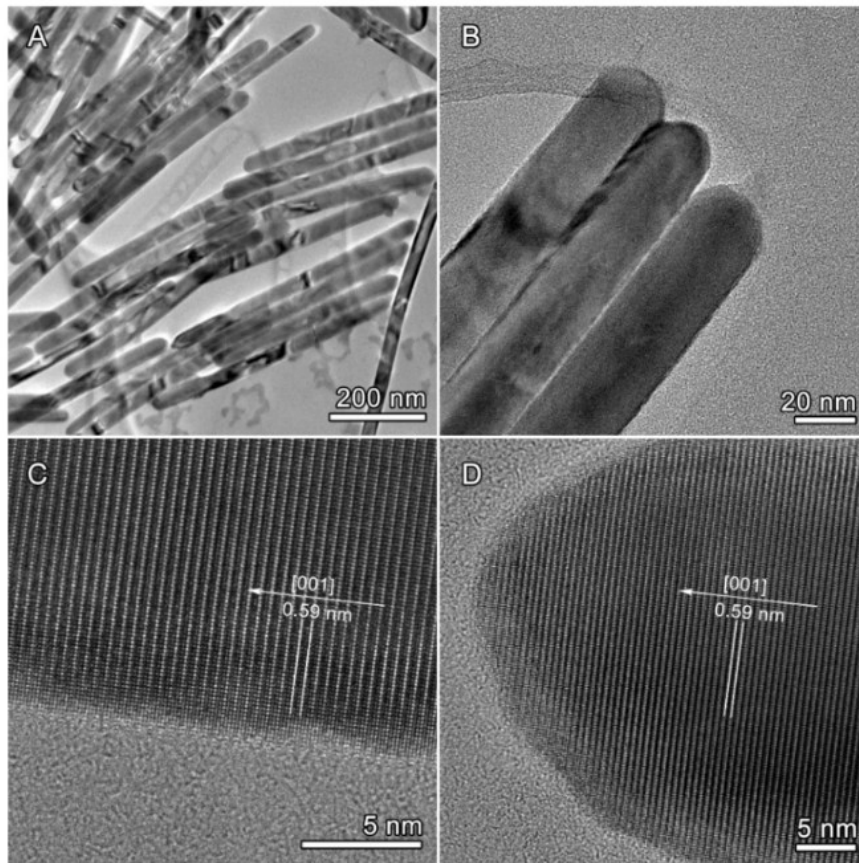


Figure 12. TEM images of Te nanowires (**TeB 90 °C**) obtained from a scaled-up synthesis in the presence of Pluronic® F68. The concentration of Te was increased 20 times while the concentration of H_3PO_2 was increased 10 times in comparison to the standard synthesis.

In addition, the amorphous phase tip present in the Te nanowhisker disappeared when the temperature of the synthesis was raised from 40 °C to 90 °C as illustrated in Figure 13.

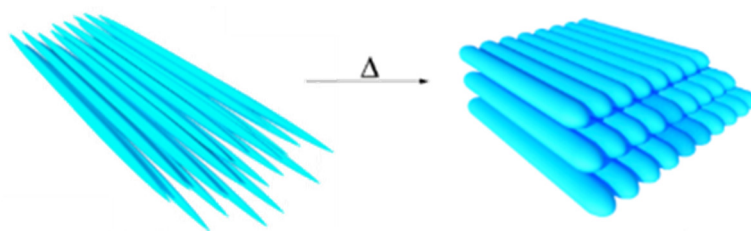


Figure 13. Schematic illustration highlighting the structure evolution from spike-like Te nanostructures to round-tip Te nanowires when the temperature was raised from room temperature to 90 °C, respectively.

We can assume that the amorphous material present in the tip of the Te nanowires would be completely transferred into the trigonal form through Ostwald ripening. Obviously, this process could be accelerated with the increase of the temperature.

We evaluated the alignment of the nanostructures by using the liquid-liquid-air interface approach rather than achieve high dispersion of Te1D nanostructures in nonpolar solvent (i.e. CH_3Cl , CH_2Cl_2) highly desired to Langmuir-Blodgett technique. Recently, Ariga group have explored this approach for the alignment of hydrophobic C_{60} nanowires in an interface of water (bottom layer) – isopropanol (top layer) – air under vortex stirring.³¹ With evaporation of isopropanol, side-by-side and head-to-head assembly of C_{60} nanowires was achieved at the air water interface. Herein, we used an inverted setup where Te1D nanowhiskers dispersed in isopropanol was dropwise on hydrophobic layer of CH_3Cl .

3.2.2. *Liquid-liquid-air interface (polar/apolar solvent)*

The attempt to align Te1D nanostructures was leveraged by subjecting the pristine suspension of nanowhiskers (e.g. from scale-up synthesis) to assemble in the liquid-liquid interfaces with CF_3Cl . On the course of the time, a layer of Te nanowhisker was formed in the isopropanol- CF_3Cl interface. Subsequently, we transferred this layer by a liftoff process where a clean glass substrate was slowly shifted over the path of a glass cuvette as shown in Figure 14.

SEM images of the glass surface covered with the Te layer are shown in Figure 14, C and D. The low magnification SEM images show that Te nanowhiskers were spread on the surface of glass in random orientations. A magnified SEM image of the deposited Te layer reveals the formation of bundles of Te nanowhiskers attached side-by-side. In fact, few reports show the preparation of Te bundles nanostructures. To date, Ma et al³² developed an alternative route to grow Te bundles assisted by ionic liquid. The authors report that the aggregation of Te nanowires into bundles was driven by compression of electric double-layer of the nanocrystals due to high ionic strength during the growth. In this work, we suggest that such aggregation is a response of

the dehydration of poly(ethylene oxide) and poly(propylene oxide) groups of Pluronic® F68 polymer in the isopropanol-CF₃Cl interface.

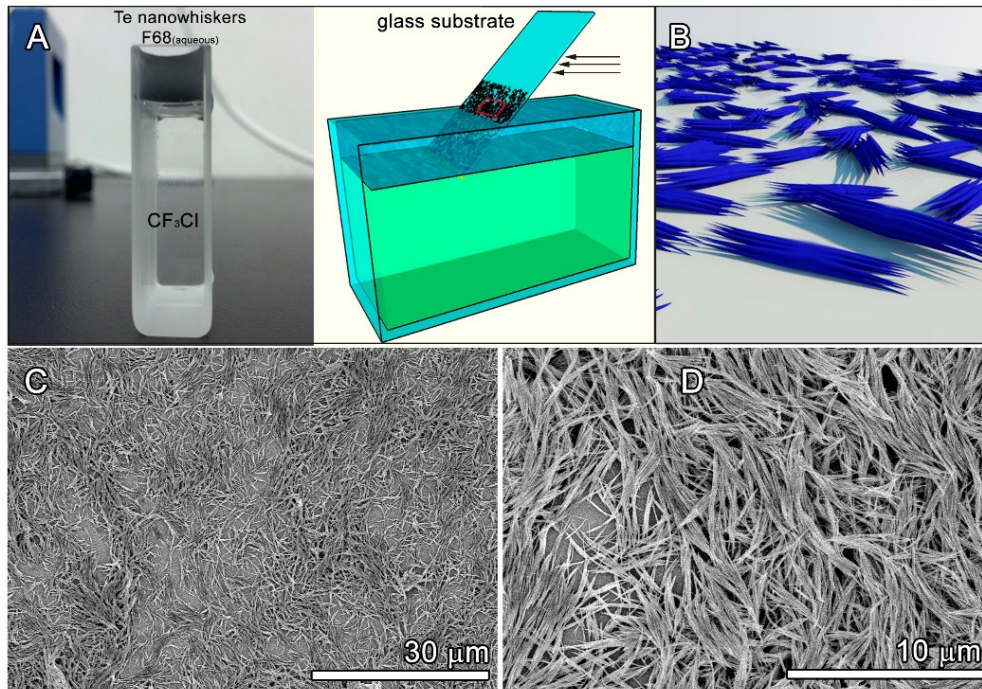


Figure 14. (A) Picture and schematic illustration of the apparatus used to perform the alignment in the liquid-liquid-air interface. A glass substrate was firstly cut with the width tightly close to the cube aperture. The substrate was slowly shifted over the entire cube aperture with a diving depth slightly beyond the liquid-liquid interface and further remove to dry at room temperature (B) Representation of Te nanowhiskers deposited onto the glass substrate surface. (C, D) SEM images of Te nanowhiskers (**TeB 40 °C**) transferred to a glass substrate from the liquid-liquid interface between an isopropanol-CF₃Cl.

3.2.3. Self-assembly by drop casting method

We also evaluated the assembly of Te nanowires as a result of drop casting of Te nanowires of different aspect ratio (AR) over hydrophilic Si/SiO₂ substrate at room temperature (~21 °C). Long Te nanowires with AR larger than 250 were obtained by replacing Pluronic® F68 with cetyltrimethylammonium bromide (CTAB) 0.032 wt% in the standard synthesis, while other parameter were kept unchanged. Figure 15 and Figure 16 show the self-assembly of low AR nanowires prepared from drop cast of a suspension from standard (**TeA 40 °C**) and scale-up (**TeB 90 °C**) synthesis, respectively. Figure 17 shows the border of a dried drop of large AR Te nanowires (or *long* Te nanowires).

Simple drop casting of Te1D nanostructures prepared in Pluronic® F68 leads to the formation of multiple rings towards the center of the droplet while the evaporation is taken place (“coffee-

ring effect”), whose rings are essentially composed of dense ordered layers of Te nanowires. The spontaneous spreading of a droplet on a hydrophilic solid surface can be considered to align 1D nanostructures towards the spreading flow upon the evaporation of the solvent.

During the evaporation of water, Te nanowires in the droplet move toward droplet edge by convective flow. Therefore, this motion provides an increased local concentration and form sequential pinned nanostructures (arrays) laterally aligned each other.

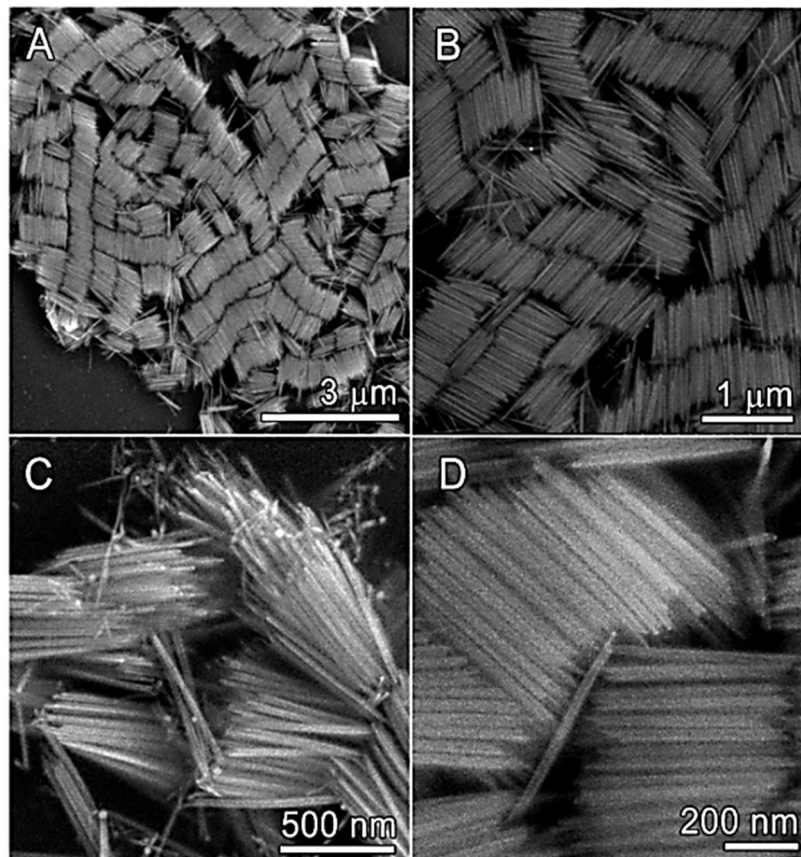


Figure 15. SEM images of TeA 40 °C nanostructures assembled into bundles through drop casting at room temperature on a Si/SiO₂ wafer.

As show in Figure 15, Figure 16 and Figure 17 the spreading process near the substrate surface led to the existence of a shear force that aligns the Te1D nanostructures towards the flow direction before they are immobilized on the Si/SiO₂ substrate. The alignment occurs due to the fact that the Te nanowires are carried out by the spreading flow and eventually they sink onto solid substrate due to the gravity effect.

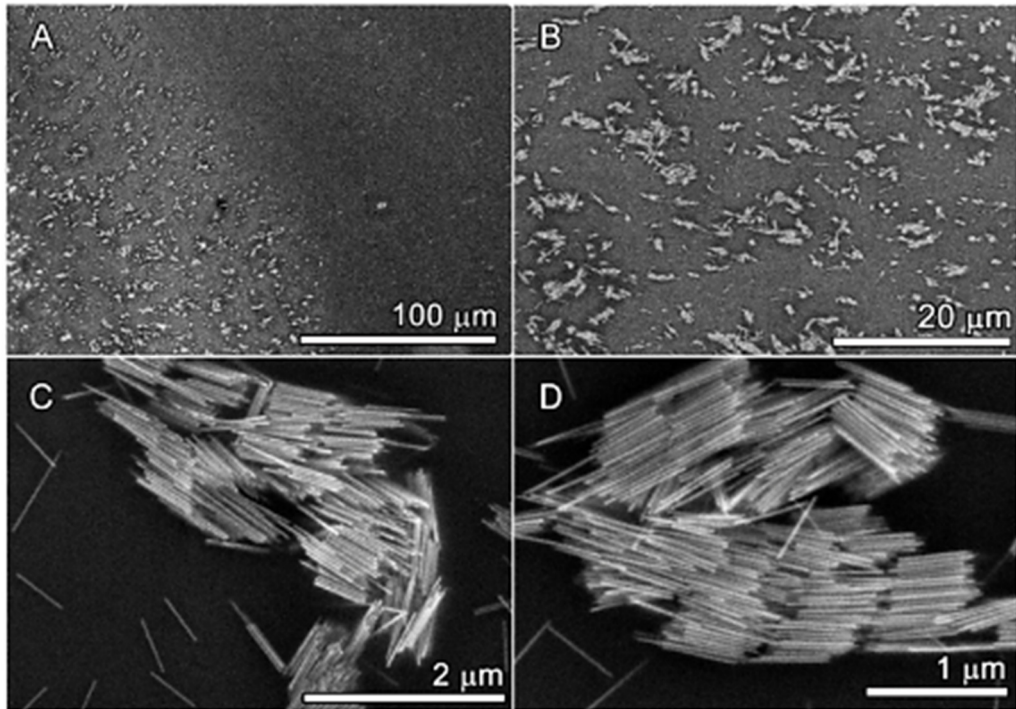


Figure 16. SEM images of Te nanowires (F68, Te:H₃PO₂ 20:100, 90 °C) obtained from a scale-up synthesis which were dropped on a Si/SiO₂ wafer. (A, B) low magnification SEM images of the edge of a droplet of Te nanowires (C, D) SEM images of the bundles of Te nanowires assembled during the drying of the droplet at room temperature on a flat surface of Si/SiO₂ wafer.

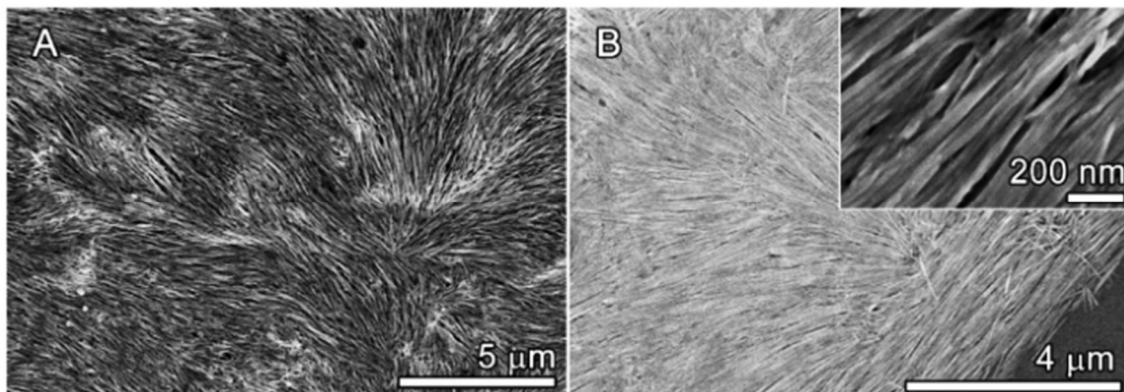


Figure 17. (A, B) SEM images of *long* Te nanowires settled on the border of a droplet. The array of Te nanowires assembled during the drying of the droplet at room temperature on a flat surface of Si/SiO₂ wafer. The inset in (B) shows a magnified region of the border formed by uniformed aligned along the spreading flow direction.

As illustrated in Figure 18, the alignment by drop casting method underlies directing self-assembly of particles in liquid-air interfaces. In this method, the particles are segregated near the liquid-air interface and an attractive interaction between the particles and the liquid-air interface localize them on the interface.

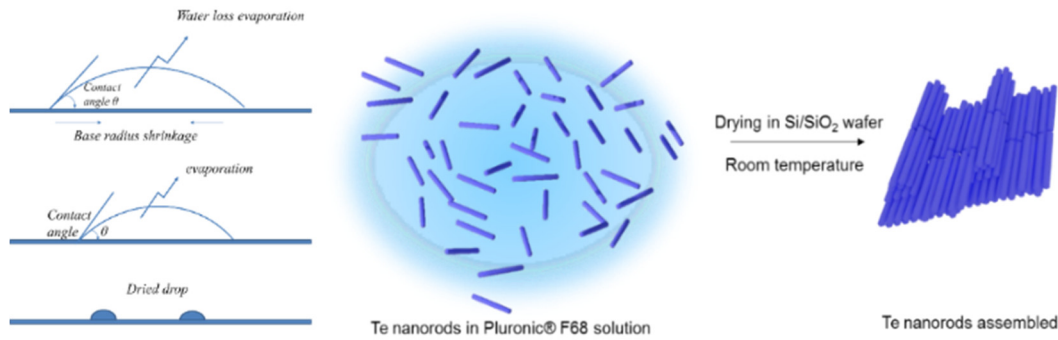


Figure 18. Schematic illustration of several steps involved on the drying of an aqueous suspension droplet into hydrophilic surfaces (left). Representation of the assembly of Te nanowires resulting from the drying of a suspension drop on the surface of Si/SiO₂.

Together, this establishes a saturated 2D solution of particles on the liquid–air interface. It is well-known that one-dimensional nanostructures will spontaneously undergo rotational ordering when their containing volume shrinks (e.g., due to solvent evaporation). A strongly attractive interaction encourages nanowires to maximize their area of contact with the substrate by lying parallel to it.

As clearly shown, drop casting method provides localized alignment of Te nanowires of different AR in hydrophilic surface. Noteworthy, in order to meet specific requirements demanded by relevant technological optoelectronics applications, it is essential to assemble 1D nanostructures into (super) lattices/structures rather than localized aggregates. However, (super) lattices were hardly achieved due to the lack of sufficient interparticle interaction and particle-substrate interactions. Commendable efforts have been put into tailoring the evaporation-induced assembly of 1D nanostructures in micro/capillary fluid flow dynamics where the flux is approximately one-directional.³³ At first glance, we suggest that Te nanowires synthesized in this work are potential candidates to conceive more complex arrays offered by micro/capillary methods.

3.2.4. Preparation of Te@Ag hybrid by using Te nanowires as template

SEM images shown in Figure 19, A and B, display that the formation of Te@Ag hybrid nanostructures is majority composed by Ag nanoparticles attached onto the surface of corroded Te nanowires when the Te:Ag molar ratio was set to 1:0.01 and 1:0.025 respectively. In this case, any surfactant was employed in the synthetic protocol. Ag nanoparticles with quasi-spherical shape and size in the range of 25–61 nm were randomly distributed along the Te nanowires.

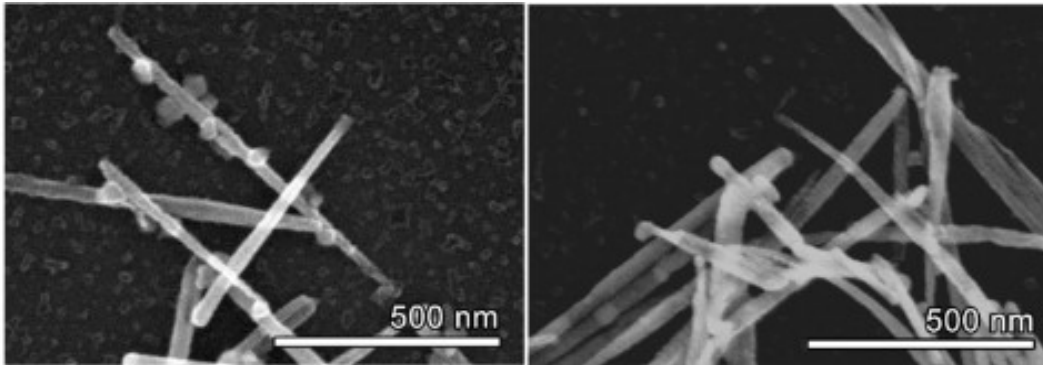
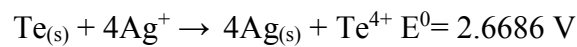


Figure 19. SEM images of 1D Te@Ag hybrid nanostructures when (a) 31.2 μL and (b) 78 μL of AgNO_3 5 mM.

We suggest that the deposition of Ag nanoparticles is due to a redox process:



We also investigated the deposition of Ag nanoparticles onto the surface of tellurium nanowires in the presence of aqueous solutions of PVP ($M_w = 55000 \text{ g mol}^{-1}$), a nonionic stabilizer or capping agent, at different concentrations in order to better control the size of Ag nanoparticles.

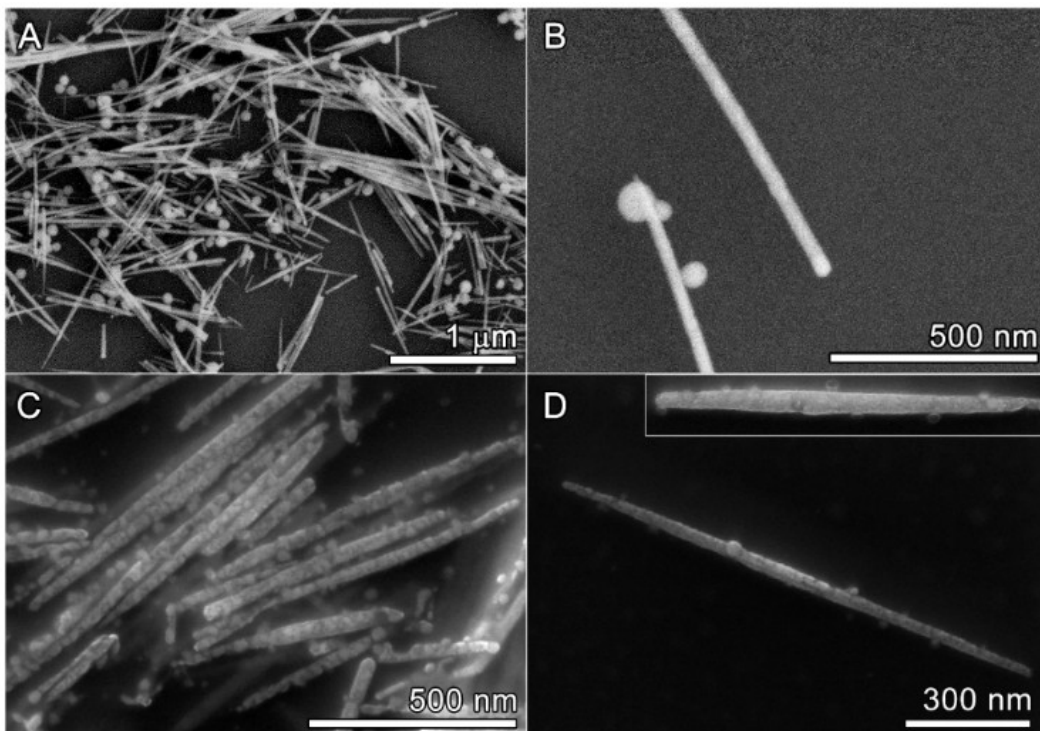


Figure 20. SEM images of 1D Te@Ag hybrid nanostructures prepared from addition of 15.6 μL of AgNO_3 5mM into Te nanowires in the presence of different concentration of PVP ($M_w = 55000 \text{ g mol}^{-1}$): (A, B) 0.058 wt% and (C, D) 0.58 wt%.

SEM images of Te@Ag derivative hybrids when the Te:Ag molar ratio was set to 1:0.005 are shown in Figure 20, C and D. When the reaction undergoes in the presence of PVP 0.058 wt%, the corrosion of Te nanowires is less noticeable. Additionally, the Ag particles are clearly more

spherical in shape comparing to those ones obtained in the absence of PVP at higher concentration of AgNO_3 . On the other hand, the size of Ag nanoparticles increases to 68-104 nm.

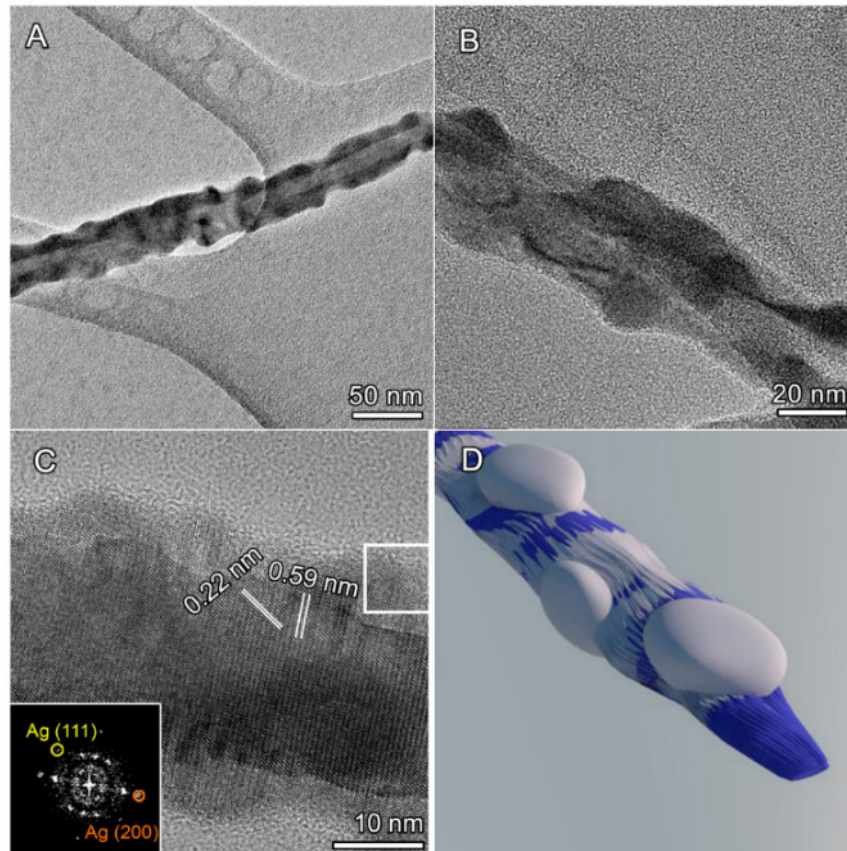


Figure 21. (A, B) Low magnification TEM images of tellurium nanowires covered with a Ag layer prepared in the presence of PVP 0.58 wt%. (c) HRTEM image of the middle portion of a single 1D Te@Ag hybrid nanostructure. The inset corresponds to the FFT of the squared region indicated in the (C). (D) Representation of the 1D Te@Ag nanostructure highlighting formation of non-homogeneous Ag nanoparticles onto the corroded surface of a tellurium nanowire.

When the concentration of PVP was increased 10 times, the number of Ag particles increases which is also accompanied by an overall size decrease of the Ag nanoparticles diameter as shown in Figure 20, C and D.

TEM images of the middle portion of a Te@Ag nanostructure in Figure 21, A and B, reveal the presence of a rough surface. It should be pointing out that considerable corrosion took place on the surface of Te nanowires as shown in Figure 21C. The formation of Ag nanoparticles could occur at cost of oxidation of tellurium. We carried out a more detailed analysis through HRTEM image of 1D Te@Ag displayed in Figure 21C. The d-spacing of 0.59 nm and 0.22 nm corresponds to the (001) and (010) of the trigonal Te phase. The d-spacing obtained from the FFT images of the edge of the 1D Te@Ag nanostructures match the face centered cubic (FCC) structure of Ag.

Beyond a capping agent, it is well known that hydroxyl end groups of PVP serve as mild reductant. We suggest that the deposition of Ag particles is maneuvered by the concentration of hydroxyl end groups of PVP as well as the available surface of Te nanowires. Once Ag^+ ions are introduced in the reaction mixture they are promptly reduced on the surface of Te nanowires. The reduction of Ag^+ ions would be kinetically controlled as a function of the concentration free hydroxyl groups of PVP. The increase of concentration of PVP could speed-up the reduction rate at the same time that narrows the size distribution of Ag nanoparticles. Therefore, Ag^0 atoms formed by both reduction performed by Te surface and PVP could feed the growth of Ag seeds deposited on the surface of Te nanowires (heterogeneous nucleation) described by Ostwald Ripening process. Nevertheless, faster reduction rates afford to the occurrence of homogeneous nucleation process. Occasionally, isolated small Ag nanoparticles were also observed together with Te@Ag hybrid nanostructures at high concentration of PVP.

3.2.5. *Tellurium nanohelices*

Surprisingly, we prepared non-conventional Te nanostructures by further scaling-up the synthesis of Te nanowires and decreasing the temperature. When we increase the batch volume by 2x (i.e. 100 mL) and set the temperature to 60 °C, Te nanohelices (**TeB 60 °C**) were prepared within 24h of synthesis. Figure 22 and Figure 23 show the TEM and HRTEM images of Te nanohelices respectively. The Te nanohelices had diameter in the range of 9-20 nm and lengths below 1 μm .

Figure 24, A and B shows the absorption spectrum in the ultraviolet-visible range and Raman spectroscopy of the suspension of Te nanohelices. Te nanohelices display two broad bands in the ultraviolet-visible range typically observed for Te 1D nanostructures.³⁴ The bands centered at 274 nm is related to electronic transitions from the valence band (ligand p-triplet) to the conduction band (antibonding p-triplet).

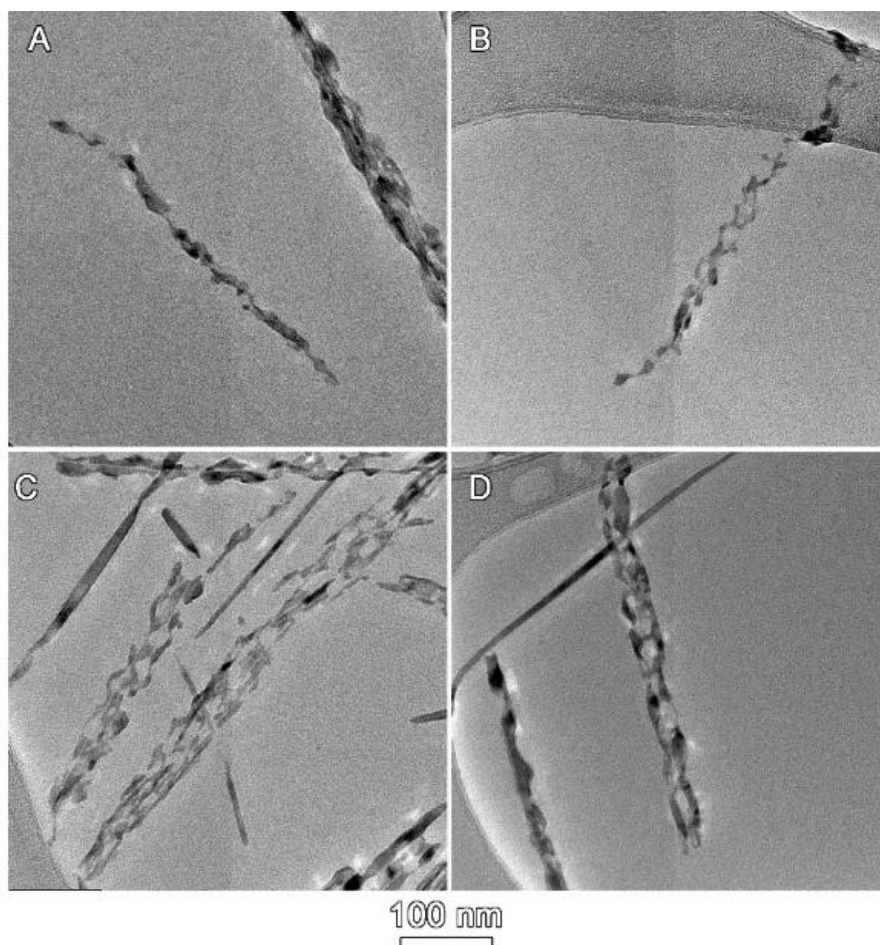


Figure 22. (A-D) TEM images of Te nanohelices achieved by scaling-up the synthesis of Te nanowires. The Te:H₃PO₂ was 40:200 comparing to the standard synthesis. The volume was set 100 mL of Pluronic® F68 0.3375 wt% and the temperature was kept at 60°C for 24 h under continuous stirring.

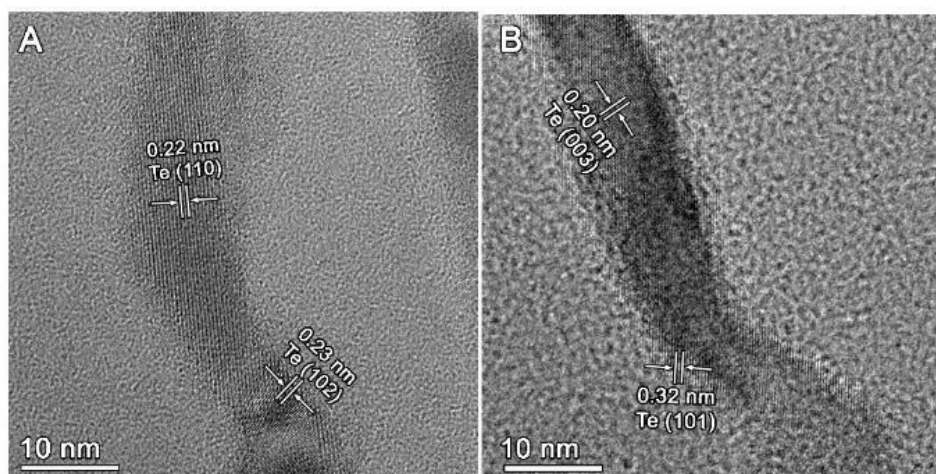


Figure 23 (A, B) HRTEM images of the middle portion of single Te nanohelices. The interplanar distances are well consistent with hexagonal lattice of Te.

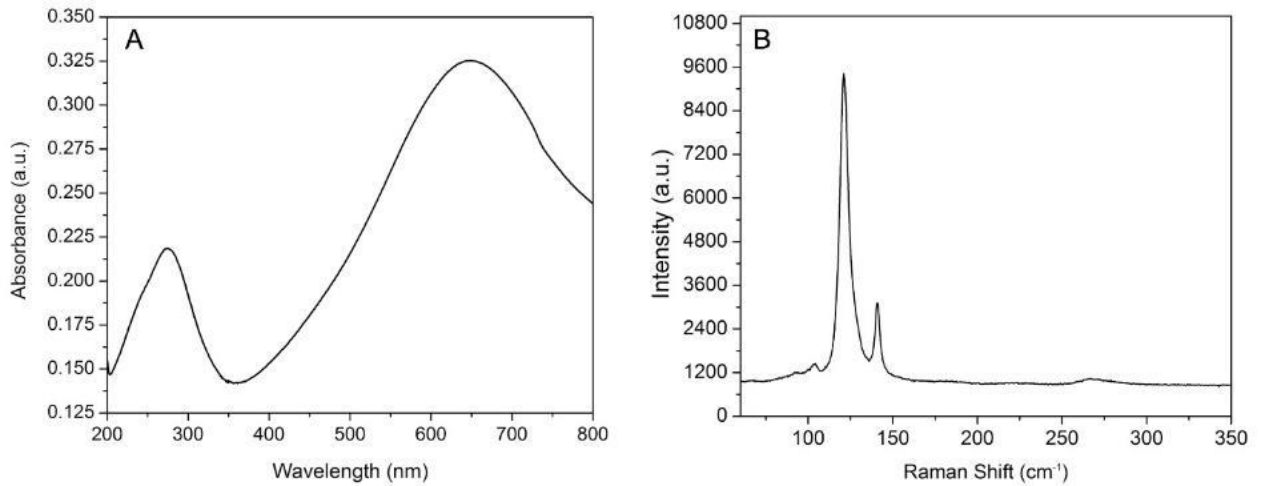


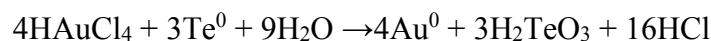
Figure 24. (A) Ultraviolet-visible and (B) Raman spectrum of Te nanohelices.

The intense and broad absorption bands centered in 648 nm is related to transitions from the valence band (non-bonding p-triplet) to the conduction band (antibonding p-triplet).³⁵ Te exhibits strong Raman-active phonon modes due to its high atomic number and large electronic polarizability. Essentially, crystal structure of trigonal Te is formed by infinite helical chains which spiral around the *c* axis with three atoms per turn. The Raman spectra show typical bands corresponding to the D_3 symmetry group of the Te lattice^{36–38} with one A_1 mode and two degenerate E modes. The strong bands at 121.7 cm^{-1} is assigned to the A_1 mode, described by the symmetric intrachain expansion and compression in the *ab* plane (basal plane);^{37,38} the weak bands centered at 103.7 cm^{-1} is assigned to $E(1)$ modes ascribed by the rigid-chain rotation over the *a*- and *b*-axis.³⁸

The bands at 141.2 cm^{-1} is assigned to the $E(2)$ mode mainly described by the asymmetric stretching along the *c*-axis.^{36,38,39} The broad bands at 266.3 cm^{-1} is related to the second order harmonic of the E mode of tellurium.^{36–38}

3.2.6. Te@Au hybrids nanostructures from Te nanohelices

Au peapod-like nanostructures were fabricated by using Te nanohelices as sacrificial template. The process can take place according to the following redox reaction:



Au^{3+} oxidizes Te and, as a result, tellurous acid (H_2TeO_3) is formed, which in turn is soluble in either acidic or basic environment. The standard redox potentials for the $\text{TeO}_3(\text{aq})^2 / \text{Te}(\text{s})$ and $\text{AuCl}_4(\text{aq}) / \text{Au}(\text{s})$ pairs are -0.57 V and 1.002 V , respectively, which indeed suggests spontaneous gold reduction. The crystalline mismatch between trigonal Te ($a = 4.495 \text{ \AA}$, $b = 3.74 \text{ \AA}$, $c = 5.912 \text{ \AA}$) and cubic Au ($a=b=c = 4.065 \text{ \AA}$) hinders the growth the possibility to grow a thin layer of Au on the surface of Te in a uniform fashion.

Interestingly, most of the Au nuclei with size smaller than 7 nm is found in the middle of the Te nanohelices along the entire longitudinal direction as shown in Figure 25, A and B.

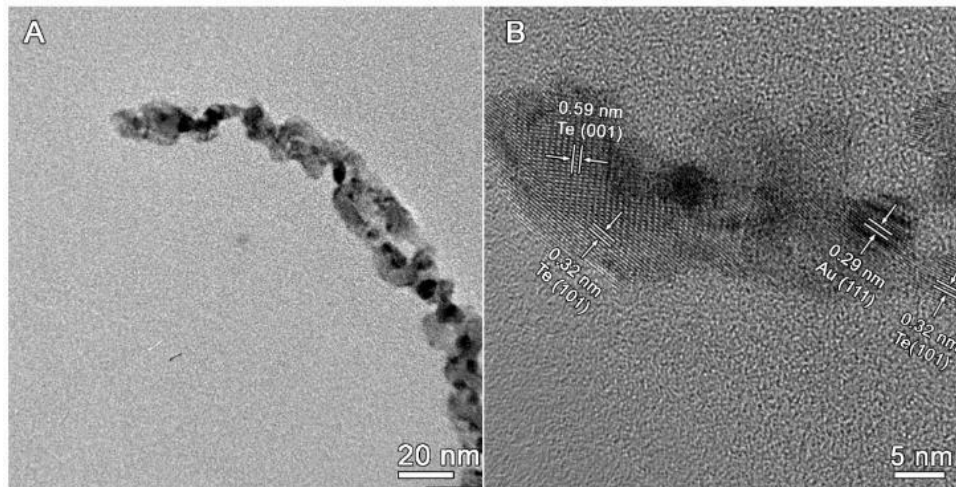


Figure 25. TEM image of Te@Au 1D hybrid during partial corrosion of Te nanohelices. The panel (B) clearly shows distinguished crystalline motifs between Au and Te.

On the course of the reaction, the continuous deposition of Au⁰ atoms over the Te nanohelices gradually increases the size of Au nuclei and, eventually, produces an interconnected chain-like structure until Te is totally depleted by oxidation. When the galvanic replacement of Te by Au is complete, full transformation into metallic gold was observed as clearly observed in Figure 26, A-E. HRTEM observation in Figure 26D of the middle portion of resulting Au 1D nanostructures. The resulting peapod-like Au nanostructures clearly display grain boundaries, suggesting a polycrystalline morphology. Figure 26F shows the extinction spectrum of Au1D nanostructure displaying characteristic plasmon band at 512 nm. The band at 652 nm observed for Te nanohelices was completely vanished after 10 min of reaction. The peapod morphology is very similar to the reported in Au 1D structures obtained by Lin et al.¹⁶

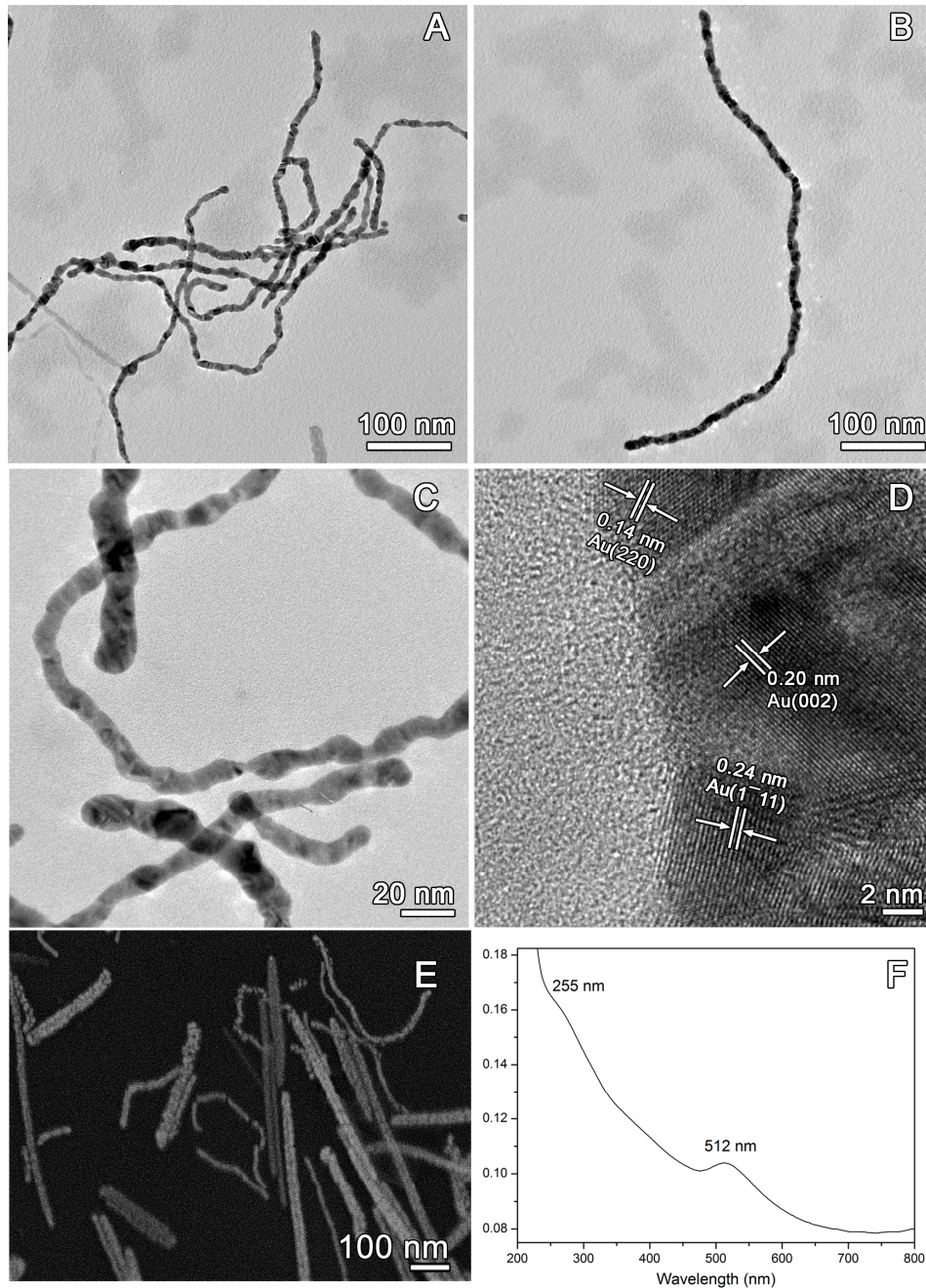
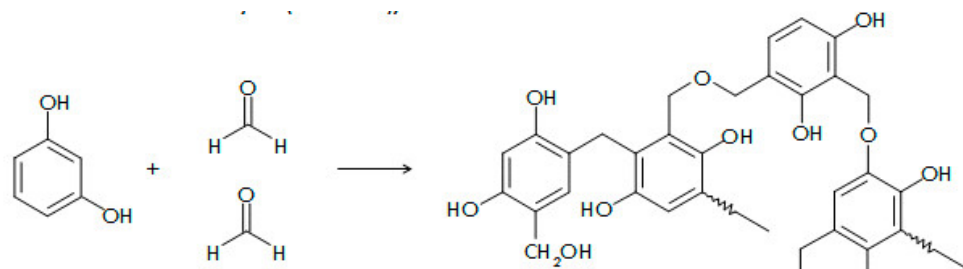


Figure 26. (A-C) TEM and (D) HRTEM images of Au1D nanostructure achieved by adding a solution of Au^{3+} to Te nanohelices suspension in the presence of PVP. The interplanar distance are compatible with the face-centered cubic lattice of Au (E) SEM image and (F) extinction spectrum of an aqueous suspension of Au1D nanostructures

3.2.7. *Te@resorcinol-formaldehyde (RF) core-shell nanocables from Te nanohelices*

We assessed several synthetic routes to coat the surface of Te nanohelices with carbon layer under amenable conditions. Carbonization of glucose by hydrothermal methods or its polymerization by sulfuric acid in the presence of Te1D nanostructures always address deleterious effect over the morphology and size of Te nanowires and nanohelices (data not shown).

We took advantage of the low temperature and all aqueous synthesis of phenol-formaldehyde resin to design functional core-shell Te1D nanostructures with preserved shape. Formaldehyde and resorcinol undergo a polymerization reaction to form resin in the presence of ammonia (as a catalyst), with the commercial tri-block polymer Pluronic® F68 as stabilizer. TEM images shown in Figure 27 reveal that the product are essentially 1D core-shell nanostructures, each of which consisted of a core nanohelix with similar diameter distribution found for pristine Te nanohelix and an average RF resin shell size of RF ~31 nm. The RF shell did not seem place substantial deleterious effect on the shape of the Te nanohelices. The SAED pattern can be indexed to the hexagonal phase of tellurium with a cell constant $a = 4.466 \text{ \AA}$, $c = 5.910 \text{ \AA}$. The structure of the resulting resins is shown below:



Due to the hydroxyl-rich surface, 1D Te@RF nanocables are more susceptible to chemical modifications than pristine Te nanohelices and more compatible to wider range of solvents. Additionally, the phenolic source can be easily replaced by other derivatives ones containing specific groups (e.g. carboxyl, amine, thiol, etc). It is important to highlight that RF resin is an interesting carbon precursor. One of the biggest advantages for making Te nanohelices coated with RF resin is that route offers an intermediate pathway to prepare Te@C nanocables by further heat treatment.

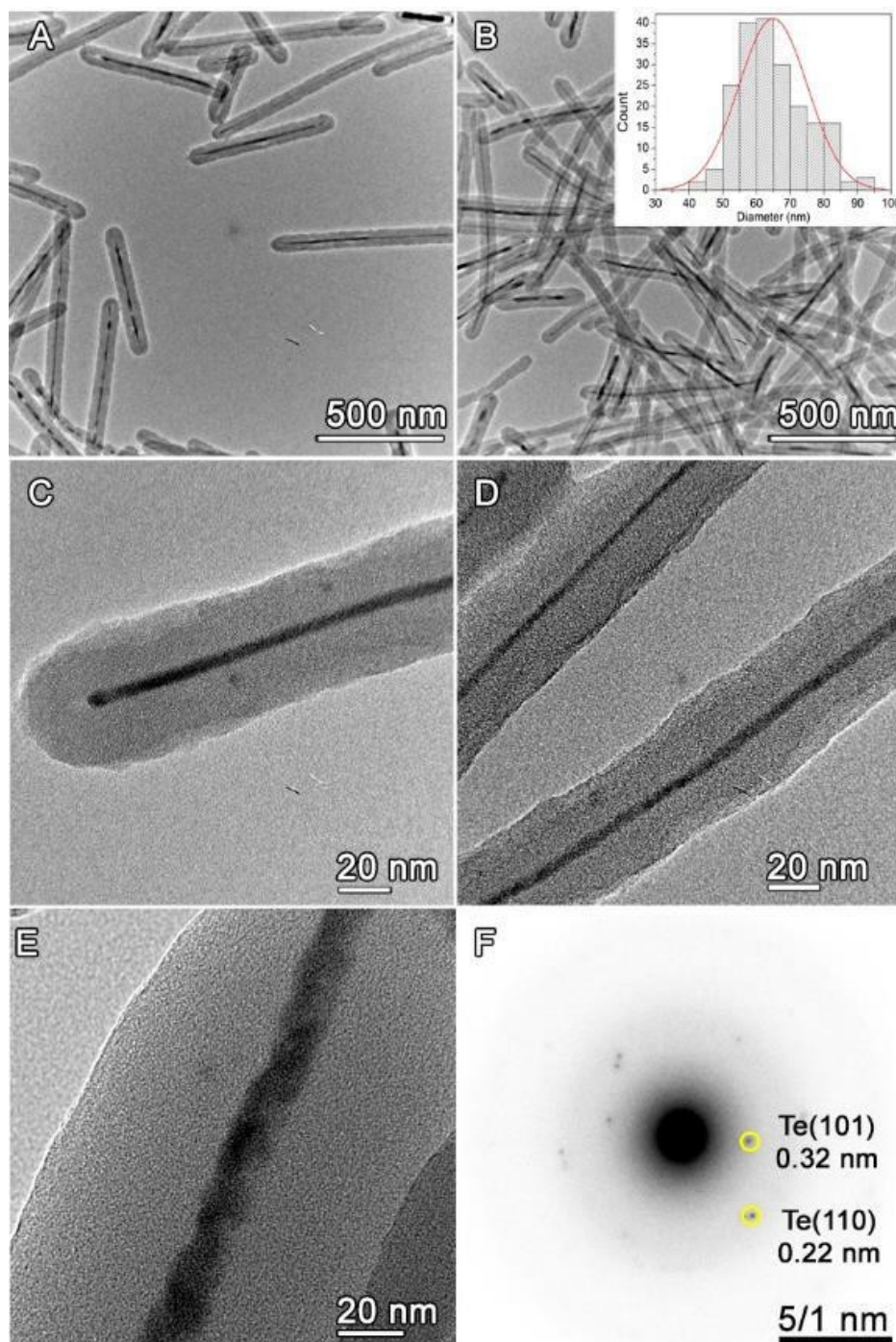


Figure 27. (A-E) TEM images and (F) Selected area electron diffraction (SAED) images of Te nanohelices coated with resorcinol-formaldehyde resin. The inset shown in (B) displays the size distribution of the diameter of Te@RF core-shell structures.

This synthetic route is highly reproducible and allows facile control over the size of the RF shell thickness. Noteworthy, the RF shell thickness could be easily tuned by controlling the ratio of Te nanohelices and resorcinol/formaldehyde while keeping the other synthetic parameters constant.

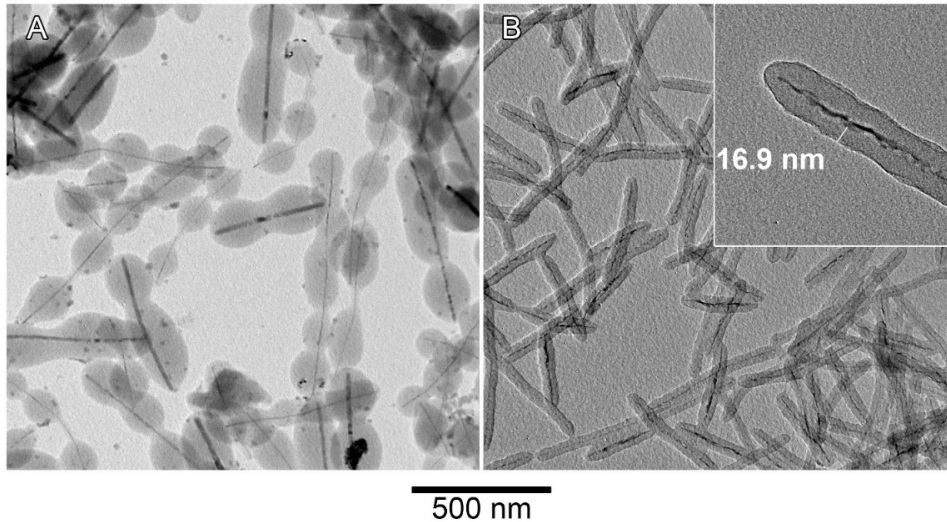


Figure 28. 1D Te@RF with different RF content: A) eight times, and B) half of resorcinol and formaldehyde utilized in the standard synthesis of Te@RF whilst other parameters were kept unchanged.

Figure 28, a and b, shows the TEM images of Te@RF nanocables prepared with 8 times more and half of the RF resin used in the standard synthesis.

Figure 29 shows the vibrational spectrum of Te@RF nanocables. The bands at 3207 cm^{-1} is due to phenolic O-H. The bands at 2912 and 2871 cm^{-1} are attributed to aliphatic CH_2 asymmetric and symmetric stretching, respectively.⁴² Typical aromatic ring C=C bands vibration modes can be recognized at 1614 - 1606 cm^{-1} .⁴²

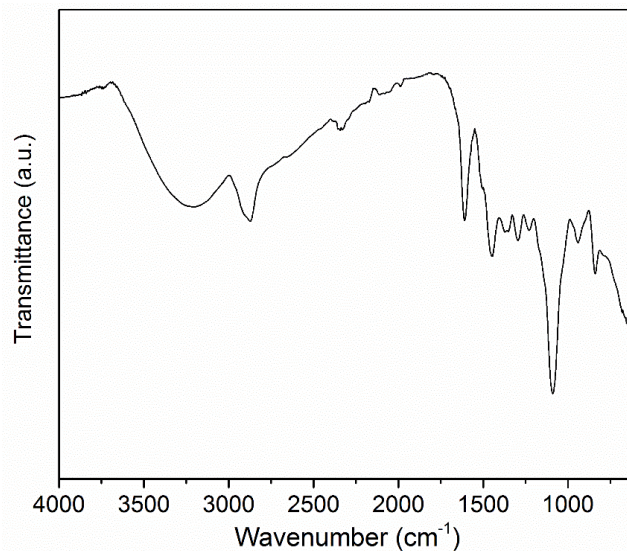


Figure 29. Attenuated total reflection - Fast Fourier Transform Infrared (ATR-FTIR) spectrum of Te@RF nanocables prepared in a standard synthesis.

The band at 1454 cm^{-1} can be attributed to the overlapping of aliphatic CH_2 scissor bend and aromatic ring stretching.⁴² The strong band at 1090 cm^{-1} can be attributed to alcoholic C-O stretching, probably from residual hydroxymethyl groups.⁴²

3.2.8. Synthesis of Te@RF hybrid materials

RF shells offers many advantages once there exist activated hydroxyl groups available for chemical modification. Two different approaches were evaluated to prepare Te@RF hybrid structures.

The first methodology concerns one-pot synthesis of 1D Te@RF hybrid with the direct incorporation of previously synthesized nanoparticles during the coating of Te nanohelices with RF resin. Luminescent YVO₄:Eu³⁺ nanoparticles (5 nm), Au nanoparticles (8 nm), and Ag nanocubes (35 nm) were evaluated to prepare 1D Te@RF hybrid materials.

The synthesis of YVO₄:Eu³⁺ nanoparticles concerns the precipitation of lanthanide vanadate in alkaline medium (pH 12.5-13.0). Lanthanide citrate was firstly prepared and thereafter employed as lanthanide source. Citrate complexing agents have dual key roles in the synthesis of aqueous colloidal suspension of YVO₄:Eu³⁺ nanoparticles:⁴³ a) the precipitation of Y³⁺/Eu³⁺ citrate complex limit the growth of nanoparticles upon the introduction of VO₄³⁻ ions. B) citrate ions ensure the colloidal stability and minimize the aggregation among nanoparticles through electrostatic and steric repulsions in neutral and alkaline aqueous suspensions. The outcome is citrate-capped YVO₄ nanocrystals doped with 10 mol% Eu³⁺. The as prepared nanoparticles were not subjected to thermal annealing in order to preserve the colloidal stability.

As shown in Figure 30, A and B, TEM images of as prepared products are hardly to snapshot due to the small size and poor crystallinity of YVO₄:Eu³⁺ nanoparticles. However, the energy-dispersive spectroscopy (EDS) confirms compositional purity of the products, clearly shown by the presence of prominent peaks for Y, V, O and Eu. Copper and carbon peaks correspond to the TEM holding grid. From the excitation spectrum of aqueous suspension of YVO₄:Eu³⁺ nanoparticles YVO₄:Eu³⁺ nanoparticles a broad band around 300 nm is attributed to the charge transfer (CT) from the oxygen ligands to the central V atom inside the VO₄³⁻ absorption.⁴⁴ It is also possible to outline the characteristic transitions within Eu³⁺ 4f⁶ configuration at 396 and 467 nm weak relative intensity assigned to ⁷F₀-⁵L₆ and ⁷F₀-⁵D₂ transitions.

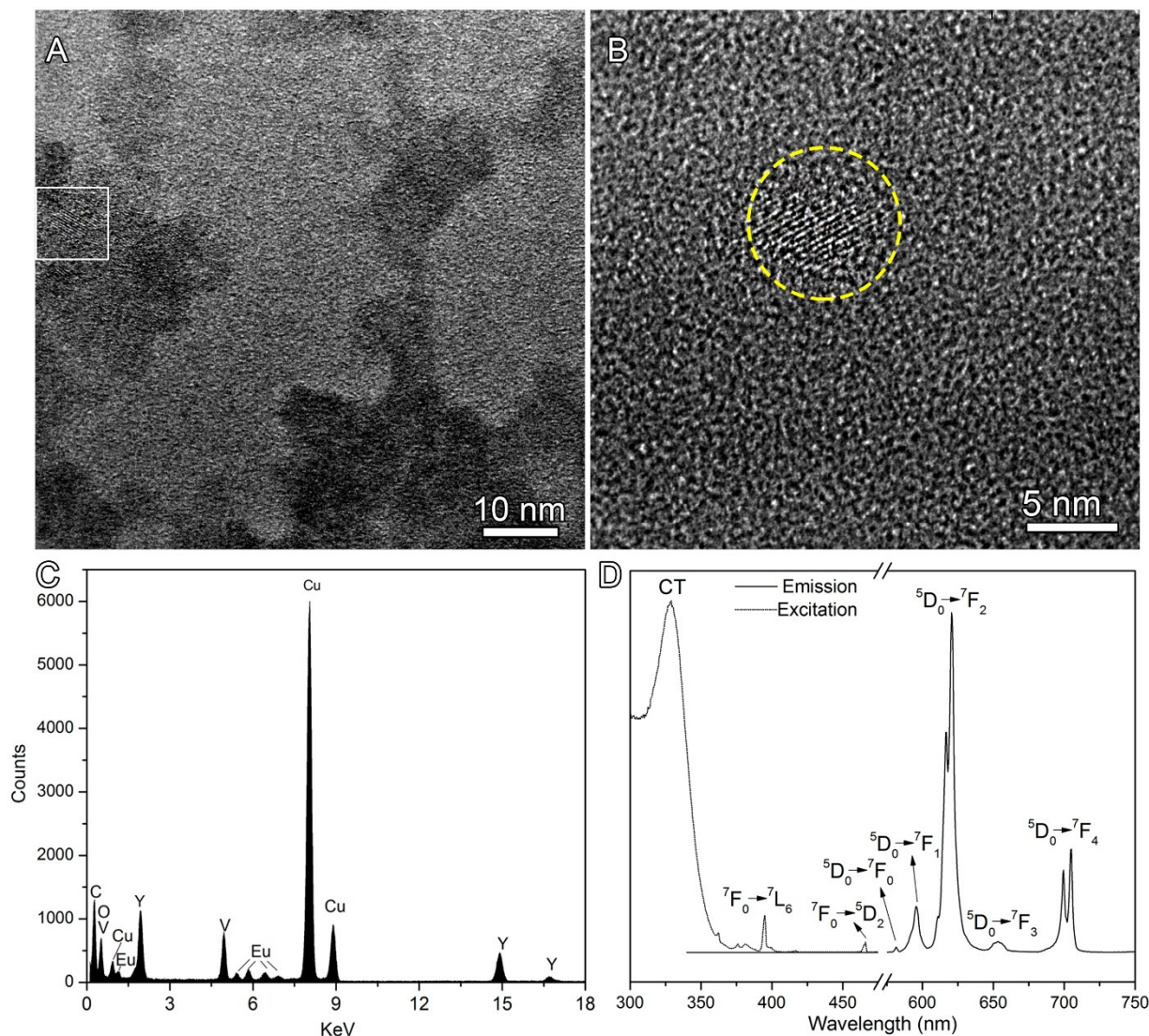


Figure 30. A) and B) TEM images, C) Energy-dispersive spectroscopy (EDS) of YVO₄:Eu³⁺ nanoparticles D) Excitation ($\lambda_{em} = 620$ nm) and emission ($\lambda_{exc} = 303$ nm) spectra of an aqueous suspension of as-prepared YVO₄:Eu³⁺ nanoparticles

The emission spectrum shows typical narrow bands assigned to Eu³⁺ 4f⁶ transitions from the ⁵D₀ excited state to the ⁷F_J manifold (J= 0, 1, 2, 3 and 4). The most intense emission band of Eu³⁺ concerns the hypersensitive transition ⁵D₀ - ⁷F₂ at about 620 nm because Eu³⁺ ions are located at low symmetric local sites in the YVO₄ host lattice.

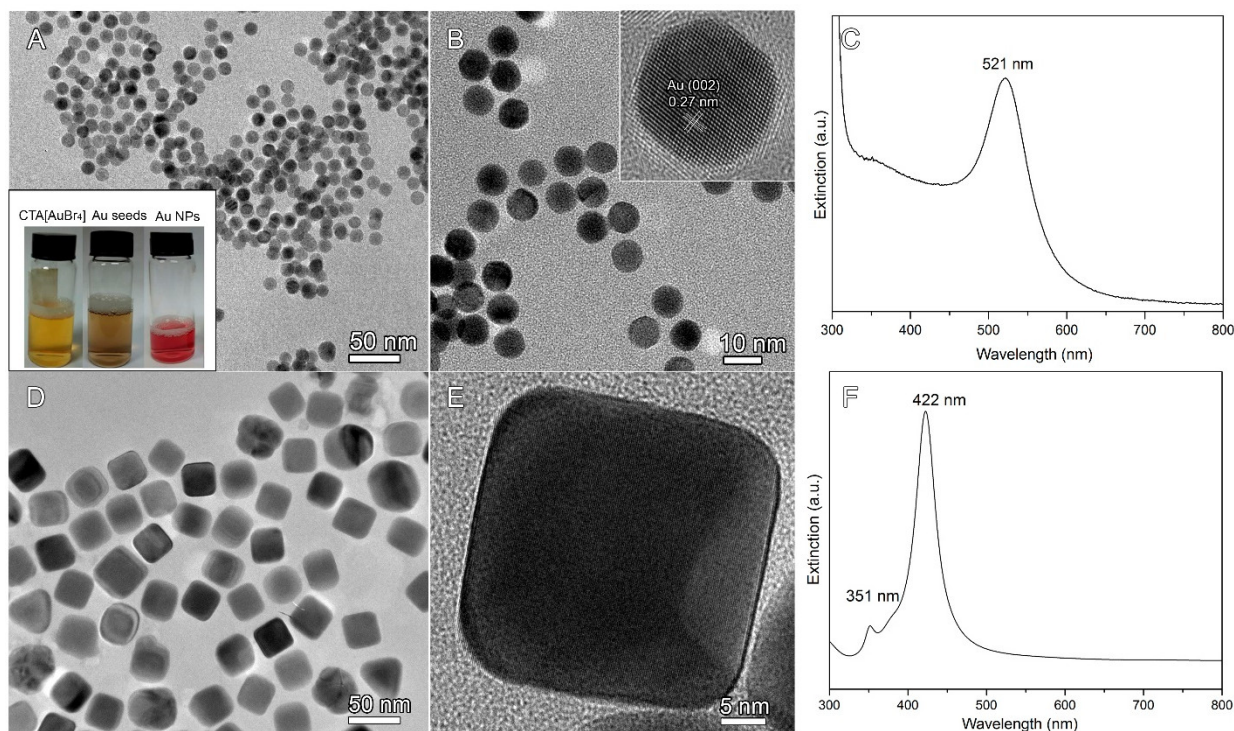


Figure 31. (A, B) TEM images and C) UV-vis extinction spectrum of Au nanoparticles. (D, E) TEM images, and F) UV-vis extinction spectrum of Ag nanocubes. The insets in A) show the photography of CTA[AuBr₄], Au seeds and aqueous suspension of Au NPs. The inset in B) show the high-resolution TEM of a single Ag nanospheres.

In general, the chemical principle of the Au nanoparticles synthesis is the reduction of gold (III) derivatives. In the first step of the synthesis of Au nanoparticles, HAuCl₄ solution is mixed with CTAB solution. Chloride ions are exchanged by Br⁻ ions resulting in the formation of [CTA][AuBr₄] and delivering a yellowish solution as shown in the inset of Figure 31. Therefore, an ice-cold aqueous solution of NaBH₄ was rapidly injected over the mixture of HAuCl₄ and CTAB and a brownish color is immediately developed being associated with the formation of Au seeds. Au seeds are mostly composed by small Au clusters with an average size of six Au atoms as reported previously by Zheng et al.⁴⁵ The growth of Au nanoparticles (AuNPs) is conducted by placing a certain amount of initial seeds into a mixture of aqueous solution of HAuCl₄, CTAC, and AA at room temperature. The molar ratio of AA: Au (150:1) is a hundred times higher than necessary to reduce Au³⁺. Although AA is a reducing agent significantly weaker than NaBH₄, a relative high concentration of AA ensures a fast reduction rate inducing the growth of single-crystal nanoparticles as shown in the inset of Figure 31. The solution became instantaneously reddish within few second after the introduction of Au seeds indicating the formation of Au nanoparticles. Figure 31, A and B, shows TEM images of Au NPs. The nanoparticles are quite spherical and shape and display an average diameter of ~8 nm. Figure 31c shows the extinction

spectrum of Au NPs dispersed in water in the UV-vis region. The spectrum shows a single broad localized surface plasmon resonance (LSPR) band at 521 nm whose position corresponds with LSPR peak of aqueous suspensions of Au NPs with similar size described in the literature.⁴⁵

We also evaluated the introduction of larger Ag particles in the shape of the cubes for the fabrication of 1D Te@RF hybrids. The Ag nanocubes were synthesized through one-pot protocol polyol method.^{46,47} Ethylene glycol (EG) is both solvent and source of reducing agent (glycolaldehyde). Essentially, the polyol synthesis of Ag nanocubes involves the injection of a cold solution of Ag precursor and a polymeric capping agent such as poly(vinyl pyrrolidone) (PVP) into EG at an elevated temperature. From previous reports,⁴⁸ the development of Ag nanocubes could be easily monitored at different reaction times by replacing AgNO₃ with CF₃COOAg. As an additional outcome, better reproducibility could be achieved. Poly(vinyl pyrrolidone) is a specific capping agent of {100} facets of Ag. It is worth to pointing up that multiple-twin Ag seeds are thermodynamically favorable rather than single-crystal seeds during the nucleation step of Ag nanocubes synthesis. However, the high yield of Ag nanocubes depends of the concentration of single-crystal Ag seeds. Twin boundary defects of multiple-twin Ag seeds can be easily vanished through oxidative etching. The introduction of Cl⁻ ions (i.e. from HCl) plays a key role as oxidative etching agent together with oxygen gas adsorbed in EG during the pre-heating of EG.⁴⁹ Oxidative etching can be ascribed as a redox reaction between Ag atoms and dissolved O₂ gas, with Cl⁻ acting as a charge carrier.⁵⁰

The addition of bisulfide (SH⁻) ions also promotes the formation of single-crystal seeds.⁵¹ Ag⁺ ions immediately react with S²⁻ to produce insoluble Ag₂S clusters (K_{sp} = 10⁻⁵²) and drain the Ag precursor in the earlier stages of the synthesis. Most importantly, Ag₂S clusters act as heterogeneous nucleation sites for the deposition of Ag atoms and subsequent formation of single-crystal nanocubes. Despite the mismatch of Ag lattice (face-centered cubic) and Ag₂S (monoclinic), the size of clusters are too small to place substantial impact on the growth of Ag nanocubes. Although the {100} facet has higher surface energy than {111} facet, PVP is an efficient surface capping agent of Ag(100) facets and decreases its surface energy, ruling the kinetics of the deposition of Ag atoms. As a result, the remaining Ag atoms are continuously deposited on the {111} facets (highest surface energetic sites) providing the corners of Ag nanocubes. From previous reports, the source of Ag precursor can play an important role on the reduction kinetics of the Ag nanocubes synthesis.

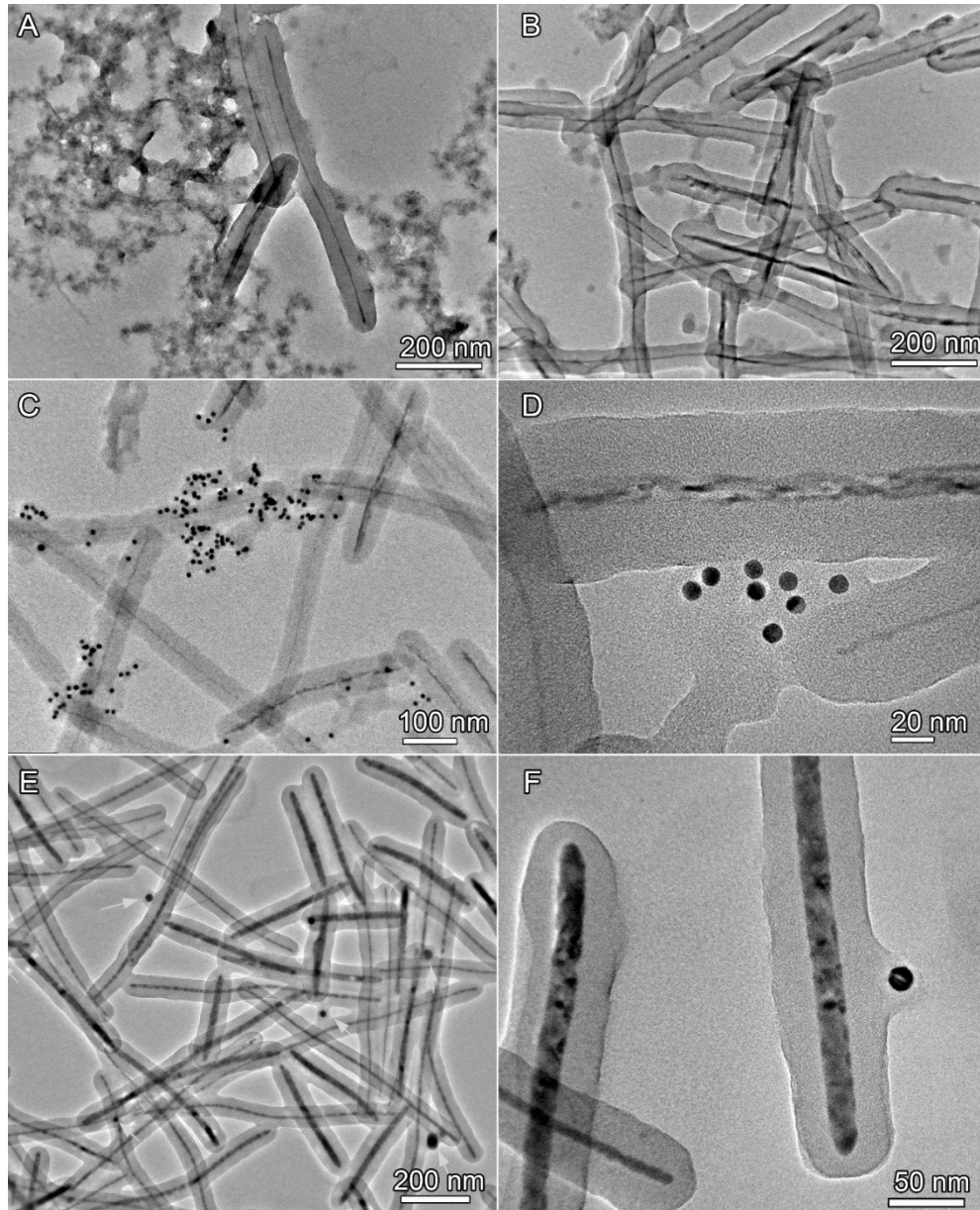


Figure 32. TEM of (A, B) 1D Te@RF/YVO₄:Eu³⁺, (C, D) 1D Te@RF@AuNPs, (E,F) Te@RF@AgNC nanostructures.

Figure 32 shows of 1D Te@RF/X (X= YVO₄:Eu³⁺ nanoparticles, Au nanospheres or Ag nanocubes)

The loading of lanthanide vanadate or metallic nanoparticles during the coating of RF resin on Te nanohelices was not successful. Indeed, Te nanohelices were fully coated with RF resin at room temperature. On the other hand, agglomerate of nanoparticles were coated with RF resin and attached in an inhomogeneous fashion on the surface of Te@RF nanocables. Usually, those nanoparticles were positioned in coalescence sites that merge the Te@RF nanocables each other. Specially, Ag nanocubes were hardly detected on the surface of Te@RF nanocables or even crushed into agglomerates as shown in Figure 32, A and F. One can suggest the effect of the

stabilizing nature of the molecules that cover the nanoparticles. Citrate capped $\text{YVO}_4:\text{Eu}^{3+}$ and CTAC capped Au nanoparticles can drive electrostatic interactions with hydroxyl groups and phenyl ring of resorcinol comparing with weaker van der Waals interactions provided by non-ionic PVP molecules that cover the surface of Ag nanocubes.

The second methodology was based on the post-modification of Te@RF nanocables with lanthanide hydroxycarbonates via precipitation or direct attachment of Au nanoparticles on the RF resin surface via reduction of Au^{3+} ions.

The adsorption of significant amount of La^{3+} , Ce^{3+} and Tb^{3+} ions on the hydroxyl-rich surface of RF shell ensures the restricts the precipitation of lanthanide hydroxycarbonates during the decomposition of urea. The process can be described with the following reactions:

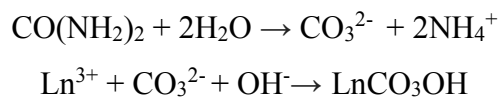


Figure 33 and Figure 34, A-D, display TEM images of Te@RF nanocables decorated with different content of $(\text{La}_{45\%}\text{Ce}_{45\%}\text{Tb}_{10\%})\text{CO}_3\text{OH}$ nanoparticles. The average size of nanoparticles was roughly smaller than 5 nm with diverse shape in the lowest concentration of Ln/urea as highlighted in Figure 33D. The HRTEM image pictured in Figure 33D clearly show the Te core and RF shell resin coated with amorphous $(\text{La}_{45\%}\text{Ce}_{45\%}\text{Tb}_{10\%})\text{CO}_3\text{OH}$ nanoparticles with poorly defined shaped. Figure 34, A-C, displays the TEM images of the products when the Ln/urea ratio was threefold higher. the number of merged 1D nanostructures significantly increased as clearly shown in Figure 34C. Eventually, the local concentration of nanoparticles was sufficient to fashion a dense layer of $(\text{La}_{45\%}\text{Ce}_{45\%}\text{Tb}_{10\%})\text{CO}_3\text{OH}$ (Figure 34, B and C). Despite aggregation issues, most of hybrid structures consisted of Te@RF nanocables decorated with amorphous quasi-spherical nanoparticles with average size around 10 nm. Noteworthy, those nanoparticles were homogenously distributed over the whole surface of Te@RF nanocables.

Figure 33 and Figure 34, E-F, display the excitation and emission spectra of 1D Te@RF@ $(\text{La}_{45\%}\text{Ce}_{45\%}\text{Tb}_{10\%})\text{CO}_3\text{OH}$ hybrid structures acquired at room temperature. The spectral profile are essentially the same with the exception of the relative intensity of the Te@RF@ $(\text{La}_{45\%}\text{Ce}_{45\%}\text{Tb}_{10\%})\text{CO}_3\text{OH}$ hybrid, which is dependent of content of LnCO_3OH .

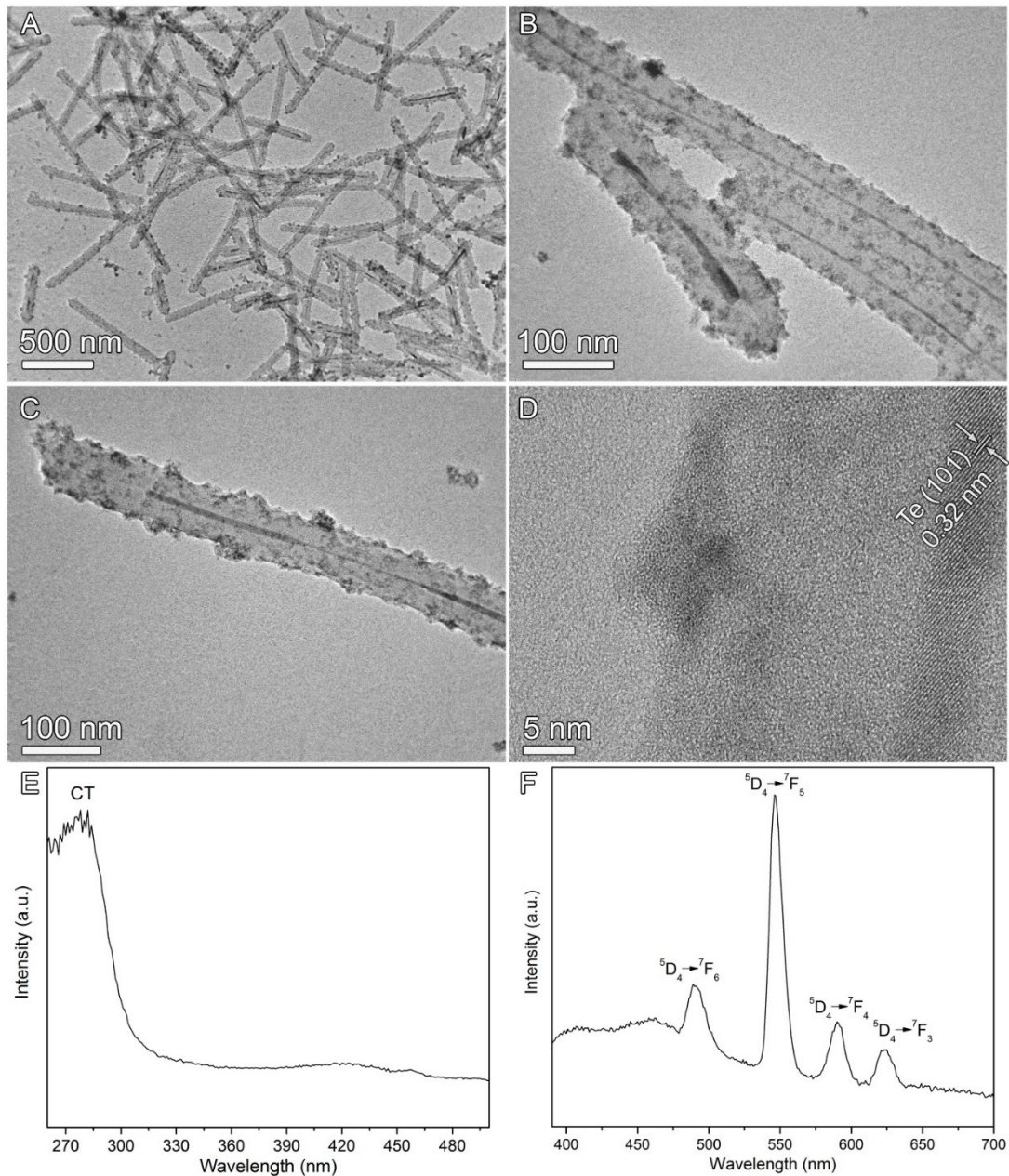


Figure 33. (A-D) TEM images, (E) excitation ($\lambda_{em} = 543$ nm), and (F) emission ($\lambda_{exc} = 280$ nm) of Te@RF nanocables decorated with $(La_{45\%}Ce_{45\%}Tb_{10\%})CO_3OH$.

Upon monitoring at 543 nm, the excitation spectrum consists of a broad and single band in the UV region centered at 278 nm. This band is attributed to the host excitation. The emission spectrum shows characteristic bands of Tb^{3+} ion being all attributed to $^5D_4 \rightarrow ^7F_J$ ($J = 6, 5, 4, 3$) transitions: $^5D_4 \rightarrow ^7F_6$ (490 nm), $^5D_4 \rightarrow ^7F_5$ (546 nm), $^5D_4 \rightarrow ^7F_4$ (590 nm), and $^5D_4 \rightarrow ^7F_3$ (623 nm). The loss of resolution of the bands at lower concentration can be explained by site-to-site inhomogeneities which place variations in the crystal- field strength felt by the different Tb^{3+} ions.

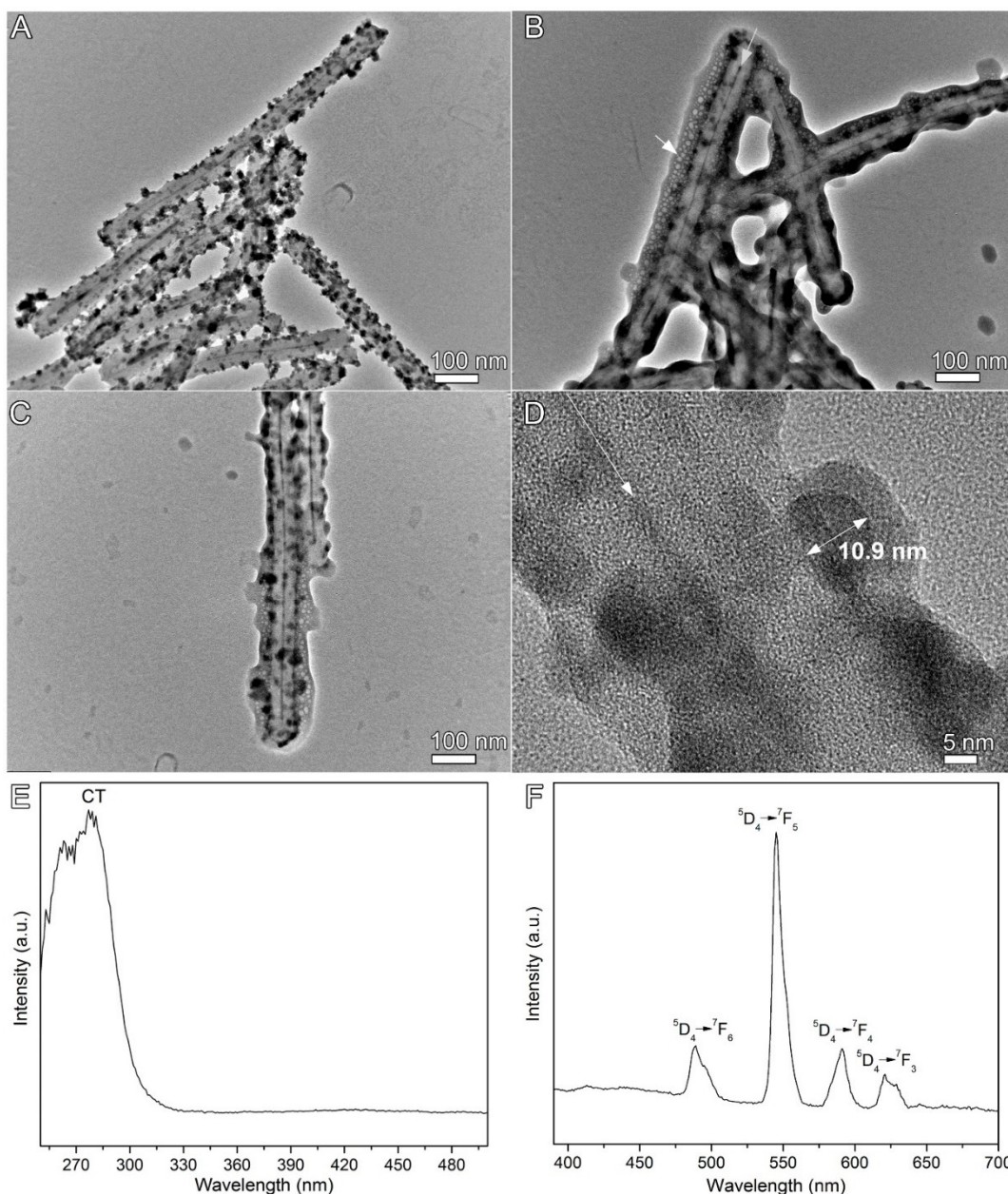


Figure 34. (A –D)TEM images of Te@RF nanocables decorated with $(\text{La}_{45}\text{Ce}_{45}\text{Tb}_{10})\text{CO}_3\text{OH}$ with the relative concentration threefold times higher than standard synthesis. (E) Excitation ($\lambda_{\text{em}} = 543 \text{ nm}$), and (F) emission ($\lambda_{\text{exc}} = 280 \text{ nm}$) of a aqueous suspension of Te@RF nanocables decorated with $(\text{La}_{45}\text{Ce}_{45}\text{Tb}_{10})\text{CO}_3\text{OH}$

3.2.9. Synthesis of 1D Te@RF/Au nanostructures

The preparation of 1D Te@RF@Au hybrid nanostructures was performed towards the reduction of Au^{3+} with NaBH_4 . Firstly, an aqueous solution of NaBH_4 was mixed with the Te@RF nanocables. Borohydrate ions could adsorb on the surface of RF resin.

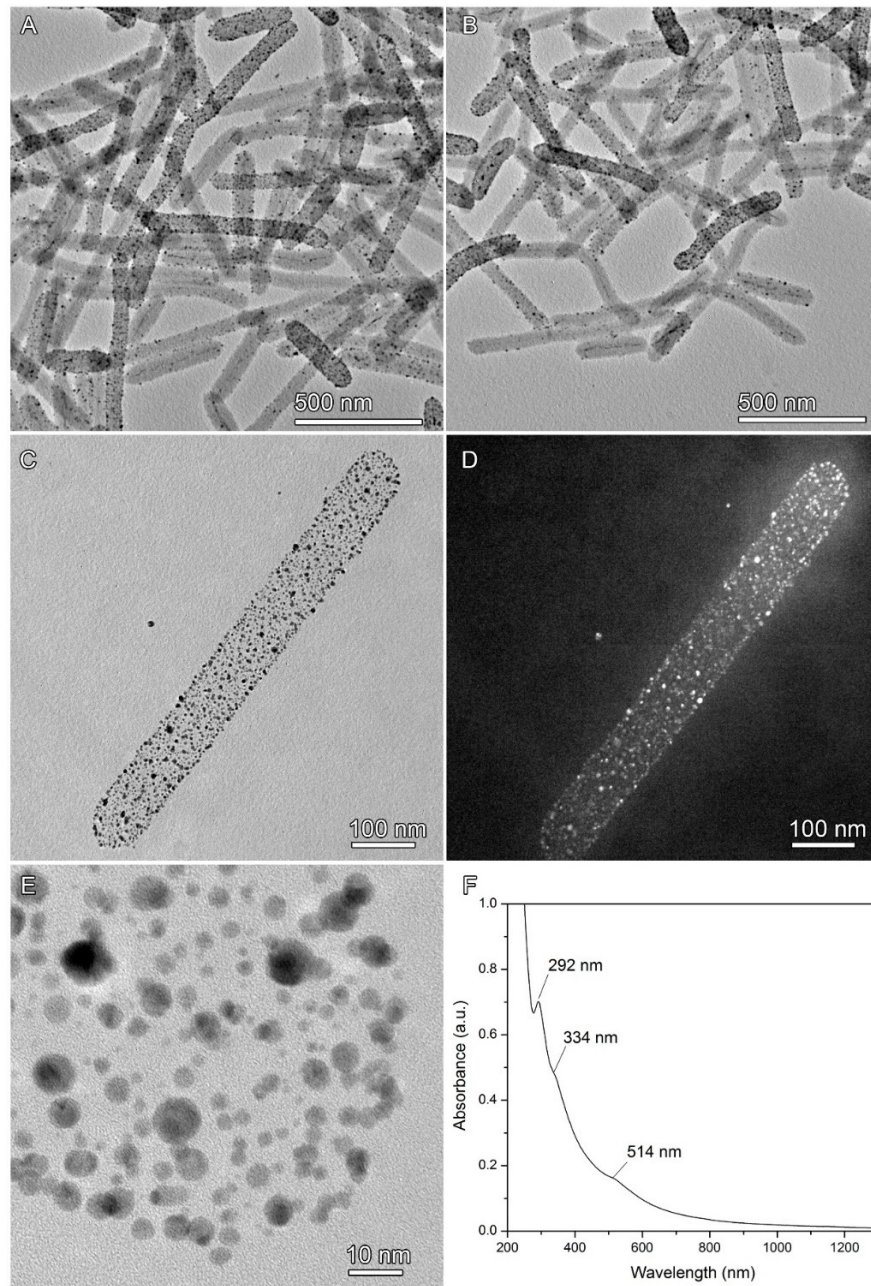


Figure 35. (A-C) TEM images of Te@RF@Au hybrid nanostructures. (D) Dark-field TEM image of a single 1D hybrid nanostructure. (E) TEM image from the tip of 1D hybrid nanostructure. (F) UV-vis spectra of an aqueous suspension of Te@RF@Au hybrid nanostructures.

Upon addition of Au^{3+} ions, small crystalline Au nanoparticles were instantaneously produced on the surface of Te@RF nanocables as shown in Figure 35, A-E. The Au nanoparticles were quasi-spherical in shape and had a broad distribution size in the range of 2-10 nm as shown in Figure 35E. In Figure 35F, the UV-vis absorption spectra of the nanocomposite show two main absorption bands at 290 and 514 nm associated with π - π^* transitions of aromatic rings from RF resin and LSPR band of Au nanoparticles. One can notice that it is not possible to observe the

absorption band of Te nanohelices. Probably, Te was eventually oxidized with the addition of Au^{3+} ions.

3.3. Conclusions

One-dimensional Te nanostructures (Te1D) in the shape of whiskers, wires and helices were easily prepared by a facile one-pot synthesis in the presence of Pluronic® F68 at low temperatures ($< 100\text{ }^{\circ}\text{C}$). To the best of our knowledge, this is the first report describing the all-aqueous one-pot synthesis of Te nanohelices. On the pursuit of the fabrication of complex nanoarchitectures we also evaluated some techniques to assemble Te1D nanostructures such as liquid-liquid and drop-casting self-assembly. Te1D hybrid structures have been conceived by using Te as sacrificial template to attach Ag nanoparticles or even produce Au 1D nanostructures with peapod-like morphology. Furthermore, Te nanohelices were coated with resorcinol-formaldehyde resin, a carbon polymer precursor, at mild conditions. Noteworthy, the hydroxyl-rich surface of resorcinol-formaldehyde resin shell allowed us to fashion an intermediate pathway to explore the deposition of optical active compounds like lanthanide hydroxycarbonates or metallic nanoparticles. Ongoing efforts goal to explore the deposition of other lanthanide hosted matrices or lanthanide complex as well as metallic nanoparticles. Regardless, multiple RF shell composed by alternate layers of metallic/lanthanide nanoparticles can be easily fashioned with the current protocol.

References

- (1) Zhu, Y.; Zhu, Y.; Elim, H. I.; Elim, H. I.; Foo, Y.-L.; Foo, Y.-L.; Yu, T.; Yu, T.; Liu, Y.; Liu, Y.; et al. Multiwalled Carbon Nanotubes Beaded with ZnO Nanoparticles for Ultrafast Nonlinear Optical Switching. *Adv. Mater.* **2006**, *18* (5), 587–592.
- (2) Wang, Y.; Tang, Z.; Podsiadlo, P.; Elkasabi, Y.; Lahann, J.; Kotov, N. A. Mirror-Like Photoconductive Layer-by-Layer Thin Films of Te Nanowires: The Fusion of Semiconductor, Metal, and Insulator Properties. *Adv. Mater.* **2006**, *18* (4), 518–522.
- (3) Jin Bae, E.; Hun Kang, Y.; Jang, K.-S.; Yun Cho, S. Enhancement of Thermoelectric Properties of PEDOT:PSS and Tellurium-PEDOT:PSS Hybrid Composites by Simple Chemical Treatment. *Sci. Rep.* **2016**, *6*, 18805.
- (4) Wang, Y.; Zhang, S. M.; Deng, Y. Flexible Low-Grade Energy Utilization Devices Based on High-Performance Thermoelectric Polyaniline/tellurium Nanorod Hybrid Films. *J. Mater. Chem. A* **2016**, *4* (9), 3554–3559.

- (5) Zaia, E. W.; Sahu, A.; Zhou, P.; Gordon, M. P.; Forster, J. D.; Aloni, S.; Liu, Y.-S.; Guo, J.; Urban, J. J. Carrier Scattering at Alloy Nanointerfaces Enhances Power Factor in PEDOT:PSS Hybrid Thermoelectrics. *Nano Lett.* **2016**, *16* (5), 3352-3359.
- (6) Lin, S.; Li, W.; Chen, Z.; Shen, J.; Ge, B.; Pei, Y. Tellurium as a High-Performance Elemental Thermoelectric. *Nat. Commun.* **2016**, *7*, 10287.
- (7) Wang, Z.; Wang, L.; Huang, J.; Wang, H.; Pan, L.; Wei, X. Formation of Single-Crystal Tellurium Nanowires and Nanotubes via Hydrothermal Recrystallization and Their Gas Sensing Properties at Room Temperature. *J. Mater. Chem.* **2010**, *20* (12), 2457.
- (8) Her, Y. C.; Huang, S. L. Growth Mechanism of Te Nanotubes by a Direct Vapor Phase Process and Their Room-Temperature CO and NO₂ Sensing Properties. *Nanotechnology* **2013**, *24* (21), 215603.
- (9) Lee, T. Il; Lee, S.; Lee, E.; Sohn, S.; Lee, Y.; Lee, S.; Moon, G.; Kim, D.; Kim, Y. S.; Myoung, J. M.; et al. High-Power Density Piezoelectric Energy Harvesting Using Radially Strained Ultrathin Trigonal Tellurium Nanowire Assembly. *Adv. Mater.* **2013**, *25* (21), 2920–2925.
- (10) Liang, H.-W. W.; Liu, J.-W. W.; Qian, H.-S. S.; Yu, S.-H. H. Multiplex Templating Process in One-Dimensional Nanoscale: Controllable Synthesis, Macroscopic Assemblies, and Applications. *Acc. Chem. Res.* **2013**, *46* (7), 1450–1461.
- (11) Qian, H.-S.; Luo, L.-B.; Gong, J.-Y.; Yu, S.-H.; Li, T.-W.; Fei, L. Te@Cross-Linked PVA Core Shell Structures Synthesized by a One-Step Synergistic Soft Hard Template Process. *Cryst. Growth Des.* **2006**, *6* (2), 607–611.
- (12) Zhang, W.; Wu, Z.-Y.; Jiang, H.-L.; Yu, S.-H. Nanowire-Directed Templating Synthesis of Metal–Organic Framework Nanofibers and Their Derived Porous Doped Carbon Nanofibers for Enhanced Electrocatalysis. *Journal of the American Chemical Society.* **2014**, *136* (41), 14385–14388.
- (13) Liu, Y.-Y.; Liu, L.; Xue, L.; Mao, L.-B.; Gao, H.-L.; Xu, L.; Yu, S.-H. Charged Inorganic Nanowire-Directed Mineralization of Amorphous Calcium Carbonate. *ChemNanoMat* **2016**, *2* (4), 259–263.
- (14) Qian, H.; Zhu, E.; Zheng, S.; Li, Z.; Hu, Y.; Guo, C.; Yang, X.; Li, L.; Tong, G.; Guo, H. One-Pot Synthesis of Biocompatible Te@phenol Formaldehyde Resin Core–shell Nanowires with Uniform Size and Unique Fluorescent Properties by a Synergized Soft–hard Template Process. *Nanotechnology* **2010**, *21* (49), 495602.

- (15) Mayers, B.; Xia, Y. Formation of Tellurium Nanotubes Through Concentration Depletion at the Surfaces of Seeds. *Adv. Mater.* **2002**, *14* (4), 279–282.
- (16) Lin, Z.-H.; Chang, H.-T. Preparation of Gold Tellurium Hybrid Nanomaterials for Surface-Enhanced Raman Spectroscopy. *Langmuir* **2008**, *24* (2), 365–367.
- (17) Liu, Z.; Hu, Z.; Liang, J.; Li, S.; Yang, Y.; Peng, S.; Qian, Y. Size-Controlled Synthesis and Growth Mechanism of Monodisperse Tellurium Nanorods by a Surfactant-Assisted Method. *Langmuir*. **2004**. *20* (1), 214–218.
- (18) Liu, Z.; Hu, Z.; Xie, Q.; Yang, B.; Wu, J.; Qian, Y. Surfactant-Assisted Growth of Uniform Nanorods of Crystalline Tellurium. *J. Mater. Chem.* **2003**, *13* (1), 159–162.
- (19) Xi, G.; Liu, Y.; Wang, X.; Liu, X.; Peng, Y.; Qian, Y. Large-Scale Synthesis, Growth Mechanism, and Photoluminescence of Ultrathin Te Nanowires. *Cryst. Growth Des.* **2006**, *6* (11), 2567–2570.
- (20) Wang, S.; Guan, W.; Ma, D.; Chen, X.; Wan, L.; Huang, S.; Wang, J. Synthesis, Characterization and Optical Properties of Flower-like Tellurium. *CrystEngComm*. **2010**. *12* (1), 166–171.
- (21) Panahi-Kalamuei, M.; Mousavi-Kamazani, M.; Salavati-Niasari, M. Self-Assembly of Nanoparticles to Form Tree-like Tellurium Nanostructures Using Novel Starting Reagents. *Mater. Lett.* **2014**, *136*, 218–221.
- (22) Ben-Moshe, A.; Wolf, S. G.; Sadan, M. B.; Houben, L.; Fan, Z.; Govorov, A. O.; Markovich, G. Enantioselective Control of Lattice and Shape Chirality in Inorganic Nanostructures Using Chiral Biomolecules. *Nat. Commun.* **2014**, *5*.
- (23) Mo, M.; Zeng, J.; Liu, X.; Yu, W.; Zhang, S.; Qian, Y. Controlled Hydrothermal Synthesis of Thin Single-Crystal Tellurium Nanobelts and Nanotubes. *Adv. Mater.* **2002**, *14* (22), 1658–1662.
- (24) Lima, L. R.; Moraes, M. L.; Nigoghossian, K.; Peres, M. F. S.; Ribeiro, S. J. L. Silk Fibroin-Antigenic Peptides-YVO₄:Eu³⁺ Nanostructured Thin Films as Sensors for Hepatitis C. *J. Lumin.* **2016**, *170*, 375–379.
- (25) Barker, M. G.; Hooper, A. J. Preparation and X-Ray Powder Diffraction Patterns of the Sodium Vanadates NaVO₃, Na₄V₂O₇, and Na₃VO₄. *J. Chem. Soc. Dalton Trans.* **1973**, (15), 1513-1517.
- (26) Giaume, D.; Buissette, V.; Lahlil, K.; Gacoin, T.; Boilot, J.-P.; Casanova, D.; Beaurepaire, E.; Sauviat, M.-P.; Alexandrou, A. Emission Properties and Applications of

- Nanostructured Luminescent Oxide Nanoparticles. *Prog. Solid State Chem.* **2005**, *33* (2-4), 99–106.
- (27) Marshall, H.; Waitkins, G.; Shutt, R.; Heath, R. E. Hexahalogenotellurates(IV): (Halotellurites). In *Inorganic Syntheses*; John Wiley & Sons, Inc., 1946; pp 188–190.
- (28) Vanysek, P. Electrochemical Series. In *CRC Handbook of Chemistry and Physics*; Lide, D. R., Ed.; Chemical Rubber Publishing Company: Boston, 1991; pp 8–23.
- (29) Johnson, R. A. Production, Particle Characteristics, and Spectra of Tellurium Hydrosols for Spectrophotometry. *Anal. Chem.* **1953**, *25* (7), 1013–1017.
- (30) Liu, J.-W.; Xu, J.; Hu, W.; Yang, J.-L.; Yu, S.-H. Systematic Synthesis of Tellurium Nanostructures and Their Optical Properties: From Nanoparticles to Nanorods, Nanowires, and Nanotubes. *ChemNanoMat* **2016**, *2* (3), 167–170.
- (31) Krishnan, V.; Kasuya, Y.; Ji, Q.; Sathish, M.; Shrestha, L. K.; Ishihara, S.; Minami, K.; Morita, H.; Yamazaki, T.; Hanagata, N.; et al. Vortex-Aligned Fullerene Nanowhiskers as a Scaffold for Orienting Cell Growth. *ACS Appl. Mater. Interfaces* **2015**, *7* (28), 15667–15673.
- (32) Ma, J.; Lian, J.; Duan, X.; Liu, Z.; Peng, P.; Liu, X.; Kim, T.; Zheng, W. Growth of Tellurium Nanowire Bundles from an Ionic Liquid Precursor. *CrystEngComm* **2011**, *13* (7), 2774–2778.
- (33) Liu, J.-W.; Wang, J.-L.; Huang, W.-R.; Yu, L.; Ren, X.-F.; Wen, W.-C.; Yu, S.-H. Ordering Ag Nanowire Arrays by a Glass Capillary: A Portable, Reusable and Durable SERS Substrate. *Sci. Rep.* **2012**, *2*, 987.
- (34) Liu, J.-W.; Chen, F.; Zhang, M.; Qi, H.; Zhang, C.-L.; Yu, S.-H. Rapid Microwave-Assisted Synthesis of Uniform Ultralong Te Nanowires, Optical Property, and Chemical Stability. *Langmuir* **2010**, *26* (13), 11372–11377.
- (35) Isomaki, H. M.; Boehm, J. Von. Optical Absorption of Tellurium. *Physica* **1982**, *25* (6A) 801-803.
- (36) Pine, A.; Dresselhaus, G. Raman Spectra and Lattice Dynamics of Tellurium. *Phys. Rev. B* **1971**, *4* (2), 356–371.
- (37) Martin, R.; Lucovsky, G.; Helliwell, K. Intermolecular Bonding and Lattice Dynamics of Se and Te. *Phys. Rev. B* **1976**, *13* (4), 1383–1395.
- (38) Marini, C.; Chermisi, D.; Lavagnini, M.; Di Castro, D.; Petrillo, C.; Degiorgi, L.; Scandolo, S.; Postorino, P. High-Pressure Phases of Crystalline Tellurium: A Combined Raman and Ab Initio Study. *Phys. Rev. B* **2012**, *86* (6), 064103.
- (39) Vasileiadis, T.; Dracopoulos, V.; Kollia, M.; Yannopoulos, S. N. Laser-Assisted Growth

- of T-Te Nanotubes and Their Controlled Photo-Induced Unzipping to Ultrathin Core-Te/sheath-TeO₂ Nanowires. *Sci. Rep.* **2013**, *3*, 1–7.
- (40) Song, J.; Lin, Y.; Zhan, Y.; Tian, Y.; Liu, G.; Yu, S. Superlong High-Quality Tellurium Nanotubes: Synthesis, Characterization, and Optical Property. *Cryst. Growth Des.* **2008**, *8* (6), 1902–1908.
- (41) Safdar, M.; Zhan, X.; Niu, M.; Mirza, M.; Zhao, Q.; Wang, Z.; Zhang, J.; Sun, L.; He, J. Site-Specific Nucleation and Controlled Growth of a Vertical Tellurium Nanowire Array for High Performance Field Emitters. *Nanotechnology* **2013**, *24* (18), 185705.
- (42) Costa, L.; di Montelera, L. R.; Camino, G.; Weil, E. D.; Pearce, E. M. Structure-Charring Relationship in Phenol-Formaldehyde Type Resins. *Polym. Degrad. Stab.* **1997**, *56* (1), 23–35.
- (43) Huignard, A.; Buissette, V.; Laurent, G.; Gacoin, T.; Boilot, J.-P. Synthesis and Characterizations of YVO₄:Eu Colloids. *Chem. Mater.* **2002**, *14* (5), 2264–2269.
- (44) Wang, G.; Qin, W.; Zhang, D.; Wang, L.; Wei, G.; Zhu, P.; Kim, R. Enhanced Photoluminescence of Water Soluble YVO₄:Ln³⁺ (Ln = Eu, Dy, Sm, and Ce) Nanocrystals by Ba²⁺ Doping. *J. Phys. Chem. C* **2008**, *112* (44), 17042–17045.
- (45) Zheng, Y.; Ma, Y.; Zeng, J.; Zhong, X.; Jin, M.; Li, Z.-Y.; Xia, Y. Seed-Mediated Synthesis of Single-Crystal Gold Nanospheres with Controlled Diameters in the Range 5–30 nm and Their Self-Assembly upon Dilution. *Chem. - An Asian J.* **2013**, *8* (4), 792–799.
- (46) Sun, Y. Shape-Controlled Synthesis of Gold and Silver Nanoparticles. *Science* (80-.). **2002**, *298* (5601), 2176–2179.
- (47) Ruditskiy, A.; Xia, Y. Toward the Synthesis of Sub-15 nm Ag Nanocubes with Sharp Corners and Edges: The Roles of Heterogeneous Nucleation and Surface Capping. *J. Am. Chem. Soc.* **2016**, *138* (9), 3161–3167.
- (48) Zhang, Q.; Li, W.; Wen, L.-P.; Chen, J.; Xia, Y. Facile Synthesis of Ag Nanocubes of 30 to 70 nm in Edge Length with CF₃COOAg as a Precursor. *Chem. - A Eur. J.* **2010**, *16* (33), 10234–10239.
- (49) Im, S. H.; Lee, Y. T.; Wiley, B.; Xia, Y. Large-Scale Synthesis of Silver Nanocubes: The Role of HCl in Promoting Cube Perfection and Monodispersity. *Angew. Chemie Int. Ed.* **2005**, *44* (14), 2154–2157.
- (50) Zheng, Y.; Zeng, J.; Ruditskiy, A.; Liu, M.; Xia, Y. Oxidative Etching and Its Role in Manipulating the Nucleation and Growth of Noble-Metal Nanocrystals. *Chem. Mater.* **2014**, *26* (1), 22–33.

- (51) Siekkinen, A. R.; McLellan, J. M.; Chen, J.; Xia, Y. Rapid Synthesis of Small Silver Nanocubes by Mediating Polyol Reduction with a Trace Amount of Sodium Sulfide or Sodium Hydrosulfide. *Chem. Phys. Lett.* **2006**, *432* (4-6), 491–496.

4. SILK FIBROIN BIOPOLYMER FILMS AS EFFICIENT FLEXIBLE HOST FOR DISTRIBUTED FEEDBACK LASER¹

Distributed feedback (DFB) lasers are devices that operate in longitudinal single-mode oscillation due to a grating structure existing throughout the gain medium, providing the feedback for lasing. From an applied point of view a DFB laser is the most straightforward device to detect the wavelength shift induced by (bio)chemical agents present in the grating surroundings. Spectroscopic applications already known include for example high sensitivity bio-¹⁻³ or chemosensing⁴⁻⁷. Further, DFB lasers are key features in the development of light sources for medical diagnosis⁸ and are also applied into dense wavelength division multiplexing (DWDM) devices that produce stable and accurate signals for optical communications. DFB lasers may be simple to fabricate and inexpensive polymers or glass matrices are generally used⁹⁻¹⁴. Due to optical properties such as broad transparency range and low laser threshold, poly(methyl methacrylate) (PMMA) or co-polymers of methyl methacrylate (MMA) and 2-hydroxyethyl methacrylate) (HEMA) have been used in the fabrication of polymer doped dye DFB^{15,16} lasers. However, the lack of biocompatibility and biodegradability can be a challenge to use these materials in biological applications due to harmfulness or toxicity related to the release of monomers in biological media^{17,18}. In this sense, biopolymers have been used to overcome these limitations by improving flexibility and functionality besides the well-known suitable biological response¹⁹⁻²¹.

The use of biopolymers from renewable resources as DFB matrices is attractive because they have a natural ability to self-assembly in complex structures by facile and green synthetic routes. The final complex structure will derive from the natural physical crosslinks that lead to thermodynamically stable structures exhibiting in general appropriate mechanical properties, excellent homogeneity and good optical properties.^{22,23} In addition, biopolymeric matrices can be doped or chemically modified with optically responsive molecules to yield photonic devices²⁴⁻²⁷. Biopolymers such as poly-L-lactic acid, polycaprolactone²⁸, dextran^{29,30}, melanine³¹, phospholipid^{32,33}, chitin³⁴⁻³⁸, collagen³⁹, gelatin-glutaraldehyde⁴⁰ and gelatin-chitosan⁴¹ have been used in the fabrication of grating patterned films. However, few reports are found exploiting

¹ This chapter contains results from previously published article (see permission grant in Attachments section of this thesis):

Silva, R. R. et al. *Journal Materials Chemistry C*, v. 1, n. 43, p. 7181-7190, 2013.
Available at <http://dx.doi.org/10.1039/C3TC30903G>

biopolymers as matrices for DFB lasing mainly due to photodegradation and poor thermo and mechanical characteristics that are detrimental for lasing.

On the other hand, DFB dye lasers have been successfully investigated with new matrices such as a hybrid biopolymer composed by a complex of surfactant/recycled marine biowaste deoxyribonucleic acid (DNA)⁴². In a recent study, the lasing thresholds of hybrid DFB lasers made with DNA - hexacetyltrimethyl-ammonium chloride (cationic surfactant) thin film doped with hemicyanine derived²⁵ and sulforhodamine dye^{26,27} were 11 mJ/cm² and 0.03 mJ/cm², respectively.

In the fabrication of diffraction grating patterns from biopolymeric matrices different methodologies have been employed like lithography^{28-32,36}, embossing^{43,44}, or direct-writing techniques^{33,45}. Few works are based on low cost replica-casting method (RC method)^{27,35,46} to the preparation of gratings for DFB lasers or other devices. This is due to the low accuracy of details or poor replica fidelity presented by biopolymers. In addition, detachment of the biopolymer film from grating pattern template is observed due to thermal shrinkage during solvent evaporation or poor interface interaction.

In this work, we used silk fibroin (SF) films doped with Rhodamine 6G (Rh6G) and also containing silica (SiO₂) or silver (Ag) nanoparticles (NPs) to fabricate DFB dye lasers. Our devices were obtained by the RC method templating a regenerated SF film with a periodical grating pattern of polycarbonate layer of a commercial DVD blank. The casting of a fibroin protein at a commercial DVD makes the process very simple and inexpensive and confers additional versatility when compared with others methods; the film quality is ensured by the incredible good mimic engineering of fibroin protein.⁴⁶ In comparison with synthetic polymers such as PMMA or HEMA, SF is more appropriate for biodevices fabrication because of its large biocompatibility and biodegradability. The devices based on SF are mechanically robust and present excellent surface quality and optical transparency.^{50,51} These features allow the manufacture of photonic elements containing micro and nanopatterns with relative ease for applications in biology.^{47,51}

Recently, grating devices based on SF protein have been prepared for biological sensors⁴⁸⁻⁵² and can be considered as a good candidate for DFB lasing.⁵³⁻⁵⁵ Fibroin is a silk protein found in natural spider cobweb silk fibers and silkworm cocoons filaments that represent the strongest and toughest natural fibers known⁵⁶. Silk has been used commercially in textiles over millennia and for decades have been used in biomedical sutures⁵⁷. Regenerated fibroin solution is used for processing materials having multiples geometrical shapes such as hydrogels, coatings, porous 3D matrices, fibers and films with thicknesses ranging from nanometers to centimeters⁵⁸. The amino acid chains provide remarkable enhancement in chemistry SF functionalization. SF solutions can be used to

produce good optical quality films by self-assembly of high and low molecular weight fibroin chains (almost 390 KDa and 25 KDa) into highly crystalline β -sheet conformation. Due to the good optical properties combined with the biocompatible behavior, suitable SF films containing periodic nanopatterns were used to evaluate the cell adhesion of corneal fibroblast⁵⁹ as well as to sensing the glucose concentration⁶⁰ or hemoglobin-oxygen binding^{51,52}. Biodegradable microfluidic^{56,57} and optical waveguides with low optical loss ($< 0.1 \text{ dB cm}^{-1}$)⁴⁵ based in SF matrix have been fabricated for applications to bio-microelectromechanical systems (Bio-MEMS) and biophotonic applications.

Toffani et al⁵⁵ demonstrated a DFB laser operation in dye doped SF matrix. The authors have been reported lasing threshold of 45 KW/cm^2 for SF thin films regarding grating period of 275 nm using a pumping laser at 427 nm. Organic lasers based on DFB resonators and also random laser structures have been studied for many years. But a combination of DFB resonators and a random distribution of NPs supported by a silk fibroin matrix was not investigated before.

As shown hereafter besides the operation of a conventional DFB laser, we report the operation of a modified DFB Laser based on SF films with scattering particles randomly distributed on the grating. In the modified DFB laser we exploited the multiple scattering of light occurring in the laser active medium due to the presence of SiO_2 NPs. The influence Ag NPs was also exploited aiming the improvement of the laser action because of the intensified local field in the vicinities of the NPs. The multiple scattering of light in random media is the dominant feedback mechanism that enables for example the operation of Random Lasers (RLs) in different systems such as colloidal dye solutions, polymer films containing dielectric or metallic NPs⁶¹⁻⁶³ and semiconductor nanopowders⁶⁴. In previous studies^{65,66}, some of us have exploited the use of SiO_2 and Ag NPs in RLs. In the present case we exploited the previous experience with RLs and introduced NPs in the DFB active medium to enhance the DFB laser intensity and to reduce the laser threshold.

4.1. Experimental Section

4.1.1. Extraction of silk fibroin

Fibroin was extracted from *Bombyx mori* silk cocoons. Initially, sections of raw cocoon scaffolds were cut and treated in a boiling solution of Na_2CO_3 0.02 mol L^{-1} in order to remove sericin (degumming). After, the purified SF fibers was introduced in a tertiary solvent system of CaCl_2 : Ethanol: H_2O (1:2:8 molar) until complete dissolution. The resulting solution was filtered and dialyzed against deionized water; the final fibroin concentration was 7% (w/v). The solution used for fabrication of the DFB dye laser was prepared by mixing Rh6G (10^{-4} M) in aqueous solution with fibroin solution 7% at 1:60 – 1:3 (v/v) proportions. Afterwards, silver or SiO_2 NPs in various

concentrations were added to the solution in order to study their influence on the emission characteristics from dye-doped DFB films.

4.1.2. Preparation of silver nanoparticles

The synthesis of Ag NPs was carried out using the procedure described by Jin et al.⁶⁷. 1 mL of aqueous solution of NaBH₄ (5×10^{-2} mol L⁻¹) was added to 100 mL of AgNO₃ 10^{-4} mol L⁻¹ in the presence of 3×10^{-4} mol L⁻¹ of trisodium citrate. The obtained solution was kept under vigorous stirring at room temperature. Immediately after, 2 mL of the particle stabilizing agent Bis(p-sulfonatophenyl) phenylphosphine dehydrated dipotassium salt solution 5×10^{-2} mol L⁻¹ was added and kept under vigorous stirring during 0.5 h. The resultant yellowish solution was put into a glass flask and covered by an aluminum foil to prevent chemical reactions due to surrounding light.

4.1.3. Synthesis of silica nanoparticles

The SiO₂ NPs were synthesized by the modified Stober method⁶⁸. 4 mL of tetraethylorthosilicate (TEOS) were added to 50 mL ethanol, the solution pH was increased until 14 by subsequently drop-wise of 4 mL ammonium hydroxide 28%. The final solution was sonicated for 2 hours and the resultant solid was kept in a petri dish to evaporate the ammonium vapor excess for 2 hours. The complete removing of the solvent was undertaken placing the solid in an oven at 70°C for 6 h followed by sequential heating at 120 °C for another 6 h. An aqueous colloidal suspension of SiO₂ NPs was obtained dispersing the dried white powder into 100 mL of deionized water and sonicating for 2 h.

4.1.4. Fabrication of DFB silk fibroin gratings

The DFB grating structures in the SF films were obtained by template-patterning the regenerated SF solution using the grating surface of a blank commercial DVD. First, the grating surface was exposed by carefully peeling apart the double layer of DVD into polycarbonate and aluminum foil portions. The polycarbonate mold was kept in a cleaning solution composed by an ethanol: 2-propanol 50% vol. Finally, the samples of DFB dye laser were obtained casting the final SF solution onto a surface of 3 cm diameter of the polycarbonate layer that has a grating with pitch (average distance between successive grooves/tracks) of ≈ 740 nm. These samples were placed in an oven at 40 °C for 24 h to evaporate the water content. After casting, SF films adhered to the polycarbonate master pattern were easily removed by peeling-off with a collet and directly used to further characterization and lasing measures .

4.1.5. Characterization

Conventional transmission electron microscopy (TEM) images of silver nanoparticles were acquired on a FEI model Morgagni 268D operating at an accelerating voltage of 100 KV by dropping the suspension onto carbon coated copper grids (300 mesh) which were allowed to dry in air ready for TEM. The corresponding high-resolution transmission electron microscopy (HRTEM) images were archived on a Gatan model 2100 operating at 300KV. Scanning Electron Microscopy images of SF films were obtained on a field emission JEOL model 7500F (FEG-SEM), equipped with an solid Si(Li) state energy-dispersive X-ray (EDX) detector with an energy resolution of 132 eV for the Mn-K α emission. Attenuated Total Reflection -Fourier Transform Infrared (ATR-FTIR) spectra of the SF films were recorded on Fourier transform infrared (FTIR) model Spectrum 2000 (Perkin Elmer; Norwalk, CT, USA), under accumulation of 128 scans and resolution of 4 cm⁻¹ using a ZnSe trough plate crystal.

The ATR-FTIR data were processed using a Peakfit® 4.12 (Systat Software Inc., Chicago, IL). All FTIR spectra were subjected to Savitzky-Golay algorithm smoothing (< 3%) and linear best-fit baseline correction. The curve-fitting to amide I region (1700-1585 cm⁻¹) was performed using a Voigt amplitude function^{69,70}, a mixture of Gaussian with a minor contribution of Lorentzian curves (<10%).

UV-Vis spectra for both silver nanoparticles and SF films were recorded on a Varian Cary 500 spectrometer. The effective refraction index of SF films was measured using the prism- coupling (m-lines) technique.

4.1.6. Experimental setup for the lasing measurements

Lasing in the SF samples was achieved using as pumping source the second harmonic of a Nd:YAG pulsed laser (Ultra CFR, Big Sky Laser Tech. Inc., Bozeman, USA) at 532 nm with a Q-switched pulse duration of 6 ns. A cylindrical lens was used to obtain a stripe beam of $\approx 15 \mu\text{m} \times 8 \text{ mm}$ focused perpendicularly to the film surface that contained the DFB structure. As the grating structure in the SF films at micron-scale had a circular pattern, to characterize the laser emission, the DFB devices were placed on rotary stage to align the stripe beam perpendicularly to tangent of grating at the point of incidence. The emitted light, detected from the film edge, was analyzed using a monochromator model SPEX 2000 (resolution: 0.1 nm, slit aperture: $\approx 200 \mu\text{m}$) equipped with a CCD camera, which can operate at single shot configuration. The representative image of experimental setup is shown in Figure 36.

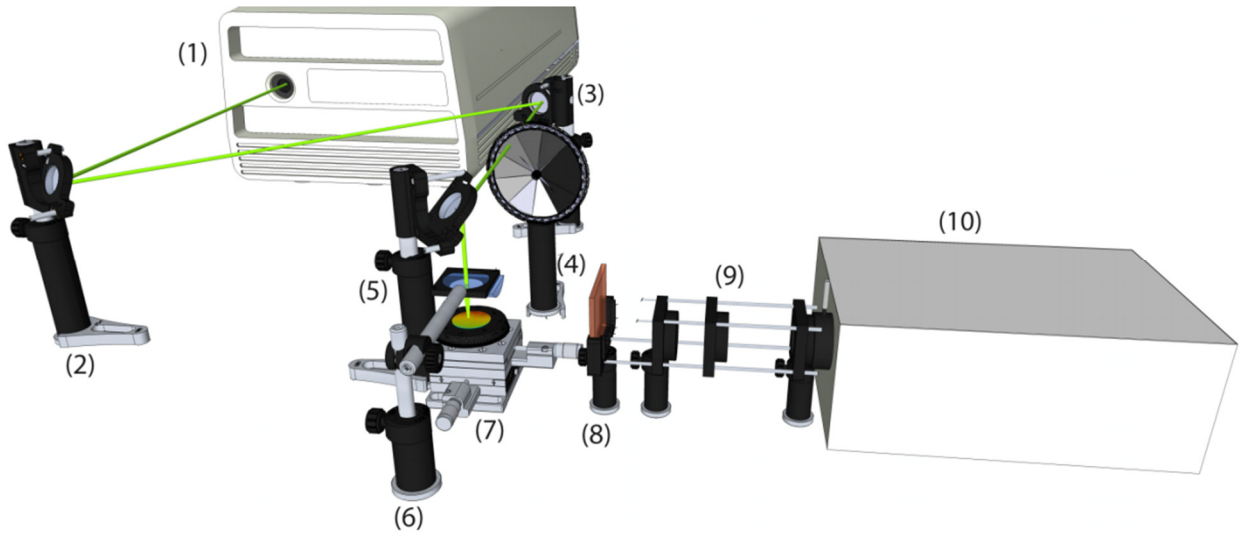


Figure 36. Experimental apparatus: (1) laser source; (2), (3), (5) mirrors, (4) circular stepped neutral density filter (6) cylindrical lens (7) rotational support for sample loading (8) optical low-pass filter (9) lens array and (10) detector.

4.2. Results and discussion

SF solutions doped with Rh6G dye and containing silica (average diameter: ≈ 123 nm) or Ag (average diameter: ≈ 10 nm) NPs were prepared. The SF films with a DFB grating structure were obtained by the RC method. The films were 0.11 ± 0.01 mm thick having a homogeneous appearance, being mechanically flexible and robust. The dye concentration in the films, after solvent evaporation, was estimated to be $\approx 2.8 \times 10^{-7}$ mol g⁻¹ (4×10^4 mol L⁻¹).

Citrate-stabilized spherical Ag NPs were prepared by using NaBH₄ as reducing agent for Ag⁺ in aqueous solution of AgNO₃. The representative TEM images in Figure 37a revealed that the Ag NPs have average diameter of ≈ 10 nm.

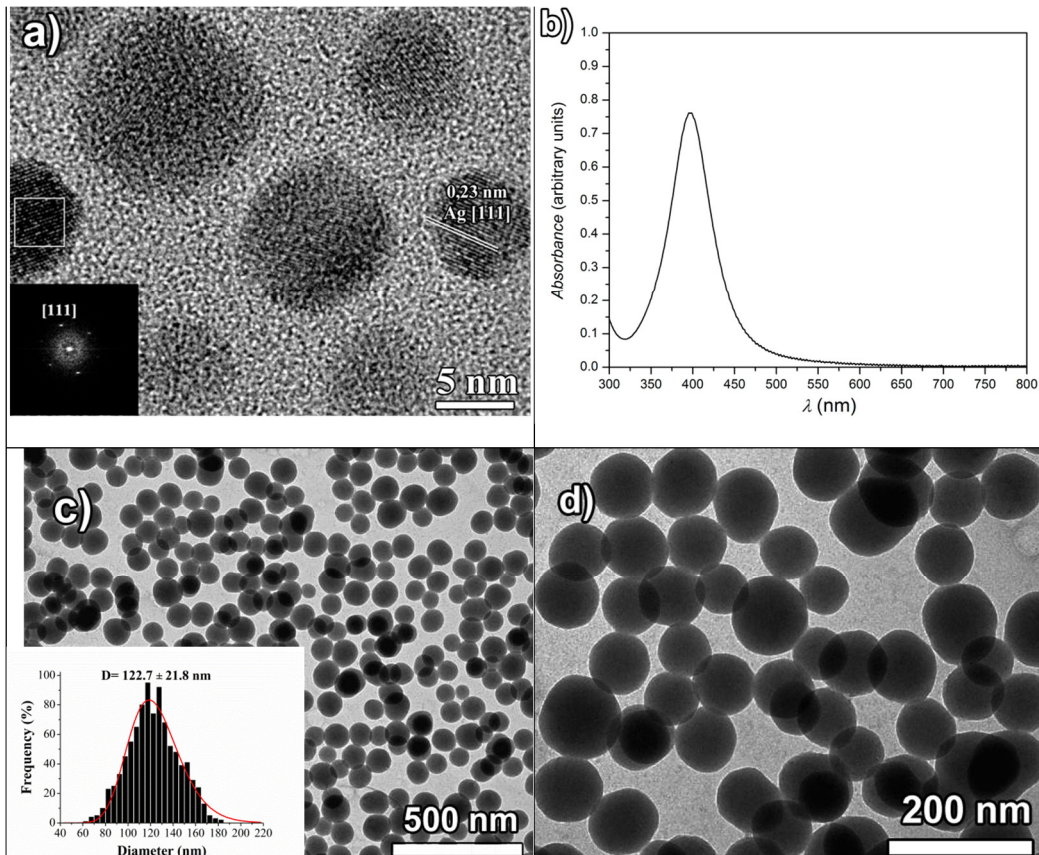


Figure 37. a) HRTEM image and b) UV-VIS absorbance spectrum of Ag NPs. c) and d) TEM images of silica NPs at different magnifications. The inset in a) is the Fast Fourier Transform (FFT) image showing [111] planes of Ag NPs. In c) the inset shows a histogram of the SiO₂ NPs diameter distribution.

This result correlates well with the localized surface plasmons (LSP) absorption band at ≈ 400 nm shown in Figure 37b obtained by UV-VIS spectroscopy. The SiO₂ NPs were synthesized by a modified Stober method⁶⁸. TEM images of SiO₂ NPs at two different magnifications are shown in Figure 37, c and d.

The SF samples containing different silica NPs densities were labeled as SFSiN (N=1-3) and the SF samples containing Ag NPs were labeled SFAg; their respective names and NPs contents are shown in Table 1.

Table 1. Parameters of the samples: dye concentration, NPs density, thickness scattering mean free path (l_s), scattering cross section (σ_s).

Sample	SiO ₂ NPs	Ag NPs	σ_s	l_s	kl_s
	$1.7 \times 10^{10} \text{ cm}^{-3}$	$[\times 10^{12} \text{ cm}^{-3}]$	$[\times 10^{-4} \mu\text{m}^2]$	[cm]	$[\times 10^5]$
Dye-doped SF					
SFSi1	1.7		5.3	11.1	12.2
SFSi2	3.5		5.3	5.4	5.9
SFSi3	8.8		5.3	2.1	2.3
SFAg		4.2	3.2×10^{-5}	7400	8.5×10^2

The high quality of the SF gratings obtained can be understood considering the intrinsic capability of silk materials to bend through intermolecular self-assembly into replicate periodical grating films. The hydrogen intra- and inter-molecular bonds lead to high fibroin crosslink during the drying step. Additional driving force could be attributed to the van der Waals interactions between polycarbonate layer material and the silk interface that results in the wealth of details in the nanometric scale provided by the mimicking process.

The results also indicate that SiO₂ NPs enhance the conformational crystallization among silk polymorphs. ATR-FTIR spectroscopy was used to study the conformational behavior of the SF films after the addition of SiO₂ NPs. The SF can assume two main distinguished conformations: a water-soluble /amorphous silk I and an insoluble/crystalline silk II secondary structure. Indeed, the regenerated SF solution undergoes a partial crystallization of silk I (random coil) to silk II (random coil + β -sheet) transition during the drying step of the films production. The absorption spectra for a pure dried silk film and dye-doped film with different SiO₂ NPs contents are shown in Figure 38.

The absorption bands observed at 1637 cm^{-1} (amide I), 1520 cm^{-1} (amide II) and 1230 cm^{-1} (amide III) are assigned to the silk II conformation. The silk II structure presents a typical β -sheet antiparallel chain structure and has a predominant conformation in all grating films studied mainly at the highest SiO₂ NPs density although the presence of silk I domains could still be detected. Curve fitting of the amide I band ($1600\text{-}1700 \text{ cm}^{-1}$) was performed to estimate the structural conformation components at SF films (Figure 39 and Table 2).

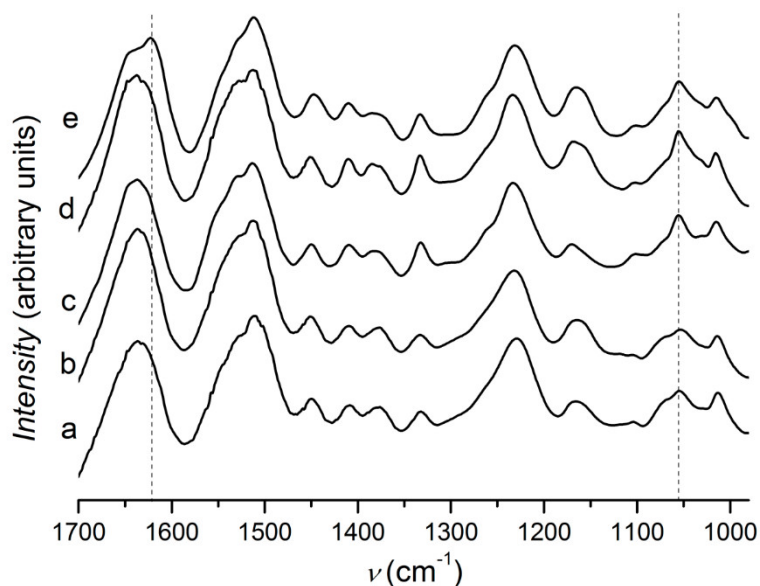


Figure 38. ATR-FTIR spectra of silk fibroin (SF) films. Pure SF film (curve a), dye-doped SF film (curve b), sample SFSi1 (curve c), sample SFSi2 (curve d) and sample SFSi3 (curve e).

The amide I comprises vibrations mainly due to C=O stretching modes with minor contribution from N-H bending and C-N stretching. The band centered at 1624 cm^{-1} (band VI) is assigned to the β -sheet structure and contributes to the 31 % of the total intensity at SFSi3 in comparison to 23% in SFSi2, 22% in SFSi1 and about 20% to the pure and dye-doped SF film. The addition of dye as used in this work does not induce any observable structural changes in the films.

SiO_2 NPs contribute to increase the β -sheet structure relative content in SF films. It is already known that the β -sheet structure of SF is due to the self-assembly of repetitive and regular strands of hydrophobic peptides Gly-Ala-Gly-Ala-Gly-Ser into antiparallel orientation⁷¹. Comparing the curves in Figure 40 corresponding to the DFB films containing SiO_2 NPs (SFSi1, SFSi2 and SFSi3) and the DFB film without SiO_2 NPs (Dye-doped SF), it is observed that in the presence of NPs there is an increase of the band peaked at 1054 cm^{-1} which is assigned to the overlap between rising Si-O-Si asymmetric stretching modes and skeletal C-C stretching mode of silk II.

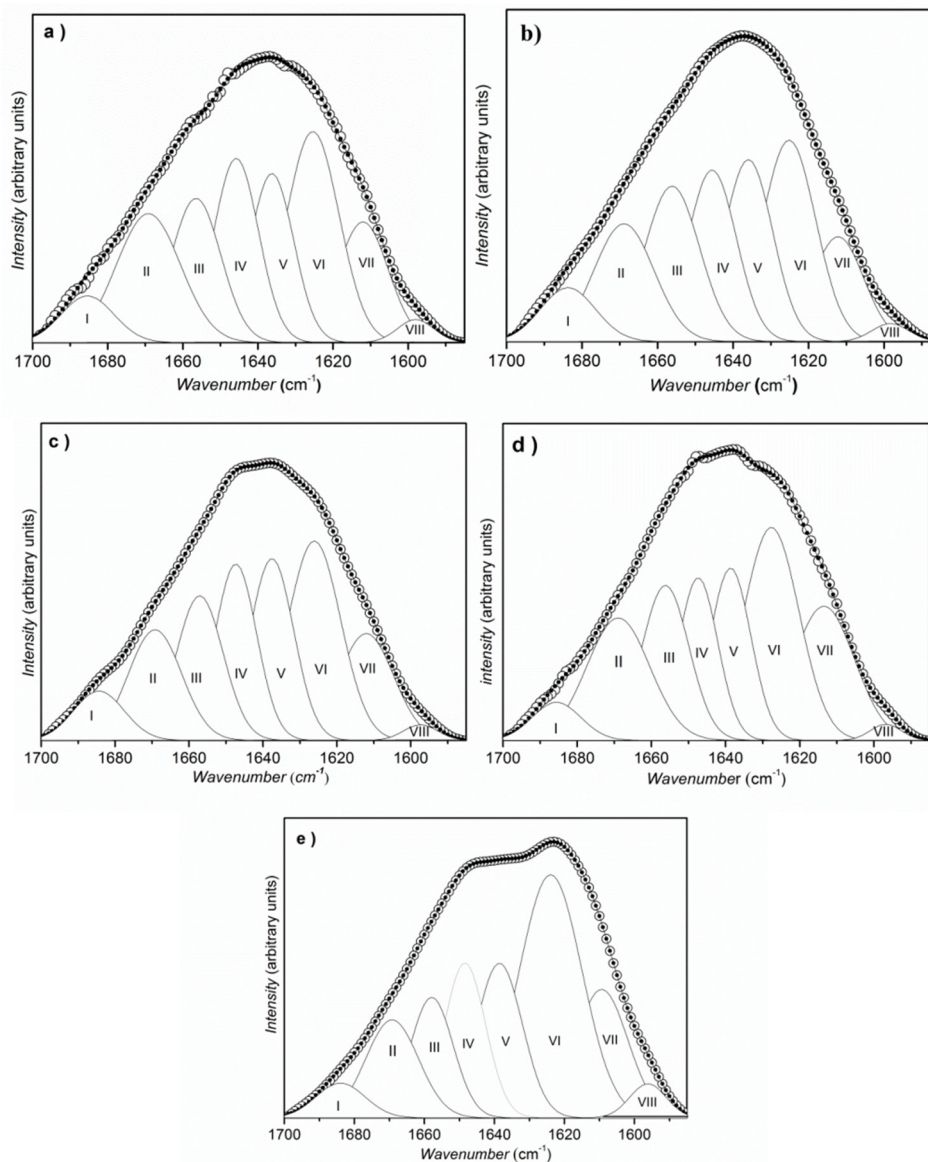


Figure 39. Curve fitting of the amide I band observed in the ATR-FTIR spectrum: a) Pure SF b) Dye Doped SF c) SFSi1 d) SFSi2 and e) SFSi3

Table 2. Relative Area (%) corresponding the curve fitting of amide I ATR-FTIR spectra of SF films

	I	II	III	IV	V	VI	VII	VIII
Pure SF	4.70	16.0	13.9	16.0	14.3	21.6	11.9	1.63
Doped SF	5.58	13.5	16.2	15.9	16.8	20.5	10.3	1.27
SFSi1	5.22	12.4	14.3	15.6	16.8	22.3	12.3	1.13
SFSi2	3.66	15.2	14.3	12.6	13.9	23.3	16.2	0.99
SFSi3	3.48	10.6	10.5	13.1	14.6	31.3	13.9	2.54

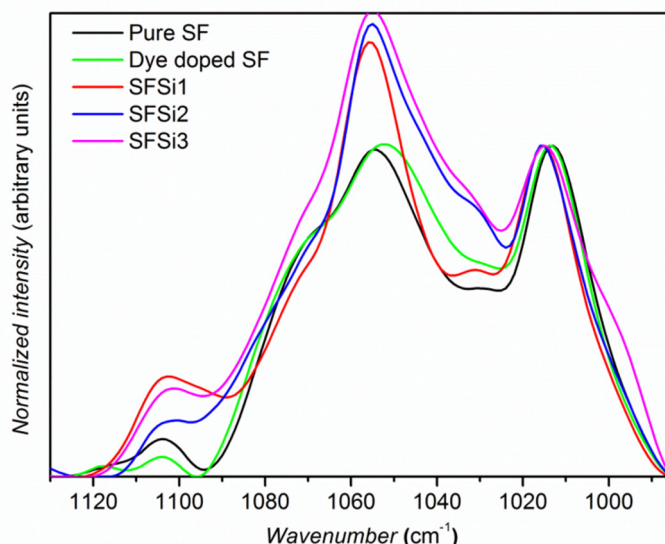


Figure 40. ATR-FTIR spectra of SF films: pure film, dye doped SF film, SFSi1, SFSi2 and SFSi3.

To obtain a better evaluation of the SF films microstructure, scanning electronic microscopy (SEM) and atomic force microscopy (AFM) analysis were performed. Figure 41a shows three steps of the procedure to obtain the films. Figure 41b and Figure 41c display the SEM and high resolution amplitude modulation AFM images of the surface grating structure in a SF film obtained by casting SF solution onto a commercial DVD. These images show the high quality of the grating structure.

The optical diffraction pattern from a pure SF grating without Rh6G or NPs is showed in Figure 41d using a green laser pointer. Figure 41e and Figure 41f show the tri-dimensional and bi-dimensional AFM images of the grating structure. Figure 41g illustrates the DFB structure of SF with a sinusoidal pattern with a depth of ≈ 75 nm and grating period of ≈ 750 nm while Figure 41, b-d demonstrate the high fidelity replica of the periodical pattern existing in the DVD.

Figure 42a shows schematically the DFB dye laser set up used to study the laser behavior of films without any NPs (Dye doped SF), with SiO₂ NPs in low (SFSi1) and high (SFSi3) relative contents as shown in Figure 42b, c and d, respectively. SiO₂ NPs incorporated into SF grating were observed by using back-scattered electrons (BSE) detection (Figure 42e) and verified by Energy-dispersive X-ray spectroscopy (EDX). The EDX spectrum (Figure 42f) shows a peak at 1.74 KeV corresponding the K α line of Si in the SFSi3 sample. The SiO₂ NPs yield a color contrast with the SF grating matrix. In addition, the BSE mode provides image contrast as a function of elemental composition and as a function of the height difference and explains the difference in brightness between white (higher) and black (lowest) stripes.

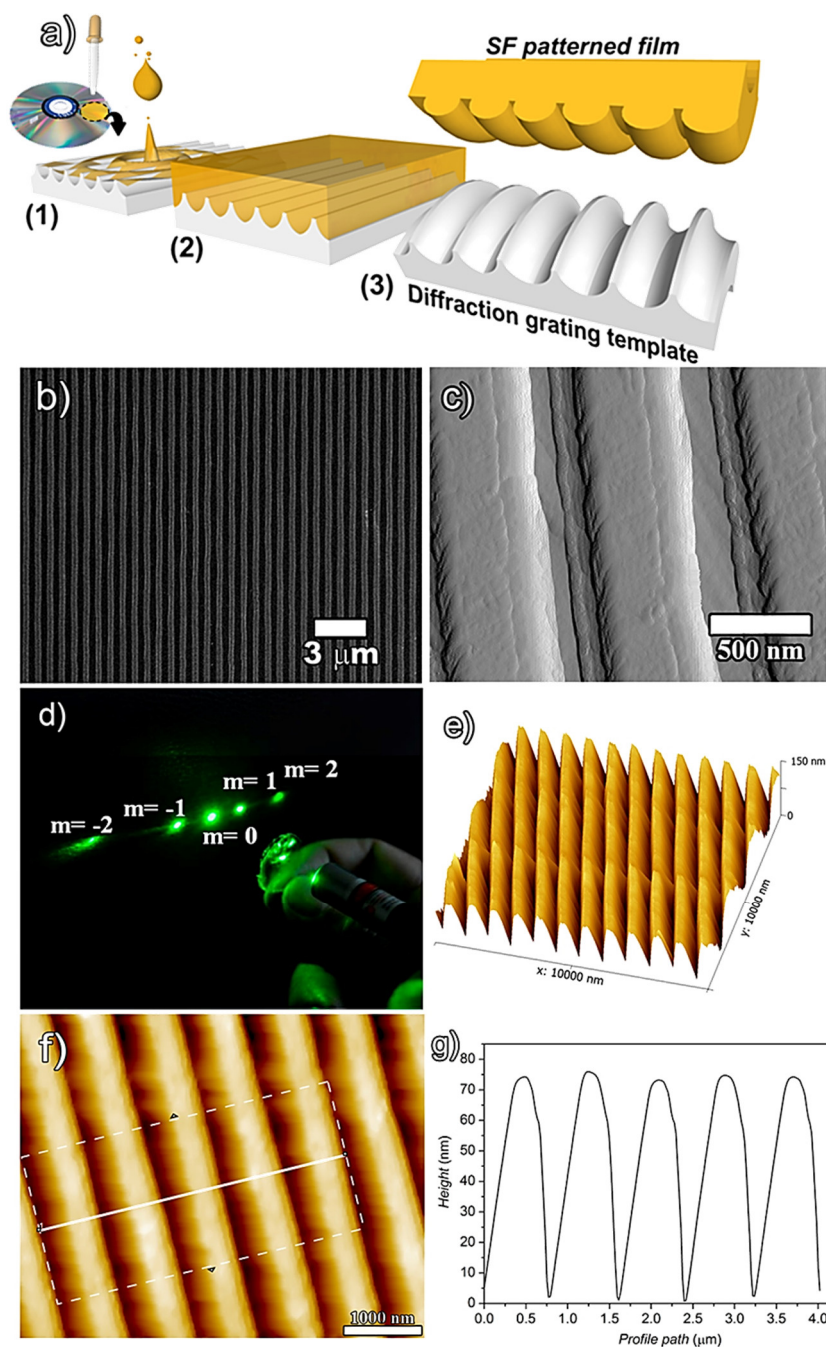


Figure 41. a) Procedure to preparation of DFB grating using SF films by the RC method over a DVD patterning template: (1) casting and (2) drying of the SF solution deposited over a blank DVD, (3) detachment of free-standing SF patterned films. b) FEG-SEM images of SF films. c) High resolution amplitude modulation AFM images showing two adjacent grooves of a ruled SF grating. d) Optical diffraction pattern of a SF grating without NPs neither dye molecules when illuminated by a green laser pointer. AFM images in e) 3D and f) 2D representations. g) Height variations averaged over 100 grating lines.

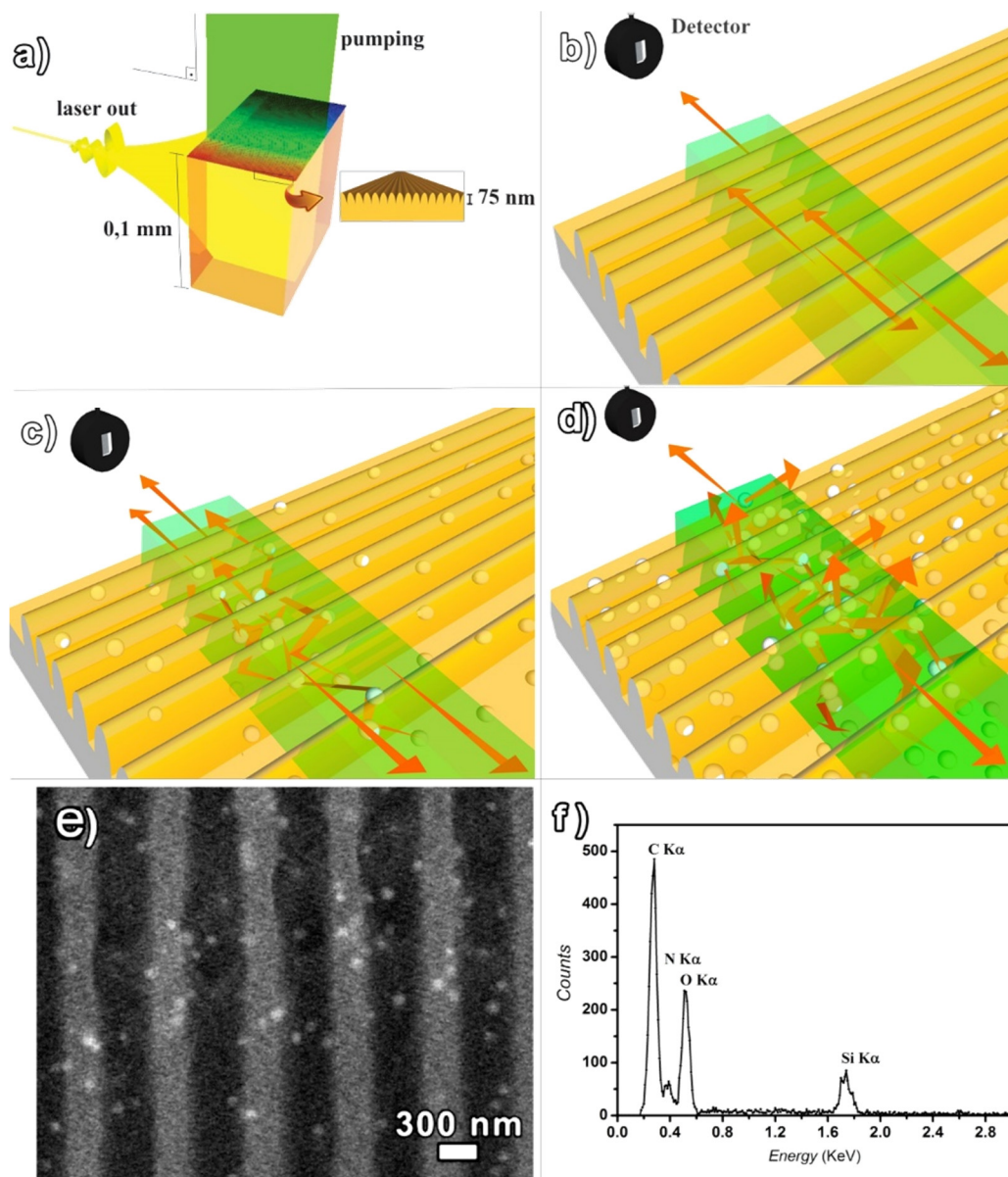


Figure 42. a) Schematic representation of the experimental configuration to study the DFB laser behavior in a SF grating; b) system without NPs (dye-doped SF film); c) e d) system containing low and supersaturated SiO_2 NPs, respectively; e) BSE image and f) EDS spectrum of the SFSi3 sample. The white points in BSE image are due to the SiO_2 NPs present in the SF film.

In order to evaluate the optimal dye concentration three DFB SF films doped with Rh6G were prepared (SFRod1, SFRod2 and SFRod3). Their absorption and emission spectra are shown in Figure 43.

Absorption and emission intensities increase according to the dye concentration. The absorption spectrum obtained for SFRod3 film shows a second absorption band centered at ≈ 500 nm that can be attributed to non-fluorescent dimers of Rh6G⁷². Usually, at relative high concentrations of Rh6G fluorescent (J-type) and non-fluorescent (H-type) dimers are formed. The J-type dimers

emission is red shifted with respect to the monomer emission and the total emission spectrum shows overlap of the emission spectra from two molecular species⁷³. The J- type dimers of Rh6G may generate a multi-mode operation in the DFB grating and cause broadening of the laser spectrum as shown in Figure 43. From this analysis, the dye concentration corresponding to the SFRod2 film was chosen to fabricate the DFB laser samples.

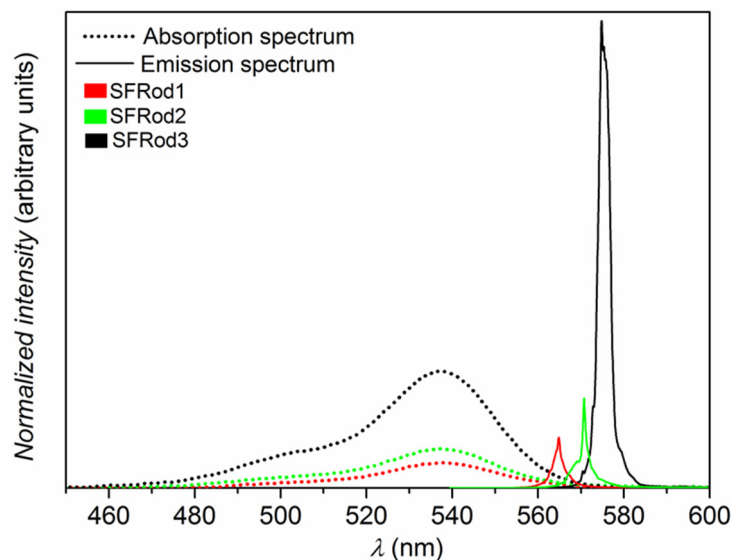


Figure 43. Absorption and emission spectra of SF films for different Rhodamine 6G concentrations. The dye concentrations are 1.43 , 2.86 and $4.76 \times 10^{-7} \text{ mol g}^{-1}$ corresponding to samples SFRod1, SFRod2 and SFRod3, respectively. The emission spectra were obtained for excitation pulses of 5.19 mJ.

The experimental setup to characterize the lasing regime is presented in Figure 36. Figure 44a and Figure 44b show the laser intensity behavior for three samples containing different SiO₂ NPs relative contents (SFSi1, SFSi2 and SFSi3), a sample containing Ag NPs (SFAG) and a sample without NPs. All samples have identical thickness and same dye concentration as indicated in The laser thresholds determined from Figure 44a are shown in Table 3.

The inset in Figure 44a is a magnification of pumping region where the laser threshold occurs. Laser threshold is observed at $\approx 1.3 \text{ mJ/pulse}$ (288 KW/cm^2) for the dye doped SF sample, $\approx 0.9 \text{ mJ/pulse}$ (200 KW/cm^2) for SFSi1 sample and $\approx 0.8 \text{ mJ/pulse}$ (177 KW/cm^2) for SFAG sample. Figure 44a and Figure 44b show that the addition of NPs enables enhanced emission. Figure 44a shows that the SFSi1 sample which has the lowest SiO₂ NPs density ($1.7 \times 10^{10} \text{ cm}^{-3}$), presents the highest peak intensity. On the other hand, Figure 44b shows that the narrower bandwidth is observed for SFAG sample for smaller excitation pulse energy than the others samples. Due to the presence of SiO₂ NPs, the gain medium in the DFB grating behaves also like a random gain

medium and similarly as in an incoherent RL,⁶¹ the absorption of light and the stimulated emission are enhanced due to the multiple scattering of light.

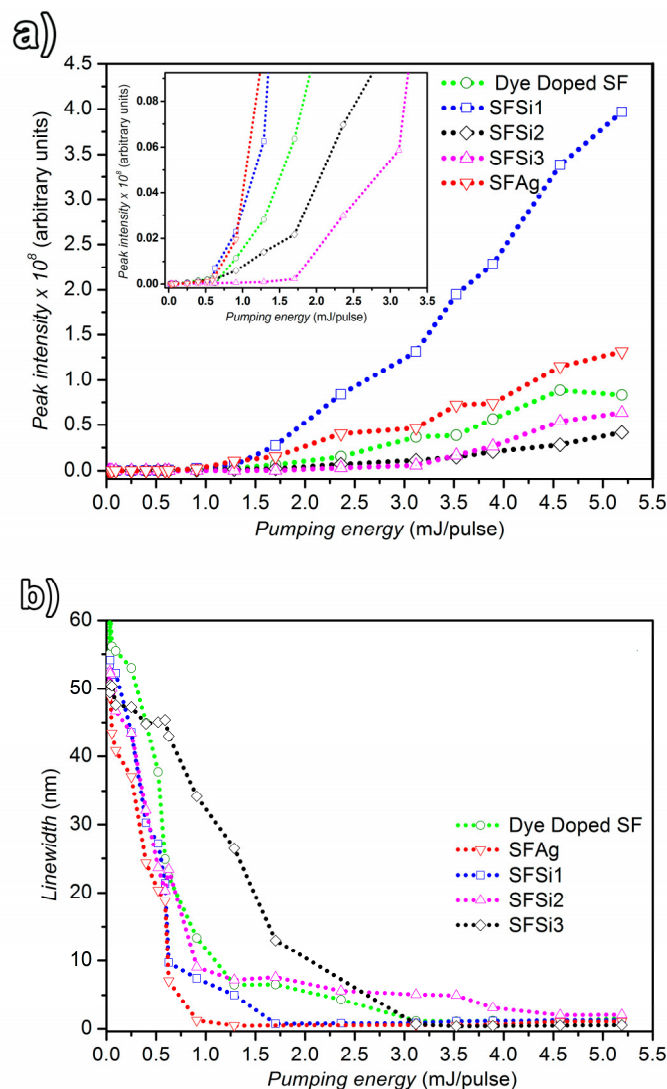


Figure 44. Comparison of laser characteristics between the sample without SiO₂ or Ag NPs (Dye-doped SF) and samples containing Si (SFSi1, SFSi2 and SFSi3) or Ag NPs (SFAg) with similar thickness and dye concentrations (a) Peak intensity as a function of the excitation pulse energy. The inset in a) is a magnification for low pumping energy region near to the threshold (b) Linewidth as a function of the excitation pulse energy.

The threshold growth observed for samples containing SiO₂ NPs densities above $1.7 \times 10^{10} \text{ cm}^{-3}$ (SFSi2 and SFSi3), is due to the filling of the grating grooves by the SiO₂ NPs ($\approx 123 \text{ nm}$). Note that the refractive index of silica and SF are close to each other and the grating depth ($\approx 75 \text{ nm}$) becomes filled with SiO₂ NPs. Therefore, the large SiO₂ NPs relative content reduces the feedback provided by the Bragg grating. Additionally, the increased number of scattering centers may raise the contribution of photons provided by multiple light scattering that induce stimulated emission

at optical frequencies different from the frequency determined by grating spacing. This effect contributes to linewidth broadening

Table 3. Lasing threshold and minimum DFB laser linewidth (spectrometer resolution: 0.1 nm). The parameter R was defined as the ratio $\lambda/\Delta\lambda$.

Sample	Threshold [mJ/pulse]	Threshold [KW/cm ²]	λ [nm]	$\Delta\lambda$ [nm]	R
Dye-doped SF	1.3	288	570.7	1	571
SFSi1	0.9	200	567.7	0.5	1135
SFAg	0.8	177	564.9	0.4	1412

The feedback in the SFSi samples is provided by the SiO₂ NPs and by the grooves of the SF grating. Therefore the best SiO₂ NPs relative content for operation of the DFB is $1.7 \times 10^{10} \text{ cm}^{-3}$. For this particular sample the lasing threshold was reduced ≈ 1.4 times in comparison with samples without NPs. Analogous results were obtained by Watanabe et al.⁷⁴ in a planar dual-layered waveguide dye laser doping with SiO₂ NPs using a dye concentration 10 times larger than the concentration used in the present work. Therefore incoherent RL operation in the SFSiO₂ samples is competing with the single-mode lasing from the DFB resonator. However, the SiO₂ NPs contributes for confinement of the incident and the emitted light and thus a larger fraction of the exciting laser beam is absorbed; consequently reduction of laser threshold occurs as shown in Table 3. In order to quantify the scattering regime for the SiO₂ doped samples, we calculated its scattering mean free path length, $l_s = 1/N\sigma_s$, where N is the SiO₂ density and σ_s is its respective scattering cross section (see Table 1) we find values above 10^6 . These results show us that the scattering regime of our samples is ballistic⁷⁵. Theoretical and experimental RL action going from localized to ballistic regimes has been reported previously⁷⁵⁻⁷⁸. Examining the linewidth and the peak intensity behavior as a function of the excitation pulse energy for the samples SFSi1 and SFAg (in Figure 44a and Figure 44b, respectively), we see that the results show a fast linewidth decrease for increasing values of the excitation pulse energy. Notice that the sample SFSi1 shows larger intensity than the sample SFAg for equal excitation pulse energy. In the present study, the Ag NPs content was approximately the one used by Dominguez et al.⁶⁵ for RL based on PMMA films containing Ag NPs, but the dye concentration was much smaller ($4 \times 10^4 \text{ mol L}^{-1}$). It is important to observe that the lasing threshold for the sample with Ag NPs is slightly lower than for the other samples, due probably to the influence of the local field effect. This fact is clarified in Figure 44b where the linewidth measured for the sample with Ag NPs is narrower than for the

others samples. Further measurements will be performed in the near future to characterize the minimum linewidth that can be achieved optimizing of dye concentration and Ag NPs density.

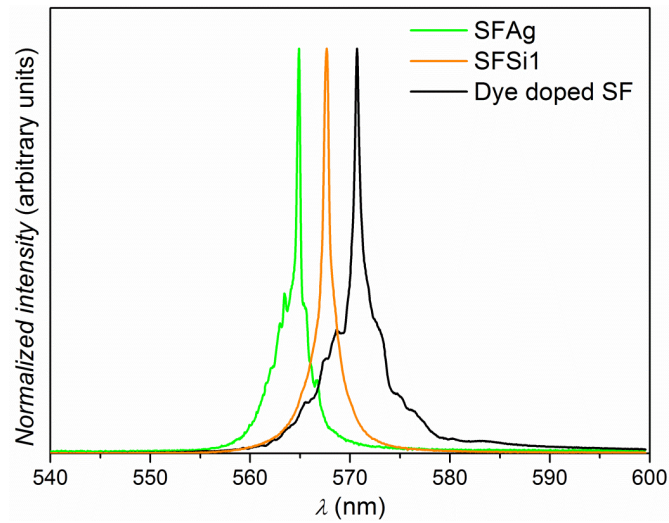


Figure 45. Normalized emission spectra of SFAg, SFSi1 and Dye-doped SF samples. The excitation energy was 3.1 mJ per pulse.

Figure 45 shows the normalized emission spectra for the dye-doped SF sample (DFB grating without NPs) and for the samples SFSi1 and SFAg. The blue shift in the emission wavelength with the addition of NPs may be attributed to the Rayleigh scattering (proportional to λ^{-4}) since light with smaller wavelength is mostly efficiently scattered favoring the gain to smaller wavelengths.

It is known that the laser wavelength in a DFB system satisfy the Bragg reflection condition⁷⁹, i. e. $m\lambda_B = 2n_{eff}\Lambda$, where m is the diffraction order, n_{eff} is the effective refractive index of the medium and Λ is grating period. The laser wavelengths observed were 570.7 nm (sample without NPs), 567.6 nm (sample SFSi) and 564.9 (sample SFAg). The refractive index of the SF film without a grating pattern was $n_0 \approx 1.55$ at 570 nm as obtained with a prism coupling technique. Therefore, assuming that n_{eff} in the SF films with the DFB pattern is equal to n_0 we conclude that the laser emission at ≈ 570 nm corresponds to the 4th diffraction order of the typical grating period of a blank DVD. As shown in Table 3, the minimum linewidth ($\Delta\lambda_{min}$) corresponding to the samples with better performance in this study were 1 nm (dye doped SF – sample without NPs, for excitation of 3.52 mJ per pulse); 0.7 nm (SFSi, for 1.7 mJ per pulse) and 0.4 nm (sample with Ag NPs, for 0.91 mJ per pulse). The parameter $R = \lambda/\Delta\lambda$ characterizing our devices may reach values larger than 10^3 for excitation intensities above the laser threshold as shown in Table 3.

In fact, the laser threshold in the DFB dye lasers depends on several parameters as dye concentration, period and order of diffraction grating, size of pumping spot, pulse duration of laser pumping, etc. In this work, the threshold depends also of the SiO₂ and Ag NPs densities. The threshold corresponding to the sample SFAg, equal to 0.8 mJ/pulse (177 KW/cm²), is four times

larger than the one reported in ref. [55] (45 KW/cm^2) for experimental conditions very different from ours. Particularly, we recall that in ref. [55] the grating period was 275 nm and the laser wavelength was 427 nm; these parameters indicate that the grating is selecting the wavelength through its second order ($m=2$). As mentioned before, in our experiment the lasing peak was at $\sim 570 \text{ nm}$, the grating period was 740 nm and the diffraction order for laser operation was $m=4$. It is known that the intensity of reflected light decays significantly when the m value is increased. However we note that even operating at 4th order the grating presents large efficiency to allow the operation of the DFB laser.

4.3. Conclusions

In this work, we report the operation of a modified DFB Laser based on SF films with scattering particles randomly distributed on the grating. The SF gratings were fabricated using the replica-casting patterning against a commercial blank digital versatile disc (DVD) as template. With the addition of SiO_2 or Ag NPs to the Bragg grating structure the laser intensity was enhanced and the linewidth was reduced. The DFB laser reported is a low cost device, its fabrication is very simple and large number of possible biophotonics and biomedicine applications can be foreseen due to great biocompatibility and biodegradability of silk fibroin.

References

- (1) M. Lu, S. Choi, U. Irfan, B. T. Cunningham, *Appl. Phys. Lett.* 2008, *93*, 111113
- (2) M. Lu, S. S. Choi, C. J. Wagner, J. G. Eden, B. T. Cunningham, *Appl. Phys. Lett.* 2008, *92*, 261502
- (3) C. Ge, M. Lu, W. Zhang, B. T. Cunningham, *Appl. Phys. Lett.* 2010, *96*, 1637021.
- (4) K. Krzempek, R. Lewicki, L. Nähle, M. Fischer, J. Koeth, S. Belahsene, Y. Rouillard, L. Worschech, F. K. Tittel, *Appl. Phys. B* 2012, *106*, 251-255.
- (5) X. Wang, S.-S. Kim, R. Roßbach, M. Jetter, P. Michler, B. Mizaikoff, *Analyst* 2012, *137*, 2322-2327.
- (6) Y. Yang, G. A. Turnbull, I. D. W. Samuel, *Adv. Funct. Mater.* 2010, *20*, 2093-2097.
- (7) R. C. Bailey, M. Parpia, J. T. Hupp, *Mater. Today* 2005, *8*, 46-52.
- (8) C. Vannahme, S. Klinkhammer, U. Lemmer, T. Mappes, *Opt. Express* 2011, *19*, 8179-86.
- (9) H.-H. Fang, R. Ding, S.-Y. Lu, J. Yang, X.-L. Zhang, R. Yang, J. Feng, Q.-D. Chen, J.-F. Song, H.-B. Sun, *Adv. Funct. Mater.* 2012, *22*, 33-38.
- (10) R. Xia, W.-Y. Lai, P. A. Levermore, W. Huang, D. D. C. Bradley, *Adv. Funct. Mater.* 2009, *19*, 2844-2850.

- (11) C. Kallinger, *Adv. Mater.* 1998, *10*, 920-923.
- (12) B. J. Scott, G. Wirnsberger, M. D. McGehee, B. F. Chmelka, G. D. Stucky, *Adv. Mater.* 2001, *13*, 1231-1234.
- (13) M. Gaal, C. Gadermaier, H. Plank, E. Moderegger, A. Pogantsch, G. Leising, E. J. W. List, *Adv. Mater.* 2003, *15*, 1165-1167.
- (14) S. Döring, M. Kollosche, T. Rabe, J. Stumpe, G. Kofod, *Adv. Mater.* 2011, *23*, 4265-4269.
- (15) S. M. Giffin, I. T. McKinnie, W. J. Wadsworth, A. D. Woolhouse, G. J. Smith, T. G. Haskell, *Opt. Comm.* 1999, *161*, 163-170.
- (16) P. Görrn, M. Lehnhardt, W. Kowalsky, T. Riedl, S. Wagner, *Adv. Mater.* 2011, *23*, 869-872.
- (17) J. Autian, *Environ. Health Perspect.* 1975, *11*, 141-152.
- (18) S. Sundstrom, B. Scolnick, J. B. Sullivan. Acrylates, Methacrylates and Cyanoacrylates. In: J.B. Sullivan, G.R. Krieger. editors. *Clinical environmental health and toxic exposures*. 2nd ed. Philadelphia: Lippincott Williams & Wilkins; 2001:1001-1006.
- (9) T. C. Santos, A. P. Marques, R. L. Reis. L.; *In vivo* tissue responses to natural-origin biomaterials. In: R. L. Reis, N.M. Neves, J. F. Mano, M. E. Gomes, A. P. Marques, H. S. Azevedo. editors. *Natural-based polymers for biomedical applications*. Cambridge: Woodhead Publishing in Materials; 2008: 683-698.
- (20) B. D. Ulery, L. S. Nair, C. T. Laurencin, *J. Polym. Sci. B Polym. Phys.* 2011, *49*, 832-864.
- (21) J. F. Mano, G. A. Silva, H. S. Azevedo, P. B. Malafaya, R. A. Sousa, S. S. Silva, L. F. Boesel, J. M. Oliveira, T. C. Santos, A. P. Marques, N. M. Neves, R. L. Reis, *J. R. Soc. Interface* 2007, *4*, 999-1030.
- (22) K. Morris, L. Serpell, *Chem. Soc. Rev.* 2010, *39*, 3445-3453.
- (23) C. Sanchez, H. Arribart, M. M. G. Guille, *Nature Mater.* 2005, *4*, 277-88.
- (24) M. Cronin-Golomb, A. R. Murphy, J. P. Mondia, D. L. Kaplan, F. G. Omenetto, *J. Polym. Sci. B* 2012, *50*, 257-262.
- (25) Sznitko, J. Mysliwiec, P. Karpinski, K. Palewska, K. Parafiniuk, S. Bartkiewicz, I. Rau, F. Kajzar, A. Miniewicz, *Appl. Phys. Lett.* 2011, *99*, 031107.
- (26) A. K. Manocchi, P. Domachuk, F. G. Omenetto, H. Yi, *Biotechnol. Bioeng.* 2009, *103*, 725-732.
- (27) Z. Yu, W. Li, J. a Hagen, Y. Zhou, D. Klotzkin, J. G. Grote, A. J. Steckl, *Appl. Opt.* 2007, *46*, 1507-1513.
- (28) G. Vozzi, A. Previti, D. D. E. Rossi, A. Ahluwalia, *Tissue Eng.* 2002, *8*, 1089-1098.
- (29) P. S. Ramanujam, *Opt. Mater.* 2005, *27*, 1175-1177.

- (30) S. Savić Šević, D. Pantelić, *Opt. Mater.* 2008, 30, 1205-1207.
- (31) C. W. Farley, A. Kassu, and a Sharma, *Opt. Lett.* 2011, 36, 1734-1736.
- (32) Sharma, M. Dokhanian, A. Kassu, A. N. Parekh, 2005, *Opt. Lett.* 30, 501-503.
- (33) S. Lenhert, F. Brinkmann, T. Laue, S. Walheim, C. Vannahme, S. Klinkhammer, M. Xu, S. Sekula, T. Mappes, T. Schimmel, H. Fuchs, *Nature Nanotechnol.* **2010**, 5, 275-279.
- (34) S. Koo, S. J. Ahn, H. Zhang, J. C. Wang, E. K. F. Yim, *Cell. Mol. Bioeng.* 2011, 4, 399-410.
- (35) C. Zhong, A. Kapetanovic, Y. Deng, M. Rolandi, *Adv. Mater.* 2011, 23 4776-4781.
- (36) J. G. Fernandez, C. A. Mills, J. Samitier, *Small* 2009, 5, 614-620.
- (37) C. S. Camilo, D. S. dos Santos Júnior, J. J. Rodrigues Júnior, M. L. Vega, S. P. Campana Filho, O. N. Oliveira Júnior, C. R. Mendonça, *Biomacromolecules* 2003, 4, 1583-8.
- (38) R. M. Reano, Y. P. Kong, H. Y. Low, L. Tan, F. Wang, S. W. Pang, A. F. Yee, *J. Vac. Sci. & Technol. B* 2004, 22, 3294.
- (39) A. Chandekar, S. K. Sengupta, J. E. Whitten, *Microsc. Res. Tech.* 2007, 70, 506-12.
- (40) L.-J. Yang, Y.-C. Ou, *Lab chip* 2005, 5, 979-984.
- (41) S. H. Yoon, W. T. Jeong, K. C. Kim, K. J. Kim, M. C. Oh, S. M. Lee, *J. Surf. Eng. Mater. Adv. Technol.* 2011, 1, 56-61.
- (42) J. Mysliwiec, L. Sznitko, A. Sobolewska, S. Bartkiewicz, A. Miniewicz, *Appl. Phys. Lett.* 2010, 96, 141106.
- (43) J. G. Fernandez, C. A. Mills, M. Pla-Roca, J. Samitier, *Adv. Mater.* 2007, 19, 3696-3701.
- (44) J. J. Amsden, P. Domachuk, A. Gopinath, R. D. White, L. Dal Negro, D. L. Kaplan, F. G. Omenetto, *Adv. Mater.* 2010, 22, 1-4.
- (45) S. T. Parker, P. Domachuk, J. Amsden, J. Bressner, J. A. Lewis, D. L. Kaplan, F. G. Omenetto, *Adv. Mater.* 2009, 21, 2411-2415.
- (46) B. H. Perry, A. Gopinath, D. L. Kaplan, L. D. Negro, G. Omenetto, *Adv. Mater.* 2008, 20, 3070-3072.
- (47) D-H. Kim, J. Viventi, J. J. Amsden, J. Xiao, L. Vigeland, Y-S. Kim, J. A. Blanco, B. Panilaitis, E. S. Frechette, D. Contreras, D. L. Kaplan, F. G. Omenetto, Y. Huang, K-C. Hwang, M. R. Zakin, B. Litt, J. A. Rogers, *Nature Mater.* 2010, 9, 511-517.
- (48) F. Galeotti, A. Andicsova, S. Yunus, C. Botta, *Soft Matter* 2012, 8, 4815.
- (49) B. H. Perry, A. Gopinath, D. L. Kaplan, L. D. Negro, G. Omenetto, *Adv. Mater.* 2008, 20, 3070-3072.
- (50) J. J. Amsden, P. Domachuk, A. Gopinath, R. D. White, L. D. Negro, D. L. Kaplan, F. G. Omenetto, *Adv. Mater.* 2010, 22, 1746-9.

- (51) B. D. Lawrence, M. Cronin-Golomb, I. Georgakoudi, D. L. Kaplan, F. G. Omenetto, *Biomacromolecules* 2008, 9, 1214-20.
- (52) P. Domachuk, H. Perry, J. J. Amsden, D. L. Kaplan, F. G. Omenetto, *Appl. Phys. Lett.* 2009, 95, 253702.
- (53) F. G. Omenetto, D. L. Kaplan, *Nature Photon.* 2008, 2, 641-643.
- (54) H. Tao, D. L. Kaplan, F. G. Omenetto, *Adv. Mater.* 2012, 24, 2824.
- (55) S. Toffanin, S. Kim, S. Cavallini, M. Natali, V. Benfenati, J. J. Amsden, D. L. Kaplan, R. Zamboni, M. Muccini, F. G. Omenetto, *Appl. Phys. Lett.* 2012, 101, 091110.
- (56) G. H. Altman, F. Diaz, C. Jakuba, T. Calabro, R. L. Horan, J. Chen, H. Lu, J. Richmond, D. L. Kaplan, *Biomaterials* 2003, 24, 401-16.
- (57) F. G. Omenetto, D. L. Kaplan, *Science* 2010, 329, 528-31.
- (58) D. N. Rockwood, R. C. Preda, T. Yücel, X. Wang, M. L. Lovett, D. L. Kaplan, *Nature protoc.* 2011, 6, 1612-31.
- (59) E. S. Gil, S.-H. Park, J. Marchant, F. Omenetto, D. L. Kaplan, *Macromol. Biosci.* 2010, 10, 664-63.
- (60) J. J. Amsden, H. Perry, S. V. Boriskina, A. Gopinath, D. L. Kaplan, L. Dal Negro, F. G. Omenetto, *Opt. Express* 2009, 17, 21271-21279.
- (61) N. M. Lawandy, R. M. Balachandran, A. S. L. Gomes, E. Sauvain, *Nature* 1994, 368, 436–438.
- (62) R. M. Balachandran, D. P. Pacheco, N. M. Lawandy, *Appl. Opt.* 1996, 35, 640–643
- (63) X. Meng, K. Fujita, S. Murai, K. Tanaka, *Phys. Rev. A* 2009, 79, 053817
- (64) R.K. Thareja, A. Mitra, *Appl. Phys. B* 2000, 71, 181–184.
- (65) C. Tolentino Dominguez, R. L. Maltez, R. M. S. dos Reis, L. S. A. de Melo, C. B. de Araújo, A. S. L. Gomes, *J. Opt. Soc. Am. B* 2011, 28, 1118–1123.
- (66) A. M. Brito-Silva, A. Galembeck, A. S. L. Gomes, A. J. Jesus-Silva, C. B. de Araújo, *J. Appl. Phys.*, 2010, 108, 033508.
- (67) R. Jin, Y. Cao, C. A. Mirkin, K. L. Kelly, G. C. Schatz, J. G. Zheng, *Science*, 2001, 294, 1901-1903.
- (68) W. Stöber, A. Fink, E. Bohn. *J. Colloid Interf. Sci.* 1968, 26, 62-69.
- (69) D. Wilson, R. Valluzzi, D. Kaplan, *Biophys. J.* 2000, 78, 2690-2701.
- (70) S. Winkler, D. Wilson, D. L. Kaplan. *Biochemistry*, 2000, 39, 12739-12746.
- (71) R. E. Marsh, R. B. Corey, L. Pauling. *Biochim. Biophys. Acta* 1955, 16, 1-34
- (72) F. L. Arbeloa, P. R. Ojeda, and I. L. Arbeloa. *J. Chem. Soc. Faraday Trans. II* 1988, 84, 1903-1912.

- (73) C. T. Dominguez, E. de Lima, P. C. de Oliveira, F. L. Arbeloa, *Chem. Phys. Lett.* 2008, 464, 245.
- (74) H. Watanabe, Y. Oki, M. Maeda, *Appl. Phys. Lett.* 2005, 86, 151123.
- (75) X. Wu; W. Fang; A. Yamilov; A. A. Chabanov; A. A. Asatryan; L. C. Botten; H. Cao *Phys. Rev. A* 2006, 74, 053812.
- (76) X. Meng, K. Fujita, S. Murai, J. Konishi, M. Mano, K. Tanaka. *Opt Express.* 2010, 18, 12153-12160.
- (77) C. Vanneste, P. Sebbah, H. Cao. *Phys Rev Lett.* 2007, 98, 143902
- (78) J. Fallert, R. J. B. Dietz, J. Sartor, D. Schneider, C. Klingshirn, and H. Kalt. *Nature Photon.* 2009, 3, 279-282.
- (79) H. Kogelnik, H.; C. V. Shank. *Appl. Phys. Lett.* 1971, 18, 152-154.

5. FUNCTIONAL AND TRANSPARENT HYBRIDS BASED ON SILK FIBROIN AND 3-GLYCIDOXYPROPYLTRIMETHOXYSILANE

A great deal of the ongoing efforts has been addressed towards the fabrication of optical materials derived from natural polymers.¹ In the last decade, silk fibroin (SF), a protein found in spider cobweb fibers and silkworm cocoons, emerged as a suitable natural polymer for optics. In particular, SF films display high transparency (ca. 95%) across the visible range,^{2,3} low surface roughness,⁴ biocompatibility and tunable biodegradability.^{3,5} Those features make SF films interesting nature-based materials for biophotonics.⁶⁻⁸

SF is primarily composed by amino acids with poorly chemically reactive residues. To date, Glycine (Gly), Alanine (Ala) and Serine (Ser) account to more than 80 mol% of the total composition. Tyrosine (Tyr) and Tryptophan (Tryp) aromatic residues account to less than 5 mol%.⁹

Transparent SF films can be easily prepared by drying SF aqueous solution over smooth or patterned surfaces.^{10,11} For instance, SF aqueous solution can be obtained by dissolving degummed native SF fibers in concentrated solution of chaotropic salts such as LiBr, CaCl₂/ethanol/water,^{12,13} LiSCN¹⁴ or ionic liquids.¹⁵ In general, pristine SF films are brittle and water soluble with low thermal stability. In addressing these issues, insoluble SF films with improved mechanical and thermal properties have been achieved by subjecting the pristine SF films to post-treatments such as: i) physical stretching¹⁶ ii) water vapor annealing¹⁷ iii) immersion in polar organic solvents,¹⁸ iv) ultraviolet radiation.¹⁹ In addition, the incorporation of organic and inorganic components such as plasticizers blends,^{20,21} layered clays,²² reinforcing fibers,²³ cross-linkers,^{24,25} and nanoparticles^{8,26,27} have been evaluated on the development of strategies to achieve transparent SF hybrid films with ameliorated chemophysical properties. Beyond that, several strategies have been devoted to introduce functional groups to SF seeking to develop new pathways, which in specific (bio) molecules can be further immobilized (e.g. antibodies, enzymes, etc.). Such strategies range since simple doping to sophisticated multi-step chemical modifications of aromatic residues. For example, many attempts have been made to modify Tyr residues such as enzyme-catalyzed with tyrosinase,²⁸ cyanuric chloride-activated coupling,^{9,29} or sulfonation with chlorosulfonic acids.³⁰ For instance, Kaplan's group has successfully modified Tyr residues with sulfonate moiety with diazonium coupling reaction enabling the further functionalization with aniline derivatives having amine, ketone, carboxylic acid or alkyl functional groups.³¹ Nevertheless, those strategies only

embrace limited functionalization in light of the restricted amount of Tyr residues present in SF backbone.

The sol-gel route is a versatile strategy to prepare hybrid materials with wealthy of functional groups. Broadly speaking, the sol-gel method combine inorganic and organic components under low temperature by hydrolytic polymerization of metal or nonmetal alkoxide precursor $M(OR)_n$ ($M= Si, Ti, Zr, etc.$). Presently, a myriad of sol-gel precursors displaying reactive functional groups are available. Recently, the sol-gel route has been used to fabricate a transparent and mechanically robust SF hybrid films by the incorporation of 3-aminopropyltrimethoxysilane, a silane alkoxide precursor containing an amine functional group.³²

In an effort to extend the fabrication of functional SF hybrids, we investigated the preparation of flexible and transparent free-standing hybrids of silk fibroin and 3-glycidyloxypropyltrimethoxysilane (GPTMS). GTPMS is an organically modified alkoxide silane, which has a terminal epoxy group. Besides the homogeneous incorporation of inorganic silica network into the SF polymeric chain, epoxy groups lead to polyethylene oxide (PEO) chains via photo, thermal and upon alkaline/acid catalytic polymerization. In addition, the GPTMS epoxy-ring can be used as coupling agent to covalently bind organic and inorganic networks. Due to such peculiarities, hybrids derived of GPTMS show exceptional optical properties for the fabrication of photonic devices such as planar waveguides,³³⁻³⁶ optical limiters^{37,38} and nonlinear optical materials.^{39,40}

In the present contribution, we have studied the preparation of high transparent (~90 %) and flexible free-standing films with high content of GPTMS (up to 70 wt%). Benefiting from this, we also investigated the fabrication of functional luminescent lanthanide films by doping transparent free-standing hybrids of SF and GPTMS with $YVO_4:Eu^{3+}$ nanoparticles on the pursuit of evaluate their potential use of in optical applications. It has been extensively demonstrated that sol-gel process is a feasible approach to tailor hybrid films with trapped Eu^{3+} fluorescent nanoparticles to produce photonic materials like fiber and planar devices. The well-known advantages of using narrow line-like emission from long-lived Eu^{3+} excited states have been recently exploited by some of us to design an optical sensor of hepatitis C.⁴¹ The detection was performed by evaluating the molecular recognition of antibody-antigenic peptide through changes in the luminescent properties of $YVO_4:Eu^{3+}$ nanoparticles incorporated on layer-by-layer SF films. Noteworthy, luminescent lanthanide nanoparticles are kinetically stable to acid/base and either solvolytic conditions and allow us to design optically active and functional films that fulfill the requirements of transparency and stability highly desired in photonic applications.

5.1. Experimental section

5.1.1. Materials

Silk cocoons produced by *Bombyx mori* silkworms were supplied by Bratac, Fiação de Seda S.A. (Bastos, Brazil). Na_2CO_3 , Na_2O , NaVO_3 , $\text{CaCl}_2 \cdot 2\text{H}_2\text{O}$, Ethanol P.A and 3-glycidyloxypropyltrimethoxysilane, and tetrazolium 3-(4,5-dimethylthiazol-2-yl)-2,5-diphenyl tetrazolium bromide (MTT) were purchased from Sigma-Aldrich. Y_2O_3 99% and Eu_2O_3 99% were purchased from Lumintech. Bovine serum, Penicillin and Streptomycin were purchased from Vitrocell

5.1.2. Preparation of aqueous SF solution

Silk fibroin was extracted from silk cocoons. The method was based on previous report.⁸ Five grams of silk cocoon pieces were degummed with 2 L of 0.02 M Na_2CO_3 solution at 100 °C for 30 minutes. The SF fibers were washed thoroughly with distilled water and allowed to dry at 40 °C. Afterwards, dried SF fibers were dissolved in ternary system solvent, $\text{CaCl}_2 \cdot \text{H}_2\text{O} : \text{Ethanol}$ with 1:8:2 molar ratio pre-heated at 80 °C for 1 h. The concentration of SF fibers was 250 g L⁻¹. The resulting viscous solution was dialyzed in Mili-Q water in a proportion 1:80 (v/v) for 6 times along 48 h. The purification of dialyzed SF aqueous solution was proceeded by centrifugation at 20,000 rpm for 20 min to remove non-dissolved impurities. An aqueous SF solution with final concentration of 3.7 wt% was achieved and stored at 4° C before use.

5.1.3. Preparation of free-standing silk fibroin/3-glycidyloxypropyltrimethoxysilane hybrid films

SF films were obtained by casting 3 mL of pristine 3.7 wt% SF solution in polystyrene dishes ($\varnothing = 30$ mm) and allowing dry at room temperature for 48 hours. The silk fibroin/3-glycidyloxypropyl trimethoxysilane (SFGPTMS) hybrid films were fabricated by introduction of 3 mL of 3.7 wt% aqueous SF solution followed by the addition of pure GPTMS. The mixture was slightly stirred with the help of a glass rod during 5 min and transferred to polystyrene dishes ($\varnothing = 30$ mm). The films were allowed to dry at 40 °C during 48 hours. The samples were named as SFGPTMS_x% with x= 10-70 % for different GPTMS mass percentage content.

5.1.4. Preparation of $\text{YVO}_4 : \text{Eu}^{3+}$ nanoparticles

Luminescent $\text{YVO}_4 : \text{Eu}^{3+}$ nanoparticles were prepared according with previous report.⁴¹ Sodium orthovanadate (Na_3VO_4) was prepared by the reaction of sodium oxide (Na_2O) with sodium metavanadate (NaVO_3) at 700 °C under a heating rate of 14 °C min⁻¹ in a nitrogen atmosphere.⁴² The mixture was kept in this temperature for additional 4 hours and then cooled to 200 °C. After

10 h, the mixture was left to cool down to room temperature and the resulting white powder, Na_3VO_4 , was dissolved in water for use in the next step.

Aqueous solutions of $\text{Y}(\text{NO}_3)_3$ 1 mol L^{-1} (9 mL) and $\text{Eu}(\text{NO}_3)_3$ 1 mol L^{-1} (1 mL) were mixed with 5 mL of sodium citrate solution 2 mol L^{-1} under vigorous stirring at room temperature. A white milky suspension was immediately formed because of precipitation of lanthanide citrate. Afterwards, 50 mL of an aqueous solution of Na_3VO_4 0.2 mol L^{-1} was added. The mixture became transparent and was stirred for 45 min at 60°C leading to the formation of nanoparticles of $\text{YVO}_4:\text{Eu}^{3+}$ stabilized by citrate ions. Subsequently the solution was cooled and dialyzed against Milli-Q water for 72 h.⁴³

5.1.5. Preparation of luminescent silk fibroin/3-glycidyloxypropyl trimethoxysilane hybrid films

Luminescent SFGPTMS hybrid film was fabricated by mixing 3 mL of aqueous solution of SF 3.7 wt% with 26 μL of GPTMS during 5 min. The final composition is similar to that described for SFGPTMS20% sample. Afterwards, an aqueous suspension of $\text{YVO}_4:\text{Eu}^{3+}$ nanoparticles was added to the mixture under slight stirring. The mixture was then transferred to polystyrene dishes ($\varnothing = 30 \text{ mm}$). The content of $\text{YVO}_4:\text{Eu}^{3+}$ nanoparticles comprises 5 wt% of the overall composition. The mixture was placed in an oven set at 40°C and allowed to dry for 48 hours.

5.1.6. Cytotoxicity assay

To perform the cytotoxicity assay, it is necessary a previous preparation of the films. Pristine SF and SFGPTMS hybrid films were weighed, minced, immersed in cell culture Dulbeccos Modified Eagle's Medium (DMEM-Vitrocell) supplemented with 10% fetal bovine serum (FBS) and antibiotics (Penicillin and Streptomycin) and subjected to intense mechanical agitation. After this step, all samples were removed and the resultant medium was filtered and placed in cell culture plate wells (96 wells) containing osteoblasts derived from calvaria of neonatal rats (cell lineage OSTE0-1) in density 15×10^3 cells/well. The plates were kept in cell culture incubator (Panasonic- CO_2 incubator MOC-19 AIC-UV) at 37°C , humidified atmosphere containing 5% CO_2 and 95% air atmosphere for 48 hours. After that period, cell viability was determined by a colorimetric method MTT (tetrazolium 3-(4,5-dimethylthiazol-2-yl)-2,5-diphenyl tetrazolium bromide). Thus, culture medium was removed from the wells, and they were washed with phosphate buffered saline (1X PBS). Aliquots of 100 μL of MTT was added to each well and the cells were kept in culture conditions for 4 hours. After this period it was added 200 μL of isopropyl alcohol and the content of the wells was mechanically homogenised until complete solubilization of the formazan. The optical density values (OD) were obtained using a

spectrophotometer (Polaris-CELER) at 570 nm. The resultant measurement were converted into percentages of cell viability relative to fibroin membranes and subjected to variance analysis (ANOVA-ONE WAY), with 5% level of significance. Cytotoxic activity was considered if the values of the pristine SF or SFGPTMS hybrid samples were significantly lower than control.

5.1.7. Instrumentation

Transmittance spectra of the films were performed in a PelkinElmer LAMBDA 1050 UV/Vis Spectrophotometer in the range of 200 to 800 nm. Refractive index (n) and thickness (w) of films were measured in a Metricon prism coupler model 2010/M using a prism with n range of 1.20 to 2.02 and a laser of 543 nm as light source.

Scanning Electron Microscopy (SEM) images were conducted in a field emission JEOL equipment model 7500F. For SEM analysis, the samples were placed and dried at 37 °C directly on silicon substrates and copper grids, respectively. The dried samples were directly subjected to analysis without any treatment.

The surface of the obtained films was evaluated by taking atomic force microscopy (AFM) images with an Agilent 5500 microscope in the intermittent contact mode under ambient conditions, and using conventional silicon multipurpose cantilevers. All images were rendered using Gwyddion AFM analysis software.

Fourier transform infrared spectroscopy (FT-IR) analysis was performed in a Spectrum 2000 FT-IR Perkin Elmer spectrophotometer, equipped with a multiple reflection, horizontal MIRacle attenuated total reflectance (ATR) attachment (ZnSe crystal). The spectra were collected over the range of 4000 - 700 cm^{-1} with an accumulation of 128 scans and resolution of 4 cm^{-1} . Raman spectra were recorded using a Raman Horiba Jobin Yvon 118 model LabRAM HR 800 spectrometer, operating with He-Ne 632.81 nm laser through a 100x objective lens and dispersed by a diffraction grating (600 lines mm^{-1}) onto a cooled charge-coupled device (CCD) detector.

The solid state Magic Angle Spinning Nuclear Magnetic Resonance of ^{13}C - ^1H (^{13}C - ^1H MAS-NMR) spectra were recorded using a Varian INOVA 500 spectrometer equipped with a 4 mm, T3-MAS probe. The experiment was carried out at spinning rate of 5 kHz, using an excitation pulse length of 3.2 μs under continuous-wave (CW) ^1H decoupling, and a 5 s delay between repetitions. Chemical shifts were reported relative to tetramethylsilane TMS referencing standard.

X-Ray diffractograms were registered in a Rigaku Rint 2000, under the following experimental conditions: 40 kV, 120 mA, $4^\circ \leq 2\theta \leq 70^\circ$, step scan of 0.005° 2θ , $\lambda\text{Cu-}\alpha$ monochromatized by a graphite crystal, divergence slit= 1/2 mm, reception slit= 0.3 mm.

Small angle X-ray diffraction (SAXS) measurements were performed at the Brazilian Synchrotron Light Laboratory (LNLS). The incident X-ray monochromatic beam was monitored by means of a photomultiplier and detected on a Pilatus detector (8x8 binning). The SAXS chamber parasitic scattering was also registered (with bias and dark-noise subtraction) and subtracted from the sample pattern after sample attenuation correction.

Thermogravimetric analysis was performed on a Thermoanalyzer TG/DTA simultaneous SDT 2960 from TA Instruments, under the following conditions: alumina crucible, synthetic air (100 mL min⁻¹), and heating at 10 °C min⁻¹, from 30 to 600 °C. Differential scanning calorimetry (DSC) was performed on about 5 mg of material in a sealed crucible using a TA2910 calorimeter (TA instruments) under flushing nitrogen (70 ml min⁻¹) in the range 0-360 °C and heating rate of 10 K·min⁻¹.

The excitation and emission spectra were recorded in Horiba Jobin Yvon Fluorolog spectrofluorimeter model FL3-222, equipped with a Hamamatsu R928 photomultiplier and Xe lamp (450 W) using front face mode with resolution of 0.5 nm.

5.2. Results and discussion

Pristine SF and SFGPTMS hybrids films with different content of GPTMS were obtained by peeling the dried films off from the plastic dishes. The thickness of the free-standing films was very similar for all compositions with standard deviation lower than 5% among the samples. Hybrid SFGPTMS films could reversibly bend in acute angles even at the lowest content of GPTMS (i.e. 10 wt%). The hybrid films were highly transparent in the visible region (up to 90 %) as shown in Figure 46

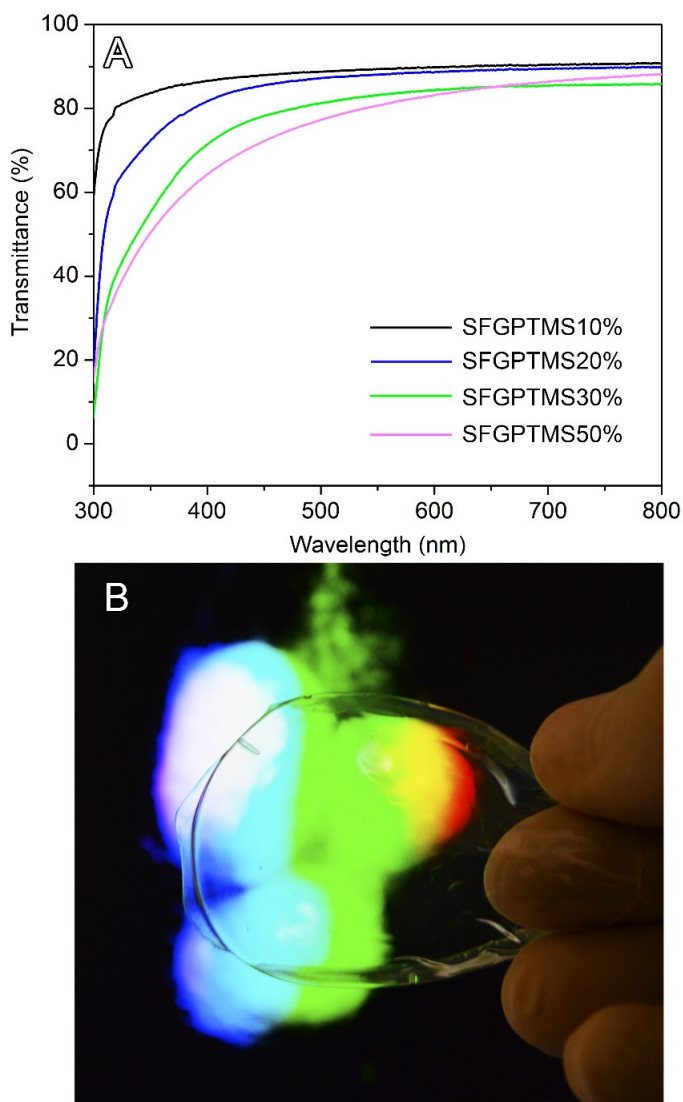


Figure 46. (A) Transmittance of SFGPTMS hybrid films with different content of GPTMS (10 - 50 wt%) in the visible region. (B) Photography of a transparent and flexible SFGPTMS hybrid film.

As an important remark, the refractive index of hybrid films decreases from 1.5493 to 1.5254 as a function of the increase of GPTMS content as shown in Figure 47. A quasi-linear relationship (with negative slope) between the refractive index and GPTMS content in the hybrid films was evidenced, demonstrating that the optical properties are strictly dependent on the weight proportion of SF and GPTMS.

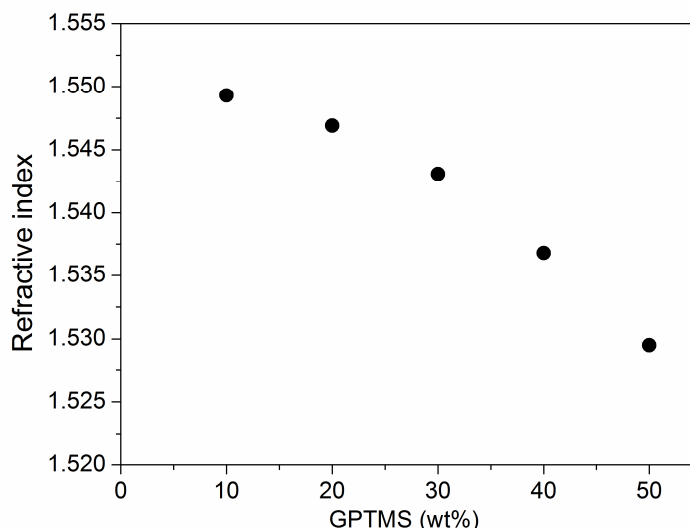


Figure 47. Refractive index of the films as function of GPTMS content.

Interestingly, we observe that the transmittance of SFGPTMS hybrid films progressively decreased to a minimum of 79 % at 550 nm as the content of GTPMS was increased to 50 wt%. Possibly, this behavior can be associated with light scattering process.

In order to get more insights about the influence of GPTMS on the surface morphology and optical properties, we conducted SEM and AFM analysis of SFGPTMS hybrid and pristine SF films depicted in Figure 48 and Figure 49, respectively.

The high magnification SEM images show a granular-like surface for SFGPTMS hybrid films with GPTMS content higher than 30 wt%. On the other hand, the SEM images of SFGPTMS 10% and pristine SF film shown in Figure 48 do not display such morphology. Interestingly, the increase of GPTMS content in the SFGPTMS hybrid films makes their surface smoother and more regular. This can be confirmed with the decrease of the roughness of the surface of investigated films strongly related to the height values of AFM images displayed in Figure 49 decreasing from 110 nm to 60 nm for pristine SF and SFGPTMS50%, respectively. The roughness (R_q) of the investigated SFGPTMS hybrid extracted from the AFM height images confirms that a hybrid surface became smoother with increase of GPTMS content. The R_q changes from 15.7 ± 3.3 nm for pristine SF to 6.9 ± 1.0 nm for SFGPTMS50%.

The roughness values of investigated SFGPTMS hybrid are in agreement with the changes in high of AFM height images. Moreover, the contrast of the AFM phase images change with increase of the GPTMS, being only 22° for pristine SF and 83° for SFGPTMS50%, leading to very regular surface. We can distinguish two different phase one corresponding to SF rich phase and the other corresponding to GPTMS rich phase indicating that hybrid surface was composed on two different materials. Phase AFM images of SFGPTMS hybrid films clearly revealed the

presence of domain boundaries with remarkably differences in contrast level even if only 10 % GPTMS was added, implying that the hybrid surface have different composition

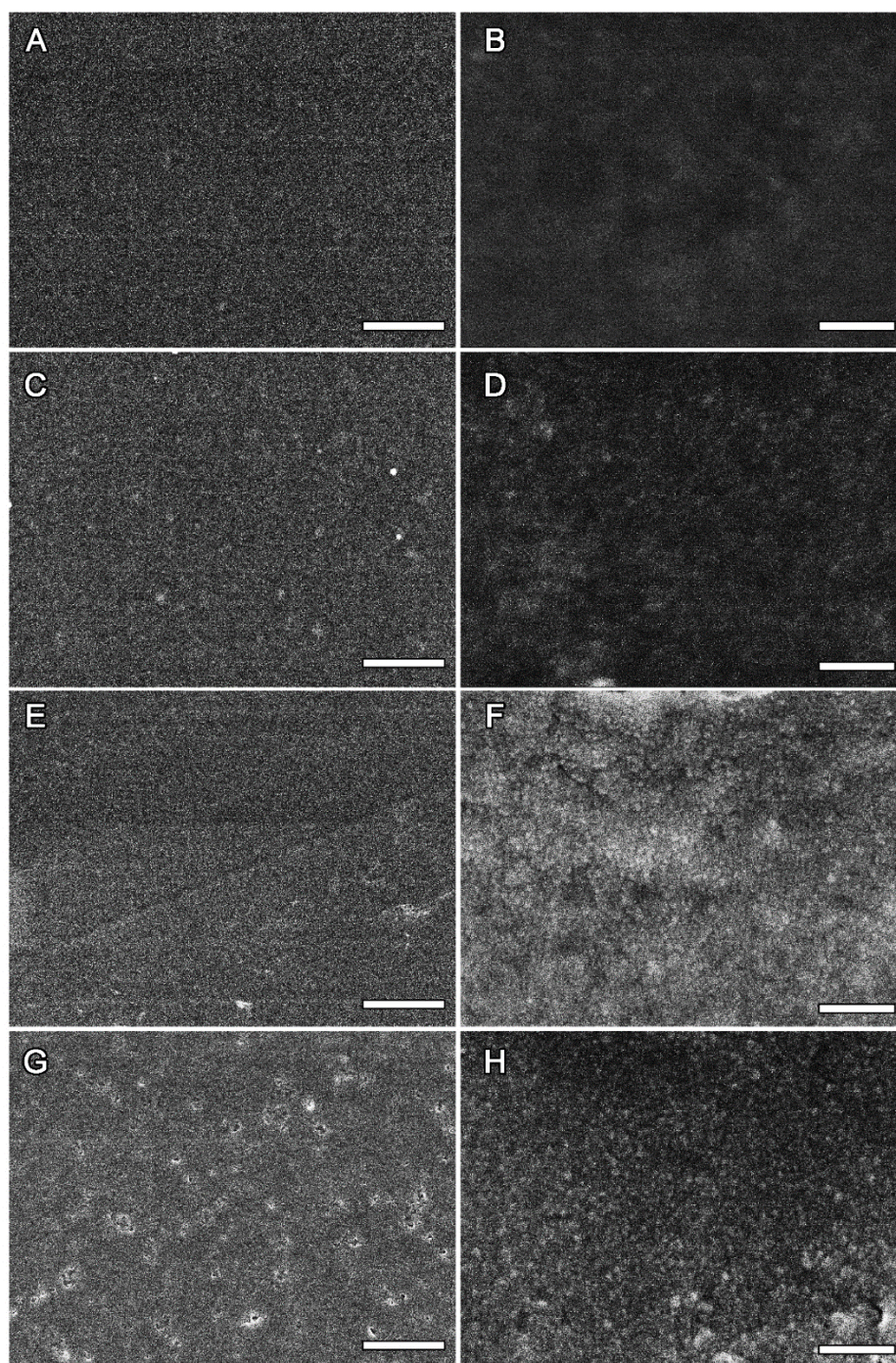


Figure 48. SEM images A, B) Pristine SF; C, D) SFGPTMS 10%; E, F) SFGPTMS 30% and; G, H) SFGPTMS 50%. The scale bar for A,C,E,G is 1 μm and for B, D, F, H is 100 nm.

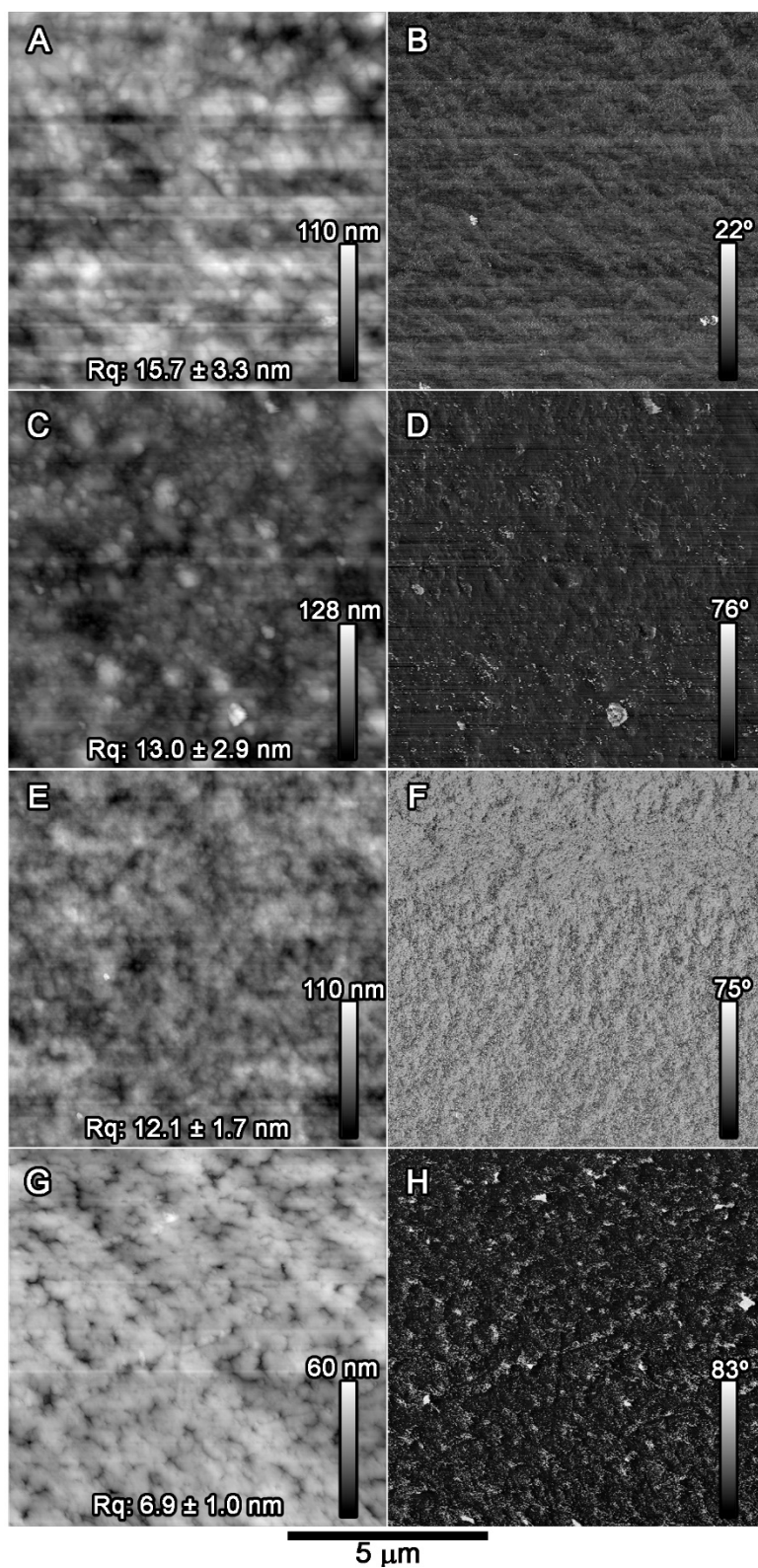


Figure 49. AFM height images of A) Pristine SF, C) SFGPTMS10%, E) SFGPTMS 30%, and G) SFGPTMS50%. AFM phase images of B) Pristine SF, D) SFGPTMS 10%, F) SFGPTMS 30%, and H) SFGPTMS 50%.

A more detailed investigation on the SF and GPTMS phases can be achieved using vibrational spectroscopy. Particularly, FTIR is a useful tool to study the conformational changes of SF. Amide I ($1700\text{-}1600\text{ cm}^{-1}$) and amide II ($1600\text{-}1500\text{ cm}^{-1}$) vibrational modes provide essential information about the secondary structures of the protein backbone.

Figure 50 shows FTIR spectra of pristine SF and SFGPTMS hybrid films.

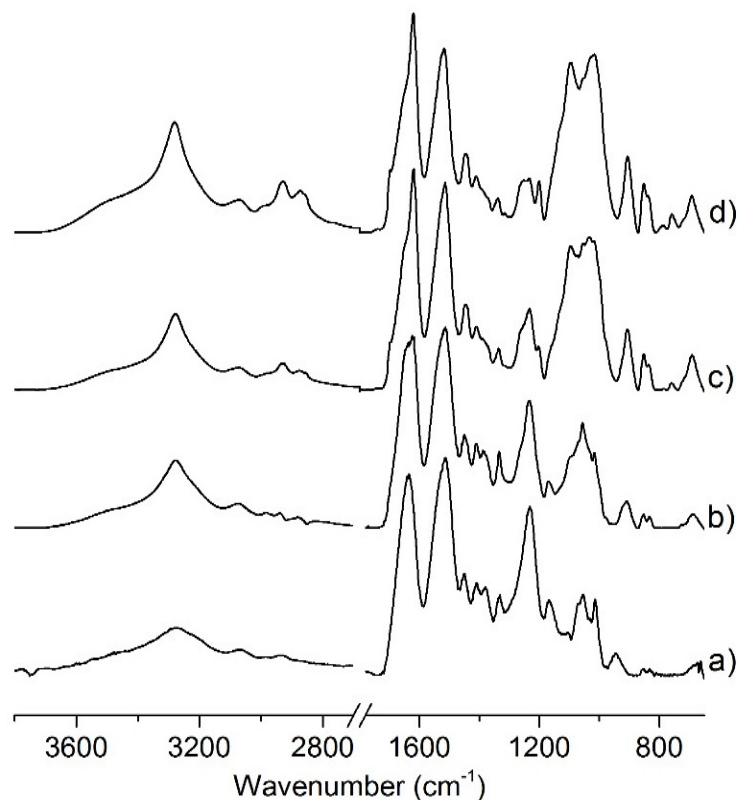


Figure 50. FTIR spectra of a) Pristine SF, b) SFGPTMS10%, c) SFGPTMS30%, d) SFGPTMS50% and e) SFGPTMS70% films.

The spectrum for pristine SF film was assigned to the Silk I conformation as evidenced by the position and intensity of the (that is, C=O stretching vibrations), amide II (C–N stretching vibrations), and amide III (N–H deformation vibrations) bands at 1655 cm^{-1} , 1540 cm^{-1} and 1235 cm^{-1} , respectively. Indeed, characteristic Silk I vibrational modes can be distinguished by the weak bands at 1409 cm^{-1} for $C_{\alpha}H_2$ stretching, 1387 cm^{-1} and 1330 cm^{-1} for CH_3 stretching of alanine residue.⁴⁴ On the other hand, Silk II is the predominant conformation after the addition of GPTMS.

The typical broad band of amide III region at 1230 cm^{-1} for pristine SF film is assigned to Silk I structure. The relative intensity of this band is significantly reduced according with the GPTMS content. At the time, a prevailing band at 1256 cm^{-1} is found in the amide III region which is assigned to epoxy ring breathing vibrational mode of GPTMS molecule coupled with β -sheet

conformation.^{44,45} Additionally, there is a relative increase of the band at 1054 cm^{-1} assigned to the overlap between Si-O-Si asymmetric stretching modes and skeletal C-C stretching mode of Silk II.^{45,46}

The bands at 1106 cm^{-1} and shoulder at 1130 cm^{-1} are assigned to $\nu_a(\text{Si-O-Si})$. The weak bands at 905 cm^{-1} and 849 cm^{-1} indicate the hydrolysis of methoxy groups with the formation of Si-OH groups and consequently an incomplete condensation of Si-O-Si net.⁴⁶

The role of silanol groups are the additional hydrogen interactions with the residues polar groups of SF backbone chain. The main N-H stretching absorption appears at 3280 cm^{-1} (amide A region). The band gets sharp and shifts as a function of the GPTMS content. In addition, a shoulder band centered at 3265 cm^{-1} raises after the introduction of GPTMS which is associated with -O-H stretching mode. Indeed, the amide A region shifts $\sim 12\text{ cm}^{-1}$ to higher wavenumbers for SFGPTMS50% sample which may be due to hydrogen interactions with GPTMS molecules, i.e. interactions between N-H bonds of protein backbone chain with Si-OH polar groups or oxygen from epoxy ring. The bands at 2936 and 2876 cm^{-1} can be clearly distinguished in the SFGPTMS hybrids being associated with CH_2 asymmetric and symmetric stretching modes of glycidoxylpropyl backbone of GPTMS molecule, respectively.⁴⁵

To complement the FTIR results, Raman spectroscopy was also investigated. The Raman spectra of pristine SF and SFGPTMS hybrids are shown in Figure 51. The Raman spectrum recorded for Pristine SF shows typical bands of Silk I conformation.⁴⁷⁻⁵⁰ The band at 1661 cm^{-1} is assigned to amide I vibration band of peptidic chain of SF.⁴⁸ SF and SFGPTMS films show almost the same bands in the amide I region. However, the amide I band undergoes a slight shift to 1664 cm^{-1} and narrowing in SFGPTMS samples which is consistent with β -sheet structures produced from the transition of Silk I to Silk II conformation after the addition of GPTMS.⁴⁷⁻⁵⁰

The band at 1255 cm^{-1} and a component at 1236 cm^{-1} observed in pristine SF film are related to amide III from Silk I. In addition, bands at 1100 cm^{-1} and a broad band at 938 cm^{-1} are assigned to C-C and C-N stretching, respectively, usually associated with some α -helices content from Silk I conformation.⁵⁰ The addition of GPTMS caused meaningful changes in the amide III region. In SFGPTMS10% a shoulder arises at 1230 cm^{-1} which is also observed for SF films whose crystallization to Silk II conformation was induced with methanol.⁴⁹

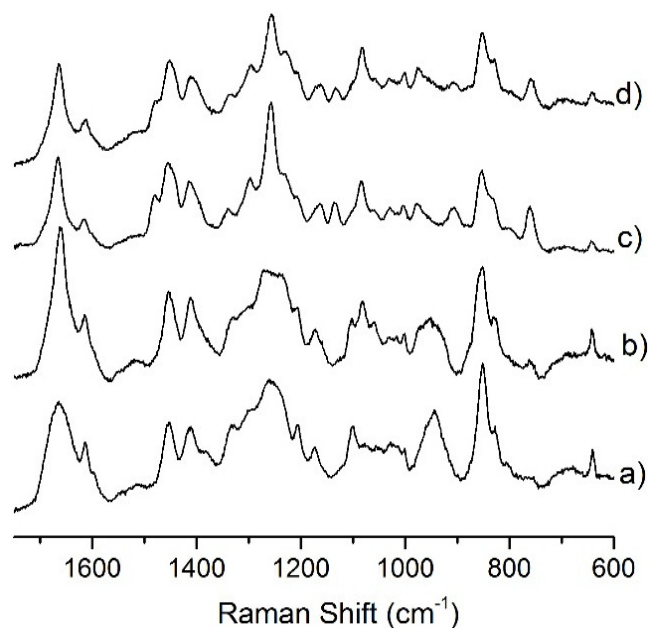


Figure 51. Raman spectra of the films in different GPTMS content: a) Pristine SF film b) SFGPTMS10% c) SFGPTMS30%, and d) SFGPTMS50%.

The modification of SF films with GPTMS is also confirmed by the presence of bands related to glycidoxypropyl backbone observed at 1030 cm^{-1} and 1133 cm^{-1} . The weak band at 1030 cm^{-1} is assigned to C-C stretch and C-O stretch of GPTMS propyl chain while the band at 1133 cm^{-1} is assigned to C-C tors, C-H (CH_2) rock and C-H rock vibration of glycidoxypropyl chain backbone⁵¹ coupled to the Si-O-Si stretching mode.⁵² Additionally, the Raman spectra of SFGPTMS films show a new component arises at 1165 cm^{-1} assigned to CH_2 rock vibration mode of propyl chain from GPTMS molecule. A strong band at 1256 cm^{-1} is observed for SFGPTMS hybrid in all compositions evaluated and assigned to C-H rock and C-C stretch vibration from epoxy ring of the GPTMS molecule.⁴⁵ An additional band centered at 763 cm^{-1} also arises as a function of the GPTMS concentration being assigned to symmetric stretching of aliphatic ether linkage.⁴⁵

The Raman spectra of SFGPTMS films also show that the condensation step was incomplete which can be assessed by the strong and broad band at 1080 cm^{-1} and 976 cm^{-1} regarding Si-O from siloxane bonds as well as from Si-OH stretching modes respectively.⁵³ It is important to note that it was not possible to observe any extra bonds between the siloxane groups and the SF protein from vibrational spectra of SFGTMS films.

We also evaluated the by ^{13}C solid state NMR spectroscopy of pristine SF and SFGPTMS hybrid films. In general, the chemical shifts of β -carbon ($\text{C}\beta$) of alanine are utilized to determine the conformation of the regenerated SF due to the variation of electron density generated owing to

twist angle of the peptides. This assumption has been shown by ^{13}C solid state NMR where the $\text{C}\beta$ carbon has increase of shielding in the following order: β -sheet < random coil < α -helix.⁵⁴ The antiparallel β -sheet (Silk II conformation) and the α -helix form of SF are well characterized based on conformation-dependence of the $\text{C}\beta$ chemical shift of Gly, Ala, and Ser residues. Concerning GPTMS component, the chemical environment of carbon nuclei observed by NMR is an important tool and can be used as a structural probe for observation of the hydrolysis/condensation process of silicon alkoxide and eventual organic network formation through polymerization of epoxy groups.

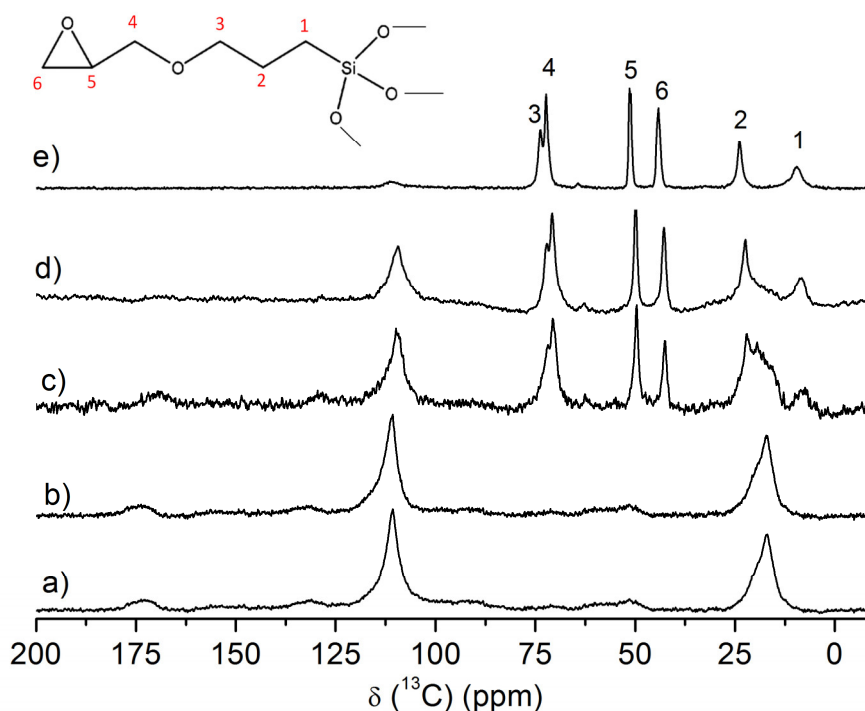


Figure 52. ^{13}C - ^1H -MAS NMR spectra of the films in different GPTMS content: a) Pristine SF film b) SFGPTMS10%, c) SFGPTMS30%, d) SFGPTMS50%, and, e) GPTMS powder. It is important to clarify that GPTMS did not result in free-standing films itself. The item e) refers to the resulting powder obtained from hydrolysis/condensation of GPTMS undertaken in same experimental conditions utilized in the protocol of fabrication of SFGPTMS hybrids, except that SF was not introduced in the reaction mixture.

Figure 52 shows the ^{13}C - ^1H MAS NMR spectra of the Pristine SF, GPTMS and SFGPTMS films prepared with different ratio. The spectrum of GPTMS shows six resonance lines and their assignments were made on the basis of previous works⁵⁵⁻⁵⁷ and identified in the spectrum of SFGPTMS70%, SFGPTMS50% and SFGPTMS30% films. They are hardly observed in SFGPTMS10%. The peaks observed at 42.6 and 49.7 ppm (positions 6 and 5, respectively), corresponding to epoxy groups, appear with the same intensity for all the hybrid films, indicating

that there was no polymerization process. These results are in agreement with vibrational spectroscopy data presented, i.e. unreacted epoxy ring from GPTMS molecule. The peak at 7.8 ppm, is referred to the $-\text{CH}_2-\text{SiO}_{3/3}$ groups (position 1).⁵⁷ The peak at 50 ppm is associated to $-\text{O}-\text{CH}_3$ (position 7) groups and was hardly identified in the spectra of SFGPTMS hybrids, which in turn is an indicative that siloxane groups were mostly hydrolyzed.⁵⁵⁻⁵⁷

Although we did not observe significant changes in the intensities and half height width of the peaks, we observed an increase of magnetic shielding for all the peaks with increase of SF, suggesting the interaction between SF and GPTMS during formation of the SFGPTMS hybrid films. As already mentioned, the chemical shift of $\text{C}\beta$ of alanine is utilized to determine the conformation of SF. The $\text{C}\beta$ of alanine was observed as one asymmetric and broad peak in the frequency range 20 to 0 ppm, showing contribution of two convoluted resonance lines, at 20.2 ppm and 17.1 ppm. This suggests that the pristine SF film was formed by β -sheets (Silk II) and random coil conformations, respectively.⁵⁸⁻⁶⁰ Lines of alanine $\text{C}\beta$ appear with decreasing intensity for the line at 17.7 ppm and increasing intensity of the line at 20.2 ppm as a function of the GPTMS content from 10 to 50 wt%. Clearly, the addition of GPTMS favors the formation of hybrid films with Silk II conformation whereas pristine SF exhibits random conformation.

The aforementioned results emphasize that most epoxy ring in SFGPTMS hybrids are available to be further modified. The epoxy groups provide a new pathway to chemically modify the SF films. Through ring-opening reactions it is possible to obtain a cross-linked hybrid matrix, which in turn can be conducted by nucleophile substitution under alkaline medium or by exposition to ultraviolet light.

X-ray diffraction (XRD) patterns are shown in Figure 53. Considering the as-cast pristine SF film, a weak diffraction peak at $2\theta=11.8^\circ$ and a broad halo peak at 22.5° corresponding to 7.5 and 3.9 Å are observed. Pristine SF film displays mostly amorphous or Silk I conformation which is in accordance with previous studies.^{16,61}

After the addition of GPTMS the d -spacing of 3.9 Å disappear and the intensity of diffraction became gradually higher and sharper at $2\theta=12^\circ$ (weak), 20.5° (moderate) and 24.5° (weak), corresponding to 7.4, 4.3 and 3.6 Å. These peaks clearly indicated that Silk I conformation presented in pristine SF films was mostly converted to crystalline Silk II conformation¹⁸ upon the addition of a minimum of 20 wt% of GPTMS. The d -spacing at 4.3 Å ($2\theta=20.5^\circ$) is attributed to intra-hydrogen-bonded β -sheet spacing.¹⁶ Beyond 30 wt% of GPTMS a new peak was observed at 6.3° and became predominant together with the peak at 20.5° .

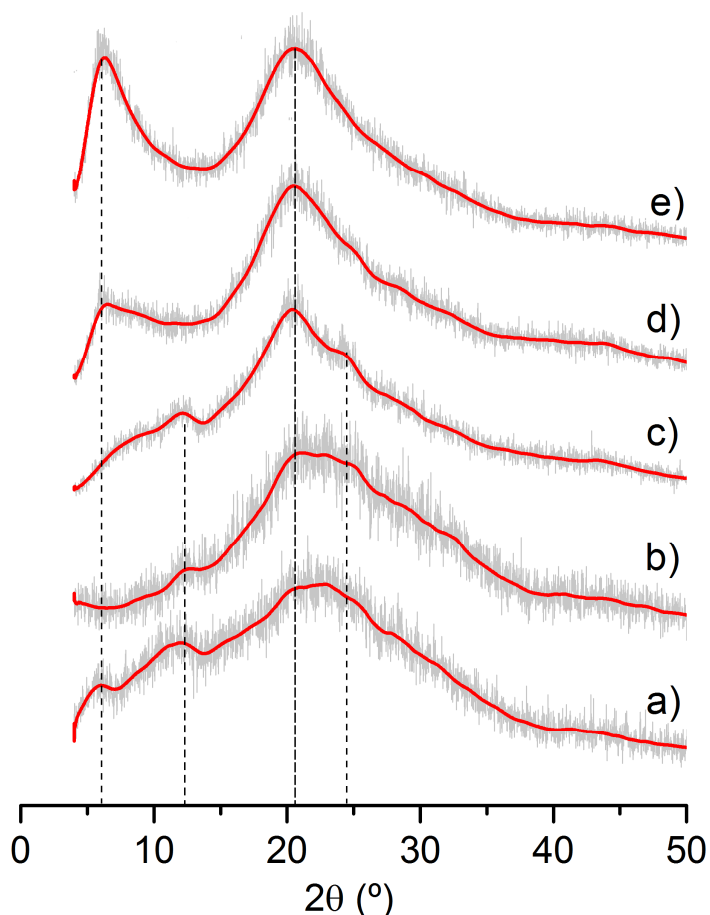


Figure 53. X-ray diffraction patterns of a) Pristine SF film, b) SFGPTMS 10% c) SFGPTMS20%, d)SFGPTMS 30%, and e) SFGPTMS50%.

The peak emerging at 6.3° in SFGPTMS hybrids have been attributed to interparticle scattering interference⁶² This peak indicates highly non-periodic fluctuation of the electronic density in the SFGPTMS hybrid films which is eventually observed due to aggregation of silica at high silylating agent concentration⁶² Once a critical concentration of GPTMS is achieved, it is reasonable to expect that the connection between Si-O- sites would overcome the steric hindrance imposed by SF polymeric chain and thus promote the formation of siloxane-rich domains as result of the hydrolysis/condensation reactions. The average inter-domains distance is estimated to be 13-14 Å and support the development of granular surface observed in SEM images and the enhancement of height uniformity among the domain boundaries observed in AFM data.

SAXS measurements of the SFGPTMS hybrid films were performed to confirm morphological heterogeneities. The SAXS curves are displayed in Figure 54 and compare Pristine SF and after the addition of GPTMS. These curves show differences in their shapes, Pristine SF, for instance, presents a wide linear region at $q < 1.0 \text{ nm}^{-1}$ whereas SF with GPTMS added (between 10 and 40%) presents a marked broad peak in this region that shifts to low q -range. In the present system,

this peak is associated to presence of interparticle correlations⁶³ induced upon addition of GPTMS. With the increase of GPTMS content (above 30%), this correlation is lost and the curves present a non-linear shape that remains constant until 50%. These results confirm that hybrid surface presents heterogeneities and is composed of two different phases that correspond to SF rich phase and GPTMS rich phase, corroborating with morphological studies observed by SEM and AFM.

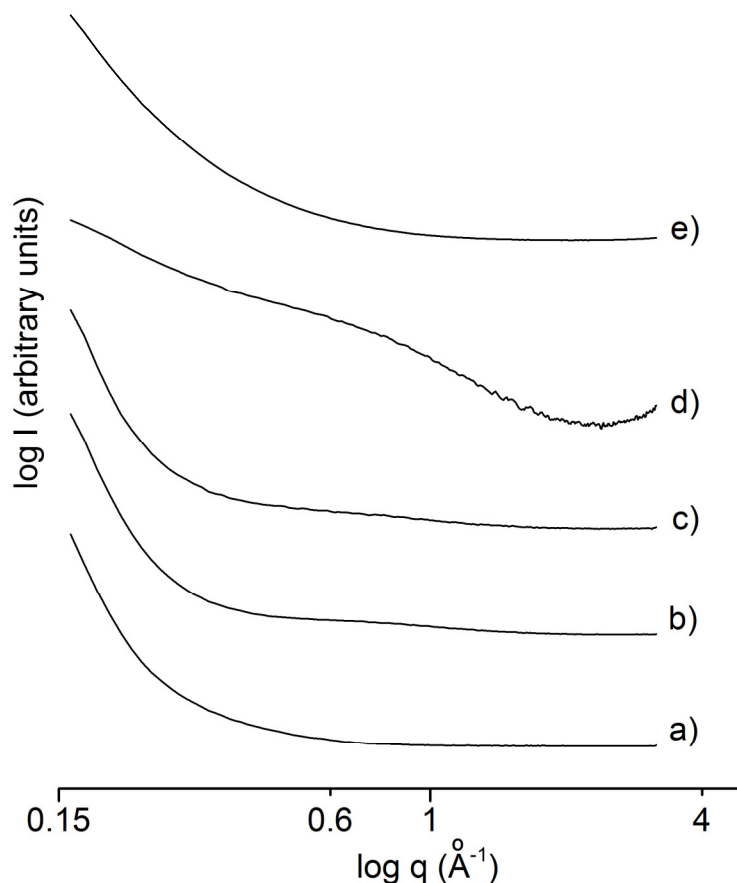


Figure 54. SAXS spectra of a) Pristine SF film, b) SFGPTMS 10% c) SFGPTMS20%, d) SFGPTMS 30%, and e) SFGPTMS50%.

Examining the region at $q > 1.0 \text{ nm}^{-1}$, we can observe that while Pristine SF shows an extended flat region, SFGPTMS hybrid film presents this same behavior up to 20% of GPTMS added. From 30 wt% to 50 wt% of GPTMS content, the curves in this region present a monotonic increase in intensity with the tendency to form a peak which corresponds to $2\theta = 6.3^\circ$ observed in XRD patterns and attributed to interparticle scattering interference from formation of siloxane-rich domains as result of the hydrolysis/condensation, as discussed previously. These results show the good consistency with XRD results.

Noteworthy vibrational, NMR spectroscopies as well as diffractometry results confirm that SFGPTMS hybrid films present high content of Silk II conformation. On the course of the drying

GPTMS could be addressed to the increase in the number of micro-sized aggregates that scatters the light.

Most significantly, the hybrid films deliver flexible transparent films rich in epoxy (organic) and silanol (inorganic, e.g. from incomplete condensation of silica network) groups available for further functionalization. Obviously, the number of those reactive functional groups depends of the content of GPTMS.

The thermal stability of the films has been investigated by thermogravimetric analyses (TGA) and differential scanning analysis (DSC). Pristine SF film has a well reported thermogravimetric curve⁶⁴ which can be divided in three subsequent regions, characterized by evident different mass loss rates and phenomena. Region I (35-40 °C to 117-170 °C) is related to the water loss. Region II (170 – 240 °C) and the region III (> 240 °C) provided evidence of SF degradation. Above 200 °C, side chain groups of aminoacid residues of silk backbone start to degrade producing small weight gas molecules such as CO, CO₂, NH₃.⁶⁵ At this temperature range, epoxy groups undertake thermal decomposition through homolytic scission of chemical bonds and simultaneous dehydration of water molecules from oxypropylene.⁶⁶ At higher temperatures, degradation proceeds faster leading to chain fission and network breakdown and, thereafter complete burning.^{65,66}

As shown in Figure 56, the mass loss in the region I gradually decreases with the increase of the GPTMS content. The mass loss was 10% for pristine SF and 4% for SFGPTMS50%. The temperature of the decomposition of SF in the region III changes to higher values with increasing the GPTMS content. The results could indicate a conformation change of SF to its β -sheet form after adding the GPTMS which are in good agreement with the aforementioned results.

As indicated in Figure 56, these characteristics could be related to the higher stability against thermal decomposition induced by β -sheet formation. The same characteristics were observed by Motta et al.⁶⁴ after inducing the crystallization (Silk II conformation) of SF films by treatment with ethanol.

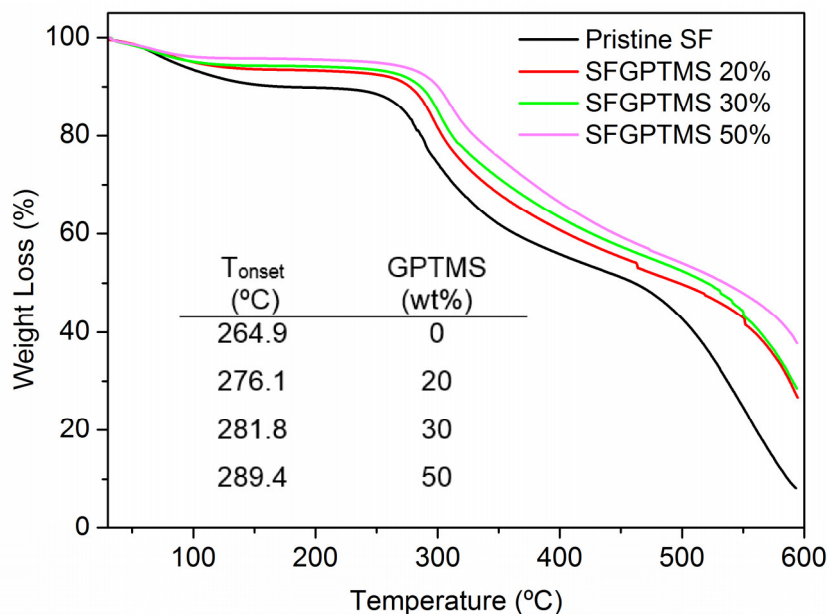


Figure 56. Thermogravimetric curves of pristine SF and SFGPTMS hybrid films. The inset table outlines the degradation onset temperature (T_{onset}) as function of GPTMS content.

DSC curves for pristine SF film and SFGPTMS films are shown in Figure 57. The DSC curve profile of pristine SF film displayed mainly three events. The first endothermic peak centered at about 82° C was attributed by many authors to the loss of adsorbed water.⁶⁷ The higher temperature of the endothermic peak (284 °C) could be attributed to the random coil - β -sheet conformational transition and to the thermal decomposition of SF chains. Thermal decomposition was also confirmed by TGA curves.

Pure SF film presented an endothermic peak related to its thermal degradation at 283 °C. Thermal degradation peaks of SF films at temperatures below 290 °C are characteristic of amorphous Silk I conformation, and are present when SF films are not submitted to any kind of physical or chemical treatment to induce its conformation to a more stable and crystalline Silk II conformation⁶⁸ The exothermic peak at 218 °C is attributed to the crystallization process from a Silk I to Silk II conformation.⁶⁸

DSC curves of SFGPTMS films show important changes comparing with Pristine SF film. The first endothermic peaks show a different profile in comparison to the pristine SF curve. This behavior can be attributed to elimination of water molecules during the condensation of GPTMS.

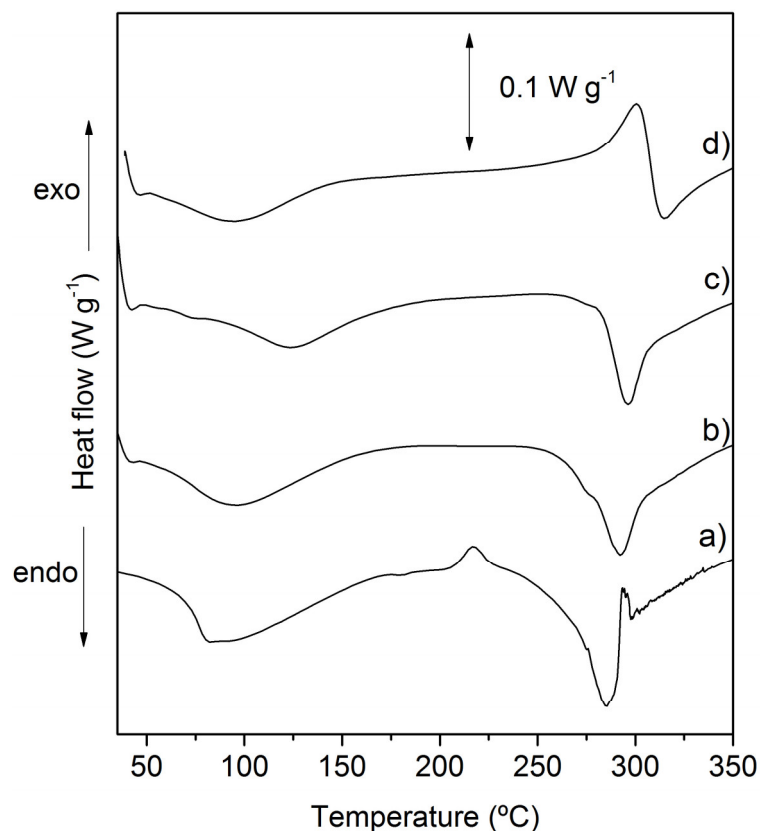


Figure 57. DSC curves of a) Pristine SF, b) SFGPTMS20%, c) SFGPTMS30%, and d) SFGPTMS50%.

Interestingly, the DSC curves of SFGPTMS hybrids do not show exothermic peak around 218 °C. The absence of this peak is due to the physical interaction between SF and GPTMS counterpart. According to the DSC curves the GPTMS should be preventing the crystallization process of SF.

Another important change on DSC curves is related to the shift of the degradation endothermic peak (from 284 °C to 292 °C) as a function of the increase of GPTMS content. These degradation temperature were also confirmed by TGA using onset temperature.

When the concentration of GPTMS is increased, the higher temperature endothermic peak related to the random coil- β sheet conformational transition shifts to higher temperature values (296 °C and 315 °C for SFGPTMS30% and SFGPTMS50%, respectively). The SFGPTMS films containing low amount of GTMS show clearly two subsequent peaks. The first one, an endothermic event is due to the SF degradation process and the second peak, an exothermic event is attributed to GPTMS degradation. Furthermore, the intensity of SF degradation peak decreases with the increase of GPTMS content. According to the DSC curves the degradation peak of SF is convoluted with the enlargement of the degradation peak of the GPTMS counterpart. The shift of

the T_m of the SF in the SFGPTMS system can be attributed to the interaction between the SF and the GPTMS with respect to hydrogen and hydrophobic bonding.

Preliminary results of cytotoxicity/viability assays for osteoblasts cells clearly indicate that there was no significant statistical difference ($p \geq 0.05$) between the cell viability of pristine SF and SFGPTMS hybrid films, regardless of GTPMS concentration.

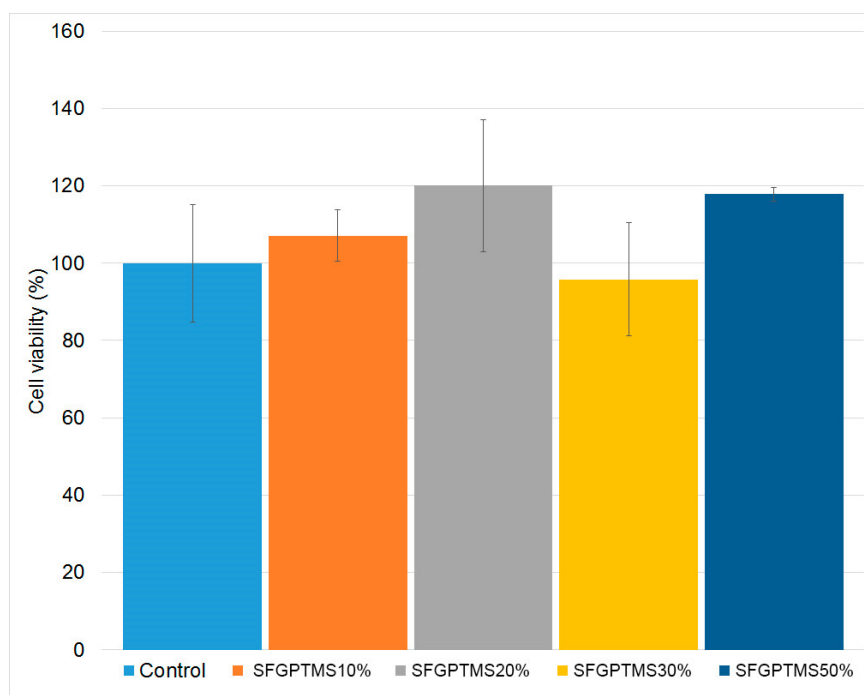


Figure 58. MTT-formazan viability/cytotoxicity assay of Pristine SF (control) and SFGPTMS hybrid films performed with osteoblasts lineage derived from calvaria of neonatal rats (OSTEO-1). Results are expressed as percentage of cell viability relative to fibroin membranes. ANOVA ONE WAY: $p = 0.244$.

Our study found that SFGPTMS films were non-cytotoxic for osteoblasts cells. Since SF is a well-known biocompatible natural polymer,⁶⁹⁻⁷² it was expected that hybrid films rich in SF component would preserve this feature. On the other hand, we also evaluated the cytotoxicity of hybrids films composed of GPTMS as major component in weight in order to identify the capabilities of SFGPMTS hybrids for biophotonics. Noteworthy, we identified that hybrids containing up to 30 wt% of GPTMS (i.e. 70% of SF – sample SFGPMTS30%) and films with opposite composition (i.e. 70 wt% of GPTMS, 30 wt% of SF – sample SFGPTMS70%) had negligible toxicity comparing with control sample. The absence of cytotoxicity for hybrids rich in epoxy groups have been also verified by recent literature studies involving the preparation of GPTMS-based organic-inorganic polymer nanocomposites.⁷³⁻⁷⁵ Remarkably, this feature enable

us further explore SFGPTMS hybrid films as potential functional biomaterial. Nevertheless, additional biological assays are in progress to gather a wider range of medical applications.

In order to evaluate the SFGPTMS hybrids films for photonics, luminescent films comprising transparent SFGPTMS20% hybrid loaded with 5 wt% $\text{YVO}_4:\text{Eu}^{3+}$ nanoparticles were prepared. The HRTEM image of Figure 59A shows that the size of non-spherical $\text{YVO}_4:\text{Eu}^{3+}$ particles is below 5 nm. The excitation and emission spectra of an aqueous suspension of $\text{YVO}_4:\text{Eu}^{3+}$ nanoparticles is shown in Figure 59B. The excitation and emission spectra of the luminescent hybrid are shown in Figure 60. From the excitation spectrum of $\text{YVO}_4:\text{Eu}^{3+}$ nanoparticles and luminescent SFGPTMS hybrid, a broad band around 300 nm is typically attributed to the charge transfer from the oxygen ligands to the central vanadium atom inside the VO_4^{3-} absorption.⁷⁶ In both excitation spectra of $\text{YVO}_4:\text{Eu}^{3+}$ nanoparticles and SFGPTMS films, the characteristic transitions within $\text{Eu}^{3+} 4f_6$ configuration are detected at 396 and 467 nm with a very weak intensity attributed to ${}^7\text{F}_0-{}^5\text{L}_6$ and ${}^7\text{F}_0-{}^5\text{D}_2$ transitions.

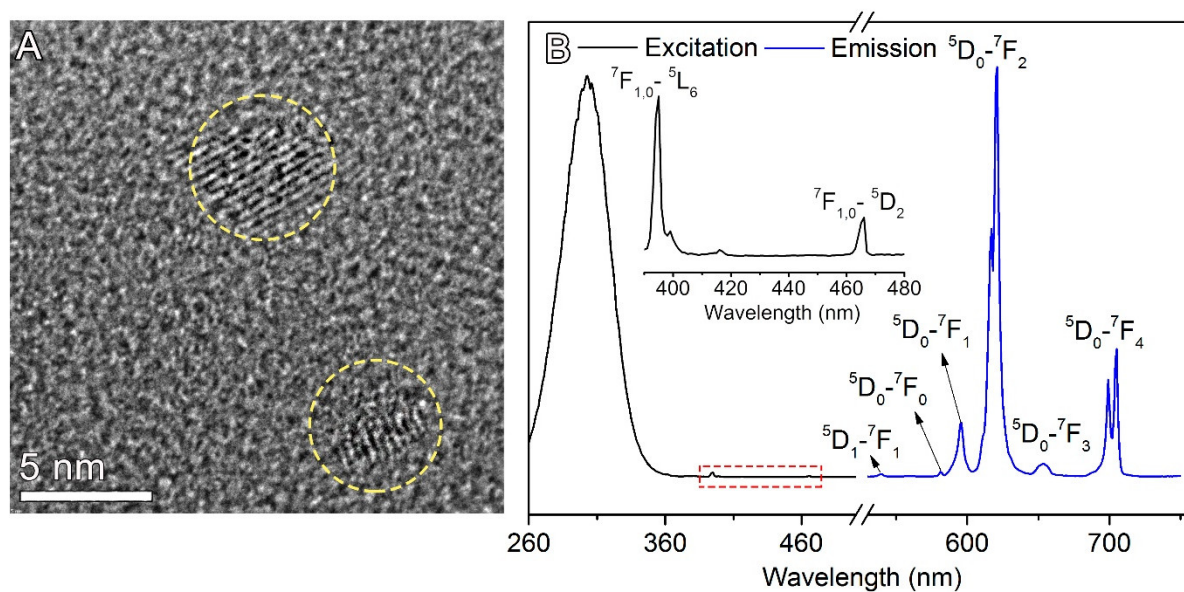


Figure 59. (A) HRTEM images and (B) Excitation ($\lambda_{\text{em}} = 620$ nm) and emission ($\lambda_{\text{exc}} = 303$ nm) spectra of an aqueous suspension of as-prepared $\text{YVO}_4:\text{Eu}^{3+}$ nanoparticles. The $\text{YVO}_4:\text{Eu}^{3+}$ nanoparticles were roughly spherical with size below 5 nm. The inset shows the amplified region highlighted in dashed red line of excitation spectrum for clearer observation

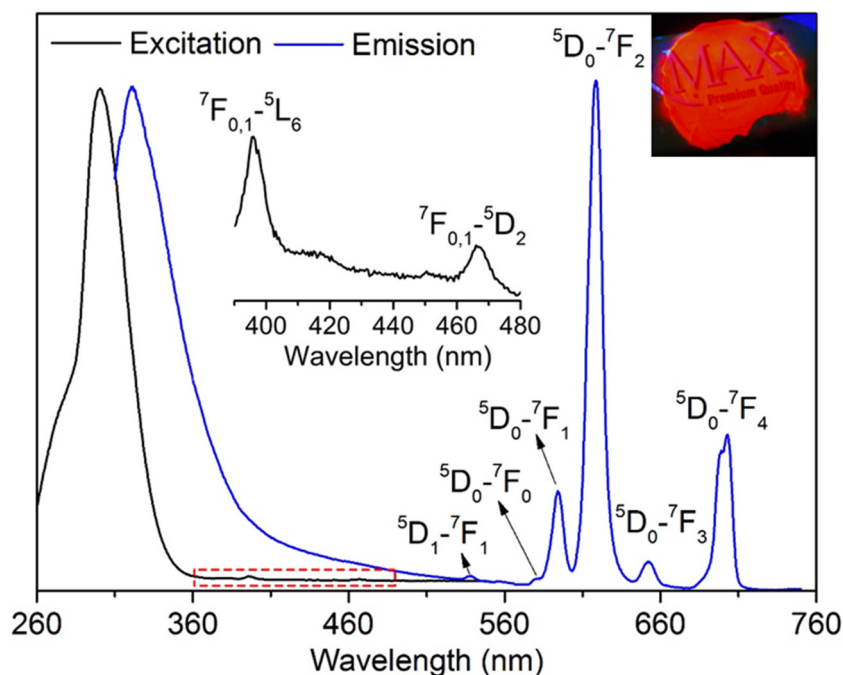


Figure 60. Excitation and emission spectra of SFGPTMS20% film containing 5 wt% of $\text{YVO}_4:\text{Eu}^{3+}$ nanoparticles. The excitation spectrum was performed by monitoring at 620 nm while the emission measurement was performed under excitation of 303 nm. The insets show the amplified region highlighted in dashed red line of excitation spectrum for clearer observation and a picture of the luminescent SF hybrid film under exposure to UV light.

A strong and broad emission band with small Stokes shift (~ 30 nm) is observed at 334 nm being mainly attributed to fluorescence of aromatic residues of SF (i.e. tyrosine and tryptophan) together with radiative recombination of SiO_2 matrix produced by sol-gel reaction of GPTMS or at aforementioned interfaces generated in SFGPTMS hybrids. Narrower bands peaking in the range of 570–710 nm region in the emission spectrum of aqueous suspension of $\text{YVO}_4:\text{Eu}^{3+}$ shown in Figure 59B is clearly detected in the emission spectrum of SFGPTMS hybrid. These bands were assigned to $\text{Eu}^{3+} 4f^6$ arising from the $^5\text{D}_0$ excited state to the $^7\text{F}_J$ manifold ($J=0, 1, 2, 3$ and 4). Once Eu^{3+} ions are located at low symmetric local sites in the YVO_4 host lattice, the most intense emission band of Eu^{3+} concerns the hypersensitive transition $^5\text{D}_0-^7\text{F}_2$ at about 620 nm. In the emission spectrum of both samples not only the characteristic transition lines from the lowest excited $^5\text{D}_0$ level of Eu^{3+} are observed, but also those from higher energy levels such as $^5\text{D}_1-^7\text{F}_1$ with a very weak intensity. When the spectra of the luminescent SFGPTMS hybrid and $\text{YVO}_4:\text{Eu}^{3+}$ nanoparticles are compared, it is evident that the resolution is better in the case of pristine nanoparticles. The loss of resolution in the hybrid matrix can be explained by site-to-site inhomogeneities caused by differences in the outer coordination sphere of Eu^{3+} resulting in small variations in the crystal- field strength felt by the different Eu^{3+} ions.

As previously reported the Eu^{3+} emission could be excited through efficient antenna effect involving vanadate charge transfer states in resonance with excited states of SF aromatic amino acids (i.e. tyrosine and tryptophan) present in the medium.⁴¹

5.3. Conclusion

In summary, we report the fabrication of flexible free-standing SF films rich in epoxy and silanol functional groups with high transparency (~90 %) even at high content of organo-functional silane (up to 70 wt%) by using all-aqueous sol-gel approach. We showed that hybrid films with remarkable optical quality were achieved at GPTMS concentration higher than 60 wt% or lower than 20 wt% of GPTMS whereas the refractive index displayed a quasi-linear dependence with GPTMS content in the films. This method allowed us to achieve SF hybrid films with relative smoother surface morphology upon the addition of GPTMS whose root-squared roughness decreased to less than half value compared to pristine SF film. Most significantly, we carefully evaluated the conformation changes of SF from amorphous Silk I to crystalline Silk II in response the introduction of GPTMS. Taking advantage of their remarkable optical properties, we demonstrated the feasibility to tailor functional and luminescent SF hybrid films by loading red emissive 5 nm $\text{YVO}_4:\text{Eu}^{3+}$ nanoparticles which offers an active optical substrate particularly attractive and functional for potential biophotonic applications such as fluorescence sensing, optical tagging, and detection.

References

- (1) Prasad, P. N. Biomaterials for Photonics. In *Introduction to Biophotonics*; John Wiley & Sons, Inc., 2003; pp 545–572.
- (2) Lawrence, B. D.; Omenetto, F.; Chui, K.; Kaplan, D. L. Processing Methods to Control Silk Fibroin Film Biomaterial Features. *J. Mater. Sci.* **2008**, *43* (21), 6967–6985.
- (3) Altman, G. H.; Diaz, F.; Jakuba, C.; Calabro, T.; Horan, R. L.; Chen, J.; Lu, H.; Richmond, J.; Kaplan, D. L. Silk-Based Biomaterials. *Biomaterials* **2003**, *24* (3), 401–416.
- (4) Omenetto, F. G.; Kaplan, D. L. A New Route for Silk. *Nat. Photonics* **2008**, *2* (11), 641–643.
- (5) Sashina, E. S.; Bochek, A. M.; Novoselov, N. P.; Kirichenko, D. A. Structure and Solubility of Natural Silk Fibroin. *Russ. J. Appl. Chem.* **2006**, *79* (6), 869–876.
- (6) Amsden, J. J.; Domachuk, P.; Gopinath, A.; White, R. D.; Negro, L. D.; Kaplan, D. L.; Omenetto, F. G. Rapid Nanoimprinting of Silk Fibroin Films for Biophotonic Applications. *Adv. Mater.* **2010**, *22* (15), 1746–1749.

- (7) Lin, D.; Tao, H.; Trevino, J.; Mondia, J. P.; Kaplan, D. L.; Omenetto, F. G.; Dal Negro, L. Direct Transfer of Subwavelength Plasmonic Nanostructures on Bioactive Silk Films. *Adv. Mater.* **2012**, *24* (45), 6088–6093.
- (8) Silva, R. R.; Dominguez, C. T.; dos Santos, M. V.; Barbosa-Silva, R.; Cavicchioli, M.; Christovan, L. M.; de Melo, L. S. a.; Gomes, A. S. L.; de Araújo, C. B.; Ribeiro, S. J. L. Silk Fibroin Biopolymer Films as Efficient Hosts for DFB Laser Operation. *J. Mater. Chem. C* **2013**, *1* (43), 7181-7190.
- (9) Zhou, C. Z.; Confalonieri, F.; Jacquet, M.; Perasso, R.; Li, Z. G.; Janin, J. Silk Fibroin: Structural Implications of a Remarkable Amino Acid Sequence. *Proteins* **2001**, *44* (2), 119–122.
- (10) Kim, D.-H.; Viventi, J.; Amsden, J. J.; Xiao, J.; Vigeland, L.; Kim, Y.-S.; Blanco, J. A.; Panilaitis, B.; Frechette, E. S.; Contreras, D.; Kaplan, D. L.; Omenetto, F. G.; Huang, Y.; Hwang, K.-C.; Zakin, M. R.; Litt, B.; Rogers, J. A. Dissolvable Films of Silk Fibroin for Ultrathin Conformal Bio-Integrated Electronics. *Nat. Mater.* **2010**, *9* (6), 511–517.
- (11) Perry, H.; Gopinath, A.; Kaplan, D. L.; Dal Negro, L.; Omenetto, F. G. Nano- and Micropatterning of Optically Transparent, Mechanically Robust, Biocompatible Silk Fibroin Films. *Adv. Mater.* **2008**, *20* (16), 3070–3072.
- (12) Harris, M.; Johnson, T. B. Study of the Fibroin from Silk in the Isoelectric Region 1. *Ind. Eng. Chem.* **1930**, *22* (5), 539–542.
- (13) Ambrose, E. J.; Bamford, C. H.; Elliott, A.; Hanby, W. E. Water-Soluble Silk: An α -Protein. *Nature* **1951**, *167* (4242), 264–265.
- (14) Yanagisawa, S.; Zhu, Z.; Kobayashi, I.; Uchino, K.; Tamada, Y.; Tamura, T.; Asakura, T. Improving Cell-Adhesive Properties of Recombinant Bombyx Mori Silk by Incorporation of Collagen or Fibronectin Derived Peptides Produced by Transgenic Silkworms. *Biomacromolecules* **2007**, *8* (11), 3487–3492.
- (15) Goujon, N.; Wang, X.; Rajkova, R.; Byrne, N. Regenerated Silk Fibroin Using Protic Ionic Liquidssolvents: Towards an All-Ionic-Liquid Process for Producing Silk with Tunable Properties. *Chem. Commun.* **2012**, *48* (9), 1278–1280.
- (16) Jin, H.-J.; Park, J.; Karageorgiou, V.; Kim, U.-J.; Valluzzi, R.; Cebe, P.; Kaplan, D. L. Water-Stable Silk Films with Reduced β -Sheet Content. *Adv. Funct. Mater.* **2005**, *15* (8), 1241–1247.
- (17) Hu, X.; Shmelev, K.; Sun, L.; Gil, E.-S.; Park, S.-H.; Cebe, P.; Kaplan, D. L. Regulation of Silk Material Structure by Temperature-Controlled Water Vapor Annealing. *Biomacromolecules* **2011**, *12* (5), 1686–1696.

- (18) Magoshi, J.; Magoshi, Y.; Nakamura, S. Physical Properties and Structure of Silk. VII. Crystallization of Amorphous Silk Fibroin Induced by Immersion in Methanol. *J. Polym. Sci. Polym. Phys. Ed.* **1981**, *19* (1), 185–186.
- (19) Bhat, N.; Ahirrao, S. Investigation of the Structure of Silk Film Regenerated with Lithium Thiocyanate Solution. *J. Polym. Sci. Polym. Chem. Ed.* **1983**, *21*, 1273–1280.
- (20) Lu, S.; Wang, X.; Lu, Q.; Zhang, X.; Kluge, J. a.; Uppal, N.; Omenetto, F.; Kaplan, D. L. Insoluble and Flexible Silk Films Containing Glycerol. *Biomacromolecules* **2010**, *11* (1), 143–150.
- (21) Jin, H.-J.; Park, J.; Valluzzi, R.; Cebe, P.; Kaplan, D. L. Biomaterial Films of Bombyx Mori Silk Fibroin with Poly(ethylene Oxide). *Biomacromolecules* **2004**, *5* (3), 711–717.
- (22) Dang, Q.; Lu, S.; Yu, S.; Sun, P.; Yuan, Z. Silk Fibroin/montmorillonite Nanocomposites: Effect of pH on the Conformational Transition and Clay Dispersion. *Biomacromolecules* **2010**, *11* (7), 1796–1801.
- (23) Noishiki, Y.; Nishiyama, Y.; Wada, M.; Kuga, S.; Magoshi, J. Mechanical Properties of Silk Fibroin-Microcrystalline Cellulose Composite Films. *J. Appl. Polym. Sci.* **2002**, *86* (13), 3425–3429.
- (24) Wang, Y. X. Y. J.; Qin, Y. P.; Kong, Z. J.; Wang, Y. X. Y. J.; Ma, L. Glutaraldehyde Cross-Linked Silk Fibroin Films for Controlled Release. *Adv. Mater. Res.* **2014**, 887–888, 541–546.
- (25) Wang, L.; Wang, Y.; Qu, J.; Hu, Y.; You, R.; Li, M. The Cytocompatibility of Genipin-Crosslinked Silk Fibroin Films. *J. Biomater. Nanobiotechnol.* **2013**, *04* (3), 213–221.
- (26) Jung, R.; Kim, H.-S. S.; Kim, Y.; Kwon, S.-M. M.; Lee, H. S.; In, H. J.; Jin, H.-J. Electrically Conductive Transparent Papers Using Multiwalled Carbon Nanotubes. *J. Polym. Sci. Part B Polym. Phys.* **2008**, *46* (12), 1235–1242.
- (27) Yin, H.; Zhou, Y.; Xu, J.; Ai, S.; Cui, L.; Zhu, L. Amperometric Biosensor Based on Tyrosinase Immobilized onto Multiwalled Carbon Nanotubes-Cobalt Phthalocyanine-Silk Fibroin Film and Its Application to Determine Bisphenol A. *Anal. Chim. Acta* **2010**, *659* (1-2), 144–150.
- (28) Freddi, G.; Anghileri, A.; Sampaio, S.; Buchert, J.; Monti, P.; Taddei, P. Tyrosinase-Catalyzed Modification of Bombyx Mori Silk Fibroin: Grafting of Chitosan under Heterogeneous Reaction Conditions. *J. Biotechnol.* **2006**, *125* (2), 281–294.
- (29) Acharya, C.; Hinz, B.; Kundu, S. C. The Effect of Lactose-Conjugated Silk Biomaterials on the Development of Fibrogenic Fibroblasts. *Biomaterials* **2008**, *29* (35), 4665–4675.

- (30) Tamada, Y. Sulfation of Silk Fibroin by Chlorosulfonic Acid and the Anticoagulant Activity. *Biomaterials* **2004**, *25* (3), 377–383.
- (31) Murphy, A. R.; John, P. St.; Kaplan, D. L. Modification of Silk Fibroin Using Diazonium Coupling Chemistry and the Effects on hMSC Proliferation and Differentiation. *Biomaterials* **2008**, *29* (19), 2829–2838.
- (32) Sagnella, A.; Zambianchi, M.; Durso, M.; Posati, T.; Del Rio, A.; Donnadio, A.; Mazzanti, A.; Pistone, A.; Ruani, G.; Zamboni, R.; Benfenati, V.; Melucci, M. APTES Mediated Modular Modification of Regenerated Silk Fibroin in a Water Solution. *RSC Adv.* **2015**, *5* (78), 63401–63406.
- (33) Brusatin, G.; Guglielmi, M.; Innocenzi, P.; Martucci, A.; Battaglin, G.; Pelli, S.; Righini, G. Microstructural and Optical Properties of Sol-Gel Silica-Titania Waveguides. *J. Non. Cryst. Solids* **1997**, *220* (2-3), 202–209.
- (34) Innocenzi, P.; Martucci, A.; Guglielmi, M.; Armelao, L.; Pelli, S.; Righini, G. .; Battaglin, G. . Optical and Surface Properties of Inorganic and Hybrid Organic–inorganic Silica–titania Sol–gel Planar Waveguides. *J. Non. Cryst. Solids* **1999**, *259* (1-3), 182–190.
- (35) Caiut, J. M. a.; Dexpert-Ghys, J.; Kihn, Y.; Vérelst, M.; Dexpert, H.; Ribeiro, S. J. L.; Messaddeq, Y. Elaboration of Boehmite Nano-Powders by Spray-Pyrolysis. *Powder Technol.* **2009**, *190* (1-2), 95–98.
- (36) Ribeiro, S. J. L.; Messaddeq, Y.; Gonçalves, R. R.; Ferrari, M.; Montagna, M.; Aegerter, M. A. Low Optical Loss Planar Waveguides Prepared in an Organic – Inorganic Hybrid System. *Appl. Phys. Lett.* **2000**, *77* (22), 3502–3504.
- (37) Innocenzi, P.; Brusatin, G.; Guglielmi, M.; Signorini, R.; Bozio, R.; Maggini, M. 3-(Glycidoxypropyl)-trimethoxysilane–TiO₂ Hybrid Organic–inorganic Materials for Optical Limiting. *J. Non. Cryst. Solids* **2000**, *265* (1-2), 68–74.
- (38) Innocenzi, P.; Brusatin, G.; Guglielmi, M.; Signorini, R.; Meneghetti, M.; Bozio, R.; Maggini, M.; Scorrano, G.; Prato, M. Optical Limiting Devices Based on C₆₀ Derivatives in Sol-Gel Hybrid Organic-Inorganic Materials. *J. Sol-Gel Sci. Technol.* **2000**, *19* (1/3), 263–266.
- (39) Brusatin, G.; Abbotto, A.; Beverina, L.; Pagani, G. A.; Casalbani, M.; Sarcinelli, F.; Innocenzi, P. Poled Sol-Gel Materials With Heterocycle Push-Pull Chromophores That Confer Enhanced Second-Order Optical Nonlinearity. *Adv. Funct. Mater.* **2004**, *14* (12), 1160–1166.

- (40) Innocenzi, P.; Miorin, E.; Brusatin, G.; Abboto, A.; Beverina, L.; Pagani, G. A.; Casalboni, M.; Sarcinelli, F.; Pizzoferrato, R. Incorporation of Zwitterionic Push Pull Chromophores into Hybrid Organic Inorganic Matrixes. *Chem. Mater.* **2002**, *14* (9), 3758–3766.
- (41) Lima, L. R.; Moraes, M. L.; Nigoghossian, K.; Peres, M. F. S.; Ribeiro, S. J. L. Silk Fibroin-Antigenic Peptides-YVO₄:Eu³⁺ Nanostructured Thin Films as Sensors for Hepatitis C. *J. Lumin.* **2016**, *170*, 375–379.
- (42) Barker, M. G.; Hooper, A. J. Preparation and X-Ray Powder Diffraction Patterns of the Sodium Vanadates NaVO₃, Na₄V₂O₇, and Na₃VO₄. *J. Chem. Soc. Dalt. Trans.* **1973**, (15), 1513.
- (43) Giaume, D.; Buissette, V.; Lahlil, K.; Gacoin, T.; Boilot, J.-P.; Casanova, D.; Beaurepaire, E.; Sauviat, M.-P.; Alexandrou, A. Emission Properties and Applications of Nanostructured Luminescent Oxide Nanoparticles. *Prog. Solid State Chem.* **2005**, *33* (2-4), 99–106.
- (44) Taddei, P.; Monti, P. Vibrational Infrared Conformational Studies of Model Peptides Representing the Semicrystalline Domains of Bombyx Mori Silk Fibroin. *Biopolymers* **2005**, *78* (5), 249–258.
- (45) Šapić, I. M.; Bistričić, L.; Volovšek, V.; Dananić, V.; Furić, K. DFT Study of Molecular Structure and Vibrations of 3-Glycidoxypropyltrimethoxysilane. *Spectrochim. Acta - Part A Mol. Biomol. Spectrosc.* **2009**, *72* (4), 833–840.
- (46) Almeida, R. M.; Pantano, C. G. Structural Investigation of Silica Gel Films by Infrared Spectroscopy. *J. Appl. Phys.* **1990**, *68* (8), 4225–4232.
- (47) Shao, J.; Zheng, J.; Liu, J.; Carr, C. M. Fourier Transform Raman and Fourier Transform Infrared Spectroscopy Studies of Silk Fibroin. *J. Appl. Polym. Sci.* **2005**, *96* (6), 1999–2004.
- (48) Monti, P.; Taddei, P.; Freddi, G.; Asakura, T.; Tsukada, M. Raman Spectroscopic Characterization of Bombyx Mori Silk Fibroin: Raman Spectrum of Silk I. *J. Raman Spectrosc.* **2001**, *32* (2), 103–107.
- (49) Monti, P.; Freddi, G.; Bertoluzza, A.; Kasai, N.; Tsukada, M. Raman Spectroscopic Studies of Silk Fibroin from Bombyx Mori. *J. Raman Spectrosc.* **1998**, *29* (4), 297–304.
- (50) Zheng, S.; Li, G.; Yao, W.; Yu, T. Raman Spectroscopic Investigation of the Denaturation Process of Silk Fibroin. *Appl. Spectrosc.* **1989**, *43* (7), 1269–1272.
- (51) Sapić, I. M.; Bistričić, L.; Volovsek, V.; Dananić, V.; Furić, K. DFT Study of Molecular Structure and Vibrations of 3-Glycidoxypropyltrimethoxysilane. *Spectrochim. Acta. A. Mol. Biomol. Spectrosc.* **2009**, *72* (4), 833–840.

- (52) Riegel, B.; Blittersdorf, S.; Kiefer, W.; Hofacker, S.; Müller, M.; Schottner, G. Kinetic Investigations of Hydrolysis and Condensation of the Glycidoxypolytrimethoxysilane/aminopropyltriethoxy-Silane System by Means of FT-Raman Spectroscopy I. *J. Non. Cryst. Solids* **1998**, *226* (1-2), 76–84.
- (53) Klein, L. C.; Kordas, G. Electron-Spin Resonance and Other Spectroscopies Used in Characterizing Sol-Gel Processing. *MRS Proc.* **1986**, *73*, 461–470.
- (54) Kaplan, D. L.; Mello, C. M.; Arcidiacono, S.; Fossey, S.; Senecal, K.; Muller, W. Silk. In *Protein-Based Materials*; McGrath, K., Kaplan, D., Eds.; Birkhäuser Boston: Boston, MA, 1997; pp 103–131.
- (55) Alonso, B.; Massiot, D.; Babonneau, F.; Brusatin, G.; Giustina, G. Della; Kidchob, T.; Innocenzi, P. Structural Control in Germania Hybrid Organic Inorganic Materials. *Chem. Mater.* **2005**, *17* (12), 3172–3180.
- (56) Brus, J.; Hlavatá, D.; Strachota, A. Self-Organization, Structure, Dynamic Properties, and Surface Morphology of Silica/Epoxy Films As Seen by Solid-State NMR, SAXS, and AFM. *Macromolecules* **2004**, *37* (4), 1346–1357.
- (57) Innocenzi, P.; Brusatin, G.; Babonneau, F. Competitive Polymerization between Organic and Inorganic Networks in Hybrid Materials. *Chem. Mater.* **2000**, *12* (12), 3726–3732.
- (58) Asakura, T.; Yao, J.; Yamane, T.; Umemura, K.; Ulrich, A. S. Heterogeneous Structure of Silk Fibers from Bombyx Mori Resolved by ¹³C Solid-State NMR Spectroscopy. *J. Am. Chem. Soc.* **2002**, *124* (30), 8794–8795.
- (59) Asakura, T.; Nakazawa, Y.; Ohnishi, E.; Moro, F. Evidence from ¹³C Solid-State NMR Spectroscopy for a Lamella Structure in an Alanine-Glycine Copolypeptide: A Model for the Crystalline Domain of Bombyx Mori Silk Fiber. *Protein Sci.* **2005**, *14* (10), 2654–2657.
- (60) Zhou, P.; Li, G.; Shao, Z.; Pan, X.; Yu, T. Structure of Bombyx Mori Silk Fibroin Based on the DFT Chemical Shift Calculation. *J. Phys. Chem. B* **2001**, *105* (50), 12469–12476.
- (61) Lu, Q.; Hu, X.; Wang, X.; Kluge, J. A.; Lu, S.; Cebe, P.; Kaplan, D. L. Water-Insoluble Silk Films with Silk I Structure. *Acta Biomater.* **2010**, *6* (4), 1380–1387.
- (62) Xi, F.; Wu, J.; Lin, X. Novel Nylon-Supported Organic–inorganic Hybrid Membrane with Hierarchical Pores as a Potential Immobilized Metal Affinity Adsorbent. *J. Chromatogr. A* **2006**, *1125* (1), 38–51.
- (63) Greving, I.; Dicko, C.; Terry, A.; Callow, P.; Vollrath, F. Small Angle Neutron Scattering of Native and Reconstituted Silk Fibroin. *Soft Matter* **2010**, *6* (18), 4389–4395.
- (64) Motta, A.; Fambri, L.; Migliaresi, C. Regenerated Silk Fibroin Films: Thermal and Dynamic Mechanical Analysis. *Macromol. Chem. Phys.* **2002**, *203* (10-11), 1658–1665.

- (65) Schoeser, M. The Science of Silk. In *Silk*; Yale University Press: New Haven, 2007; p 234.
- (66) Macan, J.; Brnardić, I.; Orlić, S.; Ivanković, H.; Ivanković, M. Thermal Degradation of Epoxy–silica Organic–inorganic Hybrid Materials. *Polym. Degrad. Stab.* **2006**, *91* (1), 122–127.
- (67) Magoshi, J.; Magoshi, Y.; Nakamura, S.; Kasai, N.; Kakudo, M. Physical Properties and Structure of Silk. V. Thermal Behavior of Silk Fibroin in the Random-Coil Conformation. *J. Polym. Sci. Polym. Phys. Ed.* **1977**, *15* (9), 1675–1683.
- (68) Moraes, M. A. de; Nogueira, G. M.; Weska, R. F.; Beppu, M. M. Preparation and Characterization of Insoluble Silk Fibroin/Chitosan Blend Films. *Polymers (Basel)*. **2010**, *2* (4), 719–727.
- (69) Yang, Y.; Chen, X.; Ding, F.; Zhang, P.; Liu, J.; Gu, X. Biocompatibility Evaluation of Silk Fibroin with Peripheral Nerve Tissues and Cells in Vitro. *Biomaterials* **2007**, *28* (9), 1643–1652.
- (70) Liu, T.; Miao, J.; Sheng, W.; Xie, Y.; Huang, Q.; Shan, Y.; Yang, J. Cytocompatibility of Regenerated Silk Fibroin Film: A Medical Biomaterial Applicable to Wound Healing. *J. Zhejiang Univ. Sci. B* **2010**, *11* (1), 10–16.
- (71) Tang, X.; Ding, F.; Yang, Y.; Hu, N.; Wu, H.; Gu, X. Evaluation on in Vitro Biocompatibility of Silk Fibroin-Based Biomaterials with Primarily Cultured Hippocampal Neurons. *J. Biomed. Mater. Res. Part A* **2009**, *91A* (1), 166–174.
- (72) Seib, F. P.; Pritchard, E. M.; Kaplan, D. L. Self-Assembling Doxorubicin Silk Hydrogels for the Focal Treatment of Primary Breast Cancer. *Adv. Funct. Mater.* **2013**, *23* (1), 58–65.
- (73) Shirosaki, Y.; Okayama, T.; Tsuru, K.; Hayakawa, S.; Osaka, A. In Vitro Bioactivity and MG63 Cytocompatibility of Chitosan-Silicate Hybrids. *Int. J. Mater. Chem.* **2013**, *3* (3A), 1–7.
- (74) Trujillo, S.; Pérez-Román, E.; Kyritsis, A.; Gómez Ribelles, J. L.; Pandis, C. Organic-Inorganic Bonding in Chitosan-Silica Hybrid Networks: Physical Properties. *J. Polym. Sci. Part B Polym. Phys.* **2015**, *53* (19), 1391–1400.
- (75) Tonda-Turo, C.; Cipriani, E.; Gnani, S.; Chiono, V.; Mattu, C.; Gentile, P.; Perroteau, I.; Zanetti, M.; Ciardelli, G. Crosslinked Gelatin Nanofibres: Preparation, Characterisation and in Vitro Studies Using Glial-like Cells. *Mater. Sci. Eng. C* **2013**, *33* (5), 2723–2735.
- (76) Wang, G.; Qin, W.; Zhang, D.; Wang, L.; Wei, G.; Zhu, P.; Kim, R. Enhanced Photoluminescence of Water Soluble $\text{YVO}_4:\text{Ln}^{3+}$ (Ln = Eu, Dy, Sm, and Ce) Nanocrystals by Ba $2+$ Doping. *J. Phys. Chem. C* **2008**, *112* (44), 17042–17045.

6. MULTIFUNCTIONAL ORGANIC-INORGANIC HYBRIDS BASED ON CELLULOSE ACETATE AND 3-GLYCIDOXYPROPYLTRIMETHOXYSILANE²

The past decade has witnessed steady growth of academic and industry interest on the development of new functionalized hybrid materials with high content of natural biopolymers [1, 2]. Biopolymers have offered remarkable bio-compatibility, eco-friendliness processability and comprise the best current alternatives to traditional non-biodegradable polymers. Among them, cellulose is the most naturally occurring biopolymer in the world. Cellulose-based materials have triggered great interest in the development of highly valuable industrial outcomes due to their appealing properties including hydrophilicity, semi-crystalline structure and high mechanical strength.[3] Despite the wide variety of end uses, neat cellulose polymer is poorly soluble in common solvents. Most of derivatives are cellulose esters and ethers with improved solubility in both aqueous and/or organic solvents. Cellulose esters have good processability enabling the fabrication of water-insoluble polymers films and fibers with excellent optical quality and stiffness. Cellulose acetate (CA) is one of the most important derivatives prepared by esterification of cellulose with main applications in CO₂ filtration membranes, photographic and cinematographic films, protective film, fibers, protective coatings (e.g. protective film of the polarizing film of the liquid crystal display), cigarette filters, etc. CA is biodegradable, nontoxic and one of the biocompatible cellulose derivatives being abundantly found in agricultural waste such as straw and biomass residues and even chemically recycled newsprint has been explored as alternative source.[4]

Despite the excellent optical properties of CA films, few reports have explored their practical use in photonic applications. For example, Lova et al.[5] prepared high quality flexible distributed Bragg reflectors constituted of ordered multilayers of CA and light scattering layer based on ZnO nanoparticles coated with polystyrene. Unno et al.[6] described the fabrication of nanogratings patterned by using thermal roll-to-roll nanoimprint technique on a CA film.

A broader use of CA in optics is mostly hampered by several limitations including relatively poor mechanical strength, low oxidation and solvent/chemical resistance. One potential route for overcoming these limitations is to combine additional organic and/or inorganic components with CA at molecular level in order to produce a hybrid with superior properties comparing to

² This chapter contains results from previously published article: Silva, R. R. et al. *Journal of Sol-Gel Science and Technology*, in press. Available at <http://dx.doi.org/10.1007/s10971-016-4089-x>

pure CA film. So far, sol-gel process is the most investigated approach to achieve organic/inorganic hybrid (OIH) materials with improved properties. The key advantages of sol-gel processing concern the low temperature processing in solution-phase, purity, and homogeneity of the resulting materials. The fabrication of CA-based OIH films using sol-gel approach was firstly proposed by Kelley et al [7, 8] by functionalization of neat CA polymer with organically modified alkoxysilanes. The authors evaluate the incorporation of alkoxysilanes possessing unsaturated polymerizable pendent groups (e.g. acrylate, vinyl), thiol and isothiocyanate groups in CA polymer aiming the fabrication of OIH films with high thermal stability and improved resistance against abrasion and organic solvent.

Gonçalves et al. [9, 10] demonstrated the feasibility to tailor a highly branched alkoxysilane CA-based OIH film by grafting pristine CA film with 3-aminopropyltriethoxysilane cross-linked with pentaerythritol triacrylate components. The outcome concerns films insoluble in organic solvents and with a significant reduction of the dimensional changes in water when compared with pure CA films. Additionally, pure CA films have also been grafted with 3-aminopropyltrimethoxysilane in order to introduce amino groups as a pathway to covalently immobilize proteins. In a recent work, Heikkinen et al.[11] successfully evaluated the biotin-binding capacities of chimeric avidin, streptavidin, chicken avidin, and rhizavidin immobilized on the surface of amino-functionalized CA films.

Achoundong et al.[12] have explored the grafting and crosslinking of vinyltrimethoxysilane on pristine CA films to produce transparent gas permeable membranes with outperformance in high concentrations of CO₂ and H₂S feeds. Noteworthy, the authors demonstrated that introduction of vinyl groups did not affect significantly the transparency of resulting hybrid films while the flexibility was considerably improved.

In an effort to extend the practical use of cellulose acetate in photonics we investigated the preparation of sol-gel hybrids with incorporation of 3-glycidoxypropyltrimethoxysilane, an organically modified alkoxide silane possessing terminal epoxy group. Epoxide groups can easily undergo ring-opening reactions via photo, thermal and ~~upon~~ alkaline/acid catalytic polymerization generating polyethylene oxide (PEO) chains. Additionally epoxy ring-opening can be used as coupling agent to covalently bind organic and inorganic compounds.

On the pursuit of evaluate their potential use ~~of~~ in optical applications, free-standing red-emissive and yet highly transparent hybrid films were prepared by incorporating europium (III) tris-(2-thenoyltrifluoroacetate), [Eu(TTA)₃(H₂O)₂] complex. Eu³⁺ complexes are largely studied for various optical applications owing to their intense, UV excited narrow emission bands in the red region with long excited-state lifetimes (i.e. in the milliseconds range). The

mutual high solubility of both CA and $[\text{Eu}(\text{TTA})_3(\text{H}_2\text{O})_2]$ complex in acetone is an advantageous feature to tailor functional and luminescent hybrid films with potential use in photonic materials.

6.1. Experimental section

6.1.1. Materials

Cellulose acetate ($M_n = 29,000 \text{ g}\cdot\text{mol}^{-1}$, acetyl content $\sim 40\%$) was purchased from Fluka. 3-glycidoxypropyltrimethoxysilane and 2-thenoyltrifluoroacetone were purchased from Sigma-Aldrich. Hydrochloric acid and ammonium hydroxide were purchased from Synth. Eu_2O_3 was purchased from Lumintek.

6.1.2. Synthesis of luminescent tris(2-thenoyltrifluoroacetato)europium(III) dihydrate complex

The synthesis of $[\text{Eu}(\text{TTA})_3(\text{H}_2\text{O})_2]$ was based on a modified protocol reported by Charles et al.[13] Firstly, an aqueous stock solution of europium chloride ($\text{pH}\approx 5$) was prepared by dissolving Eu_2O_3 (14.2 mmol, 5.0 g) in HCl 12 M (85.2 mmol, 7.12 mL) at 100°C under stirring (500 rpm). The concentration of aqueous solution of $\text{EuCl}_3\cdot 6\text{H}_2\text{O}$ was determined by EDTA titration with a value of 0.13 M. 2-thenoyltrifluoroacetone (TTA, 3.9 mmol, 0.86 g), NH_4OH 18.08 M (15 mmol, 0.450 mL) and $\text{EuCl}_3\cdot 6\text{H}_2\text{O}$ 0.13 M (1.3 mmol, 10.0 mL) were dissolved in ethanol (18.75 mL) under vigorous stirring in a round-bottom flask. After three hours, the resulting solid (i.e. $[\text{Eu}(\text{TTA})_3(\text{H}_2\text{O})_2]$ complex) was precipitated by cooling the flask in ice bath. The precipitate was filtered off and recrystallized from acetone.

6.1.3. Preparation of cellulose acetate/3-glycidoxypropyltrimethoxysilane hybrid films

0.25 g of CA was dissolved in 4 mL of acetone. After complete dissolution, GPTMS was added and stirred for 1 min. The solution was cast on flat petri dishes and covered with a thin aluminum foil. Hybrid composites were prepared with the GPTMS relative content ranging from 5 to 50 wt%.

6.1.4. Preparation of luminescent cellulose acetate/3-glycidoxypropyltrimethoxysilane hybrid film.

In a beaker, 0.25 g of cellulose acetate were dissolved in 4 mL of acetone. Then, 150 μL of GPTMS and 654 μL of an acetone solution of $[\text{Eu}(\text{TTA})_3(\text{H}_2\text{O})_2]$ 15 mM were added

dropwise. The resulting solution was placed on glass dishes ($\phi = 10$ cm) and left to dry in ambient air (relative humidity of $\sim 35\%$) during 24 h.

6.1.5. Instrumentation

Absorption spectra were measured in the wavelength range from 200 to 2000 nm with a UV-visible spectrometer Cary 500.

Scanning electron microscopic (SEM) images were taken in a field emission scanning electron microscope (FESEM, JEOL JSM - 7500F). A thin film of carbon was sputtered onto the surface of the samples before the analysis. AFM images were taken in an Agilent 5500 - AC Mode III in the intermittent contact mode under ambient conditions, and using conventional silicon multipurpose cantilevers. All images were rendered using Gwyddion AFM analysis software. It is worth pointing out that the AFM and SEM imaging were performed on the surface of hybrid films generated in the liquid/air interface from the evaporation of solvent.

Fourier transform infrared spectroscopy (FT-IR) analysis was performed in a Spectrum 2000 FT-IR Perkin Elmer spectrophotometer, equipped with a multiple reflection, horizontal Miracle attenuated total reflectance (ATR) attachment (ZnSe crystal). Spectra were collected over the range of $4000\text{--}600\text{ cm}^{-1}$ with an accumulation of 128 scans and resolution of 4 cm^{-1} .

Raman spectra were recorded using a Raman Horiba Jobin–Yvon 118 model LabRAM HR 800 spectrometer, operating with He–Ne 632.81 nm laser through a $100\times$ objective lens and dispersed by a diffraction grating ($600\text{ lines}\cdot\text{mm}^{-1}$) onto a cooled charge-coupled device (CCD) detector.

The $^{29}\text{Si}\{^1\text{H}\}$ Cross Polarization Magic Angle Spinning (CP-MAS), $^{13}\text{C}\{^1\text{H}\}$ CP-MAS and ^1H MAS spectra were obtained on a Bruker Avance III 400WB HD, operating at 9.4T, using a commercial double resonance 4mm. Typical spinning speeds were 10.0 and 12.0 kHz. $^{29}\text{Si}\{^1\text{H}\}$ CP-MAS spectra were measured with ^1H pulse length of 3.0 μs , contact time of 3.5 ms, and relaxation delay of 5 s. $^{13}\text{C}\{^1\text{H}\}$ CP-MAS spectra were measured with ^1H pulse length of 2.8 μs , contact time of 2.0 ms, and relaxation delay of 2s. All spectra were acquired with Two Pulse Phase Modulation (TPPM) proton decoupling during the data acquisition applying decoupling pulses of 5.8 μs length. The chemical shifts are reported relative to tetramethylsilane (TMS). Chemical shifts have an estimated error in ± 0.1 .

X-ray diffraction patterns were obtained using a Kristalloflex Siemens Diffractometer with a Ni filer and $\text{CuK}\alpha$ radiation from 4° to 50° , step scan of $0.02^\circ 2\theta$, $\lambda\text{Cu-}\alpha$ monochromatized by a graphite crystal, divergence slit width = $1/2^\circ$, Scattering slit = $1/2^\circ$, divergence height-limiting slit width = 5 mm and reception slit = 0.3 mm.

Thermogravimetric (TG) curves were obtained from SDT equipment from TA Instruments. The conditions used in the experiments were: synthetic air at a flow rate of 100 mL min^{-1} , heating rate of $20 \text{ }^\circ\text{C min}^{-1}$ from 20° to $600 \text{ }^\circ\text{C}$ and alumina pans.

The photoluminescence spectra measurements were performed in Horiba Jobin Yvon Fluorolog spectrofluorimeter model FL3-222, equipped with a Hamamatsu R928 photomultiplier and Xe lamp (450 W) using front face mode with resolution of 0.5 nm.

6.2. Results and discussion

Figure 61A shows the picture of a bended CA-GPTMS free-standing film exhibiting high transparency. In general, the hybrid films featured high transmittance ($>85\%$) in the visible/near infrared region for all composition investigated as displayed in Figure 61B.

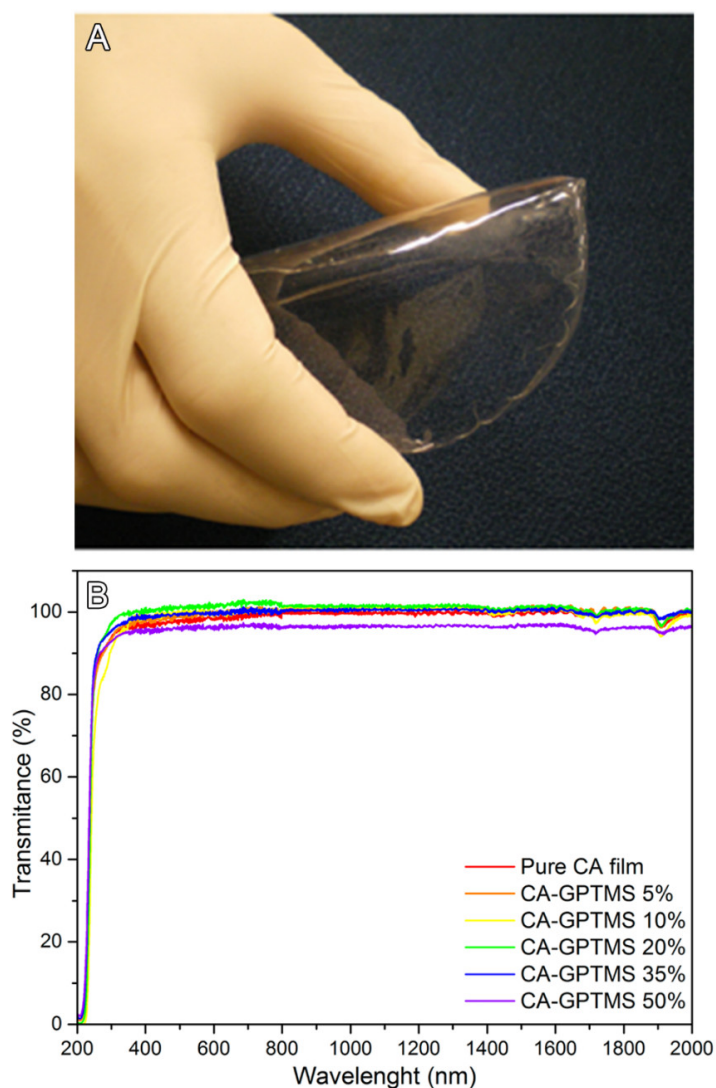


Figure 61. (Color online) A) Picture of transparent and flexible free-standing film of CA-GPTMS hybrid B) UV-vis-NIR spectra of pure CA and GPTMS hybrid films. The films were high transparent (85%) for all composition from ultraviolet to the near infrared.

The optical transmittance spectra show that both CA and CA-GPTMS films slightly absorb in the region below 300 nm. The addition of GPTMS did not place substantial deleterious effect on the optical properties of pure CA film. Additionally, SEM images depicted in Figure 62 clearly display that the surface of the films was homogeneous, indicating compatibility between CA and GPTMS and therefore, contributing to the high transparency observed for all investigated compositions.

AFM height and phase images obtained for pristine CA film and CA-GPTMS films containing 20 and 50 wt% GPTMS are shown in Figure 63. AFM phase image of pristine CA film exhibited typical regular nanometric scale topographies unveiled after the drying of the CA film.

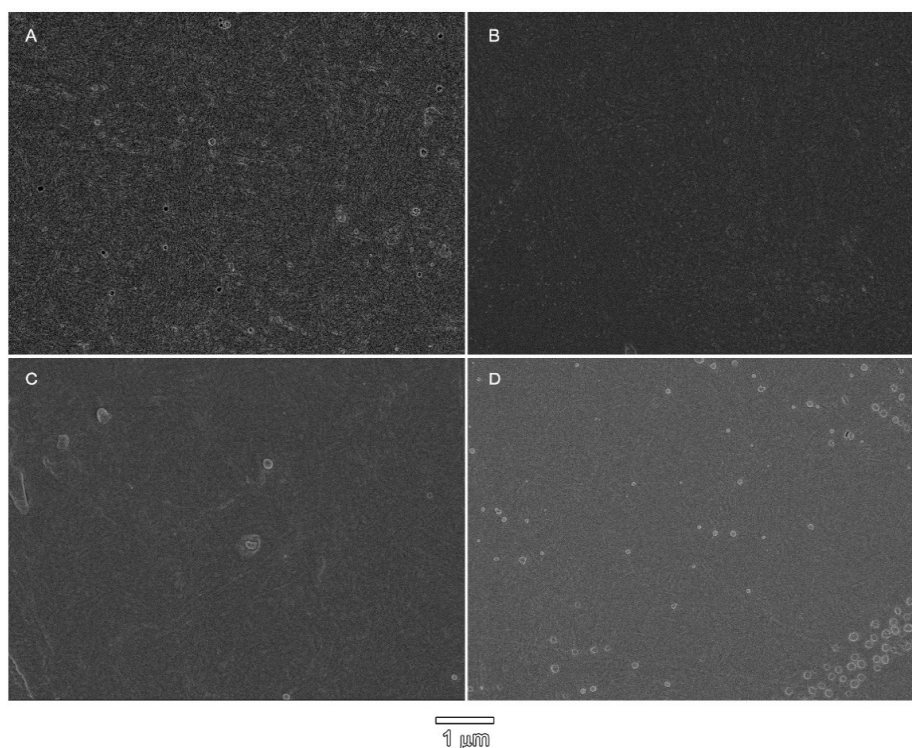


Figure 62. FE-SEM images of A) pure cellulose acetate film and sol-gel hybrid films of cellulose acetate with different contents of GPTMS: B) 20 wt%, C) 35 wt% and D) 50 wt%.

The CA film is homogenous on the analyzed surface and its average roughness extracted from AFM height image is very low (4.7 ± 2 nm). Addition of the 20 wt% of GPTMS led to considerable changes in the surface structure. The surface structure changed to homogeneously dispersed globular-like morphology with average domain size smaller than 30 nm. The average

roughness extracted from AFM height images decreased to 2 ± 0.7 nm. As shown in Figure 63F, the addition of 50 wt% of GPTMS led to an increase in the number and size of the globular-like domains. The average size became larger than 100 nm and roughness increased to 7.5 ± 1 nm. The increase of globular-like domains may have a deleterious effect in the optical properties of CA-GPTMS 50% films addressed by a slight decrease of the transmittance in as a result of light scattering process.

Figure 64 shows ATR-FT-IR spectra. The main feature of CA is the presence of band at 1738 cm^{-1} assigned to symmetric stretching of the carbonyl group (C=O) from acetyl group ($\text{CH}_3\text{C}(\text{O})\text{O}-$) [14]. Bands observed at 1222 cm^{-1} , 1160 cm^{-1} , and 1030 cm^{-1} could be assigned to asymmetric stretching of C-O, C-O-C glycosidic linkage, and asymmetric C-O-C bond stretching from the pyranose ring, respectively[14].

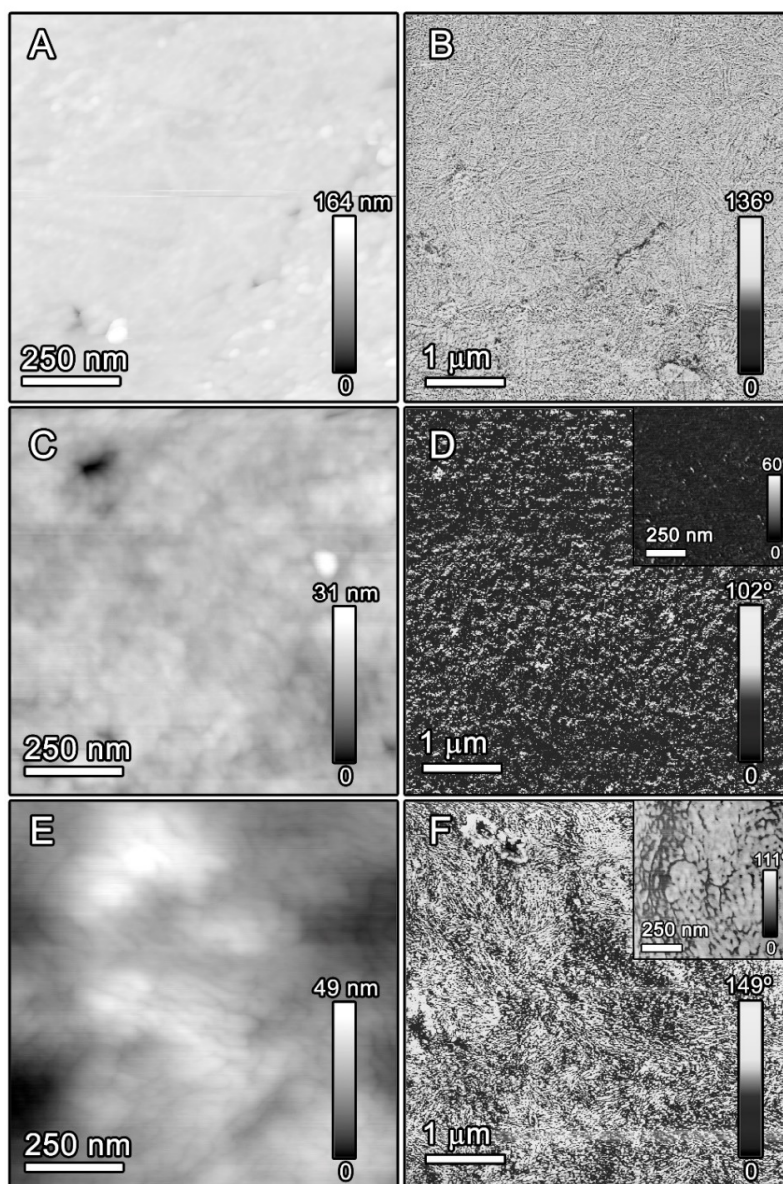


Figure 63. Height AFM images of (A) Pristine CA film, (C) CA-GPTMS 20% and (E) CA-GPTMS 50%. Phase AFM images are pictured in (B) pristine CA films, (D) CA-GPTMS 20% and (F) CA-GPTMS 50%. The inset in (D) and (F) show amplified regions of CA-GPTMS 20% and CA-GPTMS 50%, respectively.

Noteworthy, the band at 1222 cm^{-1} gets sharper as GPTMS content is increased. Upon the addition of GPTMS, narrowing and relative increase is observed for the band at 1160 cm^{-1} . The assignment of this band is related to the overlapping of CH_3 rocking combined with C-O stretching modes of methoxy groups [15].

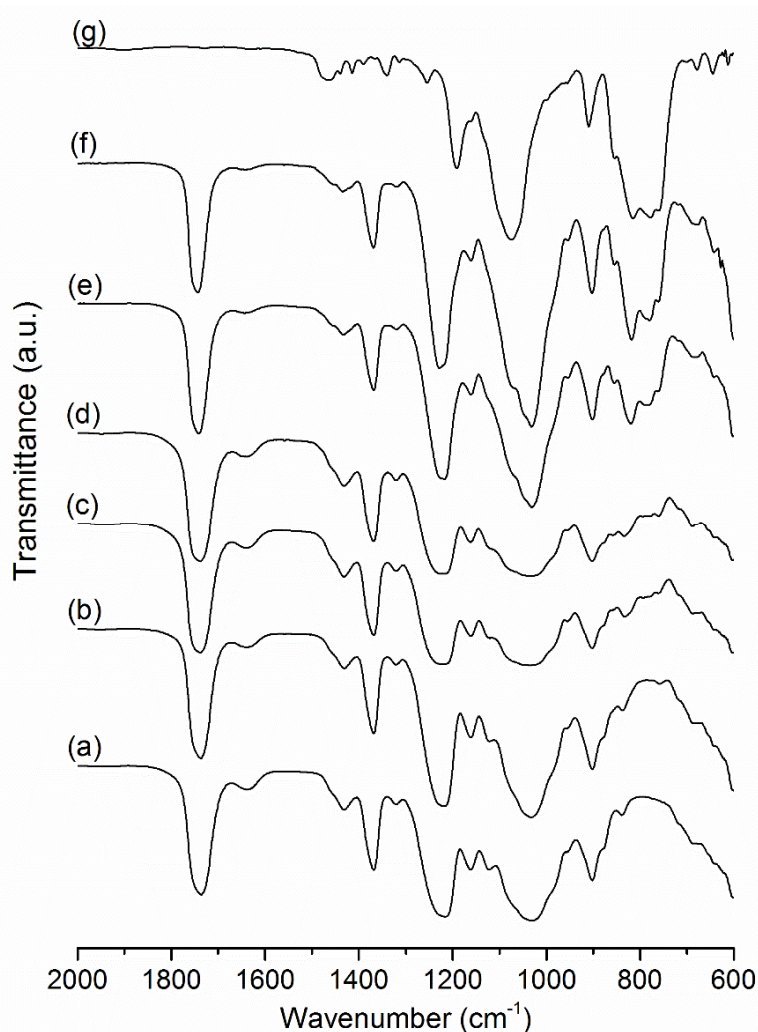


Figure 64. ATR-FT-IR of a) Pure CA film, b) CA-GPTMS 5%, c) CA-GPTMS 10%, d) CA-GPTMS 20%, e) CA-GPTMS 35%, f) CA-GPTMS 50% and g) liquid GPTMS.

Bands related to silica net vibration modes were hardly observed suggesting that GPTMS could remain non-hydrolyzed.

High intensity bands associated to epoxy ring vibrations modes occur in the 800-700 cm^{-1} region. The band at 855 cm^{-1} refers to C-O torsion and C-C stretching of epoxy ring while the band at 818 cm^{-1} is assigned to CH_2 rocking of propyl chain coupled with Si-O stretching. The band observed at 902 cm^{-1} with moderate intensity in pristine CA films has been assigned to glycosidic vibrations[16] mixed with out-of-plane O-H bending of water. Moreover, a slight increase of intensity followed by narrowing of this band is observed with increasing content of GPTMS which could be attributed to the coupling with C-O and C-C stretching besides C-O torsion of epoxy ring [15]. Additionally, C-O stretching mixed with CCO scissoring vibrations from pure epoxy ring vibrations were assigned to the emerging band at 762 cm^{-1} [15].

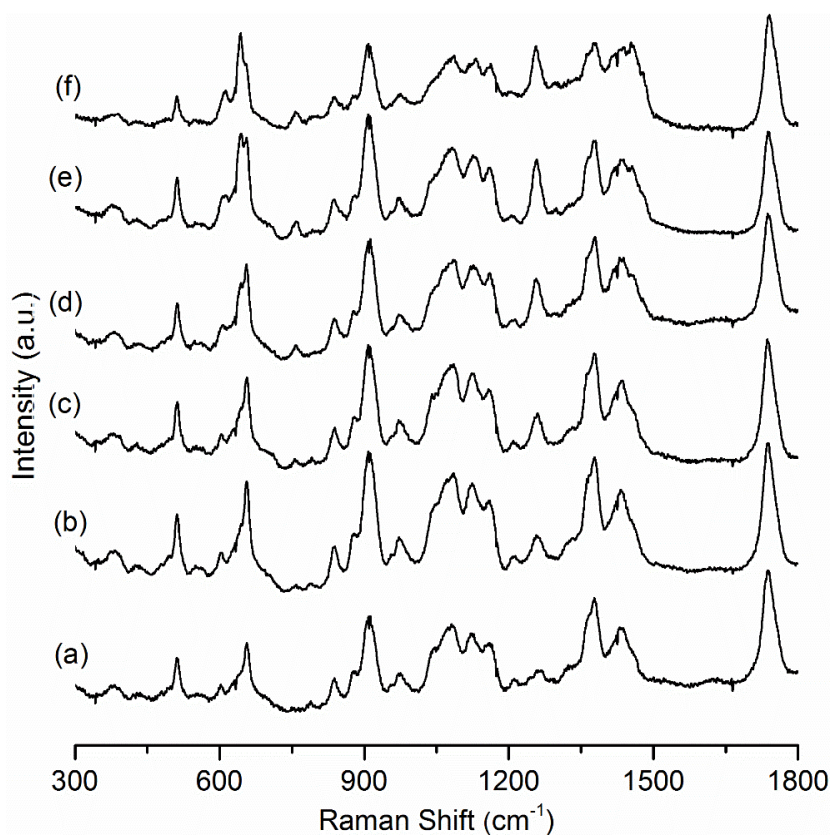


Figure 65. Raman spectra of a) Pure CA film, b) CA-GPTMS 5%, c) CA-GPTMS 10%, d) CA-GPTMS 20%, e) CA-GPTMS 35% and f) CA-GPTMS 50%.

Figure 65 displays Raman spectra. A relatively strong Raman band at 1256 cm^{-1} is observed in the all CA-GPTMS hybrid films. This band is assigned to C-H rock and C-C stretching vibration of epoxy ring [15]. An additional contribution of this band could be addressed to the coupling of Si- CH_2 -R bending vibrations from non-hydrolyzed GPTMS molecules.

Bands observed in the region between 1500 cm^{-1} and 1300 cm^{-1} comprise the vibration modes of cellulose backbone of CA polymer. This region is essentially described by deformation modes of CH_2 , H-C-C, H-C-O and C-O-H vibrations at 1378 cm^{-1} and by the deformation of

CH₃-groups within acetyl groups [17, 18] at 1434 cm⁻¹. A discrete band at 1485 cm⁻¹ is also observed with the increase of GPTMS content in the hybrid films and is assigned to CH₂ scissoring and CH rocking in epoxy ring [15]. In addition, the epoxy ring vibrations are also observed at 763 cm⁻¹ and 759 cm⁻¹ which are assigned to symmetric stretching of aliphatic ether linkage of epoxy group [15].

A relative strong band observed for all films at 910 cm⁻¹ is associated to stretching and bending modes of C-O single bond [17] of CA polymer. Bands at 1160 and 1083 cm⁻¹ are associated to asymmetric and symmetric pyranose ring breathing vibration of cellulose [19], respectively.

The doublet band observed at 644 cm⁻¹ and 612 cm⁻¹ arises with the increase in the GPTMS content. This band have been assigned to coupled symmetric and asymmetric stretching vibrations of (-Si(OCH₃)₃) group. In a previous work, Riegel et al [20], monitored the intensity of 644 cm⁻¹ Raman band as tool to investigate the hydrolysis of GPTMS hybrids containing 3-aminopropyltrimethoxysilane. The authors inferred that the intensity of the Raman band at 644 cm⁻¹ is associated with to the amount of the non-hydrolyzed trimethoxysilane-molecules (-Si(OCH₃)₃). The presence of this band in the CA-GPTMS spectra also suggests that GPTMS molecules could mostly remain non-hydrolyzed.

Figure 66 shows ¹³C{¹H} CP-MAS NMR spectra. The spectrum of CA shows broad resonance lines with assignments based on [21, 22].

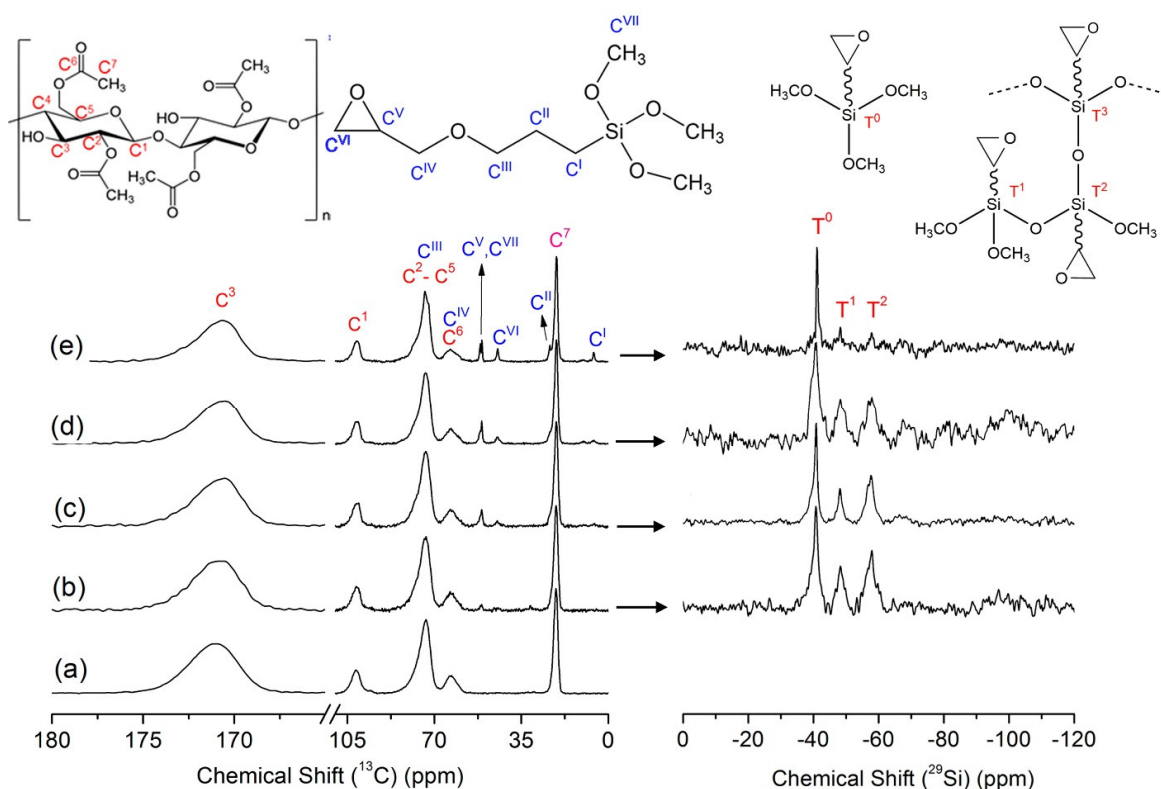


Figure 66. (Color online) In the upper panel, the assignments of the ^{13}C NMR and $^{29}\text{Si}\{1\text{H}\}$ CP-MASNMR signals are identified on the chemical structures of GPTMS and CA. The bottom left panel displays the ^{13}C NMR of (a) pristine CA, (b) CA-GPTMS 5%, (c) CA-GPTMS 20%, (d) CA-GPTMS 35% and (e) CA-GPTMS 50% films. The solid-state $^{29}\text{Si}\{1\text{H}\}$ CP-MAS NMR spectra of CA-GPTMS hybrids are displayed in the bottom right panel.

The assignments are identified in the spectrum as specified in top portion of Figure 66. Peaks observed at 21 and 40 ppm of carbon acetyl group C^5 and C^7 are present in all films spectra. The peaks observed at 42.6 and 49.7 ppm (positions C^{VI} and C^{V} , respectively) are attributed to epoxy groups. The relative intensity is the same for all CA-GTMS hybrid films, indicating that there was no polymerization process. It is interesting to highlight that the line width of the peaks of GPTMS keeps narrow to all concentrations in the hybrid films, suggesting a high mobility of epoxy group.

Results from vibrational and NMR spectra emphasize the presence of unreacted epoxy ring of GPTMS molecule in the hybrid films. The presence of epoxy groups enables a new pathway to chemically modify the CA films. Beyond that, a cross-linked hybrid matrix is feasible to be achieved by ring-opening reactions of epoxy groups, which in turn can be conducted by exposing the CA-GPTMS films to ultraviolet light, thermal activation or nucleophilic substitution reaction under alkaline/acidity media.

Hydrolysis and condensation reaction of GPTMS was investigated by ^{29}Si NMR. T^n code is used where n indicates the number of bridged Si atoms [23]. Figure 66 shows the $^{29}\text{Si}\{^1\text{H}\}$ CP-MAS NMR spectra. Three resonance lines are observed in the $^{29}\text{Si}\{^1\text{H}\}$ CP-MAS spectra. The peaks at -41 ppm, -48 ppm and -58 ppm are assigned to T^0 , T^1 and T^2 siloxane species, respectively [24, 25] - in the CA-GPTMS film. Silicon linked with three siloxane units (T^3) was hardly observed. The $^{29}\text{Si}\{^1\text{H}\}$ CPMAS NMR data indicate that hydrolysis and condensation reactions of silicon methoxides groups from GPTMS molecules partially took place during the preparation of the hybrid films. Approximately the same relative amount of T^0 , T^1 and T^2 units could be observed for GPTMS content up to 35%. With further increase in GPTMS relative content (50%) the contribution of T^0 units increases.

Figure 67 shows X-rays diffraction patterns. The pattern obtained for pure CA film shows three main broad peaks observed at 8.8° , 10.7° and 17.8° . The peak located at 8.8° is known as the main characteristic of semi-crystalline acetylated derivative cellulose. This peak position indicates the generation of disorder when cellulose is acetylated. The disorder is due to the projection of the acetyl groups along the axes (causing interfibrillar distance to increase) and is also related to the breakdown of microfibrillar structures. Similar results were found by Barud et al. in the acetylation of bacterial cellulose [26].

The peak at $2\theta = 10^\circ$ is a well known feature appearing for acetylated cellulose [27]. The peak at around 17.8° , is known as the van der Waals halo. This broad peak is observed in polymers and corresponds to the polymeric chain packing due to van der Waals forces. This diffraction pattern observed for the pure CA film corresponds to the structure of the acetylated materials [28]. Besides, it can be seen from Figure 67a that the XRD pattern of pure CA films shows partial crystalline structure.

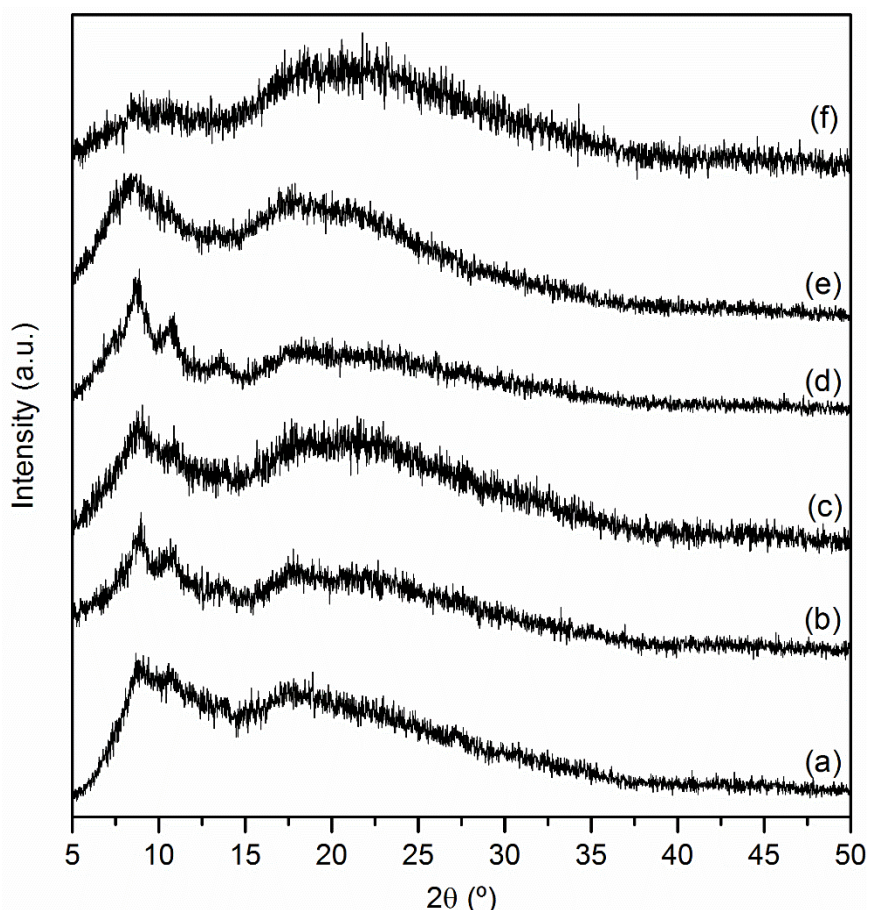


Figure 67. X-ray diffraction of a) Pure CA film, b) CA-GPTMS 5%, c) CA-GPTMS 10%, d) CA-GPTMS 20%, e) CA-GPTMS 35%, f) CA-GPTMS 50%.

Figure 67, b – d show XRD patterns obtained for CA-GPTMS hybrids containing 5, 10 and 20 wt% of GPTMS, respectively. The diffractograms are similar to the one observed for the pristine CA film (Figure 67a), except the slightly narrower peaks at 8.8° , 10.8° and 13.6° .

Figure 67, e-f show results obtained for hybrids containing 35 wt% and 50 wt% of GPTMS. For CA-GPTMS 35% (Figure 67e), peaks near 8.8° , 10.8° and 13.6° are merged into a broadened one, centered around 8.4° . For CA-GPTMS 50% (Figure 67f), the broad peak near 8.4° becomes less intense (in comparison with the broad peak near 20°), which means the crystallinity was diminished.

It can be argued that for the CA-GPTMS 5%, 10% and 20% sol-gel hybrids, the GPTMS addition slightly increases the crystallinity of cellulose acetate film. For higher amounts of GPTMS (i.e. CA-GPTMS 35% and 50%), the inverse is observed. In this case, GPTMS may interact in a higher extent with CA polymer and play a key role on the disarrangement among CA chains leading to amorphous hybrid films. Below 20 wt% of GPTMS content, it may partially induce the assembly and eventual packing of CA chains. In this case, the concentration

of GPTMS is not sufficient to produce extended silica network mostly ruled by spatial restriction due to the high relative content of CA chains.

The TG/DTG curves are displayed in Figure 68. The thermal stability of pristine CA and representatives samples CA-GPTMS 5% and CA-GPTMS 50% were evaluated in oxidative atmosphere in attempt to estimate the inorganic residues [26].

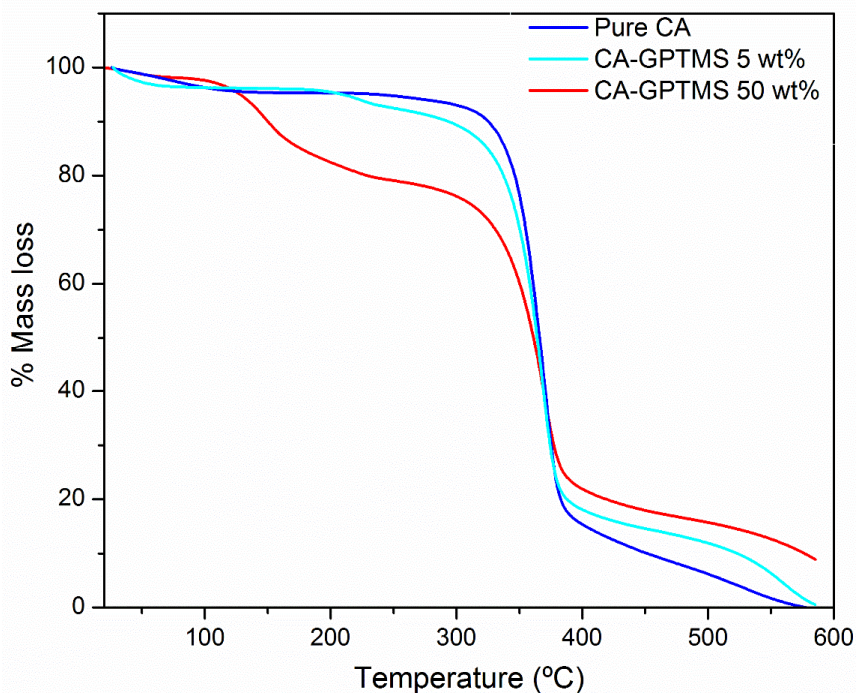


Figure 68. (Color online) Thermogravimetric curves of pure CA, CA-GPTMS 5%, and CA-GPTMS 50% films.

TGA curve for pristine CA film displays two thermal events. The first event comprises the range from ambient temperature to 120°C, whose mass-loss is mostly ascribed to the evaporation of residual solvent (i.e. acetone). The second mass-loss event occurs at around (~370 °C) is due to polymer decomposition of CA backbones [4, 26]. As expected, there is no residue at 600 °C.

The TGA curves profiles for CA-GPTMS 5% and CA-GPTMS 50% samples exhibit two additional events. From room temperature to 120 °C, the weight loss can be attributed to residual acetone desorption plus evaporation of water produced as by-product of eventual hydrolysis/condensation of GPTMS molecules. There are additional weight loss events starting at 120 °C and ending at around 250 °C addressed to removal of monomeric physisorbed silanes [30].

For CA-GPTMS composite samples, the main thermal event is due to simultaneous decompositions of GPTMS molecules and neat CA polymer components which have similar

decomposition temperature (~ 370 °C) [29]. For CA-GPTMS samples, the residue at 600 °C can be associated to the formation of silicon derivatives.

In order to estimate the potential use of functional CA-GPTMS hybrids in optical applications, luminescent films comprising transparent CA-GPTMS 40% hybrid containing 2 wt% luminescent $[\text{Eu}(\text{TТА})_3(\text{H}_2\text{O})_2]$ complex were prepared. Figure 69 shows the ATR-FT-IR spectra of pristine CA-GPTMS 40% hybrid film, $[\text{Eu}(\text{TТА})_3(\text{H}_2\text{O})_2]$ complex and CA-GPTMS 40% hybrid containing 2 wt% luminescent $[\text{Eu}(\text{TТА})_3(\text{H}_2\text{O})_2]$.

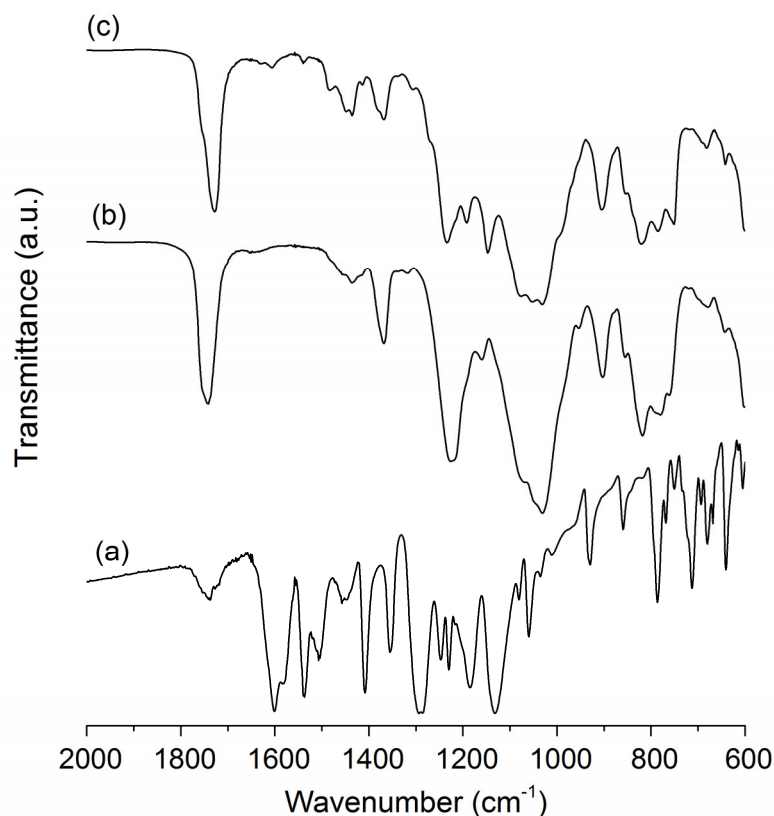


Figure 69. Fourier-transform infrared spectra of (a) $[\text{Eu}(\text{TТА})_3(\text{H}_2\text{O})_2]$ powder b) CA-GPTMS 40% and, (c) CA-GPTMS 40% doped with $[\text{Eu}(\text{TТА})_3(\text{H}_2\text{O})_2]$ 2 wt%.

The ATR-FT-IR spectrum of $[\text{Eu}(\text{TТА})_3(\text{H}_2\text{O})_2]$ complex shows bands at 1501, 1481, 1415, and 1355 cm^{-1} as fine and intense bands assigned to $\nu(\text{C}=\text{C}, \text{C}=\text{S})$ of thienyl heterocycle. Characteristic stretching vibration modes of the enol tautomer form of β -diketonate features peaks narrow and intense bands at 1601 cm^{-1} ($\nu(\text{C}=\text{O})$), 1537 cm^{-1} and 1505 cm^{-1} ($\nu(\text{C}=\text{O}, \text{C}=\text{C})$). The peaks at 1280, 740 and 712 cm^{-1} are assigned to stretching and bending vibration modes of CF_3 .

ATR-FT-IR spectrum of CA-GPTMS 40% hybrid film containing 2 wt% of $[\text{Eu}(\text{TТА})_3(\text{H}_2\text{O})_2]$ presented in Figure 69 (c) can be considered as the result of the convolution of the spectra of CA-GPTMS 40% hybrid film and $[\text{Eu}(\text{TТА})_3(\text{H}_2\text{O})_2]$ compound. In addition,

the ATR-FT-IR spectrum of doped hybrid film do not show the formation of any additional bands if compared with ATR-FT-IR spectra of pristine CA-GPTMS 40% hybrid and pristine $[\text{Eu}(\text{TTA})_3(\text{H}_2\text{O})_2]$, which confirm lack of chemical bonds between the components. The ATR-FT-IR spectra CA-GPTMS luminescent films confirm the presence of $[\text{Eu}(\text{TTA})_3(\text{H}_2\text{O})_2]$ complex.

Figure 70A shows the absorption spectra obtained for pristine CA-GPTMS 40% hybrid film and luminescent CA-GPTMS hybrid film.

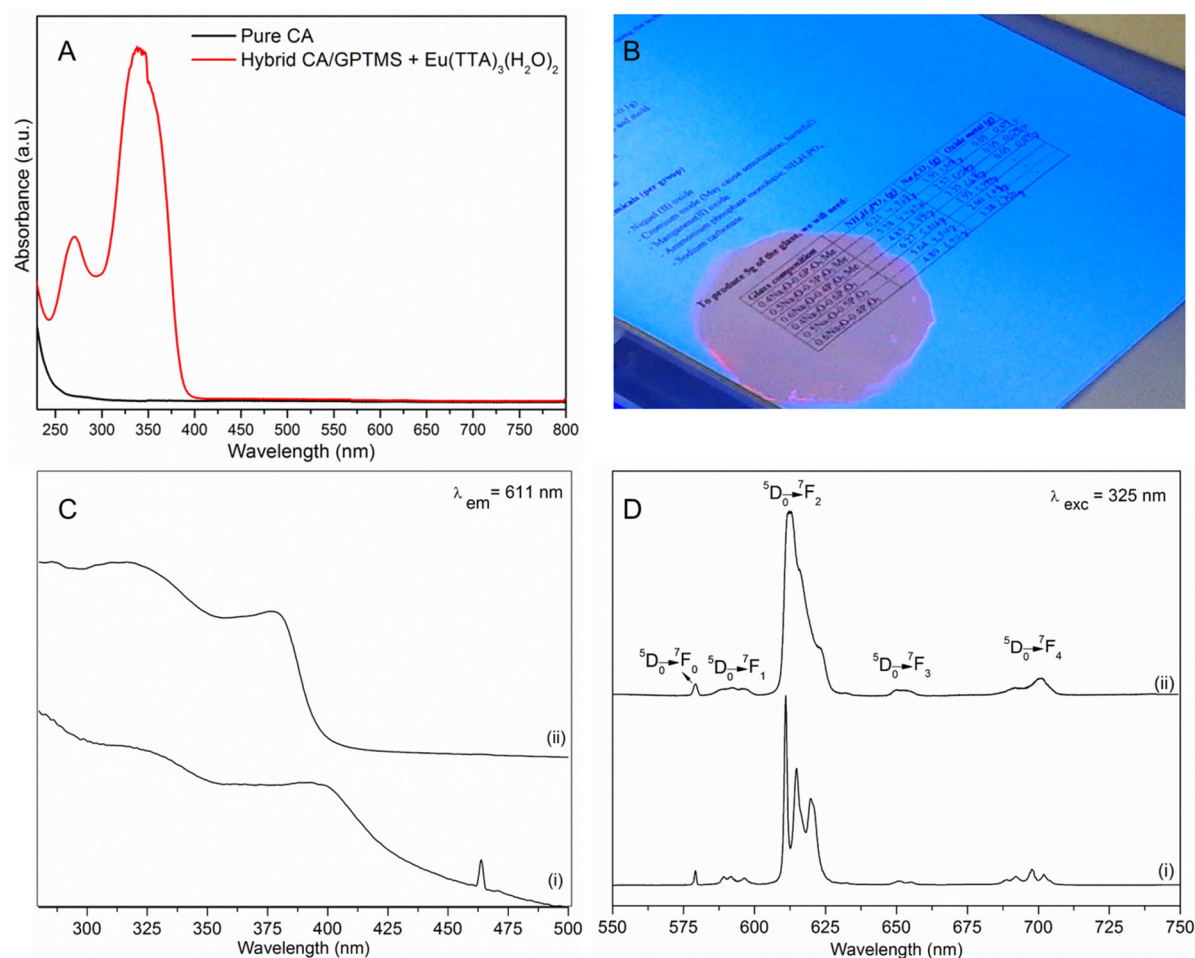


Figure 70. (Color online) (A) Absorption spectra and luminescent CA-GPTMS 40% hybrid film containing $\text{Eu}(\text{TTA})_3(\text{H}_2\text{O})_2$ 2 wt% and pristine CA-GPTMS 40% films. (B) Picture of luminescent CA-GPTMS hybrid under ultraviolet light exposure ($\lambda_{\text{max}} = 360$ nm), (C) Excitation, and (D) Emission spectra of i) pure $\text{Eu}(\text{TTA})_3(\text{H}_2\text{O})_2$ complex and ii) luminescent CA-GPTMS hybrid film.

The absorption spectrum of doped hybrid film is characterized by two relatively resolved bands centered at 269 and 339 nm which are assigned to the ligand centered $S_0 \rightarrow S_1$ (π, π^*) transition of the aromatic moiety in the TTA ligands [31, 32]. The picture featured in Figure

70B shows an intense orange–red emission of transparent CA-GPTMS 40% hybrid doped with $[\text{Eu}(\text{TTA})_3(\text{H}_2\text{O})_2]$ complex placed over a paper sheet under exposure of commercial UV light.

Figure 70C shows the normalized excitation spectra obtained for the $[\text{Eu}(\text{TTA})_3(\text{H}_2\text{O})_2]$ complex and luminescent CA-GPTMS hybrid film registered at 300 K in 250 – 500 nm range by monitoring the Eu^{3+} emission at 611 nm. These spectra exhibit broad bands, with the maximum peaking around 325 nm which is attributable to the ligand centered $S_0 \rightarrow S_1$ (π, π^*) transition of TTA ligand [32], as already observed in the absorption spectra. This broad absorption band overlaps some $4f-4f$ absorption bands corresponding to the characteristic transitions of Eu^{3+} ion, such as ${}^7F_0 \rightarrow {}^5G_6$ (361 nm), ${}^7F_0 \rightarrow {}^5H_4$ (374 nm), ${}^7F_0 \rightarrow {}^5L_6$ (394 nm) and ${}^7F_0 \rightarrow {}^5D_3$ (415 nm), except the ${}^7F_0 \rightarrow {}^5D_2$ transition which appears at 463.8 nm in the excitation spectrum of pure $[\text{Eu}(\text{TTA})_3(\text{H}_2\text{O})_2]$ complex. On the other hand, in the excitation spectrum of doped hybrid film the band at 463.8 nm does not appear once it is even weaker by comparison with the strongest one. The luminescence sensitization via ligand excitation is more efficient than the direct excitation of Eu^{3+} ion absorption levels owing to the high relative intensity of broad band associated to the ligand level when compared to $4f-4f$ absorptions bands of Eu^{3+} ion [33]. The ratio between the relative intensities of the broad bands attributable to the ligand level and the intrinsic bands of metal ion can provide the efficiency of this effect [34–36].

The emission spectrum of the of luminescent CA-GPTMS hybrid film featured in Figure 70D shows a similar emission spectrum of pure $[\text{Eu}(\text{TTA})_3(\text{H}_2\text{O})_2]$ complex. It is important to note that the emission spectrum of pure $[\text{Eu}(\text{TTA})_3(\text{H}_2\text{O})_2]$ complex displays higher resolution due to the additional separation caused by the Stark effect. The emission spectra with excitation at 325 nm are characterized by the transitions ${}^5D_0 \rightarrow {}^7F_J$, ($J = 0, 1, 2, 3$ and 4) with predominant hypersensitive ${}^5D_0 \rightarrow {}^7F_2$ transition band around 612 nm. These transitions appears in ${}^5D_0 \rightarrow {}^7F_0$ (579 nm), ${}^5D_0 \rightarrow {}^7F_1$ (589, 591 and 596 nm), ${}^5D_0 \rightarrow {}^7F_2$ (611, 614 and 619 nm) ${}^5D_0 \rightarrow {}^7F_3$ (651 and 655 nm) and ${}^5D_0 \rightarrow {}^7F_4$ (688, 691, 697 and 701 nm) for the pure $[\text{Eu}(\text{TTA})_3(\text{H}_2\text{O})_2]$ complex and ${}^5D_0 \rightarrow {}^7F_0$ (579 nm), ${}^5D_0 \rightarrow {}^7F_1$ (592 nm), ${}^5D_0 \rightarrow {}^7F_2$ (612 nm) ${}^5D_0 \rightarrow {}^7F_3$ (653 nm) and ${}^5D_0 \rightarrow {}^7F_4$ (692 and 701 nm) for the luminescent CA-GPTMS hybrid film. The incorporation of the complex into the hybrid leads to an inhomogeneous broadening of the corresponding emission lines. This effect is addressed to the heterogeneous distribution of sites the Eu^{3+} ions present into the CA-GPTMS hybrid film.

Figure 71 shows the emission decay curves of pure $[\text{Eu}(\text{TTA})_3(\text{H}_2\text{O})_2]$ complex and luminescent CA-GPTMS hybrid film. The luminescence decay curves were acquired by monitoring the hypersensitive ${}^5D_0 \rightarrow {}^7F_2$ transition at 611 nm under excitation at 325 nm. Decay

curves follow monoexponential decay law, and the decay times values so-obtained are listed in Table 4.

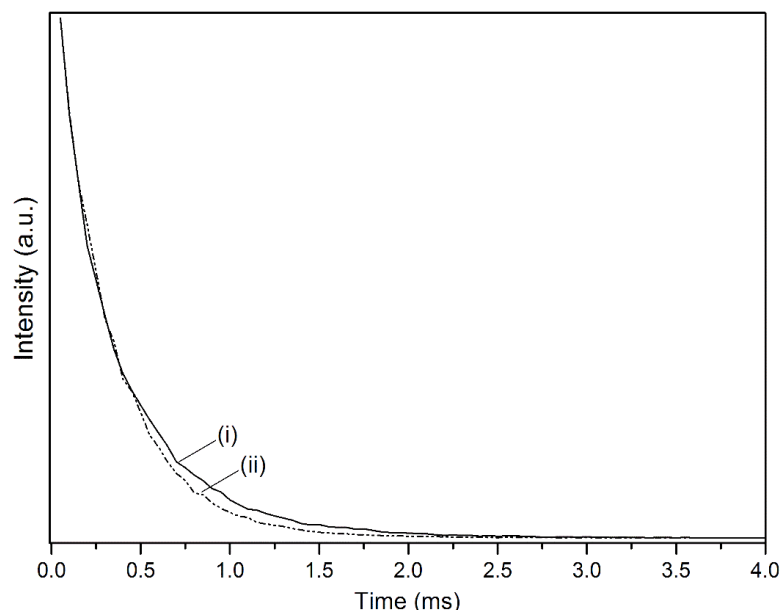


Figure 71. Emission decay curves (i) pure $[\text{Eu}(\text{TTA})_3(\text{H}_2\text{O})_2]$, and (ii) CA-GPTMS 40% hybrid film containing 2 wt% of $[\text{Eu}(\text{TTA})_3(\text{H}_2\text{O})_2]$. The emission lifetime was recorded by monitoring the emission at 611 nm under excitation at 325 nm.

Table 4. Experimental intensity parameters (Ω_λ), emission quantum efficiencies (η), lifetimes (ms), radiative (A_{rad}), nonradiative (A_{nrad}) and total (A_{total}) emission coefficient rates for the $[\text{Eu}(\text{TTA})_3(\text{H}_2\text{O})_2]$ complex and CA-GPTMS 40% hybrid film containing $[\text{Eu}(\text{TTA})_3(\text{H}_2\text{O})_2]$ 2 wt% based on emission spectra recorded at 298 K*.

Samples	Ω_2 (10^{-20}cm^2)	Ω_4 (10^{-20}cm^2)	A_{rad} (s^{-1})	A_{nrad} (s^{-1})	A_{total} (s^{-1})	τ (ms)	η (%)
$[\text{Eu}(\text{TTA})_3(\text{H}_2\text{O})_2]$	18.4	742	782.92	2411.96	3194.88	0.27	21
CA-GPTMS 40% Eu	16.8	5.14	684.39	2239.58	2923.97	0.31	22

*The calculated parameters have deviations of $\pm 10\%$.

These values are very close together, giving evidence that the complex $[\text{Eu}(\text{TTA})_3(\text{H}_2\text{O})_2]$ did not experience major changes when incorporated into the hybrid matrix. In order to get further details on the Eu^{3+} ion chemical environment in the pure $[\text{Eu}(\text{TTA})_3(\text{H}_2\text{O})_2]$ compound and luminescent hybrid film, some spectroscopy parameters were determined. Experimental Judd-Ofelt intensity parameters (Ω_2 and Ω_4), radiative (A_{rad}) and non-radiative (A_{nrad}) decay

rates and quantum efficiency (η) are also listed in the Table 4. For $A_{0 \rightarrow J}$ calculation, the equation (1) was considered [37]:

$$A_{0\lambda} = \frac{\nu_{01}}{\nu_{0\lambda}} \frac{S_{0\lambda}}{S_{01}} \cdot (A_{01}) \quad \text{eq. (1)}$$

where $\sigma_{0 \rightarrow 1}$ and $\sigma_{0 \rightarrow J}$ correspond to energy baricenters of ${}^5D_0 \rightarrow {}^7F_1$ and ${}^5D_0 \rightarrow {}^7F_J$, respectively. $S_{0 \rightarrow 1}$ and $S_{0 \rightarrow J}$ are emission curve areas corresponding to ${}^5D_0 \rightarrow {}^7F_1$ and ${}^5D_0 \rightarrow {}^7F_J$ transitions, respectively [32]. As known, the magnetic dipole allowed ${}^5D_0 \rightarrow {}^7F_1$ transition was taken as reference [38], since $A_{0 \rightarrow 1}$ rate is almost insensitive to chemical environment changes around the Eu^{3+} ion with $A_{0 \rightarrow 1} = 50 \text{ s}^{-1}$. The experimental intensity parameters Ω_λ ($\lambda = 2$ and 4) were estimated from the ${}^5D_0 \rightarrow {}^7F_2$ and ${}^5D_0 \rightarrow {}^7F_4$ transitions, respectively, in the emission spectrum of the Eu^{3+} complex. The experimental intensities parameters were calculated from the spontaneous emission coefficients ($A_{0 \rightarrow J}$), according to the following expression [31]:

$$\Omega_\lambda = \frac{3 c^3 A_{0 \rightarrow J}}{4 e^2 \omega^3 \chi \langle {}^7F_J \parallel U^{(\lambda)} \parallel {}^5D_0 \rangle^2} \quad \text{eq. (2)}$$

Where ω is the angular frequency of the transition, e is the electronic charge, c is the velocity of light, \hbar is Planck's constant over 2π and χ is the Lorentz local field correction term, given by

$$\chi = \frac{n(n+2)^2}{9} \quad \text{eq. (3)}$$

and $\langle {}^7F_J \parallel U^{(\lambda)} \parallel {}^5D_0 \rangle^2$ is a squared reduced matrix element with value of 0.0032 for the ${}^5D_0 \rightarrow {}^7F_2$ transition and 0.0023 for the ${}^5D_0 \rightarrow {}^7F_4$ one and Ω_λ are the Judd – Ofelt intensity parameters [39, 40]. The refraction index (n) has been assumed equal to 1.5. In this work, the ${}^5D_0 \rightarrow {}^7F_6$ transition was not observed experimentally; consequently, the experimental Ω_6 parameter could not be estimated. Based on the emission spectrum and lifetime of 5D_0 emitting level, the emission quantum efficiency (η) of pure $[\text{Eu}(\text{TTA})_3(\text{H}_2\text{O})_2]$ complex and luminescent CA-GPTMS hybrid film was determined. Initially the emission coefficients A_{02} and A_{04} corresponding to ${}^5D_0 \rightarrow {}^7F_2$ and ${}^5D_0 \rightarrow {}^7F_4$ transitions, respectively, were calculated according to the eq. 1. Considering the ratio between the emitting state lifetime and total decay rate, ($A_{\text{total}} = 1/\tau = A_{\text{rad}} + A_{\text{nrad}}$), the η value can be calculated by the eq. 4 [33]:

$$\eta = \frac{A_{\text{rad}}}{A_{\text{rad}} + A_{\text{nrad}}} \quad \text{eq. (4)}$$

The values of experimental intensity parameters Ω_2 and Ω_4 and quantum efficiency (η) obtained for the Eu^{3+} complex are similar than the luminescent hybrid film and they are in accordance with literature [41]. These results indicate that molecular structure of

Eu^{3+} β -diketonate complex incorporated into the CA-GPTMS 40% hybrid film is preserved upon the incorporation, as well as their photoluminescence properties. Accordingly, CA-GPTMS is an interesting hybrid matrix to incorporate molecular lanthanide complexes. Our findings demonstrated that the combination of cellulose acetate polymer and 3-glycidoxypropyltrimethoxysilane gather to the design of new hybrid material with superior properties ascribed by high flexibility and also transparency in the visible to near-infrared region even at high content of reactive epoxy and methoxysilane functions. The hybrid also meets the requirements to host luminescent complex with minimal deleterious effect on the fluorescence efficiency. This multifunctional hybrid material could find potential applications in different areas as flexible phosphors and UV-visible energy converting devices.

6.3. Conclusion

Flexible and transparent films were obtained from CA and GPTMS. These films presented high transparency, as presented in UV-Vis spectra. AFM images showed increase in the roughness and size of homogeneously dispersed globular-like domains with the relative increase of GPTMS content. XRD patterns showed that higher amounts of GPTMS turn these films more amorphous (in comparison with the neat CA ones). Spectroscopy results (vibrational spectroscopy, ^{13}C and ^{29}Si CP-MAS spectra) suggest that epoxy groups mostly remain intact and significant amount of methoxysilane groups are available after addition of GPTMS in CA. Decomposition temperature occurs around 374°C for all films. The presence of reactive epoxy groups and non-hydrolyzed GPTMS molecules highlights the multi-functionality of the prepared films for further modifications. Luminescent films were obtained by incorporating Eu^{3+} luminescent complex. The calculated spectroscopic parameters of luminescent hybrid were similar to the pure Eu^{3+} complex suggesting that the CA-GPTMS hybrids are suitable to photonic applications.

References

1. Wegst UGK, Bai H, Saiz E, et al. (2014) Bioinspired structural materials. *Nat Mater* 14:23–36. doi: 10.1038/nmat4089
2. Carro L, Hablot E, Coradin T (2014) Hybrids and biohybrids as green materials for a blue planet. *J Sol-Gel Sci Technol* 70:263–271. doi: 10.1007/s10971-013-3153-z
3. Ganster J, Fink H (2013) Cellulose and Cellulose Acetate. In: *Bio-Based Plast*. John Wiley & Sons Ltd, Chichester, UK, pp 35–62
4. Rodrigues Filho G, Monteiro DS, Meireles CDS, et al. (2008) Synthesis and

- characterization of cellulose acetate produced from recycled newspaper. *Carbohydr Polym* 73:74–82. doi: 10.1016/j.carbpol.2007.11.010
5. Lova P, Manfredi G, Boarino L, et al. (2015) Hybrid ZnO:polystyrene nanocomposite for all-polymer photonic crystals. *Phys status solidi* 12:158–162. doi: 10.1002/pssc.201400209
 6. Unno N, Mäkelä T, Taniguchi J (2014) Thermal roll-to-roll imprinted nanogratings on plastic film. *J Vac Sci Technol B, Nanotechnol Microelectron Mater Process Meas Phenom* 32:06FG03. doi: 10.1116/1.4897132
 7. Cook PM, Kelley SS (1992) Grafted cellulose esters containing a silicon moiety. 0–9.
 8. Shojaie SS, Rials TG, Kelley SS (1995) Preparation and characterization of cellulose acetate organic/inorganic hybrid films. *J Appl Polym Sci* 58:1263–1274. doi: 10.1002/app.1995.070580807
 9. Aparecida da Silva C, Maria Favaro M, Pagotto Yoshida IV, do Carmo Gonçalves M (2011) Nanocomposites derived from cellulose acetate and highly branched alkoxy silane. *J Appl Polym Sci* 121:2559–2566. doi: 10.1002/app.33974
 10. Zoppi RA, Gonçalves MC (2002) Hybrids of cellulose acetate and sol-gel silica: Morphology, thermomechanical properties, water permeability, and biodegradation evaluation. *J Appl Polym Sci* 84:2196–2205. doi: 10.1002/app.10427
 11. Heikkinen JJ, Riihimäki TA, MääTTÄ JAE, et al. (2011) Covalent Biofunctionalization of Cellulose Acetate with Thermostable Chimeric Avidin. *ACS Appl Mater Interfaces* 3:2240–2245. doi: 10.1021/am200272u
 12. Achoundong CSK, Bhuwania N, Burgess SK, et al. (2013) Silane Modification of Cellulose Acetate Dense Films as Materials for Acid Gas Removal. *Macromolecules* 46:5584–5594. doi: 10.1021/ma4010583
 13. Charles RG, Ohlmann RC (1965) Europium thenoyltrifluoroacetate, preparation and fluorescence properties. *J Inorg Nucl Chem* 27:255–259. doi: 10.1016/0022-1902(65)80222-6
 14. Silverstein RM, Webster FX, Kiemle D (2005) Spectrometric identification of organic compounds, 7th ed. John Wiley and Sons, New York, U.S.A.
 15. Sapić IM, Bistričić L, Volovsek V, et al. (2009) DFT study of molecular structure and vibrations of 3-glycidoxypropyltrimethoxysilane. *Spectrochim Acta A Mol Biomol Spectrosc* 72:833–40. doi: 10.1016/j.saa.2008.11.032
 16. Toprak C, Agar JN, Falk M (1979) State of water in cellulose acetate membranes. *J Chem Soc Faraday Trans 1 Phys Chem Condens Phases* 75:803.

- doi: 10.1039/f19797500803
17. Firsov SP, Zhbankov RG (1982) Raman spectra and physical structure of cellulose triacetate. *J Appl Spectrosc* 37:940–947. doi: 10.1007/BF00663171
 18. Socrates G (2004) Infrared and Raman characteristic group frequencies. *Infrared Raman Charact Gr Freq*. doi: 10.1002/jrs.1238
 19. Zhang K, Feldner A, Fischer S (2011) FT Raman spectroscopic investigation of cellulose acetate. *Cellulose* 18:995–1003. doi: 10.1007/s10570-011-9545-8
 20. Riegel B, Blittersdorf S, Kiefer W, et al. (1998) Kinetic investigations of hydrolysis and condensation of the glycidoxypopyltrimethoxysilane/aminopropyltriethoxy-silane system by means of FT-Raman spectroscopy I. *J Non Cryst Solids* 226:76–84. doi: 10.1016/S0022-3093(97)00487-0
 21. Kono H, Erata T, Takai M (2002) CP/MAS ^{13}C NMR Study of Cellulose and Cellulose Derivatives. 2. Complete Assignment of the ^{13}C Resonance for the Ring Carbons of Cellulose Triacetate Polymorphs. *J Am Chem Soc* 124:7512–7518. doi: 10.1021/ja010705g
 22. Kono H, Yunoki S, Shikano T, et al. (2002) CP/MAS ^{13}C NMR Study of Cellulose and Cellulose Derivatives. 1. Complete Assignment of the CP/MAS ^{13}C NMR Spectrum of the Native Cellulose. *J Am Chem Soc* 124:7506–7511. doi: 10.1021/ja010704o
 23. Keely CM, Zhang X, McBrierty VJ (1995) Hydration and plasticization effects in cellulose acetate: a solid-state NMR study. *J Mol Struct* 355:33–46. doi: 10.1016/0022-2860(95)08865-S
 24. Williams EA (1984) Recent Advances in Silicon- ^{29}Si NMR Spectroscopy. pp 235–289
 25. Innocenzi P, Brusatin G, Babonneau F (2000) Competitive Polymerization between Organic and Inorganic Networks in Hybrid Materials. *Chem Mater* 12:3726–3732. doi: 10.1021/cm001139b
 26. Barud HS, de Araújo Júnior AM, Santos DB, et al. (2008) Thermal behavior of cellulose acetate produced from homogeneous acetylation of bacterial cellulose. *Thermochim Acta* 471:61–69. doi: 10.1016/j.tca.2008.02.009
 27. Sassi J-F, Chanzy H (1995) Ultrastructural aspects of the acetylation of cellulose. *Cellulose* 2:111–127. doi: 10.1007/BF00816384
 28. Wu H, Fang X, Zhang X, et al. (2008) Cellulose acetate–poly(N-vinyl-2-pyrrolidone) blend membrane for pervaporation separation of methanol/MTBE mixtures. *Sep Purif Technol* 64:183–191. doi: 10.1016/j.seppur.2008.09.013

29. Wang J, Fan X, Tian W, et al. (2011) Ring-opening polymerization of γ -glycidoxypropyltrimethoxysilane catalyzed by multi-metal cyanide catalyst. *J Polym Res* 18:2133–2139. doi: 10.1007/s10965-011-9623-5
30. Yamazaki R, Karyu N, Noda M, et al. (2016) Quantitative measurement of physisorbed silane on a silica particle surface treated with silane coupling agents by thermogravimetric analysis. *J Appl Polym Sci* 133:n/a–n/a. doi: 10.1002/app.43256
31. Malta OL, Brito HF, Menezes JFS, et al. (1997) Spectroscopic properties of a new light-converting device $\text{Eu}(\text{thenoyltrifluoroacetate})_3 \cdot 2(\text{dibenzyl sulfoxide})$. A theoretical analysis based on structural data obtained from a sparkle model. *J Lumin* 75:255–268. doi: 10.1016/S0022-2313(97)00107-5
32. Teotonio EES, Fett GM, Brito HF, et al. (2008) Evaluation of intramolecular energy transfer process in the lanthanide(III) bis- and tris-(TTA) complexes: Photoluminescent and triboluminescent behavior. *J Lumin* 128:190–198. doi: 10.1016/j.jlumin.2007.07.005
33. de Sá G., Malta O., de Mello Donegá C, et al. (2000) Spectroscopic properties and design of highly luminescent lanthanide coordination complexes. *Coord Chem Rev* 196:165–195. doi: 10.1016/S0010-8545(99)00054-5
34. Molina C, Dahmouche K, Messaddeq Y, et al. (2003) Enhanced emission from $\text{Eu}(\text{III})$ β -diketone complex combined with ether-type oxygen atoms of di-ureasil organic–inorganic hybrids. *J Lumin* 104:93–101. doi: 10.1016/S0022-2313(02)00684-1
35. Caiut JM a., Barud HS, Santos M V., et al. (2011) Luminescent multifunctional biocellulose membranes. In: Martín-Palma RJ, Jen Y-J, Mackay TG (eds). p 81040Z–81040Z–9
36. Carlos LD, Messaddeq Y, Brito HF, et al. (2000) Full-Color Phosphors from Europium(III)-Based Organosilicates. *Adv Mater* 12:594–598. doi: 10.1002/(SICI)1521-4095(200004)12:8<594::AID-ADMA594>3.0.CO;2-S
37. de Mello Donegá C, Junior SA, de Sá G. (1997) Synthesis, luminescence and quantum yields of $\text{Eu}(\text{III})$ mixed complexes with 4,4,4-trifluoro-1-phenyl-1,3-butanedione and 1,10-phenanthroline-N-oxide. *J Alloys Compd* 250:422–426. doi: 10.1016/S0925-8388(96)02562-5
38. Raj DBA, Biju S, Reddy MLP (2008) One-, Two-, and Three-Dimensional Arrays of

- Eu³⁺ -4,4,5,5,5-pentafluoro-1-(naphthalen-2-yl)pentane-1,3-dione complexes:
Synthesis, Crystal Structure and Photophysical Properties. *Inorg Chem* 47:8091–8100.
doi: 10.1021/ic8004757
39. Judd BR (1962) Optical Absorption Intensities of Rare-Earth Ions. *Phys Rev* 127:750–761. doi: 10.1103/PhysRev.127.750
40. Ofelt GS (1962) Intensities of Crystal Spectra of Rare-Earth Ions. *J Chem Phys* 37:511. doi: 10.1063/1.1701366
41. Malta OL, Brito HF, Menezes JFS, et al. (1998) Experimental and theoretical emission quantum yield in the compound Eu(thenoyltrifluoroacetate)₃.2(dibenzyl sulfoxide). *Chem Phys Lett* 282:233–238. doi: 10.1016/S0009-2614(97)01283-9

7. THIN FILMS BASED ON POLYSTYRENE WASTES RECOVERY FOR OPTICAL APPLICATIONS

Polystyrene (PS) is a synthetic polymer obtained by polymerization of styrene, an aromatic hydrocarbon. The main commercial form produced is the expanded polystyrene (EPS), that is usually composed by 98% of air. Approximately 3 millions tons of EPS are produced every year and wastes generally ends up discarding in landfills or disposal by incineration.[1] Due to the low density of the solid waste, the issues faced in the EPS recycling are related with unattractive small-scale collection, uneconomical bulk volume storage as well as transportation cost effective for commercial purposes. Conventional EPS recycling methods involve degasification by thermal processes, which has harmful impact on the environment concerning energy consumption and global warming potential.

Recently, some studies have paid attention for new friendly-environmental strategies of EPS waste recycling by dissolutions methods in non-toxic solvents. Some advantages of recycling approach based on dissolution of EPS wastes is the low-energy consumption due to room temperature processability, preventing eventual degradation of PS and enabling easy recover of solvent afterwards. In spite the good solubility of PS in aromatic solvents, significant efforts have been devoted on the study of cyclic monoterpenes from tree essential oil as potential “green” solvent alternatives on the dissolution of EPS waste. D-limonene is a cyclic monoterpene found as the main component of oil extracted from the rinds of citrus in the orange juice production. Besides low cost of production, D-limonene is a biodegradable compound, presents low toxicity and it is obtained from renewable sources. Remarkably, it is a green solvent that can dissolve substantial quantity of PS (400 g of PS/L of D-limonene) resulting in a clear solution with tailorable viscosity. Specifically, D-limonene allows the reduction of 95% in the original EPS waste volume. Noteworthy, Nogushi et al. has been reported a prototype of an apparatus to dissolve EPS waste and a recycling plant to separate the d-limonene in industrial scale.[2]

Recovered PS polymer from EPS waste has an excellent processability and its glass transition temperature is about 100 °C. The PS has a high transparency and does not present fluorescence at UV/visible spectral range ($\lambda > 290$ nm). The PS polymer shows high refractive index ($n = 1.59$) and low spherical and chromatic aberrations, which makes it suitable material for fabrication of plastic lenses and glasses for optical measurements.[3] In comparison among others synthetic polymers, PS is very radiation resistant at non-oxidative atmosphere due to highly aromatic structure, whereby has been widely used as important base for plastic

scintillators. In addition, due to its moderate permeability, mechanical flexibility and biocompatibility, PS polymer has been studied as host matrix for the fabrication of optical gas sensing and optoelectronic nanocomposites.[4–6]

The association of recovered PS with luminescent compounds such as organic dyes, quantum dots or lanthanide complexes in solution phase offers an excellent platform to conceive functional luminescent materials which can be potentially applied to development of luminescent sensors, flexible OLED's substrates, waveguides and solar concentrators. Solution phase presents interesting advantages for the fabrication of luminescent materials like homogeneous distribution of luminophors in the polymeric matrix and processability at room temperature. Lanthanide ions (Ln^{3+}) are well-known for having sharp emission and excitation bands in the near-UV, visible and near-infrared spectral regions widely explored in a myriad of optical materials. However, Ln^{3+} display low luminescence intensity once 4f-4f transitions are parity forbidden.[7] Due to the poor ability to absorb light, lanthanide ions are usually coordinated with suitable *organic* “light harvesting” chromophores having large molar absorption coefficient. The light absorption of Ln^{3+} can be tailored by selecting appropriate organic ligand in order to sensitize the emission increasing its intensity.[8] Although Ln^{3+} complexes unveil remarkable luminophors, their use in practical applications is hindered by their limited solubility, photodegradability and thermal stability issues. The incorporation of Ln^{3+} complexes into polymers is extremely attractive, because the hybrids offers thermally and mechanically stable luminescent materials with easy processability over solution phase.[8]

Due to aforementioned striking optical properties of PS polymer, high quality fashionable materials from recycling of EPS waste could be achieved by dissolution in D-limonene driving us to produce outstanding optical materials towards environmental-friendly as well as sustainable routes. To the best of our knowledge, there is still no reports disclosing the fabrication of optical materials derived from EPS waste and luminescent Ln^{3+} complex in the literature. Hopefully our work may contribute meaningful information on the sustainable development of optical materials based on environmental-friendly recycling of non-attractive EPS waste by dissolution in green solvent.

7.1. Experimental procedure

7.1.1. Materials

Hydrochloric acid (37%), 2-propanone, ethanol, ammonium hydroxide (28%) and 2-thenoyltrifluoroacetone (99%) were purchased from Sigma-Aldrich and europium (III) oxide

(99.99 %) was purchased from Lumintech (São Paulo, Brazil). D-limonene were gift samples from Citrosuco S/A (Matão, Brazil).

7.1.2. Synthesis of luminescent $[Eu(tta)_3(H_2O)_2]$ complex

Europium chloride stock solution were prepared by dissolving europium (III) oxide (14.2 mmol, 5.0 g) in hydrochloric acid (85.2 mmol, 7.12 mL) under heating at 100 °C and slow magnetic stirring at 500 rpm until total dissolution. The solution was heated to evaporate the excess of HCl with continuous addition of MiliQ water until reach pH ~ 5. The concentration of aqueous solution of $EuCl_3 \cdot 6H_2O$ was determined by EDTA titration with a value of 0.13 mol L⁻¹. Based on previous reports [9], 2-thenoyltrifluoroacetone (3.9 mmol, 0.86 g), ammonium (15 mmol, 0.450 mL) and europium chloride (1.3 mmol, 10.0 mL) were dissolved in ethanol (18.75 mL) under vigorous stirring in a round-bottom flask. After three hours, the resulting solid was precipitated by cooling the flask in ice bath. The precipitate was filtered off and dissolved in acetone. The resulting solution was washed with cold water, filtered again and dried in vacuum.

7.1.3. Fabrication of PS-Eu thin films by spin-coating

Polystyrene (PS) thin films were prepared from recycling of expanded polystyrene (EPS) using D-limonene as solvent. PS stock solution was prepared by dissolving 15.0 g of EPS from packages of chemical bottles in 100 mL of D-limonene followed by centrifugation at 6,000 rpm to remove solid particles of impurities presents in EPS. The incorporation of luminescent complex in PS solution was achieved by dissolving different contents of $[Eu(tta)_3(H_2O)_2]$ complex (0.5, 1.0, 2.5 and 5.0 wt%) in D-limonene into PS 15 wt% stock solution. Spin coating technique was used for the film deposition onto quartz substrates that were cut in 25 mm x 25 mm. The quartz substrates were previously cleaned by sonication in base piranha etching solution being rinsed several times with water, ethanol and acetone. Uniform thin films of PS- $[Eu(tta)_3(H_2O)_2]$ were obtained in SCS spincoater, model P6700 Series, by spin coating 300 µL of PS solutions onto cleaned quartz substrates at 1,500 rpm for 60 seconds and dried in air at room temperature.

7.1.4. Instrumentation

Ultraviolet-visible (UV-Vis) transmittance spectra for PS films were recorded in a Varian spectrophotometer model Cary 5000 in the region of 800 to 200 nm with resolution of 1 nm.

The excitation and emission spectra were recorded in a Horiba Jobin Yvon Fluorolog spectrofluorimeter model FL3-222 equipped with a Hamamatsu R928 photomultiplier and Xe lamp (450 W) using the excitation mode front face with resolution of 0.5 nm at 298 K.

Fast-Fourier Transform Infrared (FTIR) spectra were registered in a Bruker spectrophotometer model Vertex 70 in the region of 4000 to 400 cm^{-1} , using 64 scans with resolution of 2 cm^{-1} in the attenuated total reflectance mode (ATR).

Refractive index (n) and thickness (w) of films are measured in a Metricon prism coupler model 2010/M using a prism with n range of 1.20 to 2.02 and a laser of 543 nm as light source.

7.2. Results and discussion

The recovery process of PS from EPS wastes by using D-limonene as solvent is presented in the schematic representation of Figure 72.

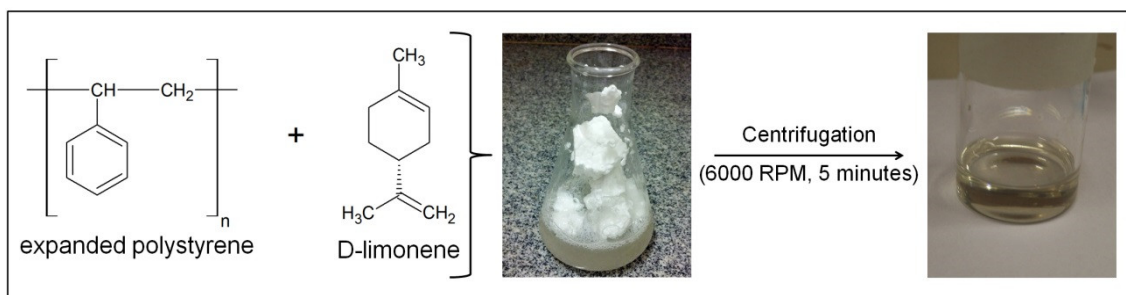


Figure 72. Preparation of PS 15 wt% stock solution. The dissolution of EPS in D-limonene releases the air present in EPS structure. Larger solid particles present in EPS are further removed by centrifugation to obtain a clean and homogeneous solution.

After the incorporation of Eu^{3+} complex in PS the stock solution, transparent and luminescent thin films were obtained by the spin coating process, as showed in Figure 72. Under UV light, the films containing $[\text{Eu}(\text{tta})_3(\text{H}_2\text{O})_2]$ complex show red emission color characteristic of Eu^{3+} ion.

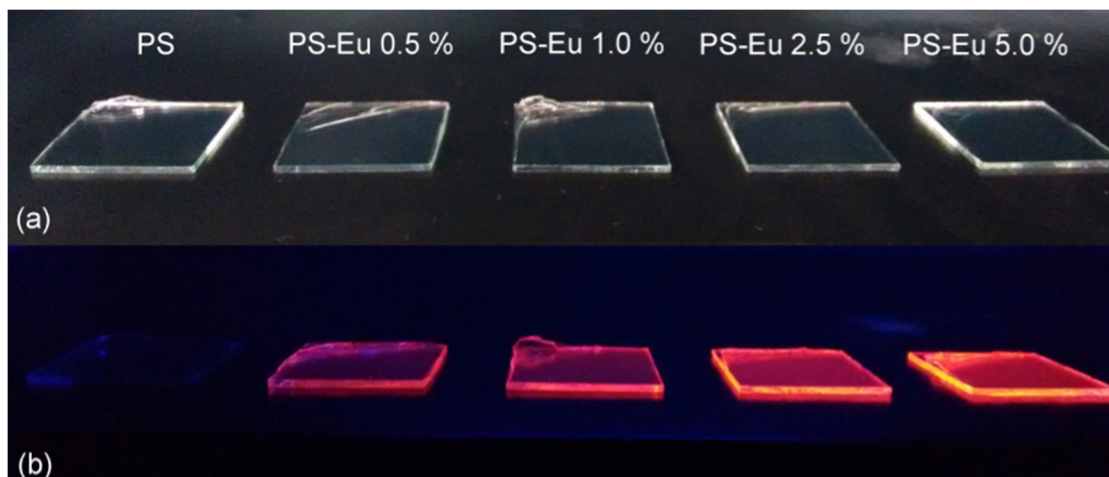


Figure 73. (a) Picture of PS and PS-Eu films obtained by spin coating technique under (a) white light, and (b) commercial UV light ($\lambda_{\text{max}} = 365 \text{ nm}$).

The high transparency of films is confirmed by absorbance spectra of PS and PS-Eu films in the Figure 73, with values above 90% of transparency in the visible region. The peak observed at 344 nm to PS-Eu samples correspond to $S_0 \rightarrow S(\pi, \pi^*)$ transition of *tta* ligand.[9, 10]

The highest concentration of $[\text{Eu}(\text{tta})_3(\text{H}_2\text{O})_2]$ in PS films studied was 5.0 wt% due to the limited solubility of the complex in the D-limonene.

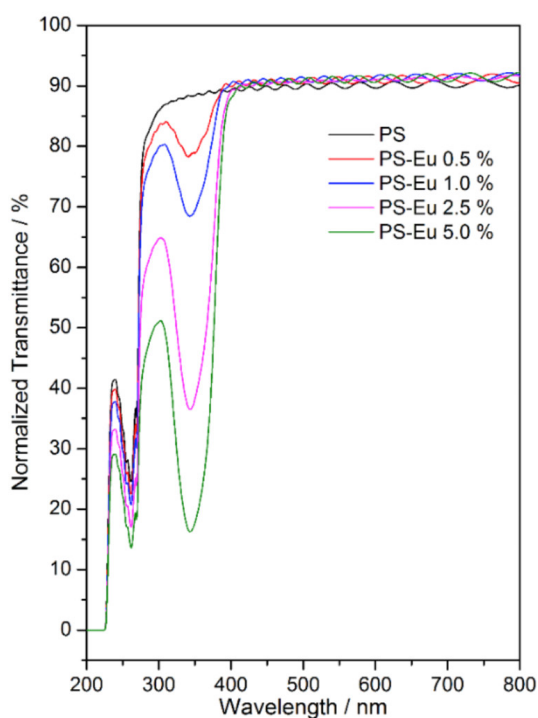


Figure 74. Ultraviolet-visible transmittance spectra of PS and PS-Eu films containing different concentration of $[\text{Eu}(\text{tta})_3(\text{H}_2\text{O})_2]$ complex.

The intense band observed at 262 nm of transmittance spectra is assigned to $\pi \rightarrow \pi^*$ transition of phenyl group of PS matrix.[11–13] It is worth to pointing up that the interference fringes observed in visible region of UV-Vis spectra provide evidence of micrometric thickness of the films.[14,15] Additionally, we estimated thickness (w) as well as the refractive index (n) of films by using the prism coupling technique and analyzing the m-line pattern in transverse electric (TE) polarization.[16,17] The data concerning n , w and number of propagating modes of light are presented in Table 5

Table 5. Optical parameters of PS and PS-Eu films measured at 543 nm with transverse electric polarization: thickness (w) and refractive index (n).

Sample	[Eu(tta) ₃ (H ₂ O) ₂] content (wt%)	n at 543 nm (± 0.0005)	w ($\pm 0.1 \mu\text{m}$)	number of modes at 543 nm
PS	-	1.5594	1.5	4
PS-Eu 0.5 %	0.5	1.5625	1.5	4
PS-Eu 1.0 %	1.0	1.5789	1.9	6
PS-Eu 2.5 %	2.5	1.5788	2.1	6
PS-Eu 5.0 %	5.	1.5862	2.5	7

The deposition of films onto quartz substrate results in waveguides, where the light is guided in the interface between the film and substrate. The number of propagating modes of light in a waveguide depends on factors like n and w and, once n and w increases with the [Eu(tta)₃(H₂O)₂] content, the number of modes also increase. The incorporation of Eu³⁺ complex in PS matrix results in a higher interaction between film components and the light source, reducing the speed of light propagation in films and, consequently, increasing n .

The Figure 75i and Figure 75ii displays the FTIR spectra of [Eu(tta)₃(H₂O)₂] complex, PS and PS-Eu films at region of 4000-400 cm⁻¹ and 1425-800 cm⁻¹, respectively. The FTIR spectra of films present basically the same profile, indicating that the incorporation of Eu³⁺ complex in PS matrix did not modify the structure of polymer.

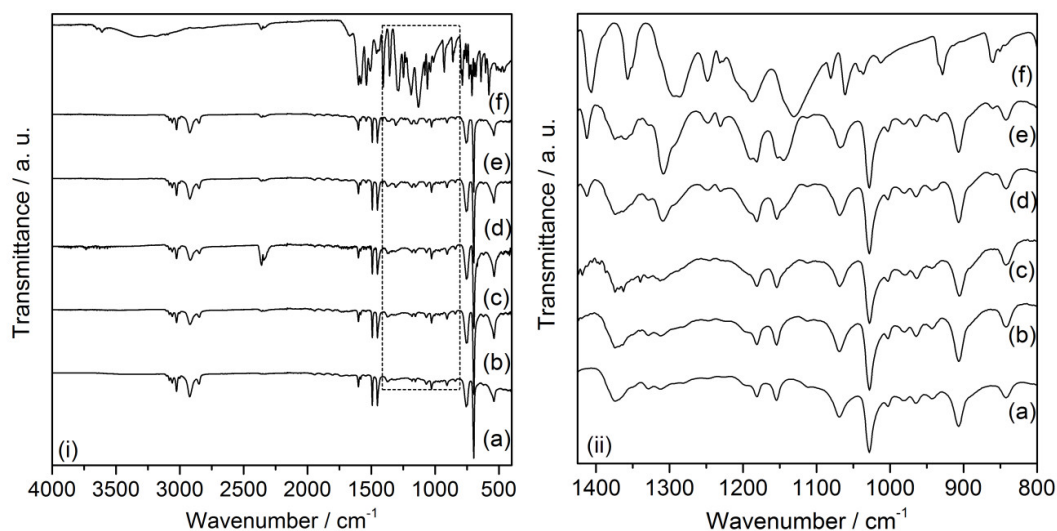


Figure 75. (i) ATR-FTIR of: (a) PS, (b) PS-Eu 0.5 %; (c) PS-Eu 1.0 %; (d) PS-Eu 2.5 %, (e) PS-Eu 5.0 % and (f) $[\text{Eu}(\text{tta})_3(\text{H}_2\text{O})_2]$. (ii) Amplified 1425-800 cm^{-1} region of samples.

The presence of bands at 1376, 1154 and 842 cm^{-1} in the spectra of films is related with amorphous phase of PS, indicating that PS recovered from EPS waste present atactic conformational structure. Additionally, the bands at 1154 and 842 cm^{-1} are associated with modes of the phenyl group.[19] The bands at 1181 and 1154 cm^{-1} of PS are broadened by the superposition with $\nu(\text{C}=\text{C})$ and $\nu(\text{C}-\text{F}_3)$ vibration modes of complex at 1188 and 1130 cm^{-1} , respectively.

The luminescence properties of complex and films were investigated by photoluminescence spectroscopy. Figure 76 shows the excitation and emission spectra of PS and PS-Eu films.

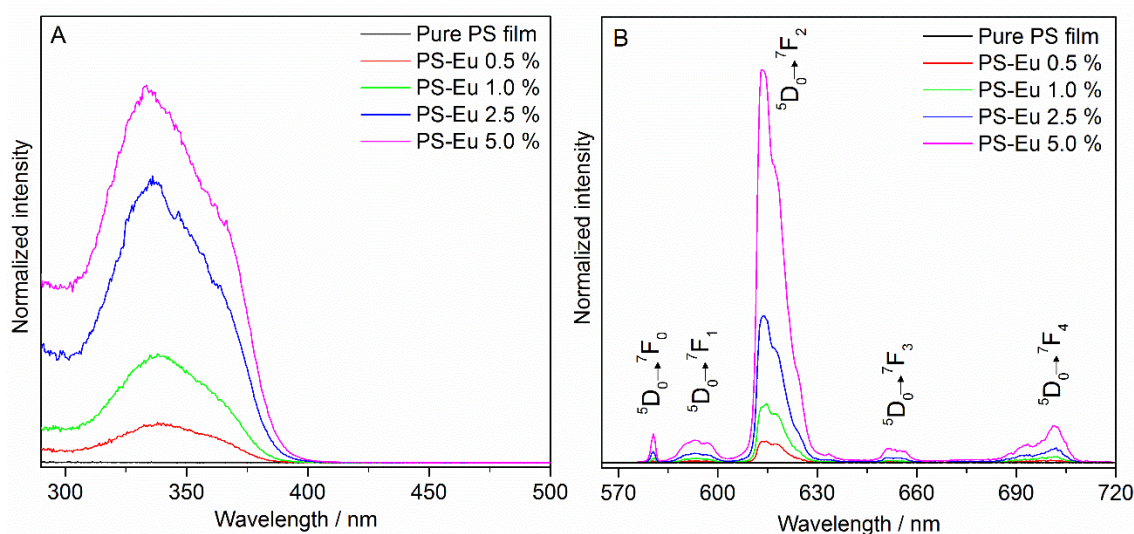


Figure 76. (A) Excitation spectra of pristine PS and PS-Eu films recorded monitoring emission at 614 nm. (B) Emission spectra of pristine PS and PS-Eu films by monitoring excitation at 335 nm.

The excitation and emission spectra of pure $[\text{Eu}(\text{tta})_3(\text{H}_2\text{O})_2]$ complex in solid state are shown in Figure 77.

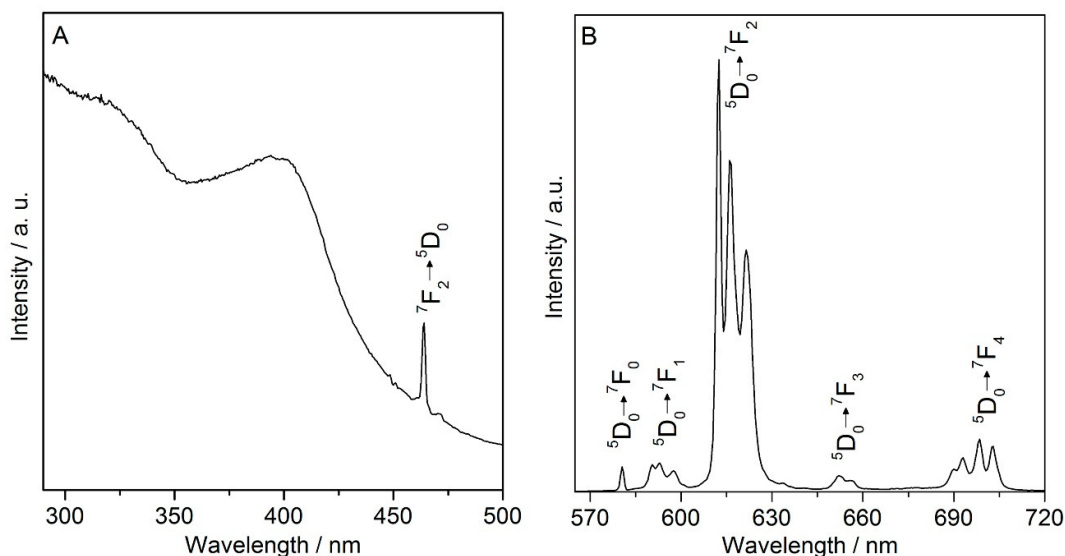


Figure 77. (A) Excitation spectra recorded of $[\text{Eu}(\text{tta})_3(\text{H}_2\text{O})_2]$ powder monitoring emission at 612 nm. (B) Emission spectrum of $[\text{Eu}(\text{tta})_3(\text{H}_2\text{O})_2]$ powder by excitation at 396 nm.

For both PS-Eu films and pure $[\text{Eu}(\text{tta})_3(\text{H}_2\text{O})_2]$ complex, the broad bands at wavelengths below 400 nm are related to absorption from *tta* ligand and energy transfer to Eu^{3+} ion.[20] Specifically, the broad band at 335 nm of the excitation spectra of PS-Eu films in Figure 76A is attributed to singlet \rightarrow singlet* transition of *tta* ligand.[10] The narrow excitation line of ${}^7\text{F}_2 \rightarrow {}^5\text{D}_0$ transition at 464 nm is only observed for the $[\text{Eu}(\text{tta})_3(\text{H}_2\text{O})_2]$ complex (Figure 77A), but it is hardly observed in the PS-Eu films. The complex in the solid state presents a high absorption cross section of light in the UV region leading to saturation and distortion of excitation spectrum.[21,22]

The spike emission lines in the spectra are characteristics of ${}^5\text{D}_0 \rightarrow {}^7\text{F}_J$ ($J=0-4$) transitions of Eu^{3+} . The strong red emission of complex and PS-Eu films is a result of high intensity of hypersensitive ${}^5\text{D}_0 \rightarrow {}^7\text{F}_2$ transition around 612 nm. The following Eu^{3+} transitions from ${}^5\text{D}_0$ to ${}^7\text{F}_J$ levels in the solid complex are observed: ${}^5\text{D}_0 \rightarrow {}^7\text{F}_0$ (580.5 nm), ${}^5\text{D}_0 \rightarrow {}^7\text{F}_1$ (590.5, 593.0 and 597.5 nm), ${}^5\text{D}_0 \rightarrow {}^7\text{F}_2$ (612.5, 616.0 and 621.5 nm), ${}^5\text{D}_0 \rightarrow {}^7\text{F}_3$ (652.0 and 655.5 nm), ${}^5\text{D}_0 \rightarrow {}^7\text{F}_4$ (690.0, 693.0, 698.5 and 703.0 nm). The distortion of emission spectrum of pure $[\text{Eu}(\text{tta})_3(\text{H}_2\text{O})_2]$ complex shown in Figure 77B comparing to the emission of PS-Eu films spectra in Figure 76B is related with the presence of Eu^{3+} in the amorphous polymeric matrix. In addition, the transition ${}^5\text{D}_0 \rightarrow {}^7\text{F}_0$ of Eu^{3+} in PS-Eu films present only one sharp line with full width at half maximum value higher than 40 cm^{-1} , suggesting the occurrence of only one site occupied by Eu^{3+} in a low-symmetry environment.[9,21]

The comparison of Eu^{3+} luminescence data in PS matrix may be more accurately performed to provide information of films structure by the calculation of a set of values: the Judd-Olfet intensity parameters (Ω_2, Ω_4), radiative rates (A_{rad}), non-radiative rates (A_{nrad}), radiative lifetimes (τ_{rad}), quantum efficiencies (η) and the number of water molecules at the Eu^{3+} first coordination shell (n_w). [23] The ratios of integrated intensities $I(^5\text{D}_0 \rightarrow ^7\text{F}_J=0-6)$ to $I(^5\text{D}_0 \rightarrow ^7\text{F}_1)$ may be applied to calculate the $^5\text{D}_0 \rightarrow ^7\text{F}_J$ radiative rates $A_{0 \rightarrow J}$. The $A_{0 \rightarrow J}$ was calculated using Eq. (1) [24]:

$$A_{0 \rightarrow J} = \frac{64\pi^4 e^2 \tilde{\nu}^3}{3 (2J + 1)} \left[\frac{n(n^2 + 2)^2}{9} \right] D_{ED} + n^3 D_{MD} \quad (1)$$

where $\tilde{\nu}$ is average transition energy in cm^{-1} , h is the Planck's constant, n is the refractive index of medium, D_{ED} and D_{MD} are the electric and magnetic dipole strengths, respectively. The $^5\text{D}_0 \rightarrow ^7\text{F}_1$ emission is purely magnetic dipolar and its radiative rate does not depend on the local ligand field. [23] Therefore, it was used as the internal standard and $^5\text{D}_0 \rightarrow ^7\text{F}_1$ oscillator strength was calculated from theory, giving $A_{0 \rightarrow 1} = 14.65n^3$ in s^{-1} , with $n = 1.5$ as medium's refractive index. From these considerations, the $A_{0 \rightarrow J}$ ($J = 0, 2-6$) may be calculated using Eq. (2) [24]:

$$A_{0\lambda} = \frac{\nu_{01}}{\nu_{0\lambda}} \frac{S_{0\lambda}}{S_{01}} \cdot (A_{01}) \quad (2)$$

Considering that $^5\text{D}_0 \rightarrow ^7\text{F}_{5,6}$ have negligible intensities values, the $A_{\text{rad}} = \Sigma A_{0 \rightarrow J}$ and the $^5\text{D}_0$ radiative lifetime ($\tau_{\text{rad}} = 1/A_{\text{rad}}$) were calculated. The $A_{0 \rightarrow 2}$ and $A_{0 \rightarrow 4}$ values are related with the Judd-Olfet intensity parameters Ω_2 and Ω_4 , calculated applying Eq. (3) [24]:

$$\Omega_\lambda = \frac{3 c^3 A_{0 \rightarrow J}}{4e^2 \omega^3 \chi < ^7F_J \parallel U^{(\lambda)} \parallel ^5D_0 >^2} \quad (3)$$

where ω is the angular frequency of the transition, \hbar is the Planck's constant under 2π , e is the elementary charge, c is the velocity of light χ is the Lorentz local field correction term, given by

$$\chi = \frac{n(n + 2)^2}{9} \quad (4)$$

and ${}^7_0F_J \parallel U^{(\lambda)} \parallel {}^5_0D_0$ is a reduced matrix element. [21]

The experimental lifetime (τ) of the $^5\text{D}_0$ of Eu^{3+} were obtained by adjust of luminescence decay curves with a first-order exponential decay function ($I = I_0 \exp(-t/\tau)$) and the quantum efficiencies η of the samples were obtained by the ratio of τ and τ_{rad} , $q = \tau/\tau_{\text{rad}}$. Based on experimental lifetime (τ) and A_{rad} rate, it was possible to determine the non-radiative rates (A_{nrad}), so $A_{\text{total}} = 1/\tau = A_{\text{rad}} + A_{\text{nrad}}$ [8]

Considering the ratio between the emitting state lifetime and total decay rate, the η value can be calculated by the Eq. 5 [21]:

$$\eta = \frac{A_{rad}}{A_{rad} + A_{nrad}} \quad (5)$$

Finally, the number of water molecules at the Eu^{3+} first coordination shell (n_w) was calculated by the Eq. (6).[21]

$$n_w = 1.11 \cdot \left(\frac{1}{\tau} - \frac{1}{\tau_{rad}} - 0.31 \right) \quad (6)$$

The values established for the $[\text{Eu}(\text{tta})_3(\text{H}_2\text{O})_2]$ complex in the solid state and PS-Eu films are presented in Table 6.

The values of non-radiative rates (A_{nrad}) and the number of water molecules (n_w) in the Eu^{3+} first coordination sphere does not present significant changes, indicating that does not occurs substitution of water molecules in first coordination sphere and, consequently, PS matrix does not act as luminescence sensitizer in the energy transfer process from polymer to Eu^{3+} as showed in the emission spectra of PS-Eu films.[9] The analysis of Judd-Ofelt intensity parameters suggest that environment of Eu^{3+} does not change, once that Ω_2 and Ω_4 values of $[\text{Eu}(\text{tta})_3(\text{H}_2\text{O})_2]$ and films are quite similar. The interaction between Eu^{3+} and PS was weak, presenting the same luminescent properties of complex in the films with low content of but enough to stabilize the rare-earth ion in the matrix in a low-symmetry environment, $[\text{Eu}(\text{tta})_3(\text{H}_2\text{O})_2]$.[23]

Table 6. Judd-Ofelt Intensity Parameters (Ω_2, Ω_4), Radiative Rates (A_{rad}), Experimental Lifetimes (τ), Radiative Lifetimes (τ_{rad}) and Quantum Efficiencies (η) and number of equivalent water molecules (n_w) of the $[\text{Eu}(\text{tta})_3(\text{H}_2\text{O})_2]$ complex and PS-Eu films.

Sample	Ω_2 .10 ⁻²⁰ cm ²	Ω_4 .10 ⁻²⁰ cm ²	A_{rad} ms ⁻¹	A_{rad} ms ⁻¹	τ_{rad} ms	τ ms	q	n_w
$[\text{Eu}(\text{tta})_3(\text{H}_2\text{O})_2]$	21.41 ± 2.1	4.40 ± 0.50	0.83 ± 0.08	2.74 ± 0.47	1.20 ± 0.12	0.28	0.23 ± 0.05	2.7
PS-Eu 0.5 %	17.10 ± 1.71	3.86 ± 0.38	0.68 ± 0.07	2.35 ± 0.35	1.47 ± 0.14	0.33	0.22 ± 0.04	2.3
PS-Eu 1.0 %	18.60 ± 1.86	3.61 ± 0.36	0.71 ± 0.07	2.23 ± 0.33	1.40 ± 0.41	0.34	0.24 ± 0.09	2.1
PS-Eu 2.5 %	20.30 ± 1.86	3.43 ± 0.34	0.77 ± 0.07	2.46 ± 0.39	1.30 ± 0.13	0.31	0.23 ± 0.05	2.4
PS-Eu 5.0 %	22.40 ± 2.24	3.44 ± 0.34	0.84 ± 0.08	2.49 ± 0.42	1.19 ± 0.12	0.30	0.25 ± 0.05	2.4

7.3. Conclusions

Transparent thin films were successfully tailored by spin-casting a solution of expanded-polystyrene waste dissolved in citrus oil derivative solvent, D-limonene. Luminescent thin films based on EPS films were prepared by simple incorporation of red emitting Eu^{3+} β -diketonate complex. The high miscibility of Eu^{3+} complex in the EPS solution in the range of 0.5-5 wt% enabled the preparation of homogenous luminescent films with tunable waveguiding properties. From FTIR and luminescent measurements, the EPS derivative films acts as inert host material for Eu^{3+} β -diketonate complex. Remarkably, recycling EPS wastes by simple dissolution in D-limonene was feasible to generate high quality optical films under low cost, sustainable and green process. To the best of our knowledge, this is the first report exploring the fabrication of optical materials from EPS waste. Owing the easy processing and elegant outcome, we highlight that others recyclable polymers or optically active compounds can be explored using this approach to fashion cheap, sustainable and still high quality optical materials.

References

- [1] P.N.S. Schmidt, M.O.H. Cioffi, H.J.C. Voorwald, J.L. Silveira, Flexural Test On Recycled Polystyrene, *Procedia Eng.* 10 (2011) 930–935. doi:10.1016/j.proeng.2011.04.153.
- [2] T. Noguchi, Y. Inagaki, M. Miyashita, H. Watanabe, A new recycling system for expanded polystyrene using a natural solvent. Part 2. Development of a prototype production system, *Packag. Technol. Sci.* 11 (1998) 29–37. doi:10.1002/(sici)1099-1522(199802)11:1<29::aid-pts415>3.0.co;2-1.
- [3] R.N. Nurmukhametov, L. V. Volkova, S.P. Kabanov, Fluorescence and absorption of polystyrene exposed to UV laser radiation, *J. Appl. Spectrosc.* 73 (2006) 55–60. doi:10.1007/s10812-006-0035-y.
- [4] J.R. Li, J.R. Xu, M.Q. Zhang, M.Z. Rong, Carbon black/polystyrene composites as candidates for gas sensing materials, *Carbon N. Y.* 41 (2003) 2353–2360. doi:10.1016/S0008-6223(03)00273-2.
- [5] F. Gu, X. Yin, H. Yu, P. Wang, L. Tong, Polyaniline/polystyrene single-nanowire devices for highly selective optical detection of gas mixtures., *Opt. Express.* 17 (2009) 11230–11235. doi:10.1364/OE.17.011230.

- [6] D. Qian, E. Dickey, R. Andrews, T. Rantell, Load transfer and deformation mechanisms in carbon nanotube-polystyrene composites, *Appl. Phys. Lett.* 2868 (2000) 4–7. doi:10.1063/1.126500.
- [7] N. Sabbatini, M. Guardigli, J.-M. Lehn, Luminescent lanthanide complexes as photochemical supramolecular devices, *Coord. Chem. Rev.* 123 (1993) 201–228. doi:10.1016/0010-8545(93)85056-A.
- [8] J. Kai, M.C.F.C. Felinto, L.A.O. Nunes, O.L. Malta, H.F. Brito, Intermolecular energy transfer and photostability of luminescence-tuneable multicolour PMMA films doped with lanthanide- β -diketonate complexes, *J. Mater. Chem.* 21 (2011) 3796. doi:10.1039/c0jm03474f.
- [9] J. Kai, D.F. Parra, H.F. Brito, Polymer matrix sensitizing effect on photoluminescence properties of Eu^{3+} - β -diketonate complex doped into poly- β -hydroxybutyrate (PHB) in film form, *J. Mater. Chem.* 18 (2008) 4549. doi:10.1039/b808080a.
- [10] O.L. Malta, H.F. Brito, J.F.S. Menezes, F.R.G.E. Silva, S. Alves, F.S. Farias, a. V.M. de Andrade, Spectroscopic properties of a new light-converting device $\text{Eu}(\text{thenoyltrifluoroacetate})_3 \cdot 2(\text{dibenzyl sulfoxide})$. A theoretical analysis based on structural data obtained from a sparkle model, *J. Lumin.* 75 (1997) 255–268. doi:10.1016/S0022-2313(97)00107-5.
- [11] M.S. Khan, W. Khan, A. Khan, Y. Iqbal, UV Absorbance Studies of Dilute Polystyrene Solutions in Different Solvents, *J. Chem. Soc. Pakistan.* 24 (2002) 237–240.
- [12] T. Li, C. Zhou, M. Jiang, UV absorption spectra of polystyrene, *Polym. Bull.* 25 (1991) 211–216.
- [13] E.R. Clark, S.G. Williams, The conformations of aromatic ethers as determined from their ultraviolet absorption spectra, *J. Chem. Soc.* 13 (1967) 859–866.
- [14] R. Swanepoel, Determination of the thickness and optical constants of amorphous silicon, *J. Phys. E.* 16 (1983) 1214–1222. doi:10.1088/0022-3735/16/12/023.
- [15] E.R. Shaaban, I.S. Yahia, E.G. El-Metwally, Validity of Swanepoel 's Method for Calculating the Optical Constants of Thick Films, *Acta Phys. Pol. A.* 121 (2012) 628–635.
- [16] S.J.L. Ribeiro, Y. Messaddeq, R.R. Gonçalves, M. Ferrari, M. Montagna, M.A. Aegerter, Low optical loss planar waveguides prepared in an organic – inorganic hybrid system, *Appl. Phys. Lett.* 77 (2000) 3502–3504. doi:10.1063/1.1329159.
- [17] R. Ulrich, R. Torge, Measurement of thin film parameters with a prism coupler., *Appl. Opt.* 12 (1973) 2901–2908. doi:10.1364/AO.12.002901.

- [18] S.J.L. Ribeiro, Y. Messaddeq, R.R. Gonçalves, M. Ferrari, M. Montagna, M.A. Aegerter, Low optical loss planar waveguides prepared in an organic–inorganic hybrid system, *Appl. Phys. Lett.* 77 (2000) 3502. doi:10.1063/1.1329159.
- [19] A.R. Albunia, P. Musto, G. Guerra, FTIR spectra of pure helical crystalline phases of syndiotactic polystyrene, *Polymer (Guildf)*. 47 (2006) 234–242. doi:10.1016/j.polymer.2005.10.135.
- [20] A.P. Duarte, L. Mauline, M. Gressier, J. Dexpert-Ghys, C. Roques, J.M.A. Caiut, E. Deffune, D.C.G. Maia, I.Z. Carlos, A.A.P. Ferreira, S.J.L. Ribeiro, M.J. Menu, Organosilylated complex [Eu(TTA)₃(Bpy-Si)]: A bifunctional moiety for the engineering of luminescent silica-based nanoparticles for bioimaging, *Langmuir*. 29 (2013) 5878–5888. doi:10.1021/la400365c.
- [21] A.P. Duarte, M. Gressier, M.-J. Menu, J. Dexpert-Ghys, J.M.A. Caiut, S.J.L. Ribeiro, Structural and Luminescence Properties of Silica-Based Hybrids Containing New Silylated-Diketonato Europium(III) Complex, *J. Phys. Chem. C*. 116 (2012) 505–515. doi:10.1021/jp210338t.
- [22] G. Blasse, A. Meijerink, C. de Mello Donegá, Vibronic rare earth spectroscopy: Results and pitfalls, *J. Alloys Compd.* 225 (1995) 24–27. doi:10.1016/0925-8388(94)07002-4.
- [23] F.A. de Jesus, S.T.S. Santos, J.M.A. Caiut, V.H.V. Sarmiento, Effects of thermal treatment on the structure and luminescent properties of Eu³⁺ doped SiO₂–PMMA hybrid nanocomposites prepared by a sol–gel process, *J. Lumin.* 170 (2016) 588–593. doi:10.1016/j.jlumin.2015.05.030.
- [24] L.D. Carlos, R.A.S. Ferreira, V. De Zea Bermudez, S.J.L. Ribeiro, Lanthanide-containing light-emitting organic-inorganic hybrids: A bet on the future, *Adv. Mater.* 21 (2009) 509–534. doi:10.1002/adma.200801635.

8. DISCUSSION

In summary, we have demonstrated a simple, versatile, and large-scale synthesis method for fabricating Te1D nanostructures in the shape of whiskers, wires and helices with diameter below 20 nm and lengths up to 1 μm in all-aqueous synthesis assisted by Pluronic® F68 under relatively low temperature. For instance, Te nanowhiskers, nanohelices and nanowires were synthesized at 40 °C, 60 °C and 90 °C, respectively while others parameters were kept unchanged. Te1D nanostructures in the shape of whiskers, wires and helices could be easily achieved by adjusting experimental parameters like temperature and ratio between tellurium oxide and hypophosphorous acid (reductant agent).

A detailed inspection of the tip end of nanowhiskers unveiled both amorphous and crystalline phases shaped into wave-like structure. The middle portion of Te nanowhiskers displayed a structure rich in plane defects such as dislocation and stacking faults. On the other hand, Te nanowires were high crystalline and defect-free both in the very end or in the middle portion of the nanostructure. It has been shown that the temperature play a pivotal role in the crystallinity of Te nanostructures and therefore, on the population of amorphous or trigonal Te nanoparticles. When the reaction temperature is set to 60 °C, crystalline Te nanohelices is achieved. The Te nanohelices had diameter in the range of 9-20 nm and lengths below 1 μm . The driving force for the assembly of Te nanohelices is unknown. Ongoing work is being undertaken to evaluate the kinetic control of amorphous and trigonal Te nanoparticles population that are hypothetically involved in the formation of Te nanohelices.

Several strategies has been evaluated on the pursuit for more complex nanoarchitectures based on the alignment of Te1D nanostructure. Bundles of Te nanowhiskers and micro-arrays of Te nanowires were achieved by liquid-liquid interfaces and drop casting methods, respectively. Although, more complex architectures of aligned 1D nanostructures arrays are restricted due to the incompatible surface of the Te nanostructures with solvents others than water.

Semiconductor/metallic 1D hybrid nanostructures were easily prepared by decorating Te nanowires with Ag nanoparticles in the presence of poly(vinylpyrrolidone). In an effort to extend this remarkably chemistry to the fabrication of derivative full metallic nanostructure, polycrystalline Au 1D nanostructures with peadpod morphology were synthesized by rapid galvanic displacement reaction (10 min) of Au^{3+} ions with Te nanohelices in the presence ascorbic acid at room temperature.

More importantly, we were able to prepare 1D nanostructures with different chemical stability in a myriad of shapes: Te whiskers, wires, helices and Au peapod-like nanostructures. Among them, Te nanohelices were selected as 1D model to investigate the fabrication of lanthanide compounds like oxides, phosphate and vanadates. However, the direct precipitation of these compounds hardly outlines 1D nanostructures (data not shown) because Te nanostructures easily undergo oxidation reaction under oxygen-rich compounds. It should be pointed that Te nanowires and nanowhiskers also displayed similar lack of chemical stability during the deposition of aforementioned lanthanide compounds. In order to overcome these issues, we have successfully demonstrated a facile method to functionalize the surface of Te nanohelices with resorcinol-formaldehyde (RF) resin of controllable thickness. Particularly, Te@RF core-shell 1D nanostructures or nanocables pave way for new template-for the design of 1D luminophors or metallic hybrids. For instance, two main strategies were evaluated: The first strategy concerns one-pot synthesis of 1D Te@RF hybrid with the direct incorporation of previously synthesized nanoparticles during the coating of Te nanohelices with RF resin. Luminescent $\text{YVO}_4:\text{Eu}^{3+}$ nanoparticles (5 nm), Au nanoparticles (8 nm), and Ag nanocubes (35 nm) were assessed to prepare 1D Te@RF hybrid materials. The loading of lanthanide vanadate or metallic nanoparticles along the coating of RF resin on Te nanohelices was not successful albeit Te nanohelices were fully coated with RF resin at room temperature. Agglomerates of nanoparticles were coated with RF resin and attached in an inhomogeneous fashion on the surface of Te@RF nanocables. Usually, those nanoparticles were located in coalescence sites that merge the Te@RF nanocables each other.

The second approach concerns the direct deposition of lanthanide compounds or metallic nanostructures on the surface of Te@RF nanocables. The hydroxyl-rich surface of resorcinol-formaldehyde resin shell enable that ions can be readily adsorbed through electrostatic interactions. By adsorbing lanthanide ions on the Te@RF nanocables surface, lanthanide hydroxycarbonates were synthesized upon urea decomposition. Green emitting 1D nanostructures were demonstrated with the deposition of La:Ce:Tb (45:45:10 molar ratio) hydroxycarbonates on Te@RF nanocables. This approach opens several opportunities to investigate the deposition of lanthanide derivative compounds with wide range of optical properties.

The reduction of Au^{3+} ions on the surface of Te@RF nanocables endows to 1D nanostructures with homogeneously distributed small Au nanoparticles. One can propose that 1D nanostructures featuring multiple alternate layers of metallic nanoparticles and lanthanide compounds are feasible by using RF resin intermediate coating and may leverage further studies

on the enhancement of luminescence, catalysis, photothermal phenomena, etc. Additionally, the RF shell can be conveniently converted into carbon through high temperature carbonization under an inert atmosphere. By removing the Te core, 1D tubular nanostructures can be used as nanocargo and nanoreactors because of their inner cavity.

Equally important, host those optically active 1D nanostructures in suitable host must be envisioned for practical applications. The current trends stem to the potential use of biopolymers or the reuse of synthetic polymers in more sophisticated applications. In this thesis, natural polymers and epoxy hybrids were assessed to host fluorescent dyes or lanthanides compounds seeking the preparation of optical materials.

Up to now, there is no report of the use of biopolymers derivative optical materials to host 1D luminescent nanostructures. We particularly explored the potential use of silk fibroin and cellulose derivative biopolymers to fabricate transparent optical films hosted with well-known luminescent compounds. In fact, we sought to investigate if those biopolymers could strike excellent platform to further incorporate arrays of 1D luminescent nanostructures.

There exists several works demonstrating the remarkable features of silk fibroin to fabricate optical materials. In Chapter 4, the efforts have been focused to conceive patterned substrates suitable for lasing studies from silk fibroin. Beyond the aesthetical appeal, silk fibroin naturally garners exceptional capability to replicate patterned surfaces downscaling to nanometric resolution (< 20 nm). We use disposable grating from digital versatile disk (DVD) as master to fabricate silk fibroin grating through replica-casting method. We successfully demonstrated the operation of a distributed feedback (DFB) laser based on SF films doped with Rhodamine 6G (Rh6G) dye. In our experiment, the lasing emission of Rhodamine 6G is centered at ~ 570 nm and correspond to the 4th diffraction grating. Our studies identified that the optimal concentration of Rhodamine 6G in SF films should be below 3×10^{-7} mol g⁻¹ for best performance of DFB operation. When the concentration of dye was twice the optimal value, we observed aggregation of dye molecules into fluorescent and non-fluorescent dimers. Therefore, pure silk fibroin displays limited capability to host dye doped DFB lasing devices at high concentration of Rhodamine 6G. Probably, the introduction of surfactants may improve the capability of SF to host higher content of Rhodamine 6G without being aggregated.

Furthermore, the emission of dye doped SF grating is substantially affected by spontaneous emission of Rhodamine 6G from portion of the film that was not patterned by grating. Notice that the grating corresponds to less than 10 % of total height. Ideally, if the thickness of the films is reduced, the emission band would become narrower at the cost of lost in mechanical strength. Otherwise, we study the introduction of light scattering components: SiO₂ particles

and Ag nanoparticles. The addition of those particles to dye doped SF grating led to enhance of the absorption and stimulated emission driven to multiple scattering of light under ballistic regime. The mechanism for emission enhancement deals with incoherent random laser operation competing with single-mode lasing from DFB resonator. Although the refractive index between SiO₂ and SF is quite similar, the concentration of those particles plays a key role on the efficiency of light scattering. At optimal concentration, SiO₂ particles contribute for the confinement of the incident and emitted light. In the case of Ag nanoparticles, narrower emission lasing peak is achieved, due probably to the influence of local electric field and scattering cross-section of Ag nanoparticles. Therefore, a larger fraction of the exciting laser beam is absorbed. It is expected that particles with higher refractive index may leverage the fabrication of more efficient lasing devices.

Ongoing efforts have been placed in the replacement of spherical scattering particles and dye laser by 1D hybrids consisting of metallic scattering particles plus high luminescent compounds (such those explored in the Chapter 5), in order to accomplish more efficient materials for laser purposes.

Due to the lack of chemically reactive groups, optical materials derivative of SF are restricted to those ones produced by doping. Moreover, optically active compounds should be compatible with all aqueous casting process applied in the fabrication of SF films. Most of the works in the literature explore the chemical modification of tyrosine residues existing at relatively low concentrations (5 mol%) and few examples bring modified SF films suitable for photonics.

In Chapter 3 we envisioned to prepare transparent SF films rich in chemical reactive groups. Flexible and transparent films (up to 90% at 550 nm) were obtained from pure SF modified with 3-glycidoxypropyltrimethoxysilane (GPTMS) at high relative content (> 50 wt%). Spectroscopy results (vibrational spectroscopy, ¹³C CP-MAS spectra) suggest that epoxy groups mostly remain intact and silanol groups are also available due to incomplete condensation of siloxane. The addition of GPTMS encompasses notable changes on the surface morphology of the films. Despite the evolution of granular-like surface in hybrid films having GPTMS content higher than 30 wt%, it was observed a decrease of average roughness for more than 50%. It was also evidenced the presence of boundaries between contrasting domains rich in GPTMS and SF. The introduction of GPTMS also play a key role on the conformational changes of SF. Silk II conformation became predominant with the increase of GPTMS content. The main implication of the conversion of Silk I to Silk II conformations endow the increase of crystallinity of SF domain, which in turn make the films insoluble in common solvent and long lasting. Hybrid films also displayed higher thermal stability comparing to pristine SF films.

These findings bring new opportunities to explore the design of optical materials by incorporation of optically active compounds through both doping or attachment intermediated by epoxy/silanol groups.

In Chapter 4, similar approach was applied to fabricate cellulose derivatives hybrids films suitable for optics. Cellulose acetate (CA) with low average molecular weight is readily soluble in acetone-based and methylene chloride-based mixed solvents. The resulting films are transparent in the visible to near infrared region. Nevertheless, pristine CA films are brittle and have restricted number of reactive groups (hydroxyl from cellulose backbone). Few examples in the literature explore the optical features of CA to fabricate photonic materials. We prepared hybrids of CA and GPTMS in solution-phase at different weight ratios. Remarkably, the resulting hybrid films were also very transparent ($> 95\%$ at 550 nm) in the visible to near infrared region. The surface morphology of films containing GPTMS content larger than 30 wt% is characterized by globular-like domains homogeneously distributed in the hybrid composition, whose size increases as a function of GPTMS concentration. Probably, the presence of domains larger than 100 nm in hybrid films at the highest GPTMS content investigated (50 wt%) may afford to light scattering causing slight decrease in transmittance in such composition. Remarkably, vibration and NMR spectroscopy reveal that the films are rich in unreacted epoxy and methoxy groups from non-hydrolyzed GPTMS molecules.

Broadly speaking, rich chemistry comes to play with ring opening reaction of epoxy functions. For example, it is possible to crosslink epoxy function with RF shell resin and, for example, covalently attach Te@RF derivative nanostructures on the surface of these films on patterned fashion.

Analogous results are expected for the assembly of 1D luminescent nanostructures in patterned silk fibroin matrices. Non-patterned host films are likewise important for photonic applications. Herein, it has showed the fabrication of flexible and transparent luminescent films in the visible region ($> 90\%$) by incorporating Eu^{3+} luminescent compounds. In general, the optical properties of luminescent hybrid films and pure Eu^{3+} compounds (i.e. $\text{Eu}(\text{tta})_3 \cdot 2\text{H}_2\text{O}$ complex or $\text{YVO}_4:\text{Eu}^{3+}$ nanoparticles) are very similar with expected broadening of the emission bands due to inhomogeneous distribution of Eu^{3+} compounds in the polymeric host.

Although natural polymers are renewable source, their feedstock is fairly limited. Therefore, it is becoming increasingly important to attempt reuse synthetic polymers in order to reduce the impact of their disposal in the environment, mainly those economically non-attractive recyclable polymers. In such perspective, we successfully prepared transparent and thin films by spin-casting a solution of expanded-polystyrene recovered from disposal of reagents' packs

in D-limonene. D-limonene is the major component of citrus oil (~90%) and completely dissolve EPS. Luminescent and waveguides films were feasible by incorporating very low concentration of $\text{Eu}(\text{tta})_3 \cdot 2\text{H}_2\text{O}$ complex. Together with natural polymers, recycled EPS conceives potential matrix to host emitting lanthanide compounds.

It should be highlighted that this work gathers three different polymers with distinguished solubility in different solvents: water, acetone and d-limonene. These solvents cover a wide range of hydrophobic or hydrophilic optically active compounds. By replacing Tb^{3+} and Eu^{3+} ions in 1D luminescent nanostructures and host films, respectively, with other lanthanide ions enable the versatile fabrication of photonic materials with emission peaking since ultraviolet to infrared regions.

9. CONCLUSION

In Chapter 3, we emphasized the engineering of novel one-dimensional Te nanostructures and derivative hybrids for photonic applications. One-dimensional Te nanostructures (Te1D) in the shape of whiskers, wires and helices were easily prepared by one-pot synthesis in the presence of Pluronic® F68 at low temperatures (< 100 °C). Most significantly, the pursuit on the fabrication of complex nanoarchitectures translates on commendable efforts into develop strategies that can better control the arrangement of Te1D nanostructures. As such, we also evaluate some techniques to assemble Te1D nanostructures. Te1D hybrid structures have been conceived by using Te as sacrificial template to attach metallic nanoparticles or even produce metallic 1D nanostructures. Furthermore, Te1D nanohelices were functionalized with resorcinol-formaldehyde resin. Noteworthy, this last route enable us to fashion an intermediate pathway to explore the deposition of optical active compounds such as lanthanide compounds and attach Au nanoparticles.

From Chapter 4 to Chapter 6, we explored the use of biopolymers for photonic applications. Particularly, silk fibroin (SF) biopolymer presents a wide range of suitable properties for photonic applications that were not fully exploited. In the present work, we demonstrate the operation of a distributed feedback (DFB) laser based on SF films doped with Rhodamine 6G (Rh6G) dye and films containing Rh6G and silica or silver nanoparticles. The SF grating structures were fabricated using a commercial blank digital versatile disc (DVD) as template. The addition of silica or silver nanoparticles to the SF film led to enhanced emission due to the multiple scattering of light by the silica nanoparticles and a reduction of the emission linewidth. The laser wavelength was centered between ≈ 560 and ≈ 575 nm corresponding to the fourth-order diffraction of a 750 nm period of the SF grating. The results show that regenerated SF films are promising matrices for DFB lasers because of the excellent optical quality and large potential for biomedicine regarding biocompatibility and benign processing conditions features.

In Chapter 5, we explored the fabrication of flexible and transparent hybrids of silk fibroin and epoxy modified siloxane for photonic applications. Regenerate silk fibroin (SF) solutions can be engineered into free-standing films with high transparency. Besides the restricted amount of chemically reactive side chains, pristine as-casted SF films are usually water soluble, brittle and have low thermal stability. The design of SF films with enhanced functionality and yet high transparency triggers new opportunities on broader range of applications in bioelectronics. Here we present a simple, functional, yet highly versatile hybrid material

derived from silica sol-gel process based on SF protein and 3-glycidyloxypropyl trimethoxysilane (GPTMS), an organically modified silicon-alkoxide owning a reactive terminal epoxy group. Specifically, we investigated the effect of the addition of GPTMS to silk fibroin solutions on the processability, morphology, crystallinity and optical properties of the resulting hybrid films. Non-cytotoxic, highly transparent (~90 %) and flexible free-standing films even at high concentration of GPTMS (up to 70 wt%) were achieved. The SF hybrid films show enhanced thermal stability and are rich in organic (epoxy) and inorganic (silanol) functional groups according to the content of GPTMS. We also evaluated the successful preparation of red emissive SF hybrid films by loading $\text{YVO}_4:\text{Eu}^{3+}$ nanoparticles at low concentration (< 5 wt%). A meaningful description of the hybrid film structure is reported from the combination of vibrational spectroscopy, solid state NMR and X-ray diffraction analysis

In Chapter 6, transparent hybrids of ester cellulose derivatives and epoxy-modified siloxanes were investigated as optical material. Organic-inorganic hybrid films have been prepared from cellulose acetate (CA) and 3-glycidyloxypropyltrimethoxysilane (GPTMS). Flexible films were fashioned with high relative content of GPTMS (up to 70 wt%) and exhibited high transparency in the visible-near infrared region. The atomic force microscopy (AFM) images of hybrid films display the presence of nanometric globular-like domains with size- and number-dependent of the content of GPTMS. XRD patterns showed decreasing crystallinity of CA hybrid counterpart with increasing amounts of GPTMS. Spectroscopy results (vibrational spectroscopy- FT-IR and Raman scattering, ^{13}C and ^{29}Si NMR spectra) suggest that epoxy groups mostly remain intact and significant amount of methoxysilane groups are available after addition of GPTMS in CA. From ^{29}Si NMR results, all compositions showed the presence of GPTMS molecules non-hydrolyzed or having mono- and di-substituted siloxane bonds. For highest relative content of GPTMS (i.e. 50 wt%) a considerable high amount of non-hydrolyzed (T^0) is observed. Moreover, the addition of GPTMS leads to an increase of the thermal stability as compared to pure CA. Luminescent films were obtained by incorporating luminescent $[\text{Eu}(\text{TTA})_3(\text{H}_2\text{O})_2]$ complex (TTA= thenoyltrifluoroacetate) into the hybrid films. Spectroscopic parameters did not significantly change with the incorporation of luminescent complex, suggesting application in photonics. The $^5\text{D}_0$ states quantum efficiency was observed to be the same for the neat complex and the luminescent hybrid film suggesting a weak interaction with the host.

In Chapter 7, we demonstrated the fabrication of transparent thin films from green processing of polystyrene-waste as potential host for luminescent lanthanide compounds. Expanded-polystyrene (EPS) is inexpensive, lightweight, long-lasting and non-economically attractive to be recycled. There exist challenges inherent in conventional recycling routes of EPS (i.e.

incineration and extrusion) and the recovered outcome usually stems to limited applications in engineering. We took advantage of the high solubility of polystyrene in D-limonene, a green solvent present as major component of citrus oil, to fabricate optical materials through environmental-friendly recycle processing of EPS waste. We successfully prepared transparent (> 90 %) and luminescent thin films by spin-casting a solution prepared by dissolving EPS pack wastes and luminescent red emitting Eu^{3+} β -diketonate complex. The incorporation of Eu^{3+} β -diketonate complex in EPS recovered matrix did not place deleterious effect on the optical properties comparing to pure complex. Beyond that, luminescent EPS films hold rich potential as waveguides materials. Remarkably, the feasible green route of fabrication herein reported paves way on the rational design of high quality optical materials from non-attractive recyclable plastics.

References

- ACHOUNDONG, C. S. K. et al. Silane modification of cellulose acetate dense films as materials for acid gas removal. **Macromolecules**, v. 46, n. 14, p. 5584-5594, 2013.
- ALBUNIA, A. R.; MUSTO, P.; GUERRA, G. FTIR spectra of pure helical crystalline phases of syndiotactic polystyrene. **Polymer**, v. 47, n. 1, p. 234-242, 2006.
- ALONSO, B. et al. Structural control in germania hybrid organic-inorganic materials. **Chemistry of Materials**, v. 17, n. 12, p. 3172-3180, 2005.
- AMSDEN, J. J. et al. Spectral analysis of induced color change on periodically nanopatterned silk films. **Optics Express**, v. 17, n. 23, p. 21271-21279, 2009.
- AMSDEN, J. J. et al. Rapid nanoimprinting of silk fibroin films for biophotonic applications. **Advanced Materials**, v. 22, n. 15, p. 1746-1749, 2010.
- ARBELOA, F. L.; OJEDA, P. R.; ARBELOA, I. L. Dimerization and trimerization of rhodamine 6G in aqueous solution. Effect on the fluorescence quantum yield. **Journal of the Chemical Society**, v. 84, n. 12, p. 1903-1912, 1988.
- ASAKURA, T. et al. Evidence from ^{13}C solid-state NMR spectroscopy for a lamella structure in an alanine-glycine copolyptide: a model for the crystalline domain of Bombyx mori silk fiber. **Protein Science**, v. 14, n. 10, p. 2654-2657, 2005.
- ASAKURA, T. et al. Heterogeneous structure of silk fibers from Bombyx mori resolved by ^{13}C solid-state NMR spectroscopy. **Journal of the American Chemical Society**, v. 124, n. 30, p. 8794-8795, 2002.
- BACA, A. J. et al. Semiconductor wires and ribbons for high-performance flexible electronics. **Angewandte Chemie International Edition**, v. 47, n. 30, p. 5524-5542, 2008.
- BANCROFT, W. D. **Applied colloid chemistry: general chemistry**. New York: McGraw-Hill Book, 1921. 368 p.
- BANCROFT, W. D. The colors of colloids. X. **The Journal of Physical Chemistry**, v. 23, n. 9, p. 603-633, 1918.
- BARUD, H. S. et al. Bacterial cellulose/poly(3-hydroxybutyrate) composite membranes. **Carbohydrate Polymers**, v. 83, n. 3, p. 1279-1284, 2011.
- BARUD, H. S. et al. Transparent bacterial cellulose-boehmite-epoxi-siloxane nanocomposites. **Composites Part A: Applied Science and Manufacturing**, v. 43, n. 6, p. 973-977, 2012.
- BARUD, H. S. et al. Optically transparent membrane based on bacterial cellulose/polycaprolactone. **Polímeros**, v. 23, n. 1, p. 135-142, 2013.
- BINNEMANS, K. Lanthanide-based luminescent hybrid materials. **Chemical Reviews**, v. 109, n. 9, p. 4283-4374, 2009.

BLASSE, G.; MEIJERINK, A.; DONEGÁ, C. M. Vibronic rare earth spectroscopy: results and pitfalls. **Journal of Alloys and Compounds**, v. 225, n. 1-2, p. 24-27, 1995

BRITES, C. D. S. et al. A luminescent molecular thermometer for long-term absolute temperature measurements at the nanoscale. **Advanced Materials**, v. 22, n. 40, p. 4499-4504, 2010.

BRUS, J.; HLAVATÁ, D.; STRACHOTA, A. Self-organization, structure, dynamic properties, and surface morphology of silica/epoxy films as seen by solid-state NMR, SAXS, and AFM. **Macromolecules**, v. 37, n. 4, p. 1346-1357, 2004.

BUNZLI, J. C. G.; ELISEEVA, S. V. Lanthanide NIR luminescence for telecommunications, bioanalyses and solar energy conversion. **Journal of Rare Earths**, v. 28, n. 6, p. 824-842, 2010.

BÜNZLI, J.-C. G.; PIGUET, C. Taking advantage of luminescent lanthanide ions. **Chemical Society Reviews**, v. 34, n. 12, p. 1048-1077, 2005.

CAO, G. S. et al. Selected-control synthesis of Te nanowires and Te/C nanocables by adjusting hydrothermal temperature. **Materials Letters**, v. 63, n. 21, p. 1778-1780, 2009.

CARLOS, L. D. et al. Lanthanide-containing light-emitting organic-inorganic hybrids: a bet on the future. **Advanced Materials**, v. 21, n. 5, p. 509-534, 2009.

CHAMBERS, M. D.; CLARKE, D. R. Doped oxides for high-temperature luminescence and lifetime thermometry. **Annual Review of Materials Research**, v. 39, p. 325-359, 2009.

CHAVAN, P. G. et al. Field emission studies of Te nanorods grown on Si (111) substrate. **Vacuum**, v. 83, n. 11, p. 1307-1310, 2009.

CHATTOPADHYAY, S.; CHEN, L.-C.; CHEN, K.-H. Energy production and conversion applications of one-dimensional semiconductor nanostructures. **NPG Asia Materials**, v. 3, n. 8, p. 74-81, 2011.

CHOU, T.-M. et al. Fabrication of Te and Te-Au nanowires-based carbon fiber fabrics for antibacterial applications. **International Journal of Environmental Research and Public Health**, v. 13, n. 2, 2016. doi: 10.3390/ijerph13020202.

CLARK, E. R.; WILLIAMS, S. G. The conformations of aromatic ethers as determined from their ultraviolet absorption spectra. **Journal Chemical Society**, v. 13, p. 859-866, 1967.

COSTA, L. et al. Structure-charring relationship in phenol-formaldehyde type resins. **Polymer Degradation and Stability**, v. 56, n. 1, p. 23-35, 1997.

DASGUPTA, N. P. et al. 25th anniversary article: semiconductor nanowires - synthesis, characterization, and applications. **Advanced Materials**, v. 26, n. 14, p. 2137-2184, 2014.

DEARING, A. W.; REID, E. E. Alkyl orthosilicates. **Journal of the American Chemical Society**, v. 50, n. 11, p. 3058-3062, 1928.

DEBASU, M. L. et al. Emission-decay curves, energy-transfer and effective-refractive index in $\text{Gd}_2\text{O}_3:\text{Eu}^{3+}$ nanorods. **Journal of Physical Chemistry C**, v. 115, n. 31, p. 15297-15303, 2011.

DING, N. et al. Tellurium@ordered macroporous carbon composite and free-standing tellurium nanowire mat as cathode materials for rechargeable lithium-tellurium batteries. **Advanced Energy Materials**, v. 5, n. 8, 2015. doi:10.1002/aenm.201401999.

DINH, D. A. Silver nanowires: a promising transparent conducting electrode material for optoelectronic and electronic applications. **Reviews in Advanced Sciences and Engineering**, v. 2, n. 4, p. 324-345, 2013.

DOMACHUK, P. et al. Bioactive “self-sensing” optical systems. **Applied Physics Letters**, v. 95, n. 25, p. 253702/1-253702/3, 2009.

DOMINGUEZ, C. T. et al. Using random laser emission to investigate the bonding energy of laser dye dimers. **Chemical Physics Letters**, v. 464, n. 4-6, p. 245-248, 2008.

DUARTE, A. P. et al. Organosilylated complex $[\text{Eu}(\text{TTA})_3(\text{Bpy-Si})]$: A bifunctional moiety for the engineering of luminescent silica-based nanoparticles for bioimaging. **Langmuir**, v. 29, n. 19, p. 5878-5888, 2013.

DUARTE, A. P. et al. Structural and luminescence properties of silica-based hybrids containing new silylated-diketonato europium(III) complex. **Journal of Physical Chemistry C**, v. 116, n. 1, p. 505-515, 2012.

EBAID, M. et al. Vertically aligned InGaN nanowires with engineered axial in composition for highly efficient visible light emission. **Scientific Reports**, v. 5, 2015. doi:10.1038/srep17003.

EBELMEN. Untersuchungen über die verbindungen der borsäure und kieselsäure mit aether. **Annalen der Chemie und Pharmacie**, v. 57, n. 3, p. 319-355, 1846.

FAN, Z. et al. Wafer-scale assembly of semiconductor nanowire arrays by contact printing. **Electrical Engineering**, v. 8, n. 1, p. 1-14, 2008.

FANG, X. et al. One-dimensional inorganic semiconductor nanostructures: a new carrier for nanosensors. **Pure and Applied Chemistry**, v. 82, n. 11, p. 2185-2198, 2010.

FERNANDES, S. C. M. et al. Novel transparent nanocomposite films based on chitosan and bacterial cellulose. **Green Chemistry**, v. 11, n. 12, p. 2023-2029, 2009.

FUENTES, S. et al. Chitosan based films. Synthesis and crystalline properties of nanocomposites with amine propyl siloxane. **International Journal of Polymeric Materials**, v. 35, n. 1/4, p. 61-70, 1997.

FUENTES, S. et al. Hybrid chitosane-mercaptopropylsiloxane films - synthesis and properties. **Molecular Crystals and Liquid Crystals**, v. 523, n. 1, p. 583-592, 2010.

FUKUI, T. et al. Fabrication of III-V semiconductor nanowires by SA-MOVPE and their applications to photonic and photovoltaic devices. In: INTERNATIONAL CONFERENCE ON INDIUM PHOSPHIDE AND RELATED MATERIALS, 22, 2010, Takamatsu. **Proceedings...** New York: IEEE xplorer, 2010. doi:10.1109/ICIPRM.2010.5516148.

GAO, F.; LU, Q.; KOMARNENI, S. Gluconate controls one-dimensional growth of tellurium nanostructures. **Journal of Materials Research**, v. 21, n. 2, p. 343-348, 2006.

GAO, J. et al. Power factor enhancement via simultaneous improvement of electrical conductivity and Seebeck coefficient in tellurium nanowires/reduced graphene oxide flexible thermoelectric films. **Synthetic Metals**, v. 210, p. 342-351, 2015.

GATES, B.; YIN, Y.; XIA, Y. A solution-phase approach to the synthesis of uniform nanowires of crystalline selenium with lateral dimensions in the range of 10-30 nm. **Journal of the American Chemical Society**, v. 122, n. 50, p. 12582-12583, 2000.

GATES, B. et al. Synthesis and characterization of uniform nanowires of trigonal selenium. **Advanced Functional Materials**, v. 12, n. 3, p. 219-227, 2002.

GAUTAM, U. K.; RAO, C. N. R. Controlled synthesis of crystalline tellurium nanorods, nanowires, nanobelts and related structures by a self-seeding solution process. **Journal of Materials Chemistry**, v. 14, n. 16, p. 2530-2535, 2004.

GOLDFARB, R. Tellurium—the bright future of solar energy. **USGS mineral resources program**. 2015. Disponível em: <<https://pubs.usgs.gov/fs/2014/3077/>>. Acesso em: 5 maio 2016.

GRAHAM, T. On the properties of silicic acid and other analogous colloidal substances. **Journal of the Chemical Society**, v. 17, n. 318, p. 318-327, 1864.

GROTE, J. G. et al. Investigation of polymers and marine-derived DNA in optoelectronics. **The Journal of Physical Chemistry B**, v. 108, n. 25, p. 8584-8591, 2004.

GU, F. et al. Polyaniline/polystyrene single-nanowire devices for highly selective optical detection of gas mixtures. **Optics express**, v. 17, n. 13, p. 11230-11235, 2009.

GUO, X.; YING, Y.; TONG, L. Photonic nanowires: from subwavelength waveguides to optical sensors. **Accounts of Chemical Research**, v. 47, n. 2, p. 656-666, 2014.

GUPTA, M. K. et al. Patterned silk films cast from ionic liquid solubilized fibroin as scaffolds for cell growth. **Langmuir**, v. 23, n. 3, p. 1315-1319, 2007.

HANGARTER, C. M.; MYUNG, N. V. Magnetic alignment of nanowires. **Chemistry of Materials**, v. 17, n. 6, p. 1320-1324, 2005.

HAN, K. et al. Multi-photon-pumped stimulated emission from ZnO nanowires: a time-resolved study. **Physics Letters A**, v. 376, n. 23, p. 1871-1874, 2012.

HE, Z.; YU, S.-H. Large scale synthesis of tellurium nanoribbons in tetraethylene pentamine aqueous solution and the stability of tellurium nanoribbons in ethanol and water. **The Journal of Physical Chemistry B**, v. 109, n. 48, p. 22740-22745, 2005.

HE, Z.; YU, S.-H.; ZHU, J. Amino acids controlled growth of shuttle-like scrolled tellurium nanotubes and nanowires with sharp tips. **Chemistry of Materials**, v. 17, n. 11, p. 2785-2788, 2005.

HEYMAN, J. N. et al. Terahertz and infrared transmission of an organic/inorganic hybrid thermoelectric material. **Applied Physics Letters**, v. 104, n. 14, p. 141912/1-141912/4, 2014.

HUANG, M. H. Room-temperature ultraviolet nanowire nanolasers. **Science**, v. 292, n. 5523, p. 1897-1899, 2001.

HUANG, Y. Directed assembly of one-dimensional nanostructures into functional networks. **Science**, v. 291, n. 5504, p. 630-633, 2001.

INNOCENZI, P.; BRUSATIN, G.; BABONNEAU, F. Competitive polymerization between organic and inorganic networks in hybrid materials. **Chemistry of Materials**, v. 12, n. 12, p. 3726-3732, 2000.

ISOMÄKI, H. M.; BOEHM, J. Optical absorption of tellurium. **Physica Scripta**, v. 25, n. 6A, p. 801-803, 1982.

JIN, H.-J. et al. Water-stable silk films with reduced β -sheet content. **Advanced Functional Materials**, v. 15, n. 8, p. 1241-1247, 2005.

JOHNSON, R. A. Production, particle characteristics, and spectra of tellurium hydrosols for spectrophotometry. **Analytical Chemistry**, v. 25, n. 7, p. 1013-1017, 1953.

JOSHI, R. K.; SCHNEIDER, J. J. Assembly of one dimensional inorganic nanostructures into functional 2D and 3D architectures. Synthesis, arrangement and functionality. **Chemical Society reviews**, v. 41, n. 15, p. 5285-5312, 2012.

JUDEINSTEIN, P.; SANCHEZ, C. Hybrid organic/inorganic materials: a land of multidisciplinary. **Journal of Materials Chemistry**, v. 6, n. 4, p. 511-525, 1996.

KAI, J. et al. Intermolecular energy transfer and photostability of luminescence-tuneable multicolour PMMA films doped with lanthanide- β -diketonate complexes. **Journal of Materials Chemistry**, v. 21, n. 11, p. 3796, 2011.

KAI, J.; PARRA, D. F.; BRITO, H. F. Polymer matrix sensitizing effect on photoluminescence properties of Eu^{3+} - β -diketonate complex doped into poly- β -hydroxybutyrate (PHB) in film form. **Journal of Materials Chemistry**, v. 18, n. 38, p. 4549-4554, 2008.

KAWABE, Y. et al. Amplified spontaneous emission from fluorescent-dye-doped DNA-surfactant complex films. **Advanced Materials**, v. 12, n. 17, p. 1281-1283, Sept. 2000.

KHAN, M. S. et al. UV absorbance studies of dilute polystyrene solutions in different solvents. **Journal of the Chemical Society of Pakistan**, v. 24, n. 4, p. 237-240, 2002.

KIM, D.-H. et al. Inorganic semiconductor nanomaterials for flexible and stretchable bio-integrated electronics. **NPG Asia Materials**, v. 4, p. e15/1-e15/9, 2012.

KIM, Y. et al. Transparent nanocomposites prepared by incorporating microbial nanofibrils into poly(l-lactic acid). **Current Applied Physics**, v. 9, n. 1, p. S69-S71, 2009.

KIMOTO, K.; NISHIDA, I. An electron microscope and electron diffraction study of fine smoke particles prepared by evaporation in argon gas at low pressures (II). **Japanese Journal of Applied Physics**, v. 6, n. 9, p. 1047-1059, 1967.

KOGELNIK, H. Stimulated emission in a periodic structure. **Applied Physics Letters**, v. 18, n. 4, 1971. doi: 10.1063/1.1653605.

KONO, H.; ERATA, T.; TAKAI, M. CP/MAS ^{13}C NMR study of cellulose and cellulose derivatives. 2. Complete assignment of the ^{13}C resonance for the ring carbons of cellulose triacetate polymorphs. **Journal of the American Chemical Society**, v. 124, n. 25, p. 7512-7518, 2002.

KWON, Y.-W.; CHOI, D. H.; JIN, J.-I. Optical, electro-optic and optoelectronic properties of natural and chemically modified DNAs. **Polymer Journal**, v. 44, n. 12, p. 1191-1208, 2012.

LAN, W.-J. et al. Dispersibility, stabilization, and chemical stability of ultrathin tellurium nanowires in acetone: morphology change, crystallization, and transformation into TeO_2 in different solvents. **Langmuir**, v. 23, n. 6, p. 3409-3417, 2007.

LAWANDY, N. M. et al. Laser action in strongly scattering media. **Nature**, v. 368, n. 6470, p. 436-438, 1994.

LAWRENCE, B. D. et al. Bioactive silk protein biomaterial systems for optical devices. **Biomacromolecules**, v. 9, n. 4, p. 1214-1220, 2008a.

LAWRENCE, B. D. et al. Processing methods to control silk fibroin film biomaterial features. **Journal of Materials Science**, v. 43, n. 21, p. 6967-6985, 2008b.

LEE, J. E. et al. Effect of binding mode on the photoluminescence of CTMA-DNA doped with (E)-2-(2-(4-(diethylamino)styryl)-4H-pyran-4-ylidene)malononitrile. **Polymer**, v. 49, n. 25, p. 5417-5423, 2008.

LEGNANI, C. et al. Bacterial cellulose membrane as flexible substrate for organic light emitting devices. **Thin Solid Films**, v. 517, n. 3, p. 1016-1020, 2008.

LI, H. H. et al. Facile electrochemical synthesis of tellurium nanorods and their photoconductive properties. **Crystal Research and Technology**, v. 6, p. 1-6, 2012.

LI, H.-H. et al. Ultrathin PtPdTe nanowires as superior catalysts for methanol electrooxidation. **Angewandte Chemie International Edition**, v. 52, n. 29, p. 7472-7476, 2013.

- LI, J.; ZHANG, J.; QIAN, Y. Surfactant-assisted synthesis of bundle-like nanostructures with well-aligned Te nanorods. **Solid State Sciences**, v. 10, n. 11, p. 1549-1555, 2008.
- LI, J. R. et al. Carbon black/polystyrene composites as candidates for gas sensing materials. **Carbon**, v. 41, n. 12, p. 2353-2360, 2003.
- LI, T.; ZHOU, C.; JIANG, M. UV absorption spectra of polystyrene. **Polymer Bulletin**, v. 25, n. 2, p. 211-216, 1991.
- LIANG, F.; QIAN, H. Synthesis of tellurium nanowires and their transport property. **Materials Chemistry and Physics**, v. 113, n. 2/3, p. 523-526, 2009.
- LIANG, H.-W. et al. An efficient templating approach for synthesis of highly uniform CdTe and PbTe nanowires. **Inorganic Chemistry**, v. 48, n. 11, p. 4927-4933, 2009a.
- LIANG, H.-W. et al. Ultrathin Te nanowires: an excellent platform for controlled synthesis of ultrathin platinum and palladium nanowires/nanotubes with very high aspect ratio. **Advanced Materials**, v. 21, n. 18, p. 1850-1854, 2009b.
- LIANG, H.-W. et al. Multiplex templating process in one-dimensional nanoscale: controllable synthesis, macroscopic assemblies, and applications. **Accounts of Chemical Research**, v. 46, n. 7, p. 1450-1461, 2013.
- LIEBER, C. M. Semiconductor nanowires: a platform for nanoscience and nanotechnology. **MRS bulletin**, v. 36, n. 12, p. 1052-1063, 2011.
- LIEBER, C. M.; WANG, Z. L. Functional nanowires. **MRS Bulletin**, v. 32, n. 2, p. 99-108, 2011.
- LIM, K. T.; LIM, C. T. Synthesis, optical properties, and chemical-biological sensing applications of one-dimensional inorganic semiconductor nanowires. **Progress in Materials Science**, v. 58, n. 5, p. 705-748, 2013.
- LIMA, L. R. et al. Silk fibroin-antigenic peptides-YVO₄:Eu³⁺ nanostructured thin films as sensors for hepatitis C. **Journal of Luminescence**, v. 170, p. 375-379, 2016. doi: 10.1016/j.jlumin.2015.08.039
- LIN, Z. H.; YANG, Z.; CHANG, H. T. Preparation of fluorescent tellurium nanowires at room temperature. **Crystal Growth & Design**, v. 8, n. 1, p. 351-357, 2008.
- LIU, J.-W. et al. Mesoscale assemblies of ultrathin superlong tellurium nanowires and their photoconductivity. **Journal of the American Chemical Society**, v. 132, n. 26, p. 8945-8952, 2010a.
- LIU, J.-W. et al. Rapid microwave-assisted synthesis of uniform ultralong Te nanowires, optical property, and chemical stability. **Langmuir**, v. 26, n. 13, p. 11372-11377, 2010b.
- LIU, J.-W. et al. Macroscale ordered ultrathin telluride nanowire films, and tellurium/telluride hetero-nanowire films. **Angewandte Chemie International Edition**, v. 51, n. 30, p. 7420-7425, 2012.

LIU, X. et al. A rational redox route for the synthesis of tellurium nanotubes. **Inorganic Chemistry Communications**, v. 7, n. 2, p. 257-259, 2004.

LIU, Z. et al. Surfactant-assisted growth of uniform nanorods of crystalline tellurium. **Journal of Materials Chemistry**, v. 13, n. 1, p. 159-162, 2003.

LIU, Z. et al. Size-controlled synthesis and growth mechanism of monodisperse tellurium nanorods by a surfactant-assisted method. **Langmuir**, v. 20, n. 1, p. 214-218, 2004.

LU, M. et al. Plastic distributed feedback laser biosensor. **Applied Physics Letters**, v. 93, n. 11, p. 111113/1-111113/3, 2008.

LU, Q.; GAO, F.; KOMARNENI, S. A green chemical approach to the synthesis of tellurium nanowires. **Langmuir**, v. 21, n. 13, p. 6002-6005, 2005.

LU, Q.; GAO, F.; KOMARNENI, S. Biomolecule-assisted reduction in the synthesis of single-crystalline tellurium nanowires. **Advanced Materials**, v. 16, n. 18, p. 1629-1632, 2004.

MA, J. et al. Growth of tellurium nanowire bundles from an ionic liquid precursor. **CrystEngComm**, v. 13, n. 7, p. 2774-2778, 2011.

MACAN, J. et al. Thermal degradation of epoxy-silica organic-inorganic hybrid materials. **Polymer Degradation and Stability**, v. 91, n. 1, p. 122-127, 2006.

MAGOSHI, J. et al. Physical properties and structure of silk. V. Thermal behavior of silk fibroin in the random-coil conformation. **Journal of Polymer Science**, v. 15, n. 9, p. 1675-1683, 1977.

MALTA, O. L. et al. Spectroscopic properties of a new light-converting device $\text{Eu}(\text{thenoyltrifluoroacetate})_3 \cdot 2(\text{dibenzyl sulfoxide})$: a theoretical analysis based on structural data obtained from a sparkle model. **Journal of Luminescence**, v. 75, p. 255-268, 1997.

MARINI, C. et al. High-pressure phases of crystalline tellurium: a combined Raman and ab initio study. **Physical Review B**, v. 86, n. 6, 2012. doi: 10.1103/PhysRevB.86.064103.

MARTIN, R. M.; LUCOVSKY, G.; HELLIWELL, K. Intermolecular bonding and lattice dynamics of Se and Te. **Physical Review B**, v. 13, n. 4, p. 1383-1395, 1976.

MAYERS, B.; XIA, Y. Formation of tellurium nanotubes through concentration depletion at the surfaces of seeds. **Advanced Materials**, v. 14, n. 4, p. 279-282, 2002a.

MAYERS, B.; XIA, Y. One-dimensional nanostructures of trigonal tellurium with various morphologies can be synthesized using a solution-phase approach. **Journal of Materials Chemistry**, v. 12, n. 6, p. 1875-1881, 2002b.

MONDIA, J. P. et al. Rapid nanoimprinting of doped silk films for enhanced fluorescent emission. **Advanced Materials**, v. 22, n. 41, p. 4596-4599, 2010.

MONTI, P. et al. Raman spectroscopic characterization of Bombyx mori silk fibroin: Raman spectrum of Silk I. **Journal of Raman Spectroscopy**, v. 32, n. 2, p. 103-107, 2001.

- MONTI, P. et al. Raman spectroscopic studies of silk fibroin from *Bombyx mori*. **Journal of Raman Spectroscopy**, v. 29, n. 4, p. 297-304, 1998.
- MOON, G. D. et al. Chemical transformations in ultrathin chalcogenide nanowires. **ACS Nano**, v. 4, n. 4, p. 2307-2319, 2010.
- MOON, G. D. et al. Assembled monolayers of hydrophilic particles on water surfaces. **ACS Nano**, v. 5, n. 11, p. 8600-8612, 2011.
- MORAES, M. A. et al. Preparation and characterization of insoluble silk fibroin/chitosan blend films. **Polymers**, v. 2, n. 4, p. 719-727, 2010.
- MUSKENS, O. L. et al. Giant optical birefringence in ensembles of semiconductor nanowires. **Applied Physics Letters**, v. 89, n. 23, p. 233117/1-233117/3, 2006.
- NARAYANAN, R. et al. Anisotropic molecular ionization at 1 V from tellurium nanowires (Te NWs). **Analytical Chemistry**, v. 87, n. 21, p. 10792-10798, 2015.
- NOGI, M. et al. Optically transparent nanofiber paper. **Advanced Materials**, v. 21, n. 16, p. 1595-1598, 2009.
- NOGUCHI, T. et al. A new recycling system for expanded polystyrene using a natural solvent. Part 2: development of a prototype production system. **Package Technoly Science**, v. 11, n. 1, p. 29-37, 1998.
- NURMUKHAMETOV, R. N.; VOLKOVA, L. V.; KABANOV, S. P. Fluorescence and absorption of polystyrene exposed to UV laser radiation. **Journal of Applied Spectroscopy**, v. 73, n. 1, p. 55-60, 2006.
- PAN, A. et al. Stimulated emissions in aligned CdS nanowires at room temperature. **The Journal of Physical Chemistry B**, v. 109, n. 51, p. 24268-24272, 2005.
- PARK, H. et al. Aqueous chemical synthesis of tellurium nanowires using a polymeric template for thermoelectric materials. **CrystEngComm**, v. 17, n. 5, p. 1092-1097, 2015.
- PARKER, S. T. et al. Biocompatible silk printed optical waveguides. **Advanced Materials**, v. 21, n. 23, p. 2411-2415, 2009.
- PERRY, H. et al. Nano- and micropatterning of optically transparent, mechanically robust, biocompatible silk fibroin films. **Advanced Materials**, v. 20, n. 16, p. 3070-3072, 2008.
- PINE, A.; DRESSELHAUS, G. Raman spectra and lattice dynamics of tellurium. **Physical Review B**, v. 4, n. 2, p. 356-371, 1971.
- PINTO, E. R. P. et al. Transparent composites prepared from bacterial cellulose and castor oil based polyurethane as substrates for flexible OLEDs. **Journal of Materials Chemistry C**, v. 3, n. 44, p. 11581-11588, 2015.

PONTIUS, B. W.; BERG, P. Rapid renaturation of complementary DNA strands mediated by cationic detergents: a role for high-probability binding domains in enhancing the kinetics of molecular assembly processes. **Proceedings of the National Academy of Sciences of the United States of America**, v. 88, n. 18, p. 8237-8241, 1991.

QI, H.; CHANG, C.; ZHANG, L. Properties and applications of biodegradable transparent and photoluminescent cellulose films prepared via a green process. **Green Chemistry**, v. 11, n. 2, p. 177-184, 2009.

QIAN, D. et al. Load transfer and deformation mechanisms in carbon nanotube-polystyrene composites. **Applied Physics Letters**, v. 2868, n. 2000, p. 4-7, 2000.

QIAN, H.-S. et al. High-quality luminescent tellurium nanowires of several nanometers in diameter and high aspect ratio synthesized by a poly (vinyl pyrrolidone)-assisted hydrothermal process. **Langmuir**, v. 22, n. 8, p. 3830-3835, 2006a.

QIAN, H.-S. et al. Synthesis of uniform carbon@silica nanocables and luminescent silica nanotubes with well controlled inner diameters. **Nanotechnology**, v. 17, n. 24, p. 5995-5999, 2006b.

QIAN, H.-S. et al. Synthesis of uniform Te@Carbon-rich composite nanocables with photoluminescence properties and carbonaceous nanofibers by the hydrothermal carbonization of glucose. **Chemistry of Materials**, v. 18, n. 8, p. 2102-2108, 2006c.

QIAN, H.-S. et al. One-pot synthesis of biocompatible Te@phenol formaldehyde resin core-shell nanowires with uniform size and unique fluorescent properties by a synergized soft-hard template process. **Nanotechnology**, v. 21, n. 49, 2010.
doi: 10.1088/0957-4484/21/49/495602

RETEGI, A. et al. Sustainable optically transparent composites based on epoxidized soy-bean oil (ESO) matrix and high contents of bacterial cellulose (BC). **Cellulose**, v. 19, n. 1, p. 103-109, 2012.

RIBEIRO, S. J. L. et al. Low optical loss planar waveguides prepared in an organic - inorganic hybrid system. **Applied Physics Letters**, v. 77, n. 22, p. 3502-3504, 2000.

RIEGEL, B. et al. Kinetic investigations of hydrolysis and condensation of the glycidoxypropyltrimethoxysilane/aminopropyltriethoxy-silane system by means of FT-Raman spectroscopy I. **Journal of Non-Crystalline Solids**, v. 226, n. 1-2, p. 76-84, 1998.

SABBATINI, N.; GUARDIGLI, M.; LEHN, J.-M. Luminescent lanthanide complexes as photochemical supramolecular devices. **Coordination Chemistry Reviews**, v. 123, n. 1-2, p. 201-228, 1993.

SAFDAR, M. et al. Site-specific nucleation and controlled growth of a vertical tellurium nanowire array for high performance field emitters. **Nanotechnology**, v. 24, n. 18, 2013.
doi:10.1088/0957-4484/24/18/185705.

SAGNELLA, A. et al. APTES mediated modular modification of regenerated silk fibroin in a water solution. **RSC Advances**, v. 5, n. 78, p. 63401-63406, 2015.

SAMAL, A. K.; PRADEEP, T. Lanthanum telluride nanowires: formation, doping, and raman studies. **The Journal of Physical Chemistry C**, v. 114, n. 13, p. 5871-5878, 2010.

SANCHEZ, C. et al. Applications of hybrid organic-inorganic nanocomposites. **Journal of Materials Chemistry**, v. 15, n. 35/36, p. 3559-3592, 2005.

SANTOS, M. V. dos et al. Random laser action from flexible biocellulose-based device. **Journal of Applied Physics**, v. 115, n. 8, p. 083108/1-083108/5, 2014.

ŠAPIĆ, I. M. et al. DFT study of molecular structure and vibrations of 3-glycidoxypropyltrimethoxysilane. **Spectrochimica Acta - Part A**, v. 72, n. 4, p. 833-840, 2009.

SCHMIDT, H. New type of non-crystalline solids between inorganic and organic materials. **Journal of Non-Crystalline Solids**, v. 73, n. 1/3, p. 681-691, 1985.

SCHMIDT, P. N. S. et al. Flexural test on recycled polystyrene. **Procedia Engineering**, v. 10, p. 930-935, 2011.

SCHOESER, M. **Silk**. New Haven: Yale University Press, 2007. 256 p.

SCHOTT GLASS TECHNOLOGIES (United States). L. M. Cook; K.-H. Mader; R. Schnabel. **Integral anti-reflective surfaces of silicate glasses**. US4434191 A, 6 Oct. 1981, 28 Feb 1984.

SEN, S. et al. Synthesis of tellurium nanostructures by physical vapor deposition and their growth mechanism. **Crystal Growth & Design**, v. 8, n. 1, p. 238-242, 2008.

SEN, S. et al. Chlorine gas sensors using one-dimensional tellurium nanostructures. **Talanta**, v. 77, n. 5, p. 1567-1572, 2009.

SHAABAN, E. R.; YAHIA, I. S.; EL-METWALLY, E. G. Validity of Swanepoel's method for calculating the optical constants of thick films. **Acta Physica Polonica A**, v. 121, n. 3, p. 628-635, 2012.

SHAMS, M. I. et al. The transparent crab: preparation and nanostructural implications for bioinspired optically transparent nanocomposites. **Soft Matter**, v. 8, n. 5, p. 1369-1373, 2012.

SHAO, J. et al. Fourier transform Raman and Fourier transform infrared spectroscopy studies of silk fibroin. **Journal of Applied Polymer Science**, v. 96, n. 6, p. 1999-2004, 2005.

SHE, G. et al. Template-free electrodeposition of one-dimensional nanostructures of tellurium. **Crystal Growth & Design**, v. 9, n. 2, p. 663-666, 2009.

SHIROSAKI, Y. et al. In vitro bioactivity and MG63 cytocompatibility of chitosan-silicate hybrids. **International Journal of Materials and Chemistry**, v. 3, n. 3A, p. 1-7, 2013.

SILVA, C. A. de et al. Nanocomposites derived from cellulose acetate and highly branched alkoxysilane. **Journal of Applied Polymer Science**, v. 121, n. 5, p. 2559-2566, 2011.

SILVA, R. R. **Estudo da preparação de nanocompósitos magneto-luminescentes unidimensionais baseados em telúrio**. 2012. 185 f. Dissertação (Mestrado em Química) - Instituto de Química, Universidade Estadual Paulista, Araraquara, 2012.

SILVERMAN, A. Use of electrochemical by-products in glass making: I. arsenic, selenium, tellurium. **Transactions of the Electrochemical Society**, v. 61, n. 1, p. 101-112, 1932.

SILVERSTEIN, R. M.; WEBSTER, F. X.; KIEMLE, D. **Spectrometric identification of organic compounds**. 7th. ed. New York: John Wiley and Sons, 2005.

SIRBULY, D. J. et al. Optical routing and sensing with nanowire assemblies. **Proceedings of the National Academy of Sciences of United States of America**, v. 102, n. 22, p. 7800-7805, 2005.

SMITH, P. A. et al. Electric-field assisted assembly and alignment of metallic nanowires. **Applied Physics Letters**, v. 77, n. 9, p. 1399-1401, 2000.

SMITHA, S. et al. Sol-gel synthesis of biocompatible silica-chitosan hybrids and hydrophobic coatings. **Journal of Materials Research**, v. 23, n. 8, p. 2053-2060, 2008.

SONG, J. et al. Superlong high-quality tellurium nanotubes: synthesis, characterization, and optical property. **Crystal Growth & Design**, v. 8, n. 6, p. 1902-1908, 2008.

SONG, X. C. et al. Fabrication and characterization of Te/C nanocables and carbonaceous nanotubes. **Crystal Growth & Design**, v. 9, n. 1, p. 344-347, 2009.

SREEPRASAD, T. S.; SAMAL, A. K.; PRADEEP, T. Bending and shell formation of tellurium nanowires induced by thiols. **Chemistry of Materials**, v. 21, n. 19, p. 4527-4540, 2009.

STADLER, P. et al. Organic field-effect transistors and memory elements using deoxyribonucleic acid (DNA) gate dielectric. **Organic Electronics**, v. 8, n. 6, p. 648-654, 2007.

STECKL, A. J. DNA - a new material for photonics. **Nature Photonics**, v. 1, n. 1, p. 3-5, 2007.

STECKL, A. J. et al. DNA as an optical material. **Optics and Photonics News**, v. 22, n. 7, p. 34-39, 2011.

STOBER, W.; FINK, A.; BOHN, E. Controlled growth of monodisperse silica spheres in the micron size range. **Journal of Colloid and Interface Science**, v. 26, n. 1, p. 62-69, 1968.

SU, W.; BONNARD, V.; BURLEY, G. A. DNA-templated photonic arrays and assemblies: design principles and future opportunities. **Chemistry - A European Journal**, v. 17, n. 29, p. 7982-7991, July 2011.

SWANEPOEL, R. Determination of the thickness and optical constants of amorphous silicon. **Journal of Physics E**, v. 16, n. 12, p. 1214-1222, 1983.

TANAKA, K.; OKAHATA, Y. A DNA-lipid complex in organic media and formation of an aligned cast film. **Journal of the American Chemical Society**, v. 118, n. 44, p. 10679-10683, 1996.

TANG, C.; LIU, H. Cellulose nanofiber reinforced poly(vinyl alcohol) composite film with high visible light transmittance. **Composites Part A: Applied Science and Manufacturing**, v. 39, n. 10, p. 1638-1643, 2008.

TAO, A. R.; HUANG, J.; YANG, P. Langmuir-Blodgetty of nanocrystals and nanowires. **Accounts of Chemical Research**, v. 41, n. 12, p. 1662-1673, 2008.

TATSUURA, S. et al. Semiconductor carbon nanotubes as ultrafast switching materials for optical telecommunications. **Advanced Materials**, v. 15, n. 6, p. 534-537, 2003.

TEOTONIO, E. E. S. et al. Evaluation of intramolecular energy transfer process in the lanthanide(III) bis- and tris-(TTA) complexes: photoluminescent and triboluminescent behavior. **Journal of Luminescence**, v. 128, n. 2, p. 190-198, 2008.

THIRUMURUGAN, A. Use of ionic liquids in synthesis of nanocrystals, nanorods and nanowires of elemental chalcogens. **Bulletin of Materials Science**, v. 30, n. 2, p. 179-182, 2007.

TOPRAK, C.; AGAR, J. N.; FALK, M. State of water in cellulose acetate membranes. **Journal of the Chemical Society**, v. 75, n. 16774, p. 803-815, 1979.

TRUJILLO, S. et al. Organic-inorganic bonding in chitosan-silica hybrid networks: Physical properties. **Journal of Polymer Science Part B**, v. 53, n. 19, p. 1391-1400, 2015.

TSAI, H.-W. et al. Electrochemical synthesis of ultrafast and gram-scale surfactant-free tellurium nanowires by gas-solid transformation and their applications as supercapacitor electrodes for p-doping of graphene transistors. **Nanoscale**, v. 7, n. 17, p. 7535-7539, 2015.

TSAI, H.-Y.; LIN, Z.-H.; CHANG, H.-T. Tellurium-nanowire-coated glassy carbon electrodes for selective and sensitive detection of dopamine. **Biosensors & Bioelectronics**, v. 35, n. 1, p. 479-483, 2012.

ULRICH, R.; TORGE, R. Measurement of thin film parameters with a prism coupler. **Applied optics**, v. 12, n. 12, p. 2901-2908, 1973.

VANYSEK, P. Electrochemical series. In: LIDE, D. R. **CRC handbook of chemistry and physics**. 71st. ed. Boca Raton: CRC Press, 1991. Sect. 8, p. 8/16-8/23.

VASILEIADIS, T. et al. Laser-assisted growth of t-Te nanotubes and their controlled photo-induced unzipping to ultrathin core-te/sheath-TeO₂ nanowires. **Scientific Reports**, v. 3, 2013. doi: 10.1038/srep01209.

VELÁZQUEZ, J. M. et al. Nanotexturation-induced extreme wettability of an elemental tellurium coating. **Journal of Materials Chemistry**, v. 22, n. 8, p. 3335-3339, 2012.

VOLDER, M. F. L. et al. Carbon nanotubes: present and future commercial applications. **Science**, v. 339, n. 6119, p. 535-530, 2013.

WANG, D. et al. Synthesis of Au-decorated tripod-shaped Te hybrids for applications in the ultrasensitive detection of arsenic. **ACS Applied Materials & Interfaces**, v. 5, n. 12, p. 5733-5740, 2013.

WANG, J. et al. Highly polarized photoluminescence and photodetection from single indium phosphide nanowires. **Science**, v. 293, n. 5534, p. 1455-1457, 2001.

WANG, J.-L. et al. Recycling nanowire templates for multiplex templating synthesis: a green and sustainable strategy. **Chemistry - A European Journal**, v. 21, n. 13, p. 4935-4939, 2015.

WANG, L. et al. Self-assembled supramolecular films derived from marine deoxyribonucleic acid (DNA)-cationic surfactant complexes: large-scale preparation and optical and thermal properties. **Chemistry of Materials**, v. 13, n. 4, p. 1273-1281, 2001.

WANG, S. et al. Synthesis, characterization and optical properties of flower-like tellurium. **CrystEngComm**, v. 12, n. 1, p. 166-171, 2010.

WANG, X. et al. Growth of uniformly aligned ZnO nanowire heterojunction arrays on GaN, AlN, and Al_{0.5}Ga_{0.5}N substrates. **Journal of the American Chemical Society**, v. 127, n. 21, p. 7920-7923, 2005.

WANG, W. et al. Direct fabrication of tellurium/carbon nanocables through a facile solution route. **Crystal Growth & Design**, v. 9, n. 5, p. 2117-2123, 2009.

WANG, Z.; WANG, L.; WANG, H. PEG-mediated hydrothermal growth of single-crystal tellurium nanotubes. **Crystal Growth & Design**, v. 8, n. 12, p. 4415-4419, 2008.

WANG, Z. et al. Formation of single-crystal tellurium nanowires and nanotubes via hydrothermal recrystallization and their gas sensing properties at room temperature. **Journal of Materials Chemistry**, v. 20, n. 12, p. 2457-2463, 2010.

WATANABE, H. et al. Waveguide dye laser including a SiO₂ nanoparticle-dispersed random scattering active layer. **Applied Physics Letters**, v. 86, n. 15, 2005. doi: 10.1063/1.1904717

WEBBER, D. H.; BRUTCHEY, R. L. Photolytic preparation of tellurium nanorods. **Chemical Communications**, v. 2, n. 38, p. 5701-5703, 2009.

WEEKS, M. E. The discovery of the elements. VI. Tellurium and selenium. **Journal of Chemical Education**, v. 9, n. 3, p. 474-485, 1932.

WEI, G. et al. Solvothermal synthesis of porous tellurium nanotubes. **Chemical Physics Letters**, v. 372, n. 3/4, p. 590-594, 2003.

WILSON, D.; VALLUZZI, R.; KAPLAN, D. Conformational transitions in model silk peptides. **Biophysical Journal**, v. 78, n. 5, p. 2690-2701, 2000.

WU, X. et al. Random lasing in weakly scattering systems. **Physical Review A**, v. 74, n. 5, 2006. doi: 10.1103/PhysRevA.74.053812

WU, Y.; SU, B.; JIANG, L. Smartly aligning nanowires by a stretching strategy and their application as encoded sensors. **ACS Nano**, v. 6, n. 10, p. 9005-9012, 2012.

XI, B. et al. Shape-controlled synthesis of tellurium 1D nanostructures via a novel circular transformation mechanism. **Crystal Growth & Design**, v. 7, n. 6, p. 1185-1191, 2007.

XI, F.; WU, J.; LIN, X. Novel nylon-supported organic–inorganic hybrid membrane with hierarchical pores as a potential immobilized metal affinity adsorbent. **Journal of Chromatography A**, v. 1125, n. 1, p. 38-51, 2006.

XI, G. et al. Synthesis, characterization, and growth mechanism of tellurium nanotubes. **Crystal Growth & Design**, v. 5, n. 1, p. 325-328, 2005.

XI, G. et al. Large-scale synthesis, growth mechanism, and photoluminescence of ultrathin Te nanowires. **Crystal Growth & Design**, v. 6, n. 11, p. 2567-2570, 2006.

YAGYU, H. et al. Chemical modification of cellulose nanofibers for the production of highly thermal resistant and optically transparent nanopaper for paper devices. **ACS Applied Materials & Interfaces**, v. 7, n. 39, p. 22012-22017, 2015.

YANG, H. et al. Environmentally benign synthesis of ultrathin metal telluride nanowires. **Journal of the American Chemical Society**, v. 136, n. 29, p. 10242-10245, 2014.

YANG, P. et al. Controlled growth of ZnO nanowires and their optical properties. **Advanced Functional Materials**, v. 12, n. 5, p. 323-331, 2002.

YANG, P. et al. One-pot synthesis of monodisperse noble metal@resorcinol-formaldehyde (M@RF) and M@Carbon core–shell nanostructure and their catalytic applications. **Langmuir**, v. 31, n. 42, p. 11701-11708, 2015.

YANG, Y. et al. A new generation of alloyed/multimetal chalcogenide nanowires by chemical transformation. **Science Advances**, v. 1, n. 10, 2015. doi:10.1126/sciadv.1500714.

YANO, H. et al. Optically transparent composites reinforced with networks of bacterial nanofibers. **Advanced Materials**, v. 17, n. 2, p. 153-155, Jan. 2005.

YE, X. et al. Morphologically controlled synthesis of colloidal upconversion nanophosphors and their shape-directed self-assembly. **Proceedings of the National Academy of Sciences of the United States of America**, v. 107, n. 52, p. 22430-22435, 2010.

YU, G.; CAO, A.; LIEBER, C. M. Large-area blown bubble films of aligned nanowires and carbon nanotubes. **Nature Nanotechnology**, v. 2, n. 6, p. 372-377, 2007.

ZHAI, T. et al. Recent developments in one-dimensional inorganic nanostructures for photodetectors. **Advanced Functional Materials**, v. 20, n. 24, p. 4233-4248, 2010.

ZHAI, T. et al. One-dimensional inorganic nanostructures: synthesis, field-emission and photodetection. **Chemical Society Reviews**, v. 40, n. 5, p. 2986-3004, 2011.

ZHANG, B. et al. 1D Tellurium nanostructures: photothermally assisted morphology-controlled synthesis and applications in preparing functional nanoscale materials. **Advanced Functional Materials**, v. 17, n. 3, p. 486-492, 2007.

ZHANG, C. et al. Synthesis and applications of organic nanorods, nanowires and nanotubes. **Annual Reports on the Progress of Chemistry, Section C: Physical Chemistry**, v. 109, p. 211-239, 2013.

ZHANG, H. et al. Straight and thin zno nanorods: hectogram-scale synthesis at low temperature and cathodoluminescence. **The Journal of Physical Chemistry B**, v. 110, n. 2, p. 827-830, 2006.

ZHANG, J. et al. Optical anisotropy of semiconductor nanowires beyond the electrostatic limit. **Physical Review B**, v. 82, n. 15, p. 15531/1-155301/6, 2010.

ZHANG, K.; FELDNER, A.; FISCHER, S. FT Raman spectroscopic investigation of cellulose acetate. **Cellulose**, v. 18, n. 4, p. 995-1003, 2011.

ZHANG, L.; WANG, C.; WEN, D. Preparation by hydrothermal techniques in a tungstosilicate acid solution system and optical properties of tellurium nanotubes. **European Journal of Inorganic Chemistry**, v. 2009, n. 22, p. 3291-3297, 2009.

ZHANG, W. et al. Nanowire-directed templating synthesis of metal-organic framework nanofibers and their derived porous doped carbon nanofibers for enhanced electrocatalysis. **Journal of the American Chemical Society**, v. 136, n. 41, p. 14385-14388, 2014.

ZHENG, S. et al. Raman spectroscopic investigation of the denaturation process of silk fibroin. **Applied Spectroscopy**, v. 43, n. 7, p. 1269-1272, 1989.

ZHONG, C. et al. A chitin nanofiber ink for airbrushing, replica molding, and microcontact printing of self-assembled macro-, micro-, and nanostructures. **Advanced Materials**, v. 23, n. 41, p. 4776-4781, 2011.

ZHOU, P. et al. Structure of Bombyx mori silk fibroin based on the DFT chemical shift calculation. **The Journal of Physical Chemistry B**, v. 105, n. 50, p. 12469-12476, 2001.

ZHU, H. et al. Controlled synthesis of tellurium nanostructures from nanotubes to nanorods and nanowires and their template applications. **The Journal of Physical Chemistry C**, v. 115, n. 14, p. 6375-6380, Apr. 2011.

ZHU, Y.-J. et al. Microwave-assisted synthesis of single-crystalline tellurium nanorods and nanowires in ionic liquids. **Angewandte Chemie International Edition**, v. 43, n. 11, p. 1410-1414, Mar. 2004.

RESUMO EXPANDIDO DA TESE

Esta seção apresenta resumidamente os principais resultados desta tese de doutoramento.

Nanoestruturas unidimensionais para fotônica

Nos últimos 10 anos a preparação de nanoestruturas unidimensionais vem atraindo atenção devido às propriedades químicas e físicas que permitem novas aplicações. Em comparação com estruturas 0-dimensionais (como nanopartículas ou pontos quânticos) as estruturas unidimensionais (nanofios, nanobastões, nanofitas e nanotubos) podem ser tomadas como sistemas modelo para o estudo de propriedades ópticas, mecanismos de transporte eletrônico como função do confinamento de tamanho e dimensionalidade.

Atenção especial deve ser dedicada a utilização de nanofios de Te como “template”, na preparação dos mais variados materiais nanoestruturados. A preparação de nanofios e nanotubos de Te com dimensões controladas, a partir de métodos relativamente simples em solução, leva a um campo grande de aplicações. A processabilidade e reatividade destas nanoestruturas permitem a sua utilização na preparação de materiais.

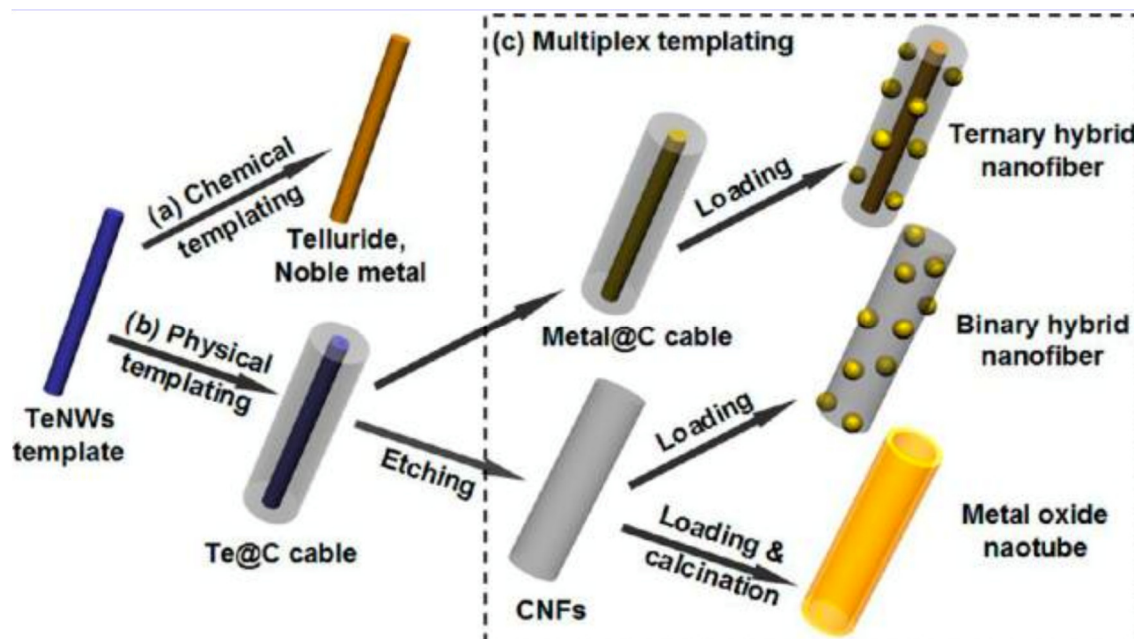
O grupo do Prof. S.H. Yu em Hefei, China certamente tem apresentado contribuições belíssimas na área. Em revisão recente (LIANG et al., 2012) o Prof. Yu apresenta o leque de materiais que podem ser preparados a partir dos nanofios de Te, como membranas, filmes, hidrogéis e aerogéis apresentando aplicações diversas que envolvem a preparação de membranas especiais para filtração/separação, catálise, superadsorventes entre outras.

A Figura 1, adaptada de (LIANG et al., 2012) mostra de maneira esquemática a versatilidade que permite os diferentes processos de preparação de materiais uni-dimensionais utilizando os nanofios de Te tratados no grupo Chinês.

No método químico (a) a reatividade do Te é utilizada para a preparação de materiais como Pd, Pt, teluretos, entre outros. No método físico (b) os nanofios de Te são usados como “template” para deposição de outros materiais como carbono (Te@C) ou mesmo resinas fenol-formaldeído (Te@fenol-formaldeído) que uma vez submetidos a remoção do Te levam a nanofibras de C ou resina de dimensões controladas. O item (c) da figura se refere ao que o autor chama de “síntese multiplex”, que envolve a utilização adicional das estruturas Te@C. Estas estruturas, devido principalmente ao método de preparação de baixa temperatura, apresentam grupos funcionais hidroxila ou carboxila em sua superfície permitindo a interação

com cátions ou nanopartículas carregadas positivamente. Nanotubos de carbono decorados com as mais diversas estruturas como óxidos ou colóides metálicos são assim obtidos.

Figura 1 - Ilustração esquemática da utilização de Te como template incluindo métodos (a) Químicos, (b) Físicos, e (c) Síntese Multiplex.



Fonte: Liang et al. (2012)

O Te é um semicondutor do tipo p com energia de band-gap direto relativamente baixa (0,35 eV) (DUN et al., 2015). Possui uma estrutura cristalina anisotrópica descrita por infinitas cadeias helicoidais empacotadas entre si por fracas interações de van der Waals (TSAI et al., 2015; WANG et al., 2009; ZHU et al., 2011). Em escala nanométrica, nanoestruturas unidimensionais de Te (Te1D) na forma de fios, bastões, tubos e fitas são tipicamente obtidas.

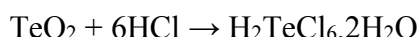
Nanoestruturas Te1D exibem propriedades bastante interessantes e versáteis tais como: fotocondutividade, sensor de gás, agente anti-bactericida, aplicações termoelétricas, eletrodos supercapacitores e cátodos de baterias.

Uma das estratégias interessantes que tem sido considerada para a fabricação controlada de nanoestruturas 1D de compostos de íons lantanídeos, envolve a utilização de uma estrutura molde (template) e seguida deposição controlada do composto lantanídico (óxidos, sais ou complexos de íons lantanídeos) (BU et al., 2005).

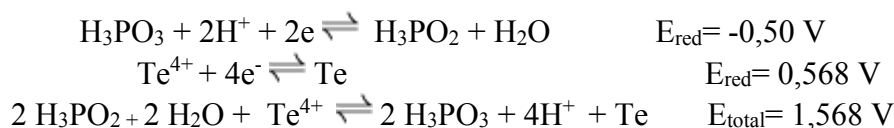
Nanoestruturas 1D de Te foram obtidas pela redução de TeO_2 por ácido hipofosforoso. A síntese de nanoestruturas de Te foi conduzida em diferentes temperaturas em soluções aquosas de Pluronic® F68 0.33745 %. Para tanto, 50 μL de uma solução aquosa de TeO_2 0.02 g L^{-1} foi adicionada a 20 mL de uma solução aquosa de Pluronic® F68 0.33745 % sob agitação vigorosa

à temperatura ambiente durante 10 min. Após, uma solução aquosa de ácido hipofosforoso (H_3PO_2) $0.3128 \text{ mol L}^{-1}$ foi rapidamente injetada sobre a mistura. A razão molar $\text{Te}:\text{H}_3\text{PO}_2$ foi estabelecida em 1:10. A mistura foi particionada em volumes iguais e transferida para 4 tubos de ensaio com tampas enroscáveis com capacidade de 10 mL. Os tubos de ensaio foram mantidos em repouso sob diferentes temperaturas: 5°C , 21°C , 60°C e 90°C .

Uma vez que TeO_2 é insolúvel em água, uma solução de HCl 35 % (v/v) foi utilizada para dissolução. Esta reação pode ser descrita pela seguinte equação:

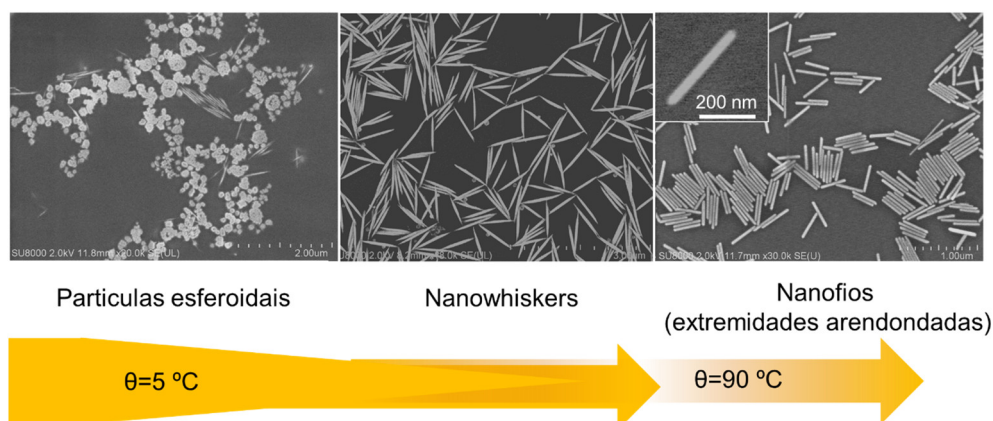


A redução de espécies de $\text{H}_2\text{TeCl}_6 \cdot 2\text{H}_2\text{O}$ por H_2PO_3 pode ser descrita de acordo com a seguinte equação (VANYSEK, 1991):



Nanoestruturas de Te com formato quasi-esférico e tamanho médio de 100 nm são formadas à baixa temperatura juntamente com uma pequena população de nanoestruturas 1D de Te na forma de espinhos (nanowhiskers). Os esferóides apresentam superfície irregular e protuberância de ramificações sobre a superfície do esferóide. Quando a reação foi conduzida em temperaturas mais elevadas, as sementes foram consumidas para produzir nanoestruturas Te1D como apresentado na Figura 2.

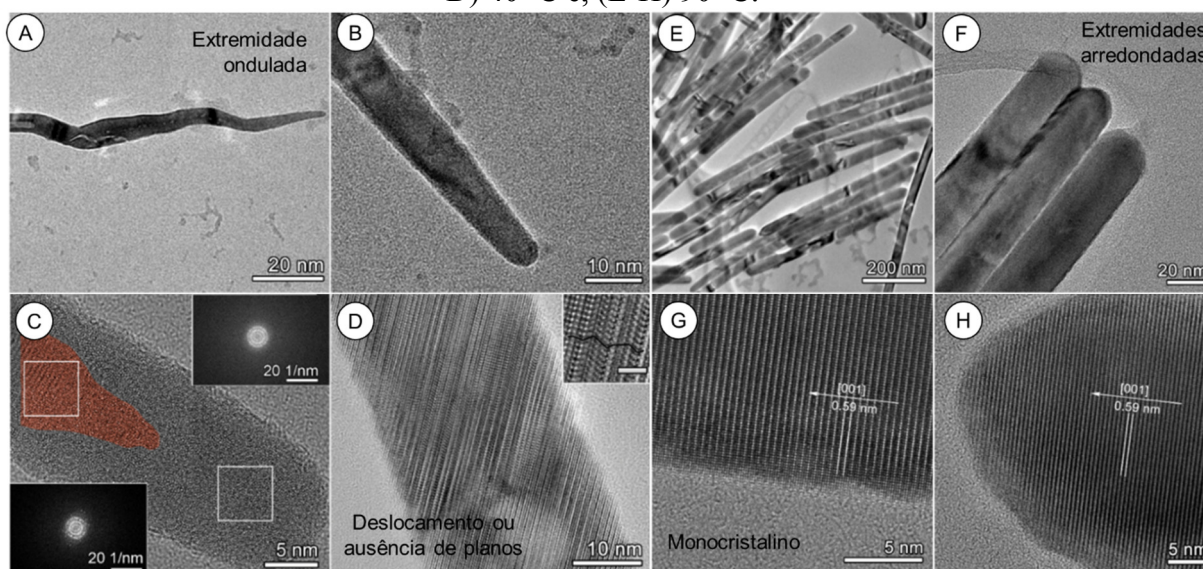
Figura 2 - Imagens de SEM demonstrando a evolução da morfologia das nanoestruturas de Te com o aumento da temperatura



Fonte: Autor

As nanoestruturas 1D produzidas em temperaturas superiores à temperatura ambiente (i.e. 21 °C) apresentam uniformidade morfológica (> 95% de nanoestruturas 1D) bem como homogeneidade da razão de aspecto (i.e. a razão entre o comprimento e o diâmetro). As nanoestruturas Te1D sintetizadas à 50 °C exibem extremidades filamentadas em comparação com as nanoestruturas obtidas à 90 °C. Essa diferença morfológica peculiar é claramente observada nas imagens de TEM da Figura 2 para nanoestruturas de Te1D sintetizadas em condições experimentais similares, porém aumentando a proporção molar Te:H₃PO₂ para 20:100, ou seja, elevando para 20x a concentração de Te e 10x a concentração de H₃PO₂ em relação síntese padrão. As amostras obtidas à 40 °C e 90 °C foram nomeadas como **TeB 40 °C** e **TeB 90 °C**, respectivamente

Figura 3 - Imagens de TEM e HRTEM de nanoestruturas de Te obtidas quando a reação foi conduzida utilizando-se a proporção molar Te:H₃PO₂ = 20:100 e diferentes temperaturas (A-D) 40 °C e, (E-H) 90 °C.



Fonte: Autor

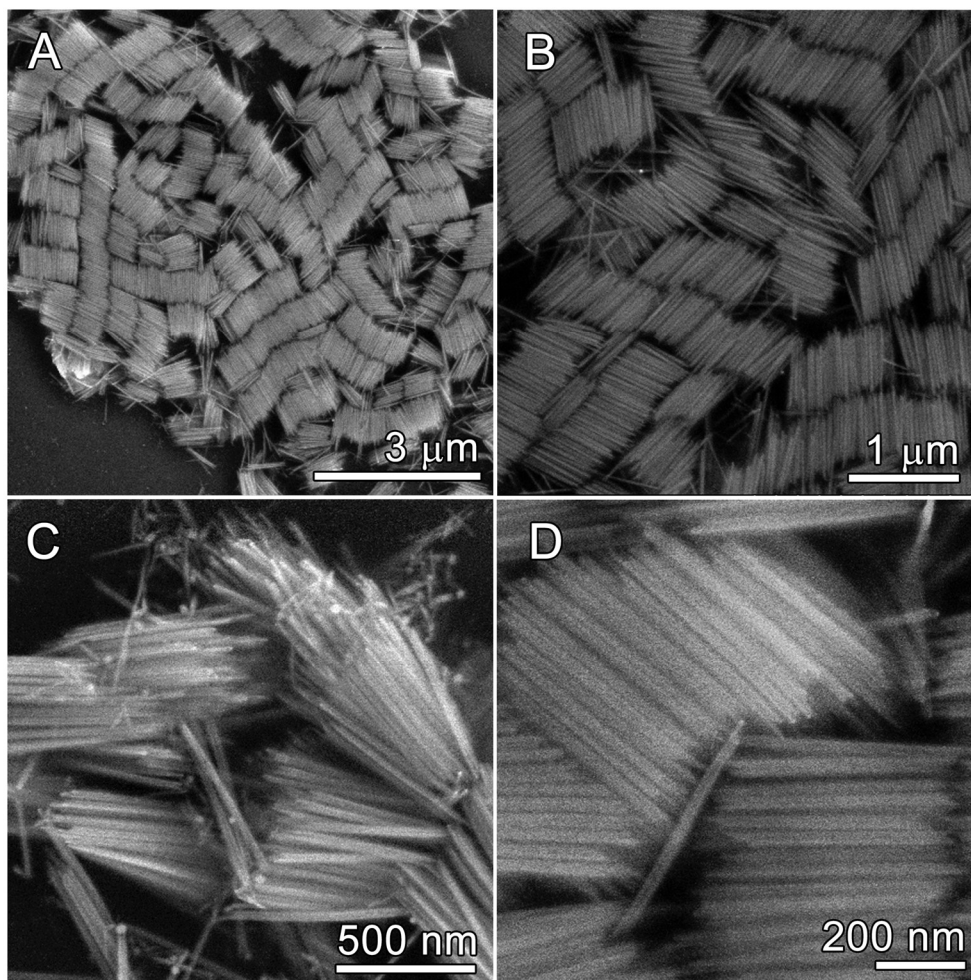
As imagens TEM mostrados na Figura 3A indica que a extremidade das nanoestruturas de Te sintetizadas à 40 °C possui uma estrutura irregular com formato ondulado. O diâmetro é continuamente reduzido em direção ao extremo da nanoestrutura (Figura 3B). Afim de se investigar a cristalinidade, aplicou-se a operação de transformada de Fourier em duas regiões distintas da extremidade das nanoestruturas de Te. A Figura 3C revela que as pontas das nanoestruturas obtidas nesta temperatura são compostas por estruturas amorfas nos extremos e estruturas cristalinas na região central menos periférica (demarcado por vermelho). Uma inspeção detalhada da porção média das nanoestruturas por HRTEM, demonstrada na Figura

3D, claramente revela a presença de defeitos cristalinos tais como desornamento de planos e “*stacking faults*”.

Figura 3, E-H apresenta imagens de TEM das nanoestruturas sintetizadas à 90 °C. A distribuição do diâmetro é homogênea com tamanho médio de 27 nm. As imagens de HRTEM claramente indica que as nanoestruturas são monocristalinas com direção de crescimento no eixo [001], além extremidades com formato arredondado. Sugere-se o material amorfo presente na ponta dos nanofios de Te obtidos à 40 °C poderiam ser completamente transferido para a forma trigonal através do processo de Ostwald Ripening acelerado com o aumento da temperatura.

Curiosamente, a secagem de gotas da suspensão de nanofios de Te à temperatura ambiente sobre a superfície de um substrato plano de Si/SiO₂ produz estruturas auto-organizadas. Durante a secagem, múltiplos anéis são formados em direção ao centro da gotícula durante a evaporação do solvente (efeito de anéis de café). Essencialmente, estes anéis são compostos por uma densa camada de nanofios de Te ordenados paralelamente uns aos outros, tal como apresentado na Figura 4. Sugere-se que o processo de espalhamento baseia-se na existência de uma força de cisalhamento que alinha as nanoestruturas Te1D no sentido da direção do fluxo e, eventualmente, são imobilizadas no substrato sólido de Si/SiO₂. Em conjunto, isto estabelece uma solução saturada de um filme de partículas na interface ar-líquido. Nanoestruturas unidimensionais sofrem espontaneamente ordenamento rotacional com a diminuição do volume (por exemplo, devido à evaporação do solvente) a fim de maximizar sua área de contato com o substrato.

Figura 4 - Auto-organização de nanoestruturas de TeA 40°C pela secagem de uma gota da suspensão aquosa sobre a superfície de Si/SiO₂.

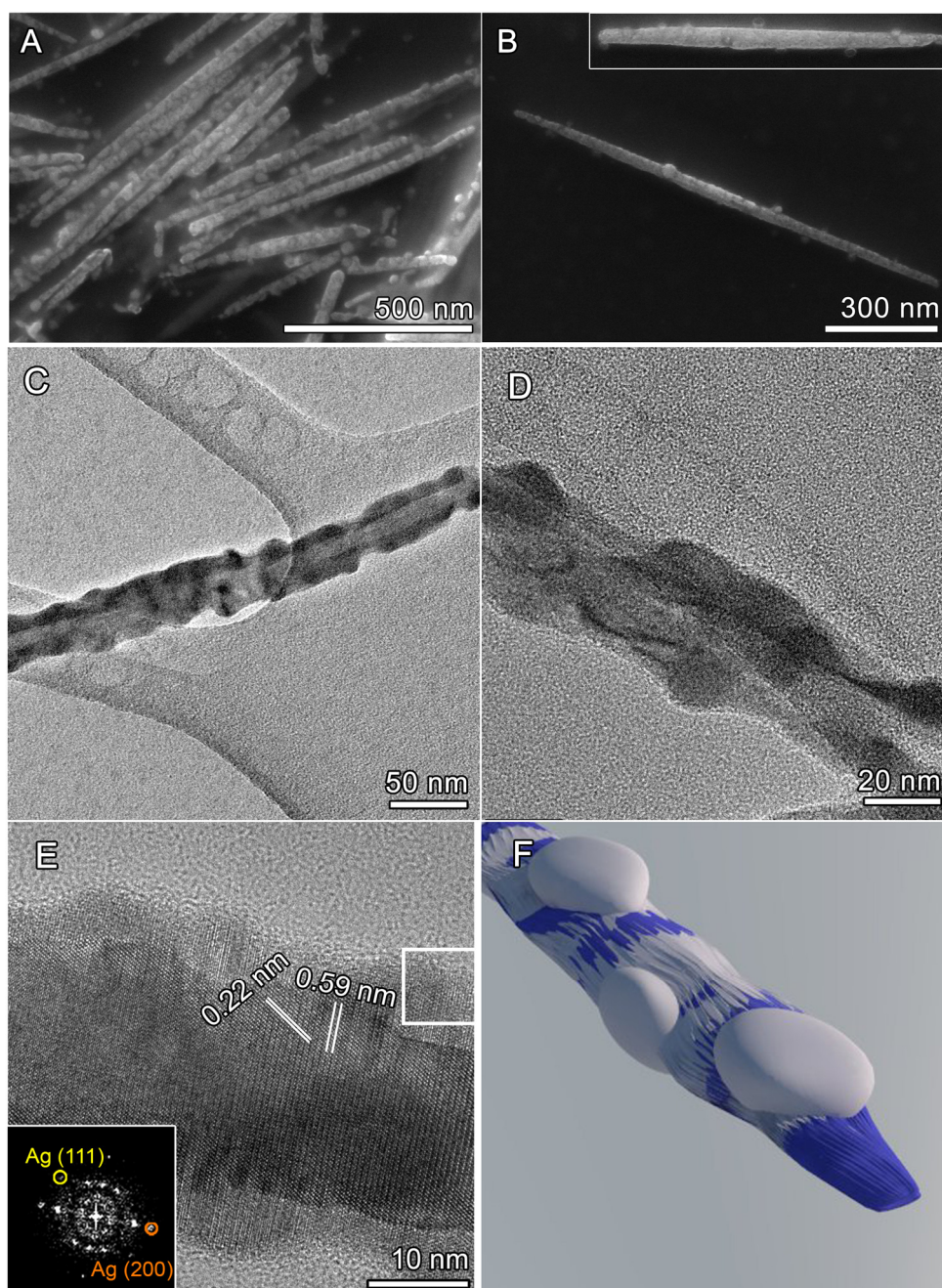


Fonte: Autor

Uma das propostas deste trabalho consiste em produzir estruturas híbridas a partir de nanofios de Te. Nanofios de Te (amostra TeB 90 °C) foram utilizados para a fabricação de nanoestruturas híbridas de Te@Ag. Neste caso, uma solução aquosa de Ag^+ e suspensão de nanofios de Te foram misturados na proporção molar 0.005:1 em uma polivinilpirrolidona (PVP) 0.58 %.

Nanopartículas de Ag com tamanho médio inferior a 20 nm podem ser observadas nitidamente na superfície dos nanofios de Te. As imagens de TEM e HRTEM revelam que a superfície de Te é irregular, provavelmente devido a corrosão por íons Ag^+ . O resultado corresponde a nanofios de Te recobertos por uma camada cristalina. O inset na Figura 5E corresponde ao FFT da região quadrada destacado em branco sob a camada cristalina que cobre os nanofios de Te. As distâncias interplanares correspondem à estrutura cúbica de face centrada de Ag elementar. As distâncias interplanares 0.59 nm e 0.22 nm indicadas na Figura 5E correspondem aos planos (001) e (010) da estrutura hexagonal de Te.

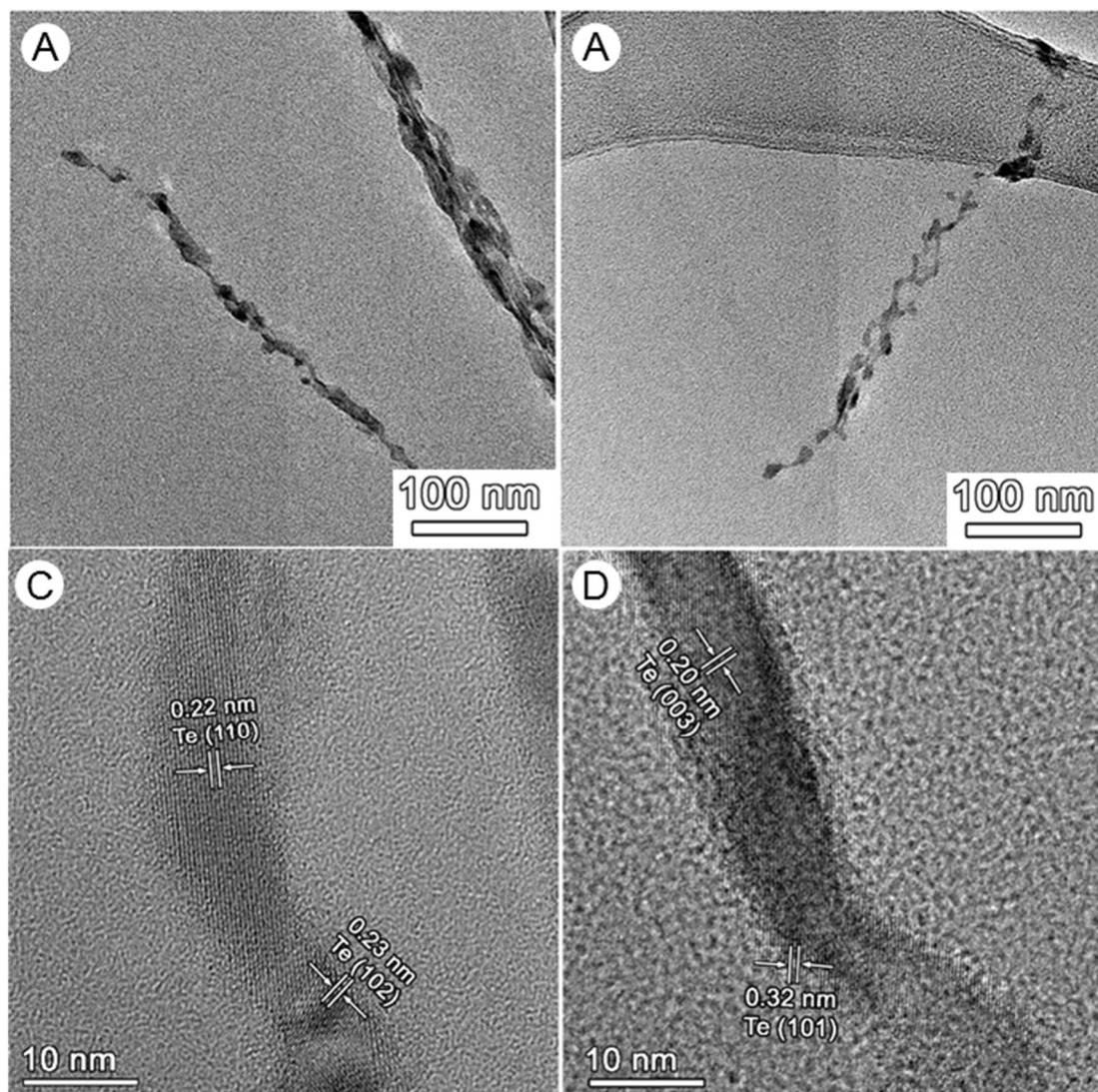
Figure 5 - Imagens de (A, B) SEM, (C, D)TEM e (E) HRTEM de nanoestruturas híbridas de Te@Ag. (F) Ilustração representando as nanoestruturas híbridas Te@Ag nanostructure.



Fonte: Autor

Nanohélices de Te foram obtidas quando a temperatura da síntese foi diminuída para 60 °C, enquanto os outros parâmetros permaneceram constantes. A Figura 6 exibe as imagens de TEM e HRTEM das nanohélices de Te. As nanohélices exibem diâmetro médio entre 9-20 nm e comprimento inferior a 1 um. As nanohélices de Te são altamente cristalinas em toda a sua estrutura.

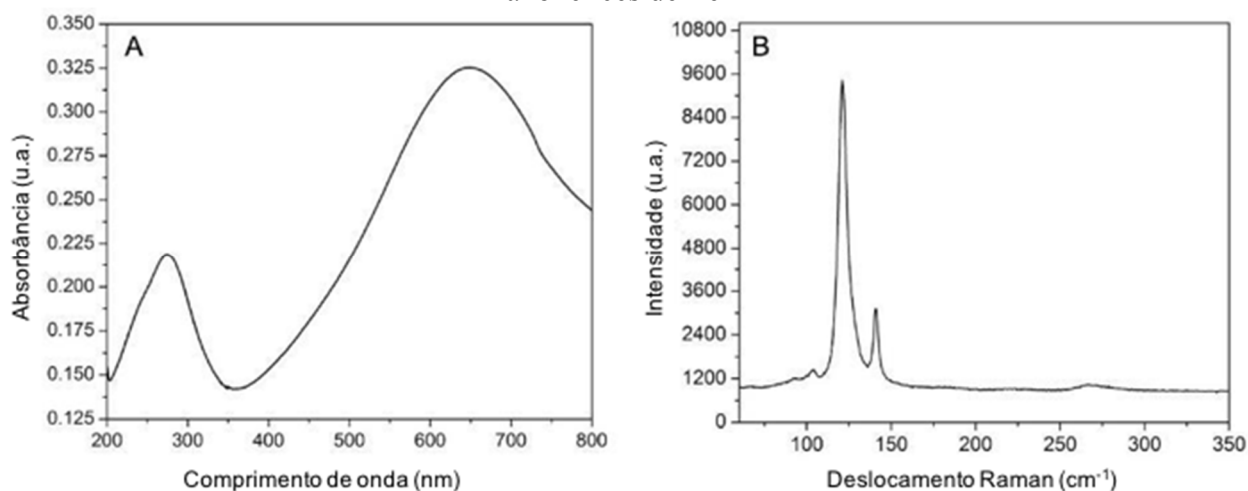
Figura 6 - Imagens de TEM e HRTEM de nanohélices de Te.



Fonte: Autor

Os espectros de absorção na região do UV-Vis indicam duas bandas características de nanoestruturas unidimensionais de Te. Na Figura 7A, as bandas de absorção menos intensas estão localizadas em 279 nm e 275 nm, respectivamente. Estas bandas se referem à transição eletrônica permitida direta da banda de valência (triplete p ligante) para a banda de condução (triplete p antiligante). A bandas de absorção mais intensa e larga está localizada em 651 nm e é associada à transições eletrônicas da banda de valência (triplete p não-ligante) para a banda de condução (triplete p antiligante) (ISOMÄKI; BOEHM, 1982).

Figura 7 - Espectros de (A) absorção na região do ultravioleta-visível e (B) Raman das nanohélices de Te



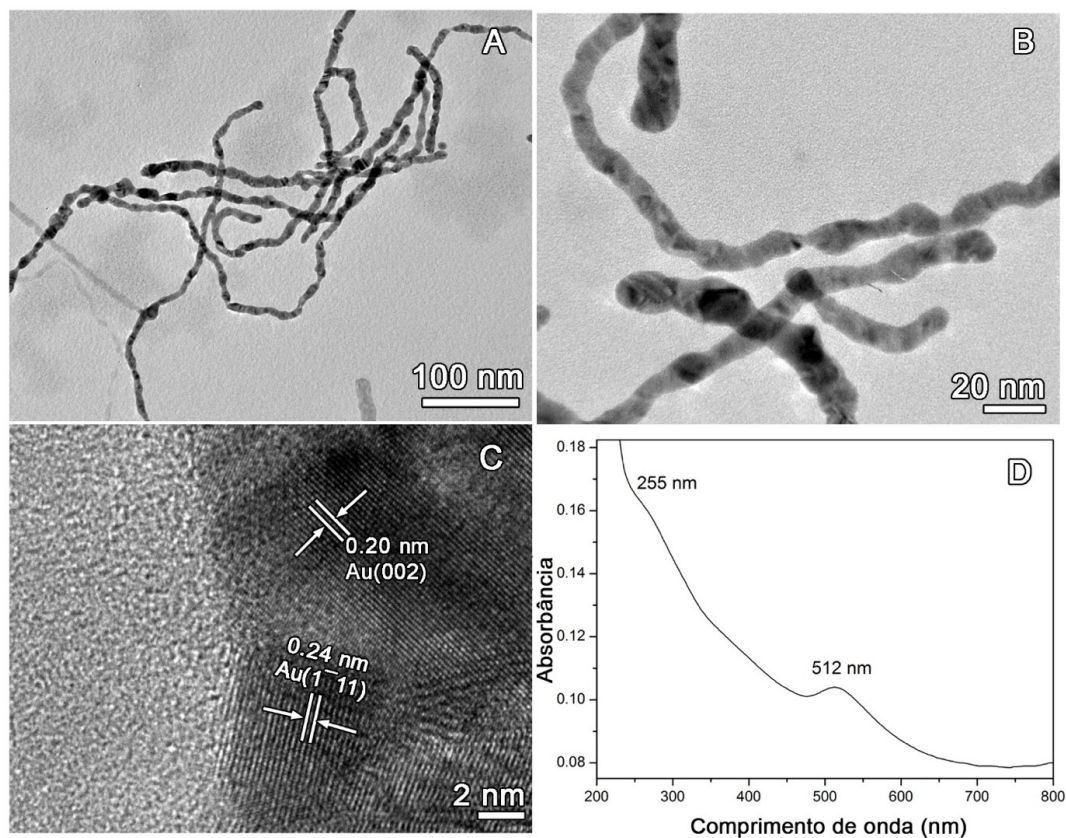
Fonte: Autor

Na Figura 7, os espectros Raman exibem bandas típicas do grupo de simetria D3 da estrutura hexagonal do Te (MARINI et al., 2012; MARTIN; LUCOVSKY; HELLIWELL, 1976; PINE; DRESSELHAUS, 1971) com três bandas na região entre 100-300 cm^{-1} . A banda mais intensa em 121.7 cm^{-1} refere-se ao modo vibracional da rede A1 e duas bandas degeneradas localizadas em 103.7 cm^{-1} e 141.2 cm^{-1} associadas ao modo E(1) e E(2), respectivamente (MARINI et al., 2012; PINE; DRESSELHAUS, 1971; VASILEIADIS et al., 2013). A banda larga em 266.3 cm^{-1} é associada ao harmônico de segunda ordem do modo E.

Nanoestruturas híbridas de Te@Au produzidas utilizando nanohélices de Te como molde de sacrifício. Neste caso, uma solução aquosa de íons Au^{3+} , ácido ascórbico (agente redutor auxiliar) e PVP (surfactante). As imagens de TEM exibidas na Figura indicam que nanoestruturas unidimensionais são irregulares com nódulos protuberantes distribuídas indistintamente. Esta morfologia assemelha-se com as estruturas obtidas por Lin et al (2008). As imagens de HRTEM dos híbridos Te@Au indicam que as nanoestruturas são policristalinas formadas unicamente por Au elementar. O espectro de absorção exibe uma banda em 512 nm referente à banda de plasmon de Au. A banda em 651 nm observa para as nanohélices de Te desapareceu completamente após 10 min que a reação foi finalizada.

As nanohélices de Te também foram utilizadas para fabricar nanoestruturas unidimensionais do tipo casca-caroço. Neste caso, uma resina polimérica de resorcinol-formaldeído foi empregada para a produção da casca.

Figura 8 - Imagens de (A, B) TEM, (C) HRTEM e (D) Espectrofotometria UV-Vis de nanoestruturas híbridas Te@Au.



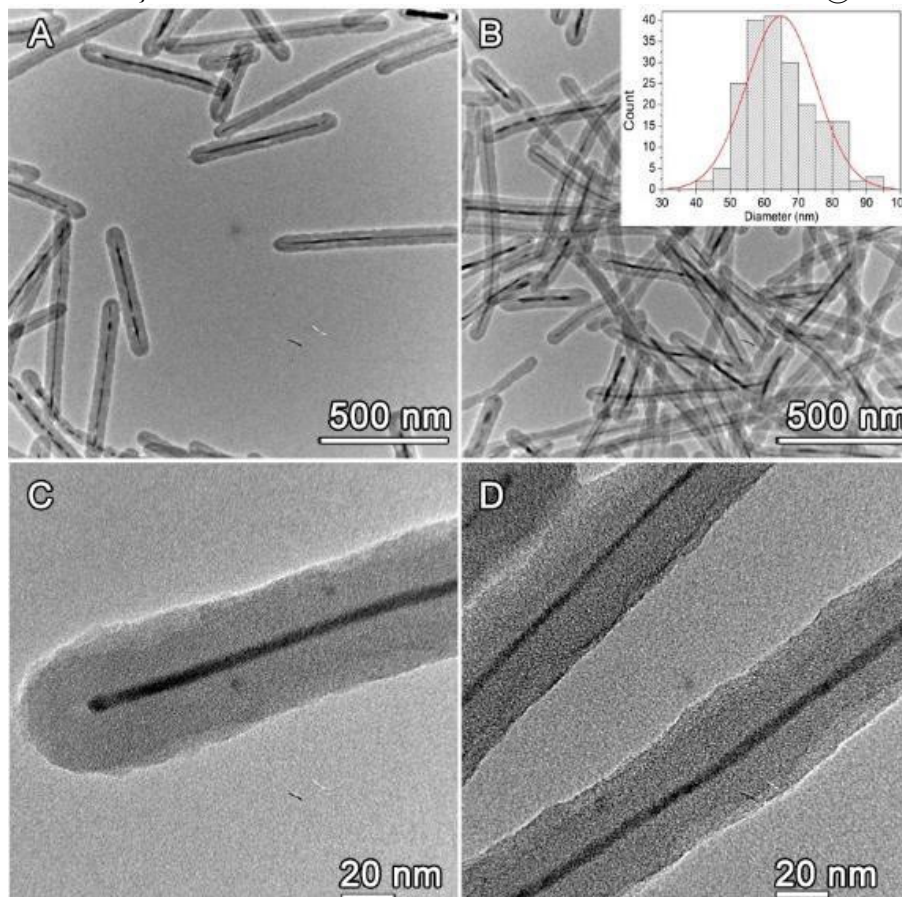
Fonte: Autor

O objetivo do recobrimento com esta resina é avaliar sua capacidade como camada intermediária para incorporar componente opticamente ativos, tais como nanopartículas baseadas em íons terra-rara (e..g óxido e hidroxicarbonato) e nanopartículas metálicas, uma vez que a superfície de Te é bastante susceptível a reações de oxidação. O protocolo de recobrimento das nanohélices de Te com resina de RF foi adaptado do procedimento descrito por Yang et al., (2015). Nesse trabalho, as nanohélices de Te foram utilizadas como “caroço” e a resina resorcinol-formaldeído como “casca”. A síntese foi realizada na presença de um surfactante - solução de Pluronic® F68 0,3375% - ao invés da H₂O somente.

Em um frasco de vidro de 20 mL, 5,962 mL da solução de Pluronic® F68 0,3375% e 7,75 mg de resorcinol foram adicionados juntamente com 1,537 mL da suspensão de nano hélices de Te dialisadas. Em seguida, 10 µL de NH₄OH foram adicionados sob agitação vigorosa. A reação foi mantida sob agitação vigorosa por 40 minutos a temperatura ambiente. O revestimento da resina resorcinol- formaldeído (RF) foi obtido pela da introdução de 22,5 µL de formaldeído. Essa mistura reacional permaneceu sob agitação por mais 4 horas. Posteriormente, foi transferida para a estufa a 40 °C, permanecendo por 12 horas. A amostra foi

centrifugada sob as seguintes condições: a 10.000 rpm por 5 minutos. Após, o precipitado foi lavado com etanol, por duas vezes. E então, redisperso em 5 mL de H₂O miliQ.

Figura 9. (A-D) Imagens de TEM de nanoestruturas de Te@RF. O inset em (C) exibe a distribuição de tamanho do diâmetro das nanoestruturas de Te@RF.



Fonte: Autor

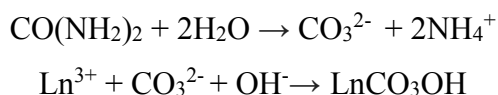
Com o intuito de diminuir a espessura da casca de RF em torno das nano hélices de Te, pensou-se em controlar as quantidades do resorcinol e do formaldeído na síntese, mantendo os outros parâmetros constantes, avaliando, posteriormente, os resultados. Assim, otimizando as condições, partiu-se de 4,625 mL da solução de Pluronic® F68 0,3375 %, 1,280 mL da suspensão de nanohélices de Te dialisado, 0,155 mL da solução aquosa de Resorcinol 0,1 % e 8,5 µL de NH₄OH e deixou-se por 40 minutos sob agitação de 4. Após, adicionou-se 2,3 µL de Formaldeído e deixou-se sob agitação, a temperatura ambiente, por 16 horas. Após, a amostra foi lavada várias vezes com H₂O miliQ.

Uma vez que a reação pode ser conduzida à baixa temperatura, a morfologia das nanohélices de Te foram preservadas. A reação de polimerização ocorre sob catálise básica onde Pluronic® F68 é utilizado como estabilizador. As imagens de TEM mostrados na Figura 9 mostram que o produto são nanoestruturas do tipo casca-caroco onde a resina RF e as nanohélices de Te

correspondem a casca e o caroço, respectivamente. O tamanho médio da casca de RF é aproximadamente 31 nm.

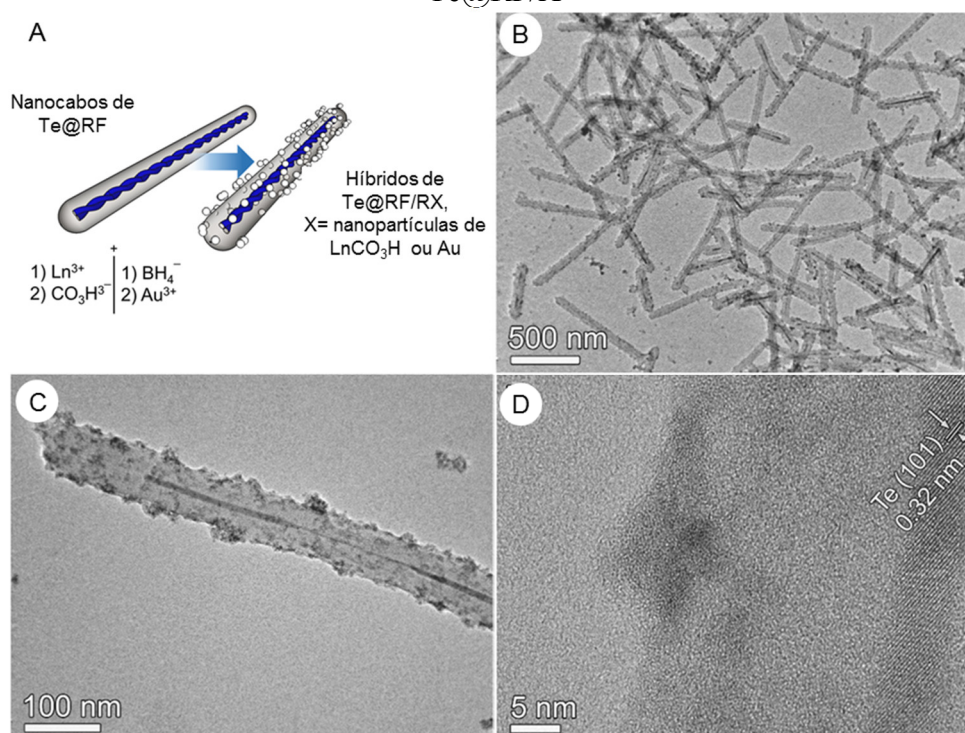
Devido à superfície rica em grupos hidroxila, nanoestruturas de Te@RF são mais suscetíveis a modificações químicas que as nanohélices de Te. Neste trabalho, nanopartículas de hidroxicarbonato de lantanídeos e nanopartículas de Au foram depositadas na superfície de nanoestruturas de Te@RF tal como representado na Figura 10A.

No primeiro caso, uma solução de cloreto de La^{3+} , Ce^{3+} e Tb^{3+} na proporção molar 45:45:10 foram adsorvidos na superfície das nanoestruturas Te@RF à temperatura ambiente. Posteriormente, a temperatura foi aumentada para 90 °C e uréia foi adicionada. A decomposição térmica de uréia permite a formação de nanopartículas de hidroxicarbonato de lantanídeos na superfície das nanoestruturas de Te@RF tal como demonstrado na Figura 10, B-D. A reação que rege a obtenção destas nanopartículas pode ser descrita a seguir:



Nanopartículas amorfas de $(\text{La}_{45\%}\text{Ce}_{45\%}\text{Tb}_{10\%})\text{CO}_3\text{OH}$ com forma indefinida e tamanho inferior a 5 nm foram sintetizadas sobre a superfície das nanoestruturas de Te@RF. As nanopartículas encontraram-se homoganeamente dispersas na superfície das nanoestruturas de Te@RF.

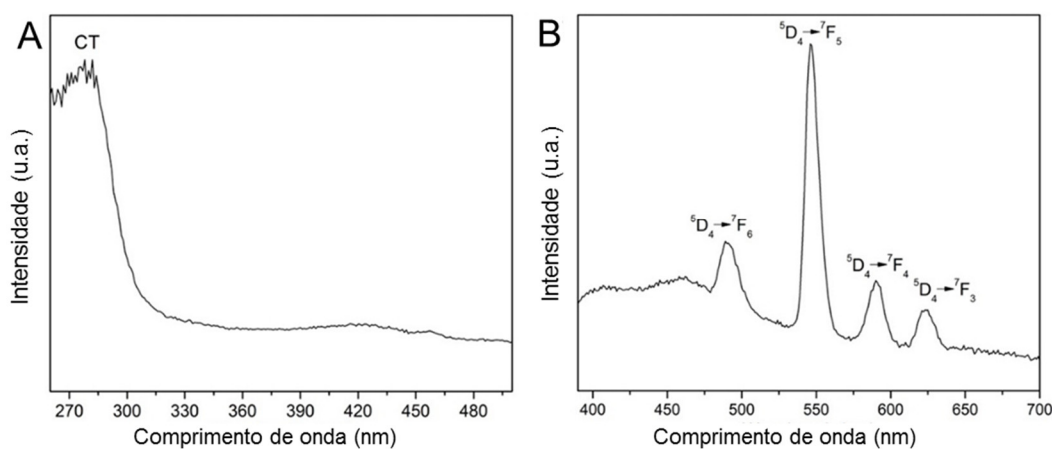
Figura 10 - A) Representação esquemática da síntese de híbridos derivados de nanoestruturas Te@RF/X



Fonte: Autor

A Figura 11 exibe os espectros de excitação e emissão de nanoestruturas de Te@RF@(La_{45%} Ce_{45%} Tb_{10%})CO₃OH obtidos à temperatura ambiente. O espectro de excitação exibe uma banda intensa localizada em 278 nm ao monitorar a emissão em 543 nm, característica da matriz hospedeira. O espectro de emissão sob excitação em 278 nm apresenta bandas características do íon Tb³⁺ sendo atribuídas a transições ⁵D₄→⁷F_J (J = 6, 5, 4, 3): ⁵D₄→⁷F₆ (490 nm), ⁵D₄→⁷F₅ (546 nm), ⁵D₄→⁷F₄ (590 nm), and ⁵D₄→⁷F₃ (623 nm).

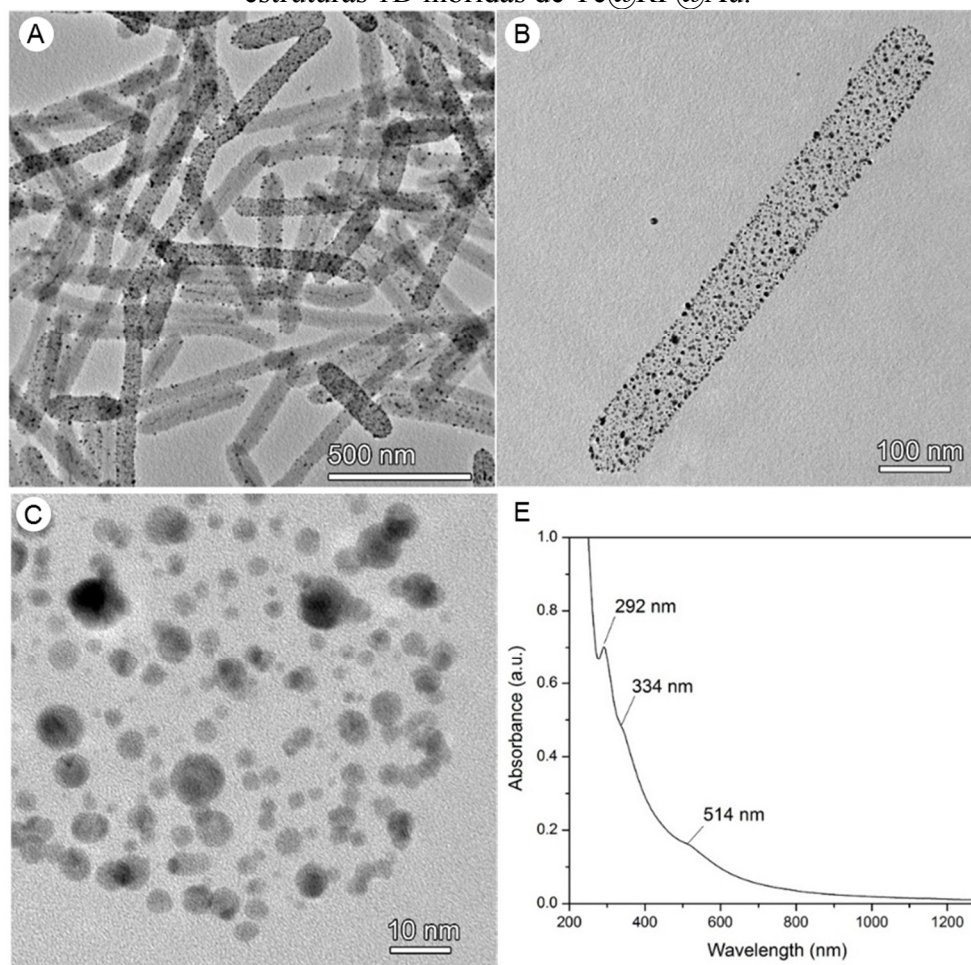
Figura 11 - Espectros de A) excitação (B) emissão de nanoestruturas casca-carço de Te@RF decoradas com nanopartículas de (La_{45%} Ce_{45%} Tb_{10%})CO₃OH.



Fonte: Autor

Nanopartículas metálicas também foram depositadas na superfície de nanoestruturas de Te@RF. Particularmente, nanopartículas de Au foram preparadas pela redução de íons Au³⁺ na superfície de nanoestruturas Te@RF. Especificamente, uma solução de NaBH₄ 10 mM foi adicionada a uma suspensão de nanoestruturas de Te@RF. Posteriormente, uma solução aquosa de íons Au³⁺ 25 mM foi adicionada. As nanopartículas de Au exibiram forma quase-esférica e distribuição de tamanho entre 2-10 nm, como mostrado na Figura 12, A-C. Na Figura 12E, o espectro de absorção UV-vis da nanoestrutura híbrida exibe duas bandas principais de absorção em 290 e 514 nm associadas com transições $\pi - \pi^*$ de anéis aromáticos da resina de RF e banda de ressonância de plasmons localizados de Au, respectivamente. Pode-se notar que não é possível observar a banda de absorção das nanohélices de Te. Provavelmente, Te foi eventualmente oxidado com a adição de íons Au³⁺.

Figura 12 - (A-C) Imagens de TEM e (D) Espectro de absorção na região do UV-vis de estruturas 1D híbridas de Te@RF@Au.



Fonte: Autor

Biopolímeros e plásticos reciclados para fotônica

Matrizes hospedeiras baseadas em biopolímeros podem ser utilizados com sucesso para a fabricação de dispositivos fotônicos multifuncionais devido às boas propriedades ópticas, biocompatibilidade, propriedades mecânicas notáveis e uma gama de grupos funcionais. Particularmente, a fibroína da seda apresenta uma série de propriedades adequadas para aplicações em fotônica que ainda não foram totalmente exploradas. Neste trabalho, nós também demonstramos a operação de um laser por retroespalhamento distribuído baseados em filmes de fibroína dopados com o corante de Rodamina 6G e filmes contendo Rodamina 6G e nanopartículas de sílica e prata. Grades de difração de fibroína foram fabricadas utilizando um disco versátil digital (DVD) como molde.

Soluções de fibroína da seda (SF) dopadas com Rodamina 6G (Rh6G) e contendo partículas de SiO₂ (diâmetro médio ≈123 nm) e nanopartículas de Ag (diâmetro médio ≈10 nm) foram preparadas. Os filmes de SF com estrutura de grades de difração foram obtidos pela secagem

das soluções mencionadas anteriormente sobre a superfície padronizada de policarbonato de um DVD comercial com um período de grade de 750 nm.

Os filmes apresentaram espessura média por volta de 0.11 ± 0.01 mm, de aparência homogênea, sendo mecanicamente flexíveis e robustos. A concentração de Rh6G nos filmes foi estimado em $\approx 2.8 \times 10^{-7}$ mol g⁻¹ (4×10^4 mol L⁻¹) após a evaporação do solvente.

Nanopartículas de Ag (AgNPs) esféricas e estabilizadas por citrato foram preparadas utilizando pela redução de íons Ag⁺ por NaBH₄. As imagens representativas de TEM revelaram que as nanopartículas tem um diâmetro médio de ≈ 10 nm.

Este resultado possui boa correlação com a banda de plasmon de superfície localizados (LSP) observada em ≈ 400 nm observada na Figura 13b. As nanopartículas de SiO₂ (SiO₂ NPs) foram sintetizadas pelo método modifica de Stober (STOBER; FINK; BOHN, 1968). As imagens TEM de SiO₂ NPs em duas magnificações diferentes são demonstradas na Figura 13, c e d.

As amostras de SF contendo diferentes densidades de SiO₂ NPs foram rotuladas como SFSiN (N=1-3) e as amostras contendo Ag NPs foram rotuladas como SFAG; A Tabela 1 apresenta a concentração dos componentes investigados neste trabalho.

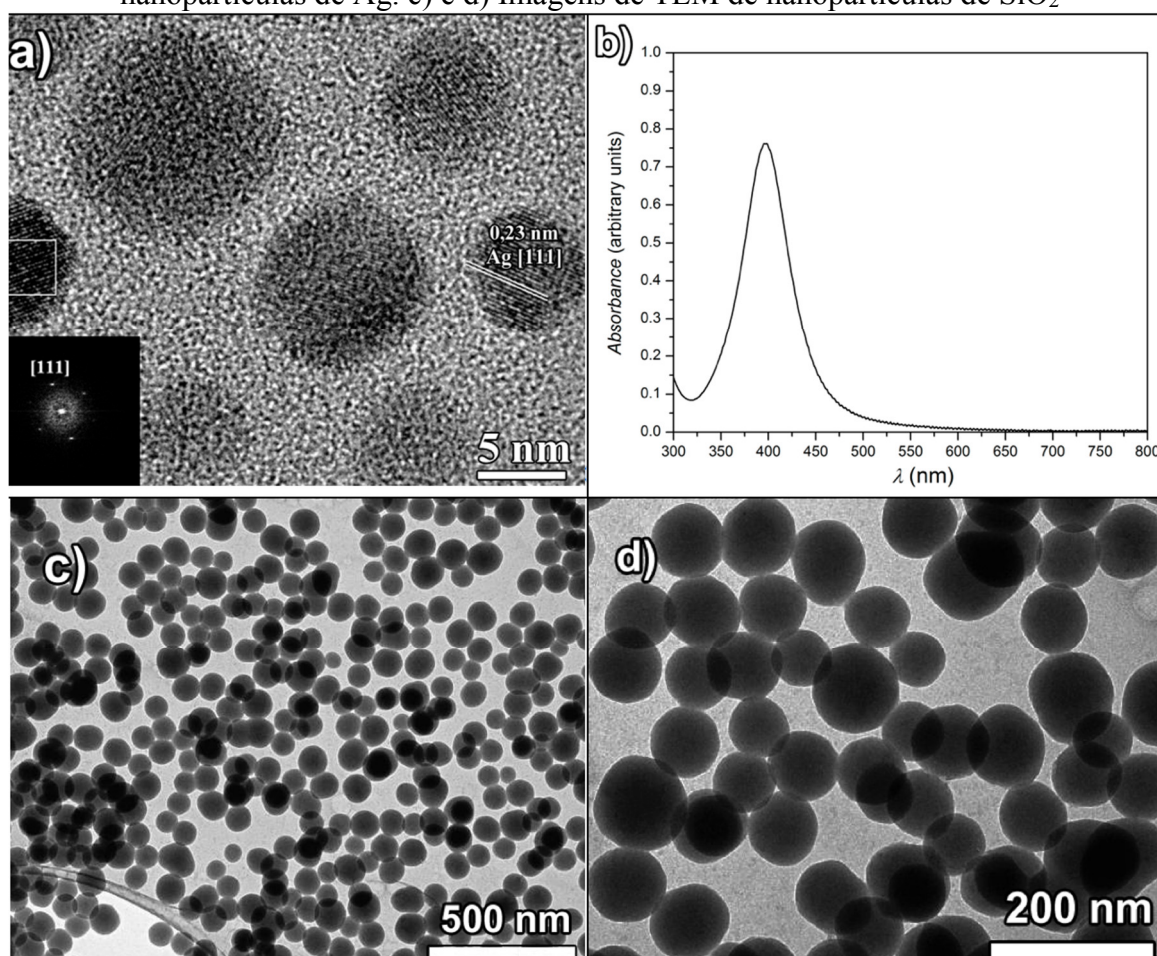
Tabela 1. Parâmetros das amostras: Concentração do corante, densidade NPs, caminho livre médio de espalhamento (l_s), seção de choque de espalhamentos (σ_s).

Amostra	SiO ₂ NPs	Ag NPs	σ_s	l_s	kl_s
Espeçura = 0.112 ± 0.01 mm	[$\times 10^{10}$ cm ⁻³]	[$\times 10^{12}$ cm ⁻³]	[$\times 10^{-4}$ μm^2]	[cm]	[$\times 10^5$]
[Rh6G] = 2.8×10^{-7} mol.g ⁻¹					
Dye-doped SF					
SFSi1	1.7		5.3	11.1	12.2
SFSi2	3.5		5.3	5.4	5.9
SFSi3	8.8		5.3	2.1	2.3
SFAG		4.2	3.2×10^{-5}	7400	8.5×10^2

A alta qualidade das grades de SF obtidas deve-se a capacidade intrínseca dos materiais de seda em replicar as grades periódicas de filmes. Além de ligações de hidrogênio intra- e intermoleculares durante a secagem, as interações de van der Waals formadas pela interface da camada de policarbonato e fibroína são também importantes para a replicação detalhada da superfície periódica com resolução nanométrica.

Espectroscopia ATR-FTIR foi utilizado para estudar a conformação da fibroína após a introdução das partículas de SiO_2 . Os espectros representados na Figura 14 indicam que a adição de SiO_2 NPs induz o aumento da cristalização da fibroína. A SF pode assumir duas conformações distintas: Silk I, solúvel em água/amorfa e Silk II, insolúvel/cristalina. De fato, a solução regenerada de SF sofre uma cristalização parcial de Silk I (*random coil*) para Silk II (*random coil* + β -folha) durante a etapa de secagem para a confecção dos filmes (WILSON; VALLUZZI; KAPLAN, 2000).

Figura 13 - a) Imagens de TEM e b) espectros de absorção na região UV-vis das nanopartículas de Ag. c) e d) Imagens de TEM de nanopartículas de SiO_2



Fonte: Autor

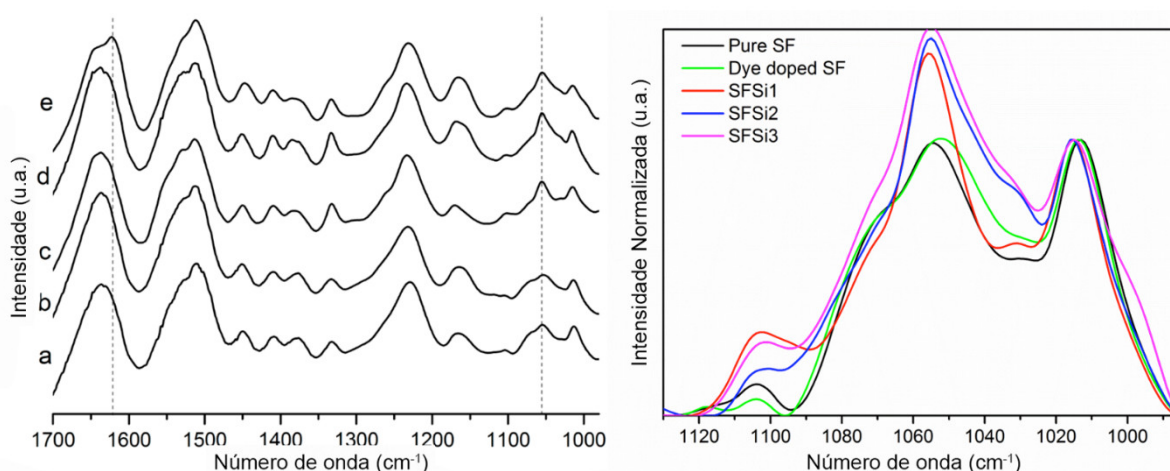
As bandas de absorção observada em 1637 cm^{-1} (amida I), 1520 cm^{-1} (amida II) e 1230 cm^{-1} (amida III) são atribuídas à conformação Silk II. A conformação Silk II apresenta estruturas do tipo β -folha como componentes predominantes. A conversão Silk I para Silk II é mais pronunciada para grades de fibroína contendo altas concentrações de SiO_2 .

Comparando as curvas de FTIR na Figura 14b correspondentes aos filmes DFB contendo SiO_2 NPs (SFSi1, SFSi2 e SFSi3) e o filme DFB sem SiO_2 NPs (Dye-dopado SF), observa-se

que há um aumento da banda em 1054 cm^{-1} na presença de NPs. Esta banda é atribuída à sobreposição dos modos de estiramento assimétrico Si-O-Si e da C-C do esqueleto polipeptídico da conformação Silk II.

A morfologia de superfície dos filmes de SF foi avaliada por microscopia eletrônica de varredura (SEM) e microscopia de força atômica (AFM). Figura 15, A e B demonstra imagens SEM e AFM de topografia da superfície da grade de difração de fibroína resultante da secagem da solução de SF sobre a superfície periódica do DVD.

Figura 14 - Espectros de ATR-FTIR dos filmes de SF e híbridos SFGPTMS.



Fonte: Autor

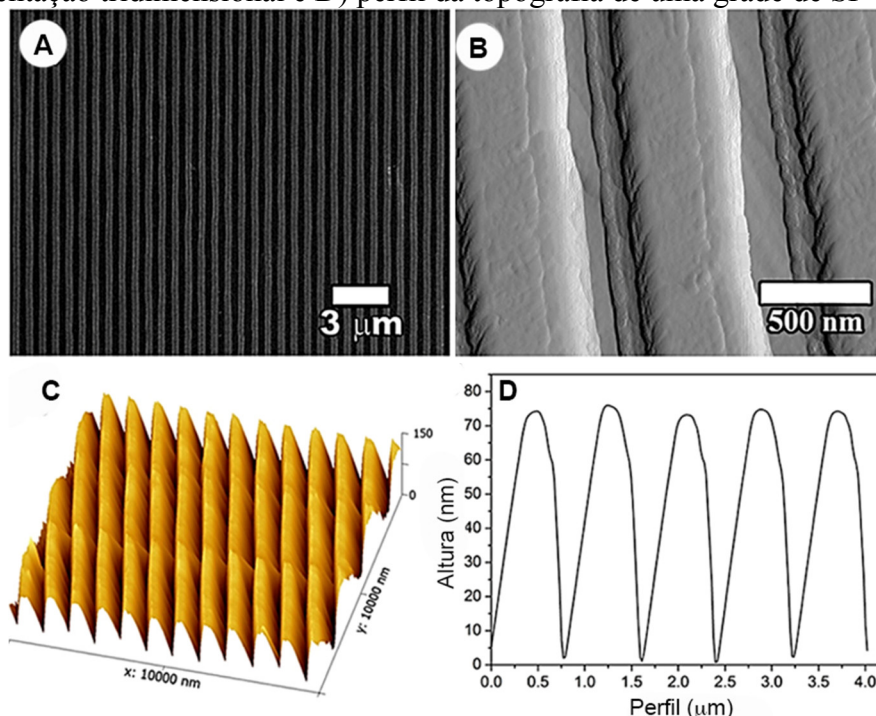
Figura 15C ilustra imagens de AFM tridimensionais da estrutura da grade de fibroína. Figura 15D revela um padrão sinusoidal com uma profundidade de $\approx 75\text{ nm}$ e período de grade de $\approx 750\text{ nm}$ enquanto que a Figura, b-d demonstra a alta fidelidade da réplica do padrão periódico mimetizado pela fibroína da superfície de um DVD.

Filmes de SF contendo diferentes concentração de Rh6G foram preparados para avaliar a concentração ótima para emissão laser: (SFRod1, SFRod2 and SFRod3). Os espectros de absorção e emissão estão apresentados na Figura 16A. As intensidades de emissão e absorção aumentam de acordo com o aumento da concentração de corante.

O espectro de absorção obtida para o filme SFRod3 indica uma segunda banda de absorção centrada em $\approx 500\text{ nm}$ que pode ser atribuída formação de dímeros de Rh6G não fluorescentes (ARBEOLA et al, 1988). Normalmente, em altas concentrações relativas de Rh6G, agregados fluorescentes do tipo J e não-fluorescentes do tipo H. O comprimento de onda máximo de emissão de agregados do tipo J é deslocada para o vermelho em relação ao monômero; Além disso, sugere-se que o alargamento da banda de emissão nesta concentração pode estar relacionado à sobreposição dos espectros de emissão dos agregados e monômeros

(DOMINGUEZ et al, 2008). Neste caso, a formação de agregados de Rh6G do tipo J pode resultar na operação multi-modo do laser de DFB. A partir da análise, a concentração do corante correspondente ao filme SFRod2 foi selecionada para fabricar as amostras de laser DFB. Nos resultados a seguir, esta amostra será denominada como “Dye doped SF”.

Figura 15 - Imagens de A) SEM, B) AFM de topografia de alta resolução. C) representação tridimensional e D) perfil da topografia de uma grade de SF típica.



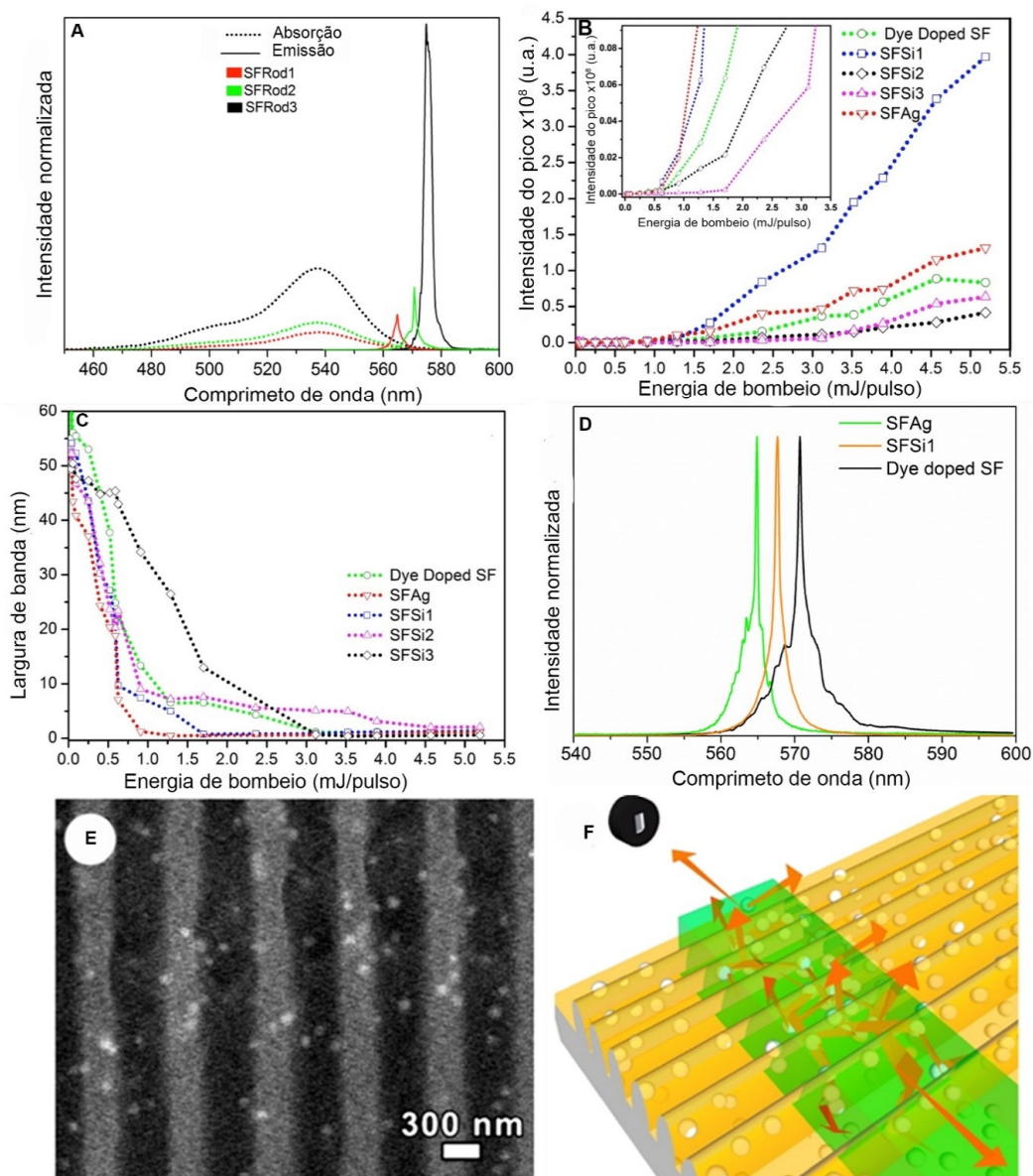
Fonte: Autor

A emissão laser das grades de fibroína dopadas com Rodamina 6G: i) sem partículas adicionadas (Dye doped SF), e ii) com diferentes concentrações de partículas de SiO_2 (SFSiN, $N=1-3$) foram estudadas utilizando como fonte de excitação pulsos de laser com λ_{exc} : 543 nm em direção perpendicular às grades. A incorporação de SiO_2 NPs pode ser confirmado pelo contraste de brilho observado nas imagens de SEM no modo detecção por elétrons retroespalhados (BSE).

Figura 16, A e B, apresenta o comportamento da intensidade de emissão laser para amostras Dye doped SF, SFSiN ($N=1-3$) e SFAg. Todas amostras possuem espessura idêntica e a mesma concentração de Rh6G tal como indicado na Tabela 1. O inset na Figura 16B revela a região ampliada onde ocorre o limiar do laser em termos de potência de bombeamento. O limiar é observado em ≈ 1.3 mJ/pulso (288 KW/cm^2) para a amostra “Dye doped SF”, ≈ 0.9 mJ/pulso (200 KW/cm^2) para amostra SFSi1 e ≈ 0.8 mJ/pulso (177 KW/cm^2) para amostra SFAg. A Figura 16, a and b, indica que a adição de nanopartículas possibilita o aumento da emissão. A

amostra SFSi1 (menor concentração de SiO₂ NPs) apresenta a maior intensidade de emissão. Por outro lado, a amostra SFAg apresentou maior estreitamento da largura da banda de emissão para pulsos de menor energia em relação a outras amostras.

Figura 16 - A) Espectros de absorção e emissão (λ_{exc} : 543 nm) de filmes de SF dopados com diferentes concentrações de Rodamina 6G. B) Gráfico do comportamento da intensidade do pico de emissão versus energia de bombeio, C) Gráfico do comportamento da largura de banda de emissão versus a energia de bombeio, D) Espectro de emissão laser das amostras de Dye doped SF contendo nanopartículas de Ag e SiO₂. E) SEM no modo de detecção por elétrons retroespalhados da amostra SFSi3, F) Representação do comportamento de espalhamento de luz em amostras contendo regime supersaturado de partículas espalhadoras.



Fonte: Autor

Na presença de uma concentração adequada de SiO₂ NPs, o meio de ganho na grade DFB de fibroína comporta-se como um meio de ganho randômico e, de maneira similar ao Laser Randômico incoerente (LAWANDY et al, 1994), a absorção de luz e a emissão estimulada são intensificadas devido ao espalhamento múltiplo de luz.

O crescimento do limiar em termos de potência do bombeamento de excitação observado para amostras contendo densidade de SiO₂ NPs acima de $1.7 \times 10^{10} \text{ cm}^{-3}$ (SFSi2 e SFSi3), é devido ao preenchimento das ranhuras das grades por SiO₂ NPs ($\approx 123 \text{ nm}$). A realimentação do meio de ganho das grades de difração SFSi2 é fornecido pelas SiO₂ NPs e pelas ranhuras da grade. Note que o índice de refração entre SiO₂ e SF é bastante próximo e a profundidade de grade ($\approx 75 \text{ nm}$) torna-se preenchida com SiO₂ NPs. Como observado, uma grande quantidade relativa de SiO₂ NPs reduz o retroespalhamento proporcionado pela grade de Bragg. Ainda, o número crescente de centros de espalhamento pode aumentar a contribuição de fótons fornecidos pelo processo de espalhamento múltiplo deluz que induz emissão estimulada em frequência óptica diferente da frequência determinado pelo período da grade. Este feito contribui par ao alargamento da largura de banda.

Para esta amostra em particular, o limiar laser foi reduzido 1.4 vezes em comparação com a amostra sem partículas espalhadoras de luz. Resultados análogos foram obtidos por Watanabe et al (2005) em um guia de onda planar de dupla camada contendo corante laser e dopada com SiO₂ NPs em uma concentração 10 vezes maior que a concentração usada no presente trabalho.

Tabela 2. Limiar laser e largura de banda (resolução do espectro: 0,1 nm). O parâmetro R foi definido pela razão $\lambda/\Delta\lambda$.

Amostra	Limiar [mJ/pulse]	Limiar [KW/cm ²]	λ [nm]	$\Delta\lambda$ [nm]	R
Dye-doped SF	1.3	288	570.7	1	571
SFSi1	0.9	200	567.7	0.5	1135
SFAg	0.8	177	564.9	0.4	1412

Afim de quantificar o regime de espalhamento para amostras dopadas com SiO₂, calculou-se o caminho livre médio (l_s), $l_s = 1/N\sigma_s$, onde N é a densidade de SiO₂ e σ_s é a sessão de choque de espalhamento. Os valores calculados encontram-se na Tabela 2. Nós encontramos que o caminho livre médio é maior que 10^6 . Estes resultados demonstram que o regime de espalhamento das amostras é balístico (WU et al, 2006). Examinando o comportamento da largura e intensidade da banda de emissão em função da energia do pulso de bombeamento do

laser de excitação para as amostras SFSi1 e SFAG, observa-se uma rápida redução da largura de banda com o aumento da energia de pulso de excitação. Nota-se que a amostras SFSi1 apresenta maior intensidade de emissão que a amostra SFAG para pulsos de excitação de mesma energia similares. É importante observar que o limiar laser para a amostra AgNPs é ligeiramente menor em relação às outras amostras. Isto provavelmente deve-se a influencia do efeito de campo local que excita o meio de ganho e estimula mais emissão para este modo, o que consiste em um mecanismo de retroalimentação.

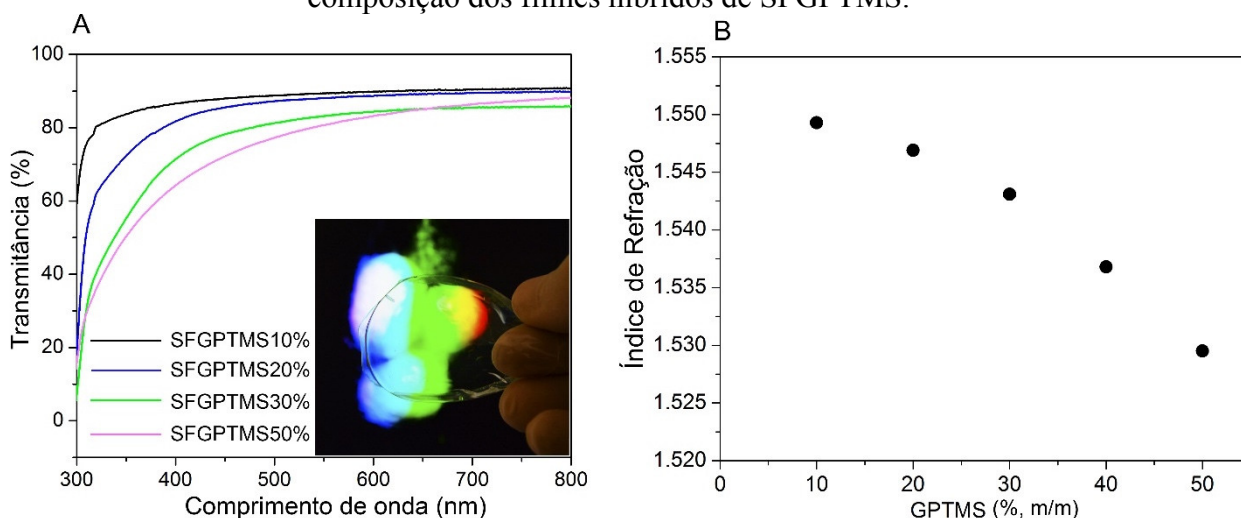
Figura 16D apresenta o espectro de emissão para a amostra de Dye doped SF e para as amostras SFSi1 e SFAG. O deslocamento do comprimento de onda de emissão para a região do azul com a adição de NPs pode ser atribuído ao espalhamento Rayleigh (proporcional a λ^{-4}) desde que a luz com menor comprimento de onda é espalhada com maior eficiência, favorecendo o ganho para menores comprimentos de onda.

É conhecido que o comprimento de onda laser de uma Sistema DFB satisfaça a condição de reflexão de Bragg (KOGELNIK, 1971), i.e. $m\lambda_B = 2n_{eff}A$, onde m é a ordem de difração, n_{eff} é o índice de refração efetivo do meio e A é o período da grade. Considerando o índice de refração dos filmes de SF como $n_{eff} \approx 1.55$ em 570 nm (medido pela técnica de acoplamento de prisma) nós concluímos que a emissão laser correspondente à 4ª ordem de difração de uma estrutura periódica típica de uma DVD. A largura mínima de banda correspondente às amostras com melhor desempenho neste estudo foram 1 nm, 0.7 nm (SFSi, para 1.7 mJ/pulso) e 0.4 nm para SFAG para 0.91 mJ/pulso).

É conhecido que a intensidade da luz refletida decai significativamente quando o valor de m é aumentado. Entretanto, nota-se que mesmo operando na 4ª ordem da grade, os filmes periódicos baseados em SF demonstram alta eficiência para operação monomodo de um laser DFB.

Híbridos transparentes de SF modificados com função epóxi foram produzidos pela adição de glicidoxipropiltrimetoxisilano (GPTMS). Filmes de SF puro e híbridos de SFGTMS com diferentes quantidades de GPTMS foram obtidos pela secagem da solução aquosa resultante da mistura de SF e GPTMS sobre placas de petri de policarbonato. A espessura dos filmes auto-sustentáveis foi bastante similar (0.1 mm) para todas as composições com desvio padrão inferior a 5% entre as amostras. Os filmes híbridos de SFGPTMS podem ser flexionados em ângulos agudos mesmo com baixa concentração de GPTMS (i.e. 10% m/m). Todos os híbridos SFGPTMS apresentaram grande transparência na região do visível (até 90%) como demonstrado na Figura 17.

Figura 17 - A) Espectro de transmitância e B) Relação entre índice de refração em função da composição dos filmes híbridos de SFGPTMS.



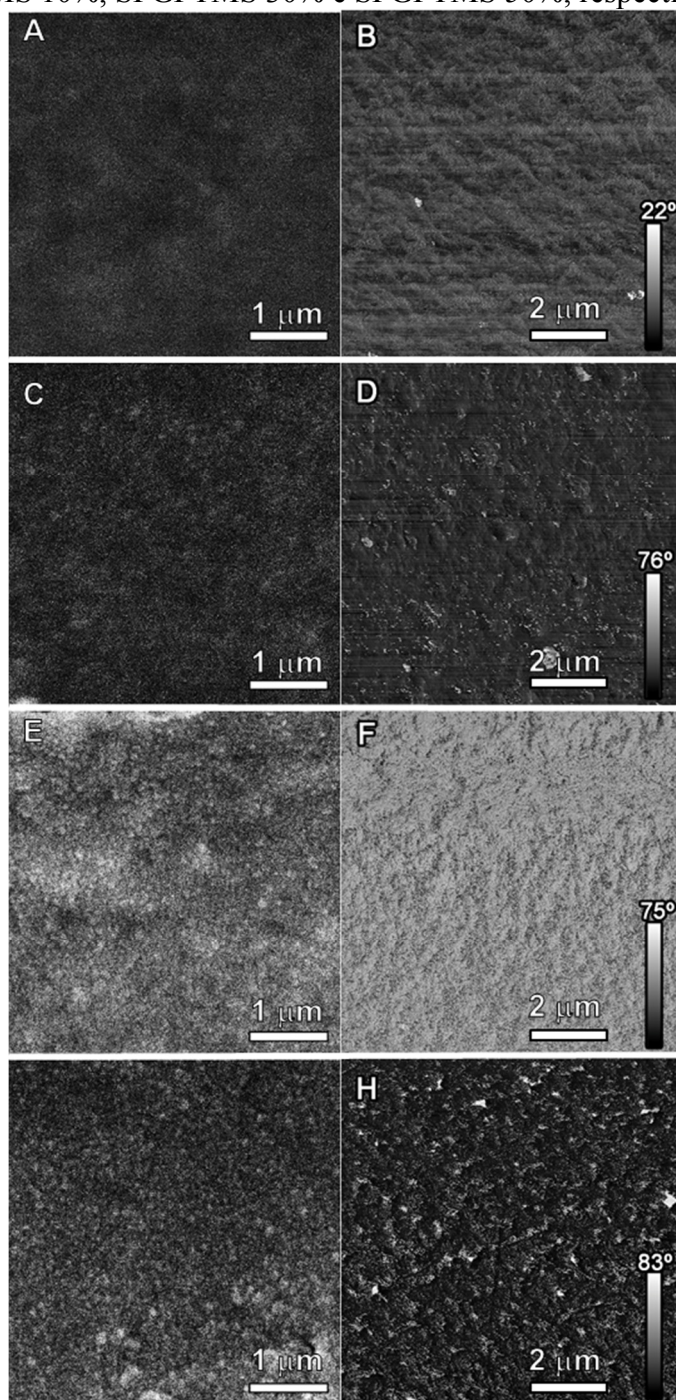
Fonte: Autor

O índice de refração dos filmes híbridos diminui de 1.5493 para 1.5254 em função do aumento da concentração de GPTMS tal como demonstrado em Figura 17. Uma relação quase-linear (com uma inclinação negativa) entre o índice de refração e a teor de GPTMS nos filmes híbridos foi evidenciado, demonstrando que as propriedades ópticas são estritamente dependentes da composição. A Figura 18 apresenta imagens de SEM e AFM de fase para diferentes composições dos híbridos de SFGPTMS.

No espectro de transmitância da Figura 17A, observamos que a transmitância dos híbridos de SFGPTMS diminui progressivamente para 79% em 550 nm quando o teor de GPTMS foi acrescido para 50 % (m/m). As imagens de SEM demonstram que a morfologia dos filmes de SFGPTMS apresentam uma superfície granular GPTMS para filmes híbridos com teor de GPTMS superior a 30%. Por outro lado, as imagens de SEM de SFGPTMS 10% e filmes de SF puro apresentados na Figura 18 não apresentam tal morfologia. Curiosamente, o aumento do teor de GPTMS nos filmes híbridos de SFGPTMS torna a sua superfície mais lisa e uniforme.

As imagens AFM de fase dos filmes híbridos SFGPTMS revelou claramente a presença de domínios com notável contraste. O contraste de fase observado nas imagens de AFM aumenta com o teor de GPTMS nos filmes híbridos. Por exemplo, o filme SF puro apresenta apenas 22° enquanto que a amostras SFGPTMS 50% exibe contraste de 83°, o que implica que a superfície dos filmes híbridos tem composição diferente com domínios ricos em GPTMS ou SF homogeneamente distribuídos.

Figura 18 - (A, C, E) Imagens de SEM e (B, D, F) AFM de fase dos filmes de SF, SFGPTMS 10%, SFGPTMS 30% e SFGPTMS 50%, respectivamente

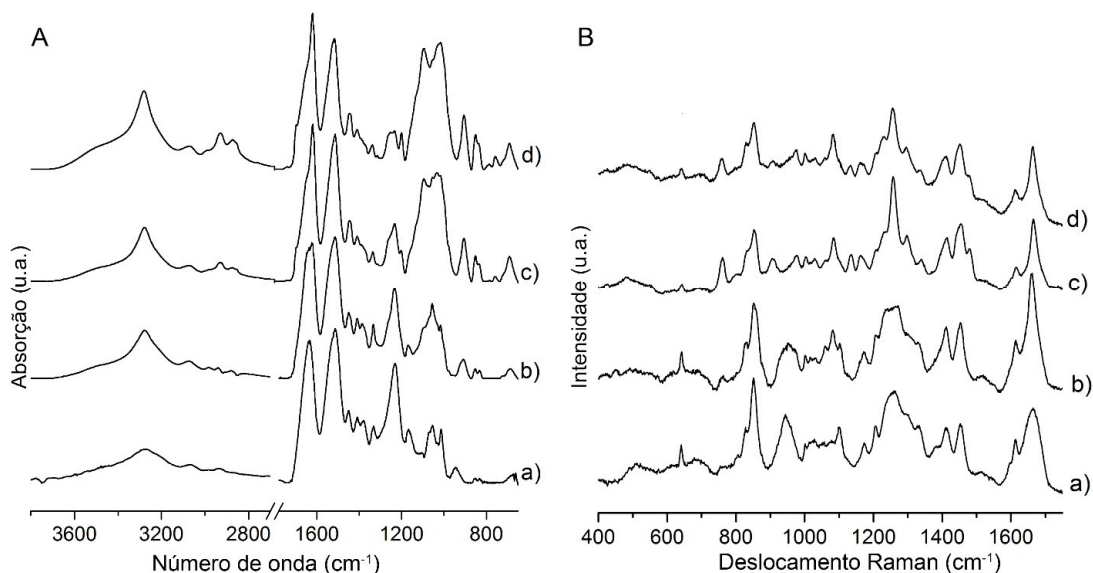


Fonte: Autor

Os espectros ATR-FTIR de SF e dos híbridos de SFGPMTS estão apresentados na Figura 19A. O espectro ATR-FTIR do filme puro de SF exibe conformação Silk I, evidenciado pela posição intensidade das bandas da amida I, amida II e amida III em 1655 cm^{-1} , 1540 cm^{-1} e 1235 cm^{-1} , respectivamente. Por outro lado, a conformação Silk II é predominante nos filmes híbridos. Isto pode ser verificado pelo estreitamento e deslocamento da banda amida I para

menores números de onda, comportamento típico observado para conformação Silk II rica em estruturas folha- β .

Figura 19 - A) Espectros de ATR-FTIR e B) Raman de a) filme puro de SF, b) SFGPTMS 10%, c) SFGPTMS 30% e, d) SFGPTMS 50%



Fonte: Autor

Uma banda larga e de média intensidade relativa é observada em 1230 cm^{-1} para filmes de SF puro cuja atribuição típica está relacionada com conformação Silk I. Com a introdução de GPTMS, a intensidade desta banda é significativamente reduzido, observado em filmes com alto teor de conformação Silk II (TADDEI, MONTI, 2005). Simultaneamente, observa-se um ombro emergente em 1256 cm^{-1} cuja intensidade é proporcional ao teor de GPTMS e cuja atribuição refere-se aos modos vibracionais da respiração do anel epóxi (ŠAPIĆ et al, 2009).

Três bandas características confirmam a polimerização de silica gel nos filmes híbridos de SFGPTMS em 1130 e 800 cm^{-1} atribuídas ao modos vibracionais estiramento assimétrico e simétrico de ligações Si-O-Si, centradas em principais características estiramento assimétrico Si-O-Si. Entretanto, sugere-se que a condensação da rede de silica nos híbridos é incompleta uma vez que bandas de baixa intensidade relacionadas a vibração de grupos Si-OH podem ser identificados em 905 cm^{-1} and 849 cm^{-1} (ALMEIDA; PANTANO, 1990). A presença de grupos Si-OH introduzem interações de hidrogênio adicionais com os resíduos polares da cadeia peptídica de SF. Isto pode ser verificado pelo deslocamento de bandas localizadas na região de absorção da Amida A. O principal modo vibracional é caracterizado pelo pelo estiramento N-H em 3280 cm^{-1} para o filme de SF puro. Esta banda torna-se estreita e desloca-se para maiores números de onda em função da quantidade de GPTMS adicionada. Para a

amostras SFGPTMS, o descolamento da banda da Amida A corresponde a $\sim 12 \text{ cm}^{-1}$. Este efeito sugere claramente possíveis interações de hidrogênio entre grupos N-H da cadeia peptídica com grupos Si-O ou glicidoxi de moléculas de GPTMS. As bandas localizadas em 2936 e 2876 cm^{-1} presente nos híbridos SFGPTMS são associadas ao estiramento assimétrico e simétrico de CH_2 da porção glicidoxipropil da molécula de GPTMS, respectivamente (ŠAPIĆ et al., 2009).

Informações complementares podem ser extraídas dos espectros Raman dos híbridos de GPTMS. Os espectros Raman dos filmes estão demonstrados na Figura 19B. O espectro Raman do filme de SF puro exibe bandas típicas da conformação Silk I (MONTI et al., 1998, 2001; SHAO et al., 2005; ZHENG et al., 1989). A banda em 1661 cm^{-1} é atribuída à banda de vibração da Amida I da cadeia peptídica de SF. Esta banda exibe estreitamento notável com a adição de GPTMS além de um sutil deslocamento para maiores números de onda, o que é consistente com a conversão da conformação Silk I para Silk II. (MONTI et al., 1998, 2001; SHAO et al., 2005; ZHENG et al., 1989). A banda em 1255 cm^{-1} e o componente em 1236 cm^{-1} observados nos espectros Raman para o filme puro de SF são associados aos modos vibracionais da região da Amida III para a conformação Silk I. Além disso, os filmes de bandas em 1100 cm^{-1} e uma banda larga em 938 cm^{-1} são atribuídas ao estiramento C-C e C-N, respectivamente, geralmente relacionadas com a presença de estruturas do tipo a-hélice características da conformação Silk I nos filmes puros de SF. A introdução de GPTMS provoca mudanças significativas nesta região principalmente elencada pelo a intensa banda em 1256 cm^{-1} associada a vibração do tipo *rocking* C-H e estiramento C-C de grupos epóxi da molécula de GPTMS.

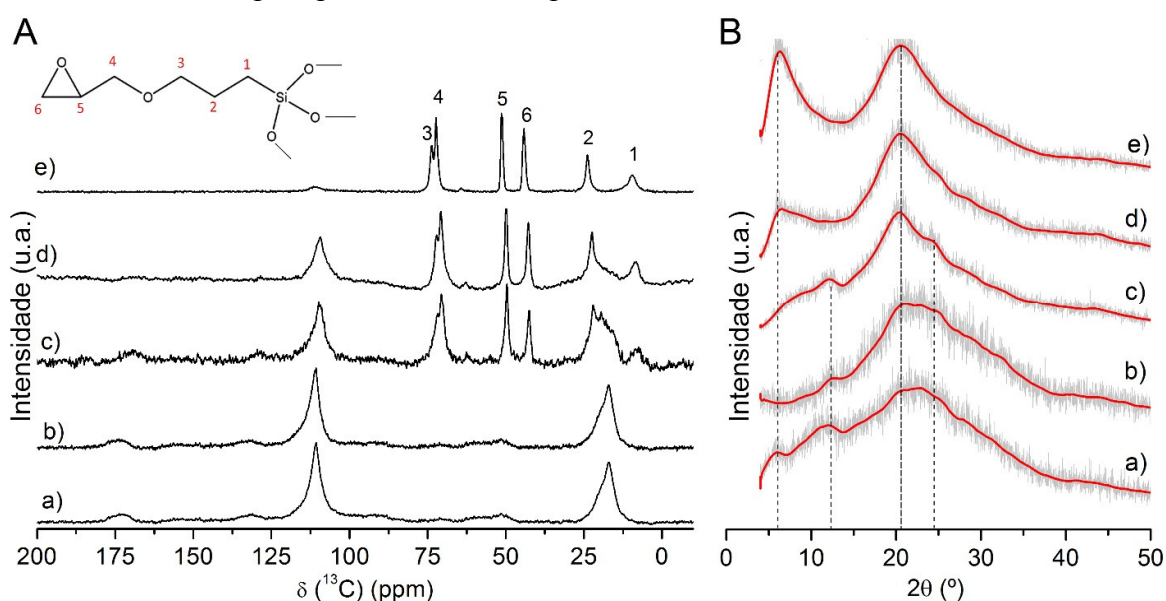
A modificação de SF com GPTMS pode ser também confirmada pela surgimento de bandas em 1030 a 1170 cm^{-1} associadas ao estiramento C-C, C-O e C-H da porção glicidoxipropil (RIEGEL et al., 1998; ŠAPIĆ et al., 2009).

Os espectros Raman dos filmes híbridos exibem uma banda localizada em 763 cm^{-1} cuja intensidade é proporcional ao teor de GPTMS. Esta banda está associada ao estiramento simétrico da ligação éter alifático da porção glicidoxipropil (ŠAPIĆ et al., 2009). Os híbridos também apresentaram bandas relacionadas a formação de sílica gel em 1080 e 986 cm^{-1} atribuídas aos modos vibracionais de Si-O-Si e Si-OH, respectivamente (SILVERSTEIN; WEBSTER; KIEMLE, 2005).

A Figura 20A apresenta os espectros de MAS NMR de ^{13}C - ^1H no estado sólido para filmes de SF puro e filmes híbridos de SFGPTMS em diferentes composições. O espectro de GPTMS exibe seis linhas de ressonância, identificados pelos números 1-6. Os picos observados em 42.6 e 49.7 ppm (posições 6 e 5, respectivamente) correspondem aos grupos epoxi e aparecem com a mesma intensidade relativa para todas as composições dos híbridos, indicando a ausência de

processos de polimerização. O pico em 7.8 ppm é atribuído a grupos $-\text{CH}_2-\text{SiO}_{3/2}$ (posição 1) (INNOCENZI; BRUSATIN; BABONNEAU, 2000). Não foi possível identificar o pico de associado a grupos $-\text{O}-\text{CH}_3$ (posição 7), confirmando que a maior das moléculas de GPTMS encontra-se hidrolizadas nos filmes híbridos (ALONSO et al., 2005; BRUS; HLAVATÁ; STRACHOTA, 2004; INNOCENZI; BRUSATIN; BABONNEAU, 2000).

Figura 20 - A) Espectros de MAS NMR de ^{13}C - ^1H no estado sólido e, B) B) Difração de raios-X para para filmes de SF puro e filmes híbridos de SFGPTMS.



Fonte: Autor

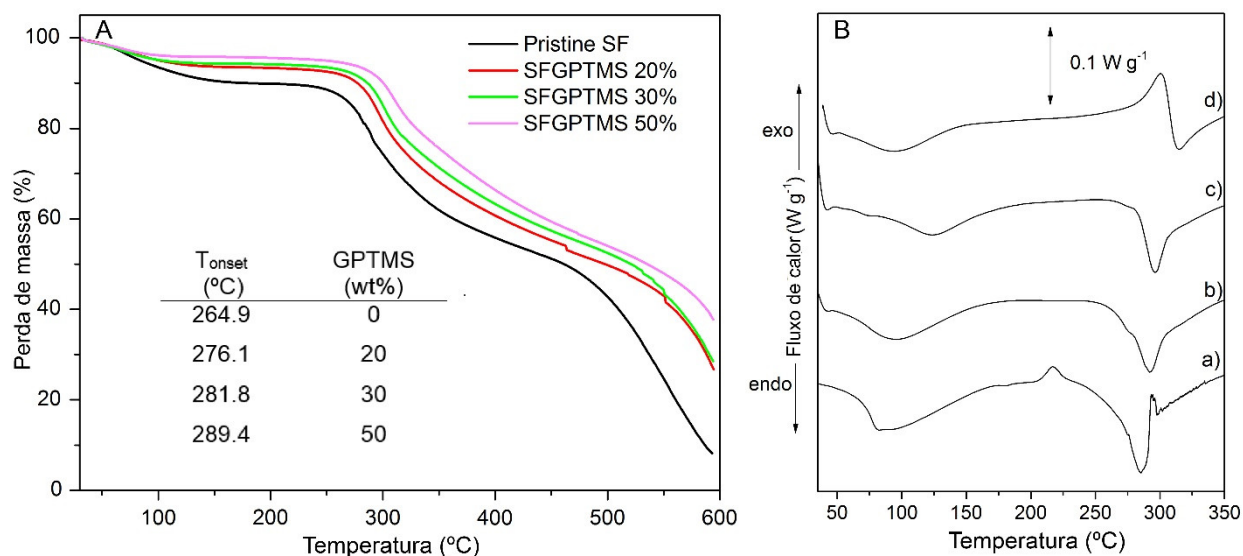
O deslocamento do carbono β ($\text{C}\beta$) da alanina é utilizado para investigar a conformação a conformação da SF. Observa-se que o pico largo de $\text{C}\beta$ da alanina encontrado na região entre 20 a 0 ppm exibe assimetria, formada basicamente por duas linhas de ressonância convoluidas em 20.2 ppm e 17.1 ppm. Isto sugere que o filme puro de SF é formado por estruturas do tipo Silk II e random coil, respectivamente (ASAKURA et al., 2002, 2005; ZHOU et al., 2001). O aumento da concentração de GPTMS induz a conversão da conformação Silk I para Silk II, o qual pode ser constatada pela diminuição da intensidade da linha centralizada em 17.7 ppm (filme puro de SF) em contrapartida do aumento da intensidade do pico em 20.2 ppm (SFGPTMS 50%) do $\text{C}\beta$ da alanina.

O espectros de difração de raios-X (XRD) estão representados na Figura 20B. O espectro do filme puros de SF apresenta um pico de difração fraco em $2\theta=11.8^\circ$ e um pico largo centralizado em 22.5° , correspondentes às distâncias de 7.5 e 3.9 Å. Os filmes puros de SF exibem majoritariamente conformação Silk I (16, 61). Após a adição de 20% (m/m) de GTMS, o pico em 22.5° desaparece e outros três picos surgem em $2\theta=12^\circ$ (fraco), 20.5° (moderado) and

24.5° (fraco), equivalentes às distâncias 7,4, 4,3 e 3,6 Å típicos da conformação Silk II. O espaçamento em 4,3 Å é característico da distância das ligações de hidrogênio intramolecular de folhas β (JIN et al., 2005). Acima de 30% (m/m) de GPTMS, um novo pico é observado em 6.3° e torna-se predominante juntamente com o pico largo em 20.5°. O pico em 6.3° nos híbridos de SFGPTMS tem sido atribuído à distância de espalhamento interpartículas (XI; WU; LIN, 2006). Este pico indica uma flutuação altamente não periódica da densidade eletrônica dos filmes híbridos de SFGPTMS eventualmente observada devido a agregação de sílica em altas concentrações de GPTMS. Uma vez que uma certa concentração crítica de GPTMS é alcançada, é razoável esperar que as conexões entre os sítios Si-O- poderiam superar o impedimento estérico imposto pelas cadeias poliméricas de SF e, portanto, promover a formação de domínios ricos em siloxano como resultado das reações de hidrólise e condensação. De acordo com o difratograma dos híbridos de SFGPTMS 30-50%, a distância média inter-domínios estimada corresponde a 13-14 Å e corrobora com a morfologia de superfície granular observada pelas medidas de SEM e AFM.

Figura 21, A e B, apresenta as curvas de estabilidade térmicas e calorimetria diferencial exploratória (DSC) dos filmes. A curva termogravimétrica do filme puro de SF pode ser dividida em três regiões subsequentes, caracterizada por eventos de perda de massa com diferentes velocidades. A região I (35-40 °C a 117-170 °C) é relacionada com perda de água. A região II (170-240 °C) e região III (> 240 °C) evidenciam a degradação da cadeia peptídica de SF. Acima de 200 °C, grupos laterais dos resíduos de aminoácido da cadeia peptídica de SF decompondo em pequenas moléculas de gás tais como CO, CO₂, NH₃ (SCHOESER, 2007). Nesta temperatura, grupos epóxi sofrem decomposição térmica através de cisão homolítica das ligações químicas e, simultaneamente, ocorre desidratação de moléculas de água proveniente da decomposição do anel epóxi e da condensação de ligações silanol (MACAN et al., 2006; SCHOESER, 2007). A Figura 21A apresenta as curvas termogravimétricas para os filmes híbridos e para o filme puro de SF. A perda de massa para região I foi de 10% para filme puro de SF e 4% para SFGPTMS50%. A incorporação de GPTMS promove o aumento da temperatura de decomposição na região III. Sugere-se que o aumento da estabilidade térmica esteja endereçado a mudanças de conformação da SF (i.e. formação de folha- β , conformação Silk II) além da influência da rede polimérica inorgânica de sílica gel nos filmes híbridos.

Figura 21 - A) Curva termogravimétrica e B) Curvas de DSC para a) filme puro de SF, b) SFGPTMS 10%, c) SFGPTMS 30% e, d) SFGPTMS 50%.



Fonte: Autor

A curva de DSC para o filme puro de SF exibe três principais eventos. O primeiro pico endotérmico centralizado em 82 °C pode ser atribuído à perda de água adsorvida (MAGOSHI et al., 1977). O pico localizado em 284 °C para o filmes puro de SF está associado a decomposição térmica característica da conformação Silk I (MORAES et al., 2010). O pico exotérmico em 218 °C é atribuído ao processo de cristalização devido a mudança de conformação de Silk I para Silk II do filme puro de SF. Entretanto, os filmes híbridos de SFGPTMS não apresentam este pico uma vez que GPTMS induz a conversão de Silk I para Silk II (cristalino) durante a preparação dos filmes. A introdução de GPTMS prova o deslocamento do pico endotérmico para maiores temperaturas: 296 °C e 315 °C para SGPTMS30% e SFGPTMS50%, respectivamente. Este comportamento também pode ser observado nas curvas de TGA e corrobora com a existência de interações intermoleculares entre SF e GPTMS previamente descritos nos resultados de espectroscopia vibracional e ressonância magnética nuclear. Sugere-se que o pico endotérmico estreito nesta região pode estar associado à degradação térmica da SF. Nesta faixa de temperatura, o filme de SFGPTMS 50% apresenta dois picos subsequentes. O evento exotérmico localizado por volta de 300 °C pode ser atribuído à degradação de GPTMS em maior parte descrita pelas reações de polimerização do anel epóxi e condensação de sílica gel. Evidentemente, a intensidade do pico endotérmico referente à degradação da proteína de SF é relativamente menor comparado aos filmes com menor teor de GPTMS.

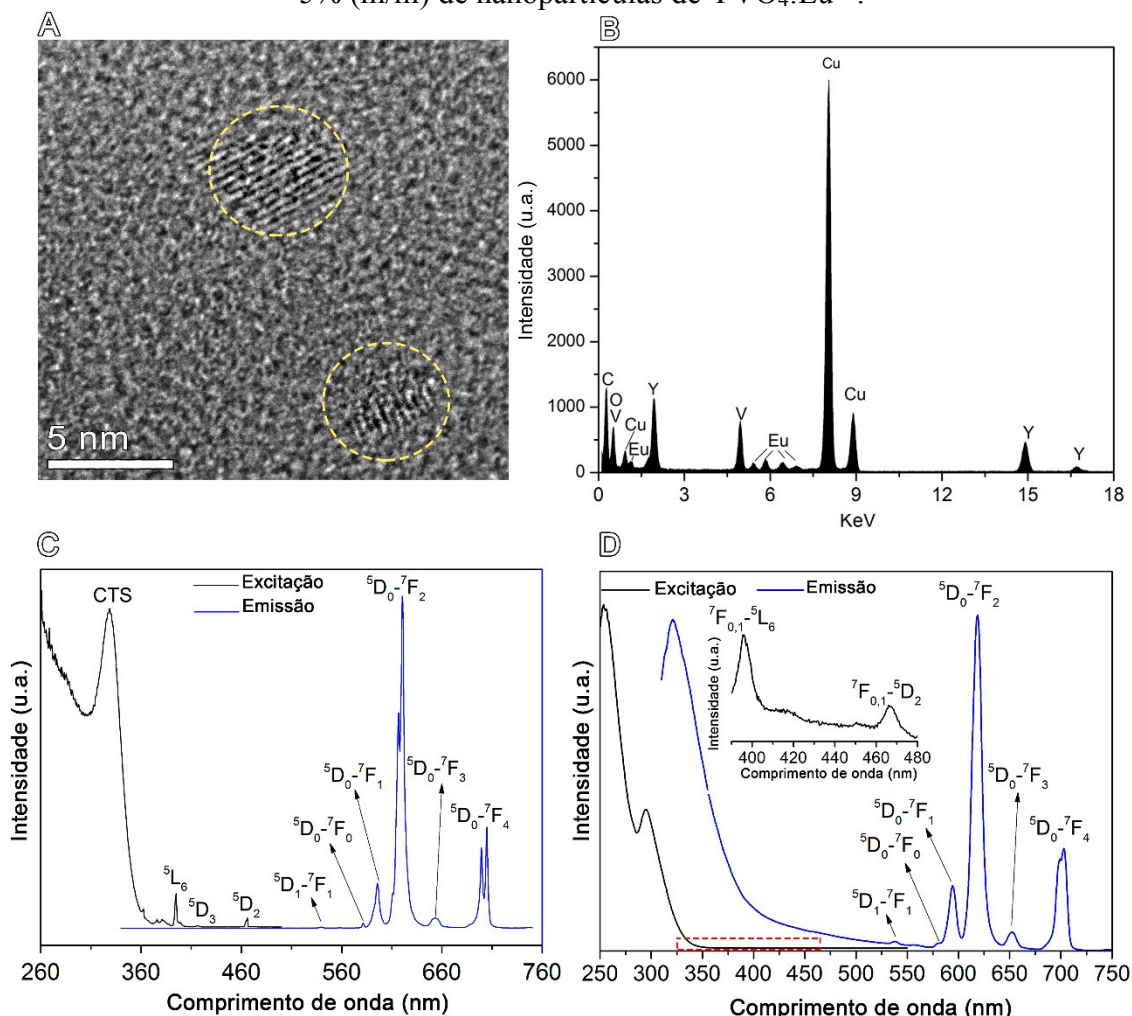
Como evidenciado nos resultados discutidos anteriormente, os filmes híbridos de SFGPTMS são caracterizados pela existência de SF na conformação Silk II. Na literatura, muitos trabalhos destacam a indução da transição de conformação entre Silk I para Silk II pela simples imersão em uma solução alcóolica. Além das interações intermoleculares claramente observadas entre os componentes de GPTMS e SF, acreditamos que a formação de metanol como subproduto da hidrólise de GPTMS, seja um fator importante para o entendimento da conformação existente nos filmes híbridos. Metanol é um agente hidrofílico com propriedade desidratante. O metanol gerado durante a fabricação dos filmes híbridos SFGPTMS poderia induzir rapidamente a cristalização de SF, aumentando a sua taxa de gelificação. Como evidenciado a partir dos resultados acima mencionados, este processo leva a transição estrutural de Silk I para a Silk II. Além disso, sugere-se que em concentrações intermédias de GPTMS (isto é, 30 - 50% em peso), a concentração de GPTMS e, por conseguinte, a concentração de metanol gerado seria suficientemente elevada para promover a formação de domínios ricos em SF e GPTMS. Esses domínios em sua maioria poderiam ser formados através do processo de desidratação da SF induzidos por metanol.

Resultados preliminares de ensaios de citotoxicidade para células osteoblastos indicam que não há uma diferença estatística ($p \geq 0,05$) entre a viabilidade celular dos filmes puros de SF e os filmes híbridos de SFGPTMS, independente do teor de GPTMS.

Nosso estudo mostra que os filmes SFGPTMS não exibem toxicidade para células osteoblastos. Por outro lado, também avaliou-se a citotoxicidade de híbridos compostos de GPTMS como componente principal em peso, a fim de identificar as capacidades de híbridos SFGPTMS para biofotônica. Identificou-se que os híbridos contendo até 30% em peso de GPTMS (isto é, 70% de SF - amostra SFGPTMS30%) e filmes com composição oposta (isto é, 70% em peso de GPTMS, 30% em peso de SF - amostra SFGPTMS70%) apresentaram toxicidade negligenciável em comparação com amostra de controle. A ausência de citotoxicidade para os híbridos ricos em grupos epóxi foram também verificados por estudos recentes da literatura que envolvem a preparação de nanocompósitos orgânico-inorgânico baseados em GPTMS (SHIROSAKI et al., 2013; TRUJILLO et al., 2015).

A fim de avaliar a utilização de filmes híbridos de SFGPTMS para fotônica, filmes luminescentes foram preparados partindo-se da composição do híbrido de SFGPTMS 20 % e acrescentando-se 5% (m/m) de nanopartículas de $\text{YVO}_4:\text{Eu}^{3+}$. A Figura 22 exibe imagem de HRTEM das nanopartículas de $\text{YVO}_4:\text{Eu}^{3+}$. As nanopartículas de $\text{YVO}_4:\text{Eu}^{3+}$ apresentam tamanho inferior a 5 nm e forma não esférica.

Figura 22 - A) Imagens de HRTEM e, B) Espectroscopia dispersiva de energia (EDS) das nanopartículas de $\text{YVO}_4:\text{Eu}^{3+}$. Espectro de excitação ($\lambda_{\text{em}} = 620 \text{ nm}$) e emissão ($\lambda_{\text{exc}} = 280 \text{ nm}$) C) das Nanopartículas de $\text{YVO}_4:\text{Eu}^{3+}$ e D) do filme híbrido de SFGPTMS 40% contendo 5% (m/m) de nanopartículas de $\text{YVO}_4:\text{Eu}^{3+}$.



Fonte: Autor

Os espectros de excitação e emissão de uma suspensão aquosa de $\text{YVO}_4:\text{Eu}^{3+}$ e do híbrido luminescente são mostrados na Figura 22, C e D, respectivamente. A partir do espectro de excitação das nanopartículas de $\text{YVO}_4:\text{Eu}^{3+}$, observa-se uma banda larga localizada em 300 nm atribuída a transferência de carga do oxigênio para o átomo central de vanádio (LIMA et al., 2016). Em ambos espectros de excitação das nanopartículas e do filme híbrido luminescente, as transições características da configuração $\text{Eu}^{3+} 4f_6$ são detectadas em 396 e 467 nm com baixa intensidade, sendo atribuídas às transições ${}^7\text{F}_{0,1}-{}^5\text{L}_6$ e ${}^7\text{F}_{0,1}-{}^5\text{D}_2$. O espectro de emissão mostrado na Figura 22D, exibe uma banda larga de alta intensidade e com pequeno deslocamento Stokes ($\sim 30 \text{ nm}$) em 334 nm. Esta banda refere-se à emissão dos resíduos aromáticos de SF juntamente com recombinação radiativa da matriz de SiO_2 formada nos híbridos. O espectro de emissão também exibe bandas finas características de transições f-f do íon Eu^{3+} na região de 570-710

nm. Estas bandas são atribuídas a transições de $\text{Eu}^{3+} 4f_6$ partindo do estado excitado $^5\text{D}_0$ para os estados $^7\text{F}_J$ ($J=0, 1, 2, 3$ e 4). Uma vez que os íons Eu^{3+} estão localizados em sítios locais de baixa simetria na matriz hospedeira de YVO_4 , a banda de emissão de maior intensidade do íon Eu^{3+} refere-se à transição hipersensitizada $^5\text{D}_0$ - $^7\text{F}_2$ por volta de 620 nm. A banda de emissão referente à transição $^5\text{D}_1$ - $^7\text{F}_1$ (com níveis de energia do estado excitado mais alto) também pode ser observada em baixa intensidade.

Quando os espectros de luminescência do híbrido luminescente e das nanopartículas de $\text{YVO}_4:\text{Eu}^{3+}$ são comparados, é evidente que a resolução das bandas é melhor definida para o último caso. A perda de resolução do espectro nos filmes híbridos pode ser explicada pela heterogeneidade sítio-a-sítio causado pelas diferenças da esfera de coordenação externa de Eu^{3+} resultando em pequenas variações da força de campo cristalino sentido por diferentes íons Eu^{3+} . Tal como reportado anteriormente, a emissão de Eu^{3+} poderia ser endereçada pelo efeito antena eficiente envolvendo estados de transferência de carga da matriz de vanadato em ressonância com os estados excitados dos resíduos aromáticos de SF (i.e. tirosina e triptofano) da SF (LIMA et al., 2016).

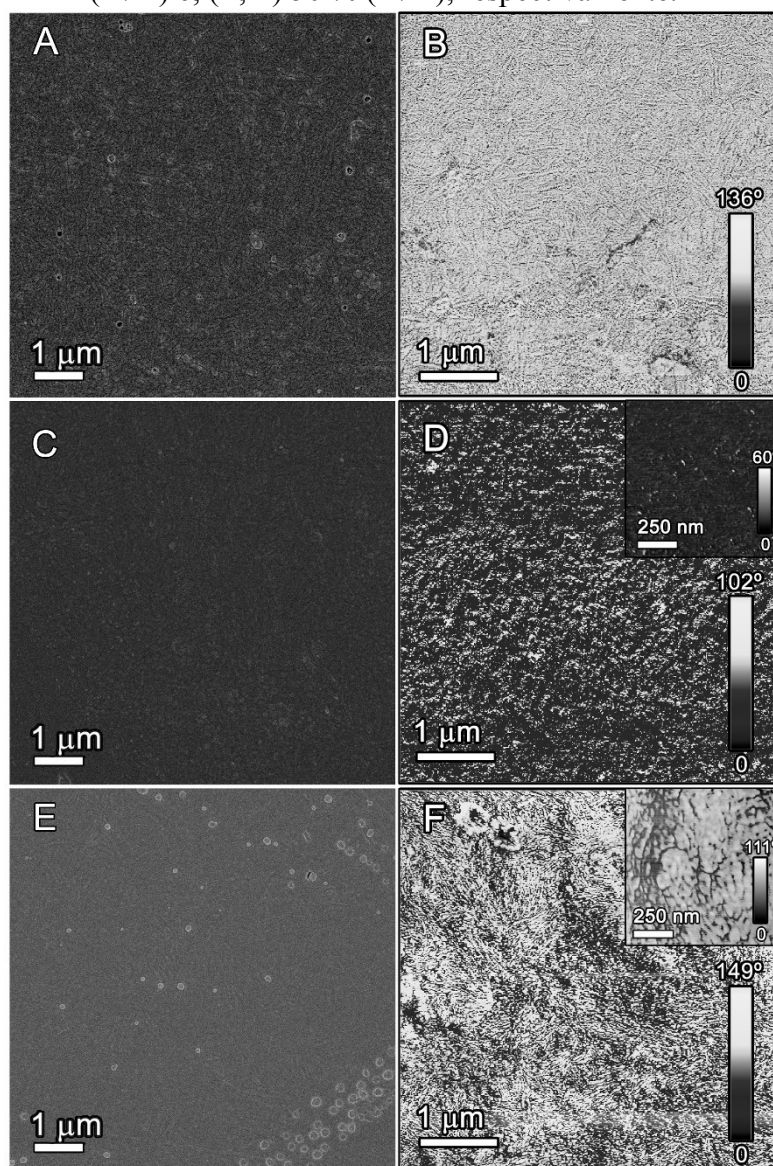
Os filmes híbridos de SF demonstram excelente transparência, composição rica em grupos epóxi e silanol disponíveis para funcionalização (ex. imobilização de enzimas, nanopartículas, etc...) além de não apresentarem toxicidade. Estas características são bastante importantes para a aplicação destes filmes em biofotônica.

Híbridos orgânico-inorgânicos baseados em acetato de celulose e GPTMS também foram preparados para aplicação em fotônica. A síntese de híbridos de acetato de celulose (CA) com GPTMS (CAGPTMS) foi conduzida com o seguinte protocolo: 0,25 g de CA foi dissolvido em 4 ml de acetona. Após dissolução completa, diferentes volumes de GPTMS foram adicionados com agitação constante durante 1 min. A solução foi transferida para uma placa de Petri e coberta com uma folha de alumínio fina. Os filmes híbridos foram preparados com o teor relativo de GPTMS variando entre 5 a 50% em peso.

Imagens de SEM e AFM de topografia e de contraste de fase dos filmes de CA puro e híbridos contendo 20 % e 50 % de GPTMS estão apresentados na Figure 23.

As imagens de AFM de contraste de fase revelam uma topografia nanométrica regular típica para filmes de AC puro. A rugosidade média extraída das imagens de AFM de topografia é consideravelmente baixa, 4.7 ± 2 nm. A adição de 20 % em massa de GPTMS induz a formação de uma superfície rica em domínios com morfologia globular homogeneamente distribuídos e com tamanho médio inferior a 30 nm. Neste caso, a rugosidade média reduziu para 2 ± 0.7 nm.

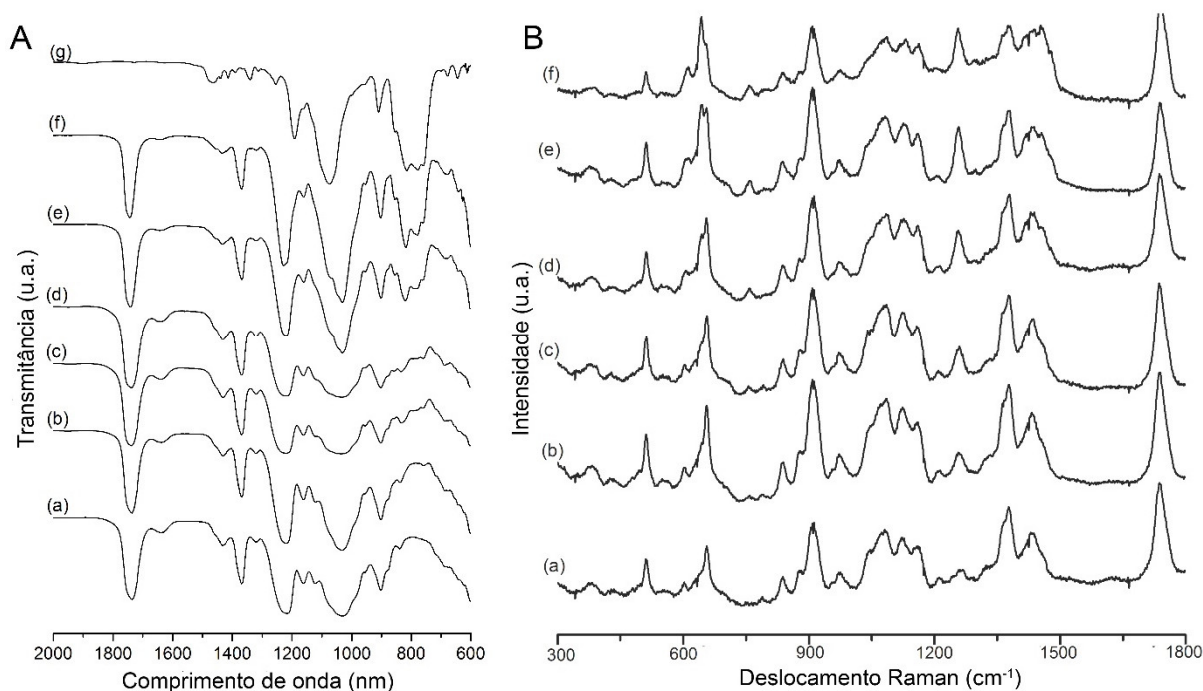
Figura 23 - Imagens de SEM e AFM de contraste de fase da superfície de (A, B) filmes de acetato de celulose puro, e híbridos contendo diferentes proporções de GPTMS (C, D): 20 % (m/m) e; (E, F) 50 % (m/m), respectivamente.



Fonte: Autor

A adição de 50 % de GPTMS em massa induz o aumento do número e tamanho médio dos domínios globulares, tal como observado na Figura 23F. O tamanho médio dos domínios aumentou para cerca de 100 nm e a rugosidade média extraída das imagens de AFM de topografia de superfície do filme híbrido foi determinada em 7.5 ± 1 nm. Sugere-se que o aumento dos domínios globulares pode induzir defeitos de superfície que, eventualmente, provocam espalhamento de luz, motivo pelo qual observa-se a diminuição da transparência de filmes híbridos contendo alta concentração de GPTMS.

Figura 24 - Espectros ATR-FTIR e Raman de a) Filme puro de CA, b) CA-GPTMS 5%, c) CA-GPTMS 10%, d) CA-GPTMS 20%, e) CA-GPTMS 35%, f) CA-GPTMS 50% e g) GPTMS líquido



Fonte: Autor

Os modos vibracionais de CA são identificados principalmente pelas bandas em 1738 cm^{-1} referentes à estiramento simétrico C=O dos grupos acetato (SILVERSTEIN; WEBSTER; KIEMLE, 2005). Modos vibracionais da cadeia de polimérica de celulose encontram-se na região de $1300\text{-}1000\text{ cm}^{-1}$. As bandas em 1222 , 1160 e 1030 cm^{-1} são associadas respectivamente ao estiramento simétrico C-O, ligação glicosídica C-O-C, estiramento assimétrico C-O-C do anel piranose (SILVERSTEIN; WEBSTER; KIEMLE, 2005). A funcionalização de filmes de CA com grupos epóxi e silanol provenientes da adição de GPTMS pode ser verificada pelo surgimento de bandas na região de $1000\text{-}700\text{ cm}^{-1}$. A banda larga centralizada em 855 cm^{-1} está associada aos modos vibracionais do anel epoxi descritos pelo estiramento C-C acoplado com torção C-O. Sugere-se que o aumento em intensidade da banda em 1160 cm^{-1} em função da concentração de GPTMS esteja associada ao acoplamento dos modos vibracionais de CA com estiramento C-O e *rocking* CH₃ do grupo metoxi (ŠAPIĆ et al., 2009). A banda observada em 902 cm^{-1} com intensidade moderada em filmes puros de CA pode ser atribuída a modos vibracionais de ligações glicosídicas (SILVERSTEIN; WEBSTER; KIEMLE, 2005). Visto que não possível identificar claramente bandas relacionadas aos modos vibracionais de ligações

siloxano ou silanol, acredita-se que a maioria das moléculas de GPTMS encontram-se não hidrolisadas.

Os espectros Raman também indicam a presença de grupos epóxi e metoxi filmes nos híbridos. A banda centrada em 1256 cm^{-1} claramente surge com a adição de GPTMS. Esta banda é atribuída ao estiramento C-C acoplado com vibrações *rocking* C-H do anel epóxi (ŠAPIĆ et al., 2009). Simultaneamente, observa-se a evolução em intensidade das bandas em 612 e 644 cm^{-1} de acordo com o aumento da concentração de GPTMS (ZHANG; FELDNER; FISCHER, 2011). Estas bandas são atribuídas aos modos vibracionais de estiramento assimétrico e simétrico de grupos $(-\text{Si}(\text{O}-\text{CH}_3)_3)$.

Os espectros RMN de ^{13}C e ^{29}Si no estado sólido dos filmes híbridos estão apresentados na Figura 24 (KONO; ERATA; TAKAI, 2002a, 2002b). Os espectros de ^{13}C para os filmes híbridos apresentam todos os picos característicos dos carbonos referente ao acetato de celulose (demarcados por C^x , com $x = 1 - 7$): $\text{C}^3 = 171\text{ ppm}$; $\text{C}^1 = 101.6\text{ ppm}$; $\text{C}^2, \text{C}^5 = 73.4\text{ ppm}$; $\text{C}^6 = 63.4\text{ ppm}$; $\text{C}^7 = 21\text{ ppm}$.

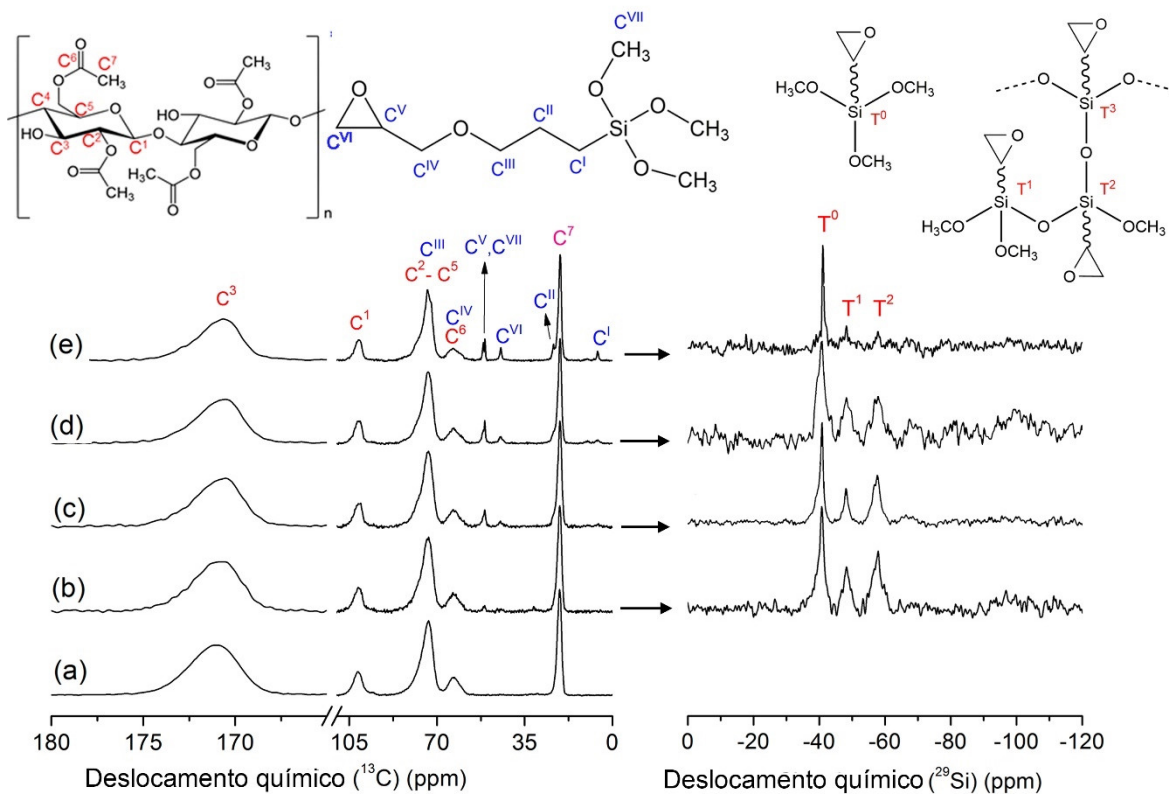
Os picos de RMN de ^{13}C no estado sólido para a molécula de GPTMS estão demarcados na Figura 24 por C^y , com $y = \text{I} - \text{VII}$. Os picos observados em 42.6 e 49.7 ppm (posição C^{VI} e C^{V} , respectivamente) são atribuídos aos grupos epóxi. A intensidade relativa é a mesma para todos os híbridos, indicando que não houve processo de polimerização.

As reações de hidrólise e condensação de GPTMS foram investigadas por RMN de ^{29}Si . Três linhas de ressonância são observadas no espectro de $^{29}\text{Si}\{\text{H}\}$ associados a unidades T^2 , T^1 e T^0 , o que indica que reações de hidrólise e condensação ocorrem de maneira parcial durante a preparação dos filmes híbridos. T^n representa o número de unidades siloxano ligadas em um silício.

Basicamente, a intensidade dos picos T^0 , T^1 e T^2 são bastante similares para híbridos contendo GPTMS em concentração inferior a 35 % em massa. Acima desta concentração, a contribuição de unidades T^0 aumenta consideravelmente, ou seja, uma maior população de moléculas de GPTMS não hidrolisadas está presente nesta proporção.

Os padrões de difração dos filmes de acetato puro e dos híbridos com concentração inferior a 20 % em massa de GPTMS exibem picos em 8.8° , 10.7° e 17.8° associados natureza semicristalina do acetato de celulose. As amostras CA-GPTMS 5%, 10% e 20% apresentam um ligeiro aumento da cristalinidade.

Figura 25 - O painel superior retrata a atribuição dos sinais de ^{13}C NMR e $^{29}\text{Si}\{1\text{H}\}$ CP-MAS NMR identificados sobre as estruturas químicas de GPTMS e CA. O painel inferior esquerdo exibe o ^{13}C NMR de (a) filme puro de CA, (b) CA-GPTMS 5%, (c) CA-GPTMS 20%, (d) CA-GPTMS 35% e (e) CA-GPTMS 50%. O espectro de $^{29}\text{Si}\{1\text{H}\}$ CP-MAS NMR no estado sólido de híbridos de CA-GPTMS híbridos estão demonstrados no painel inferior direito.



Fonte: Autor

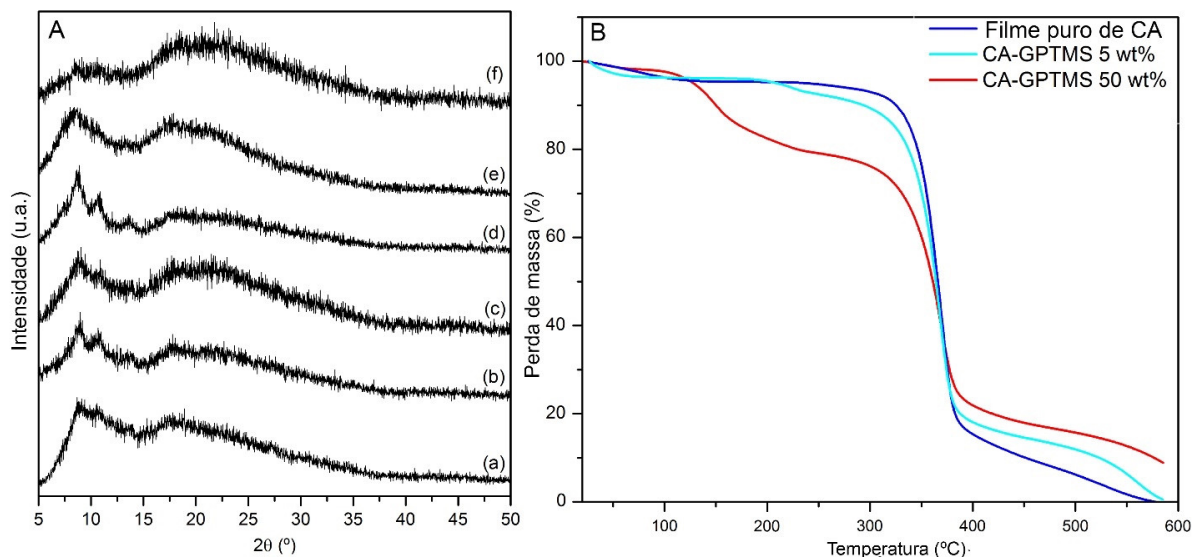
Para concentrações superiores 20% em massa de GPTMS, nota-se que os picos tornam-se menos definidos e ocorrência de alargamento. Sugere-se que o aumento de cristalinidade dos filmes híbridos contendo baixas concentrações de GPTMS seja parcialmente induzido por eventual empacotamento das cadeias de CA devido a restrições espaciais. Discute-se que este evento dá origem à morfologia globular observada com claro contraste de fase nas imagens de AFM dos filmes híbridos. Acima de 20 %, sugere-se que o desarranjo deste empacotamento é conduzido pelo crescente número de ligações intermoleculares (principalmente de ligações de hidrogênio e van der Waals) entre as moléculas de GPTMS e a cadeia de CA.

A curvas de termogravimetria estão demonstradas na Figura . A estabilidade térmica dos filmes de CA puro e dos híbridos CA-GPTMS 5 e 50% foram avaliadas em uma atmosfera oxidativa com o objetivo de estimar os resíduos inorgânicos.

As curvas para CA-GPTMS 5% e CA-GPTMS 50% exibiram dois eventos adicionais. A perda de massa observada para a região de temperaturas inferiores a 120 °C pode ser atribuída para desorção de acetona residual (solvente) e evaporação da água produzida como sub-produto

da hidrólise/condensação das moléculas de GPTMS. Eventos de perda de massa adicionais ocorrem entre 120 °C e 250 °C devido à eliminação de silanos monoméricos fisiosorvidos.

Figura 26. A) Difração de raios-X de a) filme puro de CA, b) CA-GPTMS 5%, c) CA-GPTMS 10%, d) CA-GPTMS 20%, e) CA-GPTMS 35%, f) CA-GPTMS 50%. B) Curva termogravimétrica do filme puro de CA, CA-GPTMS 5%, e CA-GPTMS 50%.



Fonte: Autor

A introdução de GPTMS não contribui para o aumento da estabilidade térmica dos filmes híbridos, independente da proporção investigada. Sugere-se que isto se deve ao fato que ambos GPTMS e CA possuem temperatura de decomposição similar (~370 °C).

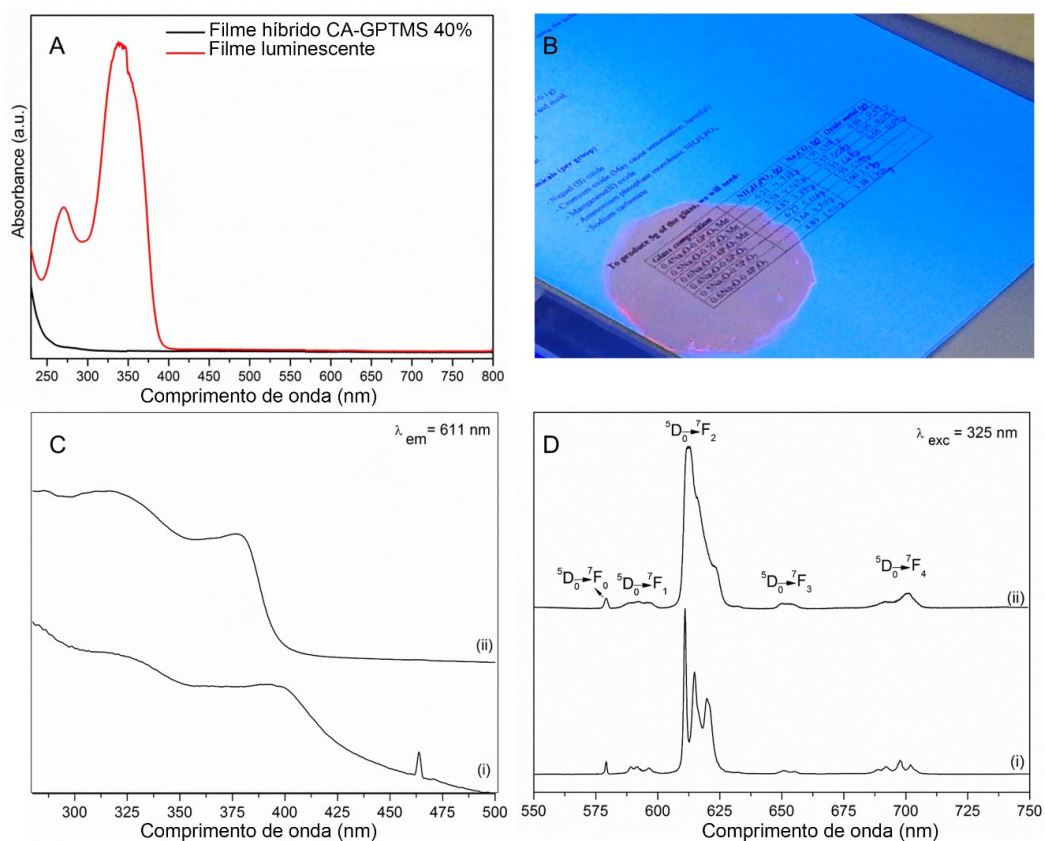
Para híbridos de CA-GPTMS, o principal evento térmico deve-se a decomposição das moléculas de GPTMS e da cadeia polimérica de CA, ambas com temperatura de decomposição similar. Para os híbridos de CA-GPTMS, o resíduo à 600 °C pode ser associado à formação de derivados de silício.

A fim de se estimar a potencial utilização de híbridos funcionais CA-GPTMS em aplicações ópticas, filmes luminescentes híbrido foram preparados utilizando a composição CA-GPTMS40% contendo 2% em peso do complexo de $[\text{Eu}(\text{TTA})_3(\text{H}_2\text{O})_2]$. Por sua vez, o complexo de $[\text{Eu}(\text{TTA})_3(\text{H}_2\text{O})_2]$ foi preparado segundo o protocolo descrito por Charles et al. (1965).

A Figura 27A exibe o espectro de absorção obtida por filmes híbrido de CA-GPTMS 40% e do filme híbrido luminescente. O espectro de absorção do filme híbrido dopado é caracterizada por duas bandas relativamente resolvidas centrados em 269 e 339 nm, que são atribuídas a transições $\pi-\pi^*$ da porção tenoil de TTA (MALTA et al., 1997; TEOTONIO et al., 2008). A

imagem destacada na Figura 27B demonstra a emissão vermelho-alaranjada intensa do filme híbrido luminescente sob uma folha de papel comum sob exposição à luz UV negra comercial.

Figura 27 - A) Espectro de absorção do filme híbrido de CA-GPTMS 40% e do filme luminescente preparado utilizando-se a composição de CA-GPTMS 40% contendo 2% (m/m) do complexo de $[\text{Eu}(\text{TTA})_3(\text{H}_2\text{O})_2]$. B) Foto de filme híbrido luminescente sob exposição à luz UV. C) Espectro de excitação e D) emissão de i) filme híbrido luminescente e ii) complexo de $[\text{Eu}(\text{TTA})_3(\text{H}_2\text{O})_2]$ (sólido).



Fonte: Autor

A Figura 27c mostra o espectro normalizado de excitação obtida para o complexo de $[\text{Eu}(\text{TTA})_3(\text{H}_2\text{O})_2]$. A banda larga observada com o máximo por volta de 325 nm é atribuída a transição do ligante localizado em S_0-S_1 (π, π^*) do ligante de TTA. Esta banda de absorção larga sobrepõe algumas bandas de absorção 4f-4f correspondentes às transições características do íon Eu^{3+} , ${}^7F_0 \rightarrow {}^5G_6$ (361 nm), ${}^7F_0 \rightarrow {}^5H_4$ (374 nm), ${}^7F_0 \rightarrow {}^5L_6$ (394 nm) e ${}^7F_0 \rightarrow {}^5D_3$ (415 nm), com exceção da banda referente à transição ${}^7F_0 \rightarrow {}^5D_2$ localizada em 463.8 nm no espectro de excitação do complexo de $[\text{Eu}(\text{TTA})_3(\text{H}_2\text{O})_2]$. O espectro de emissão do filme híbrido luminescente apresenta basicamente as mesmas bandas porém com visível alargamento, cujo efeito é endereçado à distribuição heterogênea dos sítios de íons Eu^{3+} .

Neste trabalho, também explorou-se a fabricação de materiais luminescentes a partir do reaproveitamento de poliestireno expandido (EPS). Utilizou-se D-limoneno, um solvente verde

derivado do óleo cítrico, para a dissolução de EPS em uma solução homogênea e límpida capaz de formar filmes transparentes. O D-limoneno utilizado foi concedido pela empresa Citrosuco S/A (Matão, Brasil) e a fonte de poliestireno (OS) foi obtida a partir de embalagens de EPS de caixas de reagentes.

A síntese do complexo luminescente $[\text{Eu}(\text{TTA})_3(\text{H}_2\text{O})_2]$ foi baseada no protocolo descrito por Charles et al, (1965). Filmes finos de PS foram preparados pela reciclagem de EPS usando D-limoneno como solvente. Uma solução estoque de PS foi preparada pela dissolução de 15.0 g de EPS de embalagens de reagentes em 100 mL de D-limoneno, seguida pela centrifugação a 6000 rpm para a remoção de partículas sólidas de impurezas presentes no EPS. A incorporação do complexo luminescente na solução de PS foi realizada dissolvendo diferentes porções de $[\text{Eu}(\text{TTA})_3(\text{H}_2\text{O})_2]$ (0,5; 1,0; 2,5 e 5.0 % m/v) na solução estoque de PS. A técnica de *spin coating* foi utilizada para a deposição dos filmes em substratos de quartzo que foram cortados com as dimensões de 25 mm x 25 mm. Os substratos foram previamente limpos em solução piranha e lavados diversas vezes com água, etanol e acetona. Filmes uniformes de PS- $[\text{Eu}(\text{TTA})_3(\text{H}_2\text{O})_2]$ foram obtidos em um *spincoater* SCS, modelo P6700 Series, pela deposição de 300 μL da solução de PS com diferentes porções de $[\text{Eu}(\text{TTA})_3(\text{H}_2\text{O})_2]$ sobre os substratos de quartzo a 1500 rpm por 60 segundos e secos em temperatura ambiente.

Os espectros de infravermelho (IV) foram obtidos a temperatura ambiente utilizando um espectrômetro de Transformada de Fourier Bruker modelo Vortex 70. Os espectros foram registrados no modo de reflectância total atenuada (attenuated total reflectance, ATR) no intervalo de número de onda de 4000 cm^{-1} a 400 cm^{-1} após 64 varreduras com resolução de 2 cm^{-1} .

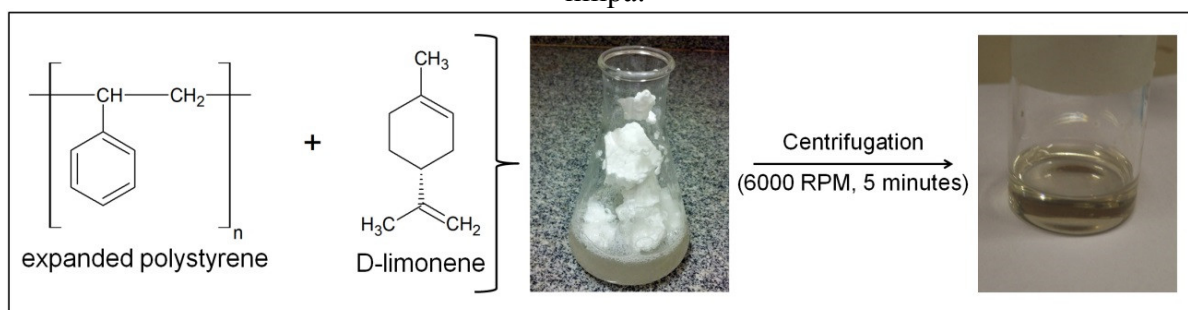
Os espectros de UV-Vis foram obtidos a temperatura ambiente utilizando um espectrofotômetro UV-Vis da marca Varian modelo Cary 5000. Os espectros de transmitância foram registrados no intervalo de comprimento de onda entre 800 nm a 200 nm com uma resolução de 1 nm.

Os espectros de emissão e excitação foram obtidos a temperatura ambiente em um espectrofluorímetro da marca Jobin-Yvon modelo Fluorolog FL3-22 e equipado com uma fotomultiplicadora R928 Hamamatsu e lâmpada de xenônio (450 W) como fonte de excitação e as medidas foram realizadas no modo *front face*.

O índice de refração (n) e a espessura (w) dos filmes foram obtidos pela técnica de acoplamento por prisma em um acoplador Metricon, modelo 2010/M usando um prisma com n na faixa entre 1,20 e 2,02 e um laser de 543 nm como fonte de luz.

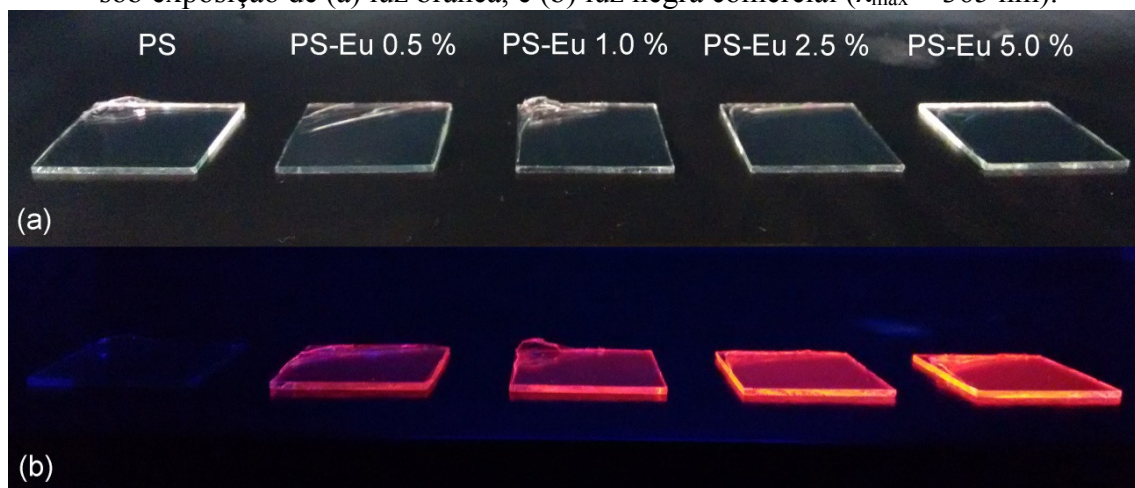
O processo de recuperação do PS a partir dos descartes de EPS usando o D-limoneno como solvente é mostrado na representação esquemática da Figura 28. Depois da incorporação do complexo de Eu^{3+} na solução estoque de PS, filmes finos, transparentes e luminescentes foram obtidos pela técnica de *spin coating*, como mostrado na Figura 29. Sob exposição à luz UV, os filmes contendo o complexo $[\text{Eu}(\text{TTA})_3(\text{H}_2\text{O})_2]$ mostram emissão de cor vermelha, característica do íon Eu^{3+} .

Figura 28 - Preparação da solução de PS 15% (m/v). A dissolução de poliestireno expandido em D-limoneno libera o ar retido em sua estrutura. Partículas maiores (impurezas) presentes no poliestireno expandido são removidas posteriormente para obter uma solução homogênea e limpa.



Fonte: Autor

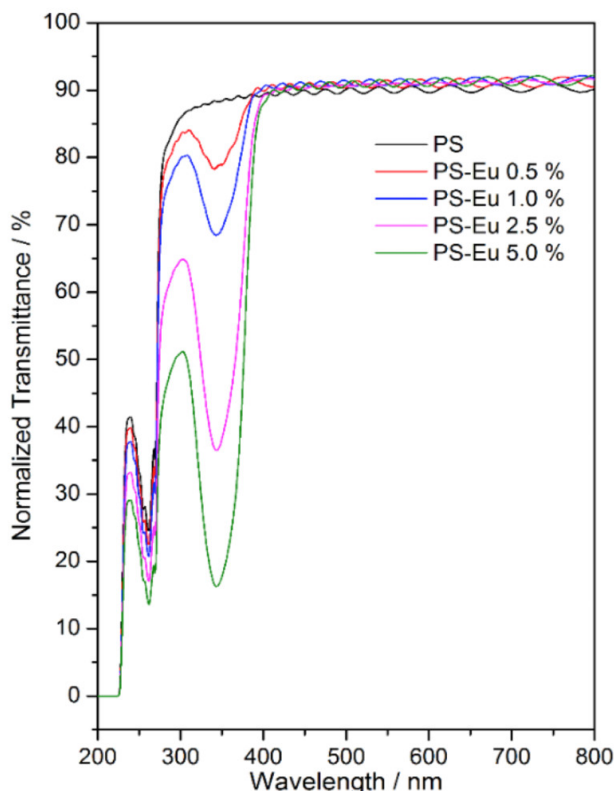
Figura 29 - Fotografia dos filmes de PS puro e PS-Eu obtidos pela técnica de “spin coating” e sob exposição de (a) luz branca, e (b) luz negra comercial ($\lambda_{\text{max}} = 365 \text{ nm}$).



Fonte: Autor

A alta transparência dos filmes pode ser confirmada pelos espectros de UV-Vis dos filmes de PS e PS-Eu na Figura 30, com valores superiores a 90% de transparência na região visível. O pico observado a 343 nm para as amostras PS-Eu corresponde à transição $\text{singlete} \rightarrow \text{singlete}^*$ do ligante tta (MALTA et al., 1997). A maior concentração de $[\text{Eu}(\text{TTA})_3(\text{H}_2\text{O})_2]$ estudada nos filmes de PS foi 5,0 % (m/v) devido à solubilidade limitada do complexo em D-limoneno.

Figura 30 - Espectro de transmitância na região do ultravioleta-visível de filmes de PS puro e PS-Eu contendo diferentes concentrações de complexo $[\text{Eu}(\text{TTA})_3(\text{H}_2\text{O})_2]$.



Fonte: Autor

A banda intensa observada em 262 nm no espectro de UV-Vis está relacionada com a transição $\pi \rightarrow \pi^*$ do grupo fenil da matriz de PS (CLARK; WILLIAMS, 1967; KHAN et al., 2002; LI; ZHOU; JIANG, 1991). Cabe ressaltar que as franjes de interferências observadas no espectro dão evidência da espessura micrométrica dos filmes (SHAABAN; YAHIA; ELMETWALLY, 2012; SWANEPOEL, 1983). Tanto a espessura (w) quanto o índice de refração (n) dos filmes foram determinados pela técnica de acoplamento por prisma analisando o padrão m-line com polarização do transversal elétrico (TE) (RIBEIRO et al., 2000; ULRICH; TORGE, 1973). Os valores referentes à n , w e o número de modos de propagação da luz são apresentados na Tabela 3.

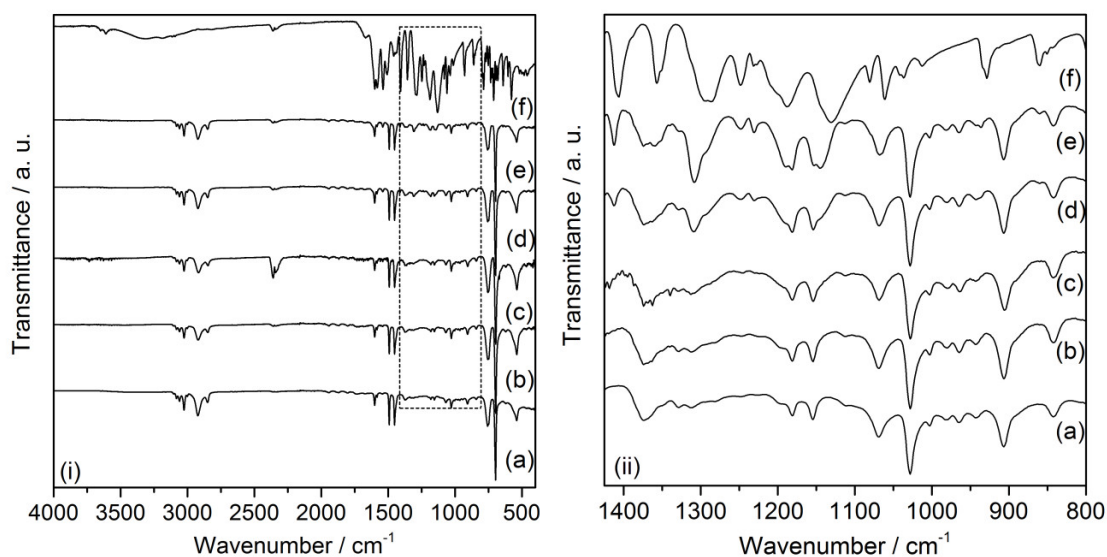
A deposição dos filmes em substratos de quartzo resulta em guias de onda, de modo que a luz é guiada entre a interface do filme e do substrato. O número de modos de propagação da luz em um guia de onda depende de fatores como n e w e, uma vez que n e w aumentam com a quantidade de $[\text{Eu}(\text{TTA})_3(\text{H}_2\text{O})_2]$ incorporada nos filmes, o número de modos também aumenta. A incorporação do complexo de Eu^{3+} na matriz de PS resulta em uma maior interação entre a luz e os componentes do filme, reduzindo a velocidade de propagação da luz e, conseqüentemente, aumentando n .

Tabela 3. Parâmetros ópticos dos filmes de PS e PS-Eu medidos em 543 nm com polarização TE.

Amostra	[Eu(TTA) ₃ (H ₂ O) ₂] (% m/v)	<i>n</i> em 543 nm (±0.0005)	<i>w</i> (± 0.1 μm)	número de modos em 543 nm
OS	-	1.5594	1.5	4
PS-Eu 0.5 %	0.5	1.5625	1.5	4
PS-Eu 1.0 %	1.0	1.5789	1.9	6
PS-Eu 2.5 %	2.5	1.5788	2.1	6
PS-Eu 5.0 %	5.	1.5862	2.5	7

A Figura 31, i e ii mostram o espectro de IV do complexo [Eu(TTA)₃(H₂O)₂] e dos filmes de PS e PS-Eu na região de 4000-400 cm⁻¹ e 1425-800 cm⁻¹, respectivamente. Os espectros dos filmes mostram basicamente o mesmo perfil, indicando que a incorporação do complexo de Eu³⁺ na matriz de PS não modifica a estrutura do polímero. A presença das bandas em 1376, 1154 e 842 cm⁻¹ nos espectros dos filmes estão relacionados com a fase amorfa do PS, indicando que o PS recuperado dos descartes do EPS tem estrutura conformacional atática. As bandas em 1154 and 842 cm⁻¹ são associadas com os modos do grupo fenil (ALBUNIA; MUSTO; GUERRA, 2006). Como resultado da presença do [Eu(TTA)₃(H₂O)₂] na matriz de PS, as bandas em 1181 e 1154 cm⁻¹ do PS são alargadas pela superposição com os estiramentos $\nu(\text{C}=\text{C})$ e $\nu(\text{C}-\text{F}_3)$ do complexo em 1188 e 1130 cm⁻¹, respectivamente.

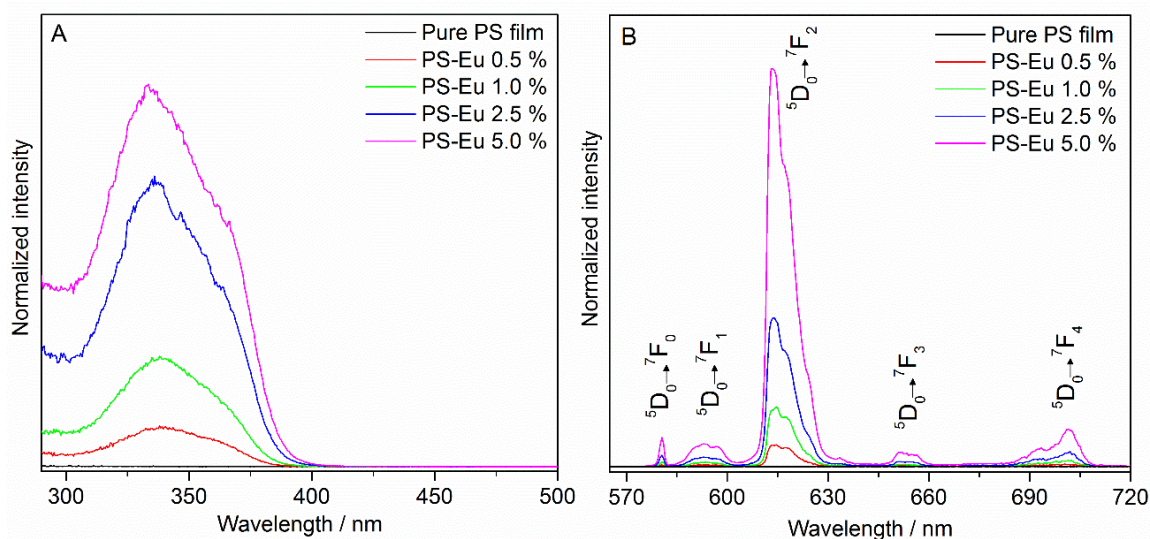
Figura 31 - Espectro vibracional na região do infravermelho por reflectância total atenuada dos filmes de (a) PS puro, (b) PS-Eu 0.5 %; (c) PS-Eu 1.0 %; (d) PS-Eu 2.5 %, (e) PS-Eu 5.0 % e, (f) pó do complexo de [Eu(TTA)₃(H₂O)₂]. (ii) Espectros das amostras (a)-(e) ampliados na região de 1425-800 cm⁻¹.



Fonte: Autor

As propriedades luminescentes do complexo e filmes foram investigadas pelos estudos de fotoluminescência. Os espectros de excitação e emissão dos filmes são mostrados na Figura 32. Os espectros de excitação e emissão do $[\text{Eu}(\text{TTA})_3(\text{H}_2\text{O})_2]$ no estado sólido é mostrado na Figura 33. Tanto para os filmes de PS-Eu quanto para o complexo puro, as bandas largas em comprimentos de onda menores que 400 nm estão relacionadas à absorção do ligante tta e à transferência de energia para o íon Eu^{3+} (DUARTE et al., 2013). Especificamente, a banda larga em 335 nm do espectro de excitação dos filmes PS-Eu na Figura 32A é atribuída à transição $\text{singlete} \rightarrow \text{singlete}^*$ do ligante tta (MALTA et al., 1997). A linha fina da transição ${}^7\text{F}_0 \rightarrow {}^5\text{D}_2$ em 464 nm é observada para o complexo $[\text{Eu}(\text{TTA})_3(\text{H}_2\text{O})_2]$ (Figura 33A), mas dificilmente observada para os filmes PS-Eu. O complexo no estado sólido apresenta uma maior seção para absorção da luz na região do UV, o que leva à saturação e distorção do espectro de excitação (BLASSE; MEIJERINK; DONEGÁ, 1995; DUARTE et al., 2012).

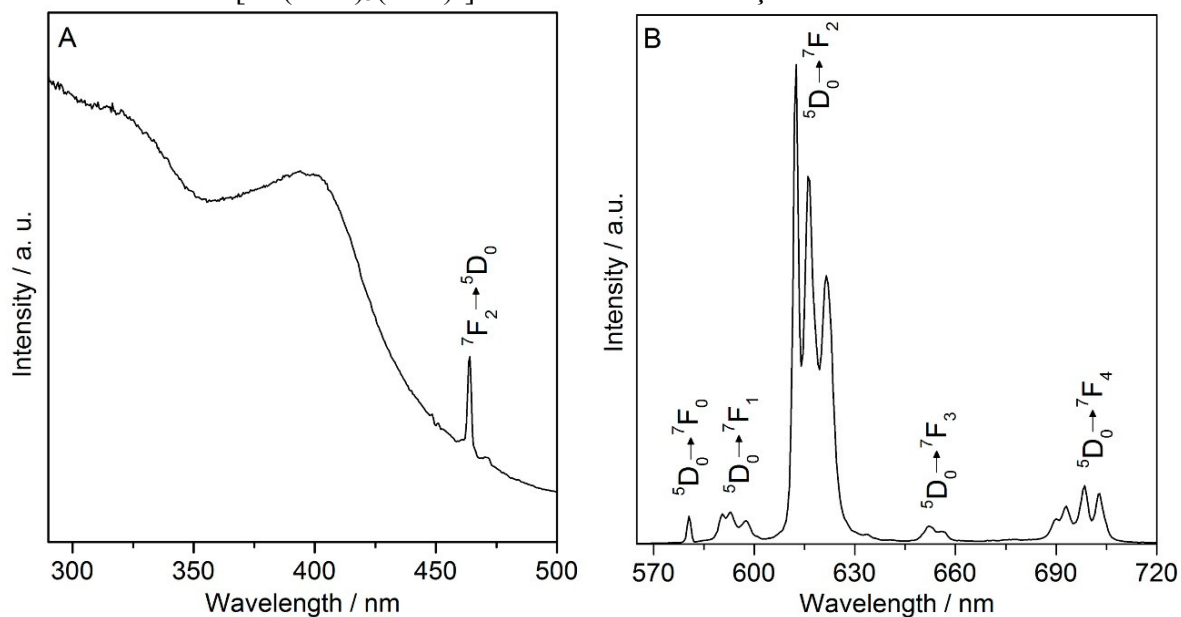
Figura 32 - (A) Espectro de excitação de filmes de PS puro e PS-Eu obtidos monitorando a emissão em 614 nm. (B) Espectro de emissão dos filmes de PS puro e PS-Eu monitorando a excitação em 355 nm.



Fonte: Autor

As linhas finas no espectro de emissão são características das transições ${}^5\text{D}_0 \rightarrow {}^7\text{F}_J$ ($J=0-4$) do íon Eu^{3+} . A forte emissão de cor vermelha do complexo e dos filmes é resultado da transição hipersensitível ${}^5\text{D}_0 \rightarrow {}^7\text{F}_2$ de alta intensidade em torno de 612 nm. As seguintes transições do nível ${}^5\text{D}_0$ para o nível ${}^7\text{F}_J$ do íon Eu^{3+} podem ser observadas para o complexo: ${}^5\text{D}_0 \rightarrow {}^7\text{F}_0$ (580,5 nm), ${}^5\text{D}_0 \rightarrow {}^7\text{F}_1$ (590,5; 593,0 e 597,5 nm), ${}^5\text{D}_0 \rightarrow {}^7\text{F}_2$ (612,5; 616,0 e 621,5 nm), ${}^5\text{D}_0 \rightarrow {}^7\text{F}_3$ (652,0 e 655,5 nm), ${}^5\text{D}_0 \rightarrow {}^7\text{F}_4$ (690,0; 693,0; 698,5 e 703,0 nm).

Figura 33 - Espectro de excitação obtido da emissão do complexo em pó de $[\text{Eu}(\text{TTA})_3(\text{H}_2\text{O})_2]$ monitorando a excitação em 396 nm.



Fonte: Autor

A distorção do espectro de emissão do complexo $[\text{Eu}(\text{TTA})_3(\text{H}_2\text{O})_2]$ mostrado na Figura 33B em comparação ao espectro de emissão dos filmes de PS-Eu na Figura 33B está relacionada com a presença do Eu^{3+} em uma matriz polimérica amorfa. Além disso, a transição ${}^5D_0 \rightarrow {}^7F_0$ do Eu^{3+} nos filmes PS-Eu apresentam apenas uma linha fina com valor de largura a meia altura maior que 40 cm^{-1} , sugerindo a ocorrência de um único sítio sendo ocupado pelo Eu^{3+} em um ambiente de baixa simetria (DUARTE et al., 2012; KAI; PARRA; BRITO, 2008).

ATTACHMENTS

Permission grants to reproduce the article Silva, R. R. et al. *Journal Materials Chemistry C*, v. 1, n. 43, p. 7181-7190, 2013. Available at <http://dx.doi.org/10.1039/C3TC30903G>

[Silk fibroin biopolymer films as efficient hosts for DFB laser operation](#)

R. R. da Silva, C. T. Dominguez, M. V. dos Santos, R. Barbosa-Silva, M. Cavicchioli, L. M. Christovan, L. S. A. de Melo, A. S. L. Gomes, C. B. de Araújo and S. J. L. Ribeiro, *J. Mater. Chem. C*, 2013, **1**, 7181

DOI: 10.1039/C3TC30903G

If you are not the author of this article and you wish to reproduce material from it in a third party non-RSC publication you must [formally request permission](#) using RightsLink. Go to our [Instructions for using RightsLink page](#) for details.

Authors contributing to RSC publications (journal articles, books or book chapters) do not need to formally request permission to reproduce material contained in this article provided that the correct acknowledgement is given with the reproduced material.

Reproduced material should be attributed as follows:

- For reproduction of material from NJC:
Reproduced from Ref. XX with permission from the Centre National de la Recherche Scientifique (CNRS) and The Royal Society of Chemistry.
- For reproduction of material from PCCP:
Reproduced from Ref. XX with permission from the PCCP Owner Societies.
- For reproduction of material from PPS:
Reproduced from Ref. XX with permission from the European Society for Photobiology, the European Photochemistry Association, and The Royal Society of Chemistry.
- For reproduction of material from all other RSC journals and books:
Reproduced from Ref. XX with permission from The Royal Society of Chemistry.

If the material has been adapted instead of reproduced from the original RSC publication "Reproduced from" can be substituted with "Adapted from".

In all cases the Ref. XX is the XXth reference in the list of references.

If you are the author of this article you do not need to formally request permission to reproduce figures, diagrams etc. contained in this article in third party publications or in a thesis or dissertation provided that the correct acknowledgement is given with the reproduced material.

Reproduced material should be attributed as follows:

- For reproduction of material from NJC:
[Original citation] - Reproduced by permission of The Royal Society of Chemistry (RSC) on behalf of the Centre National de la Recherche Scientifique (CNRS) and the RSC
- For reproduction of material from PCCP:
[Original citation] - Reproduced by permission of the PCCP Owner Societies
- For reproduction of material from PPS:
[Original citation] - Reproduced by permission of The Royal Society of Chemistry (RSC) on behalf of the European Society for Photobiology, the European Photochemistry Association, and RSC
- For reproduction of material from all other RSC journals:
[Original citation] - Reproduced by permission of The Royal Society of Chemistry

If you are the author of this article you still need to obtain permission to reproduce the whole article in a third party publication with the exception of reproduction of the whole article in a thesis or dissertation.

Permission grants to reproduce the article Silva, R. R. et al. *Journal of Sol-Gel Science and Technology*, 2016 (*in press*). Available at <http://dx.doi.org/10.1007/s10971-016-4089-x>

SPRINGER LICENSE TERMS AND CONDITIONS

Jun 22, 2016

This Agreement between Robson R Silva ("You") and Springer ("Springer") consists of your license details and the terms and conditions provided by Springer and Copyright Clearance Center.

License Number	3880980084309
License date	Jun 02, 2016
Licensed Content Publisher	Springer
Licensed Content Publication	Journal of Sol-Gel Science and Technology
Licensed Content Title	Multifunctional organic–inorganic hybrids based on cellulose acetate and 3-glycidoxypropyltrimethoxysilane
Licensed Content Author	Robson R. Silva
Licensed Content Date	Jan 1, 2016
Type of Use	Thesis/Dissertation
Portion	Full text
Number of copies	1
Author of this Springer article	Yes and you are a contributor of the new work
Order reference number	
Title of your thesis / dissertation	New photonic structures: I – Self assembly of 1D Te nanostructures; II – Multifunctional biopolymers and reused plastics
Expected completion date	Jun 2016
Estimated size(pages)	210

Requestor Location Robson R Silva
1234 Paulino Rodella Av

Araraquara, SP 14801766
Brazil
Attn: Dr. Robson Silva

Billing Type Invoice

Billing Address Dr. Robson Silva
1234 Paulino Rodella Av

Araraquara, Brazil 14801766
Attn: Dr. Robson Silva

Total 0.00 USD

Terms and Conditions

Introduction

The publisher for this copyrighted material is Springer. By clicking "accept" in connection with completing this licensing transaction, you agree that the following terms and conditions apply to this transaction (along with the Billing and Payment terms and conditions established by Copyright Clearance Center, Inc. ("CCC"), at the time that you opened your Rightslink account and that are available at any time at <http://myaccount.copyright.com>).

Limited License

With reference to your request to reuse material on which Springer controls the copyright, permission is granted for the use indicated in your enquiry under the following conditions:

- Licenses are for one-time use only with a maximum distribution equal to the number stated in your request.
- Springer material represents original material which does not carry references to other sources. If the material in question appears with a credit to another source, this permission is not valid and authorization has to be obtained from the original copyright holder.
- This permission
 - is non-exclusive

- is only valid if no personal rights, trademarks, or competitive products are infringed.
- explicitly excludes the right for derivatives.
 - Springer does not supply original artwork or content.
 - According to the format which you have selected, the following conditions apply

accordingly:

- **Print and Electronic:** This License include use in electronic form provided it is password protected, on intranet, or CD-Rom/DVD or E-book/E-journal. It may not be republished in electronic open access.
- **Print:** This License excludes use in electronic form.
- **Electronic:** This License only pertains to use in electronic form provided it is password protected, on intranet, or CD-Rom/DVD or E-book/E-journal. It may not be republished in electronic open access.

For any electronic use not mentioned, please contact Springer at permissions.springer@spi-global.com.

- Although Springer controls the copyright to the material and is entitled to negotiate on rights, this license is only valid subject to courtesy information to the author (address is given in the article/chapter).

- If you are an STM Signatory or your work will be published by an STM Signatory and you are requesting to reuse figures/tables/illustrations or single text extracts, permission is granted according to STM Permissions Guidelines: <http://www.stm-assoc.org/permissions-guidelines/>

For any electronic use not mentioned in the Guidelines, please contact Springer at permissions.springer@spi-global.com. If you request to reuse more content than stipulated in the STM Permissions Guidelines, you will be charged a permission fee for the excess content.

Permission is valid upon payment of the fee as indicated in the licensing process. If permission is granted free of charge on this occasion, that does not prejudice any rights we might have to charge for reproduction of our copyrighted material in the future.

-If your request is for reuse in a Thesis, permission is granted free of charge under the following conditions:

This license is valid for one-time use only for the purpose of defending your thesis and with a maximum of 100 extra copies in paper. If the thesis is going to be published, permission needs to be reobtained.

- includes use in an electronic form, provided it is an author-created version of the thesis on his/her own website and his/her university's repository, including UMI (according to the definition on the Sherpa website: <http://www.sherpa.ac.uk/romeo/>);
- is subject to courtesy information to the co-author or corresponding author.

Geographic Rights: Scope

Licenses may be exercised anywhere in the world.

Altering/Modifying Material: Not Permitted

Figures, tables, and illustrations may be altered minimally to serve your work. You may not alter or modify text in any manner. Abbreviations, additions, deletions and/or any other alterations shall be made only with prior written authorization of the author(s).

Reservation of Rights

Springer reserves all rights not specifically granted in the combination of (i) the license details provided by you and accepted in the course of this licensing transaction and (ii) these terms and conditions and (iii) CCC's Billing and Payment terms and conditions.

License Contingent on Payment

While you may exercise the rights licensed immediately upon issuance of the license at the end of the licensing process for the transaction, provided that you have disclosed complete and accurate details of your proposed use, no license is finally effective unless and until full payment is received from you (either by Springer or by CCC) as provided in CCC's Billing and Payment terms and conditions. If full payment is not received by the date due, then any license preliminarily granted shall be deemed automatically revoked and shall be void as if never granted. Further, in the event that you breach any of these terms and conditions or any of CCC's Billing and Payment terms and conditions, the license is automatically revoked and shall be void as if never granted. Use of materials as described in a revoked license, as well as any use of the materials beyond the scope of an unrevoked license, may constitute copyright infringement and Springer reserves the right to take any and all action to protect its copyright in the materials.

Copyright Notice: Disclaimer

You must include the following copyright and permission notice in connection with any reproduction of the licensed material:

"Springer book/journal title, chapter/article title, volume, year of publication, page, name(s) of author(s), (original copyright notice as given in the publication in which the material was originally published) "With permission of Springer"

In case of use of a graph or illustration, the caption of the graph or illustration must be included, as it is indicated in the original publication.

Warranties: None

Springer makes no representations or warranties with respect to the licensed material and adopts on its own behalf the limitations and disclaimers established by CCC on its behalf in its Billing and Payment terms and conditions for this licensing transaction.

Indemnity

You hereby indemnify and agree to hold harmless Springer and CCC, and their respective officers, directors, employees and agents, from and against any and all claims arising out of your use of the licensed material other than as specifically authorized pursuant to this license.

No Transfer of License

This license is personal to you and may not be sublicensed, assigned, or transferred by you without Springer's written permission.

No Amendment Except in Writing

This license may not be amended except in a writing signed by both parties (or, in the case of Springer, by CCC on Springer's behalf).

Objection to Contrary Terms

Springer hereby objects to any terms contained in any purchase order, acknowledgment, check endorsement or other writing prepared by you, which terms are inconsistent with these terms and conditions or CCC's Billing and Payment terms and conditions. These terms and conditions, together with CCC's Billing and Payment terms and conditions

(which are incorporated herein), comprise the entire agreement between you and Springer (and CCC) concerning this licensing transaction. In the event of any conflict between your obligations established by these terms and conditions and those established by CCC's Billing and Payment terms and conditions, these terms and conditions shall control.

Jurisdiction

All disputes that may arise in connection with this present License, or the breach thereof, shall be settled exclusively by arbitration, to be held in the Federal Republic of Germany, in accordance with German law.

Other conditions:

V 12AUG2015

Questions? customercare@copyright.com or +1-855-239-3415 (toll free in the US) or +1-978-646-2777.
